Max-Planck-Institut für Meteorologie

REPORT No. 15

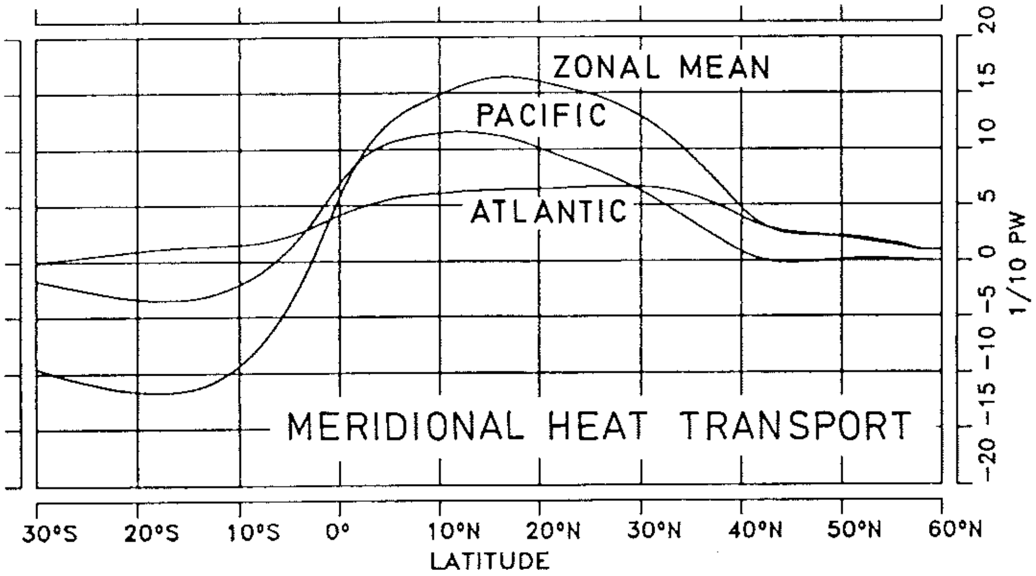

AN ATLAS BASED ON THE 'COADS' DATA SET:

THE BUDGETS OF HEAT, BUOYANCY AND TURBULENT KINETIC ENERGY AT THE SURFACE OF THE GLOBAL OCEAN

by

JOSEF M. OBERHUBER

HAMBURG, MARCH 1988

AUTHOR:

JOSEF M. OBERHUBER
MAX-PLANCK-INSTITUT
METEOROLOGIE

MAX-PLANCK-INSTITUT
FÜR METEOROLOGIE
BUNDESSTRASSE 55
D-2000 HAMBURG 13
F.R. GERMANY

Telefon nat.: (040) 41 14 - 1
Telefon int.: + 49 40 41 14 - 1
Telex-Nr.: 211092
Telemail: MPI.METEOROLOGY
Telefax nat.: (040) 41 14 - 298
Telefax int.: + 49 40 41 14 - 298

Max-Planck-Institute for Meteorology
Report No. 15

AN ATLAS BASED ON THE 'COADS' DATA SET:

THE BUDGETS OF HEAT, BUOYANCY AND TURBULENT KINETIC ENERGY AT THE SURFACE OF THE GLOBAL OCEAN

Josef M. Oberhuber
Max-Planck-Institut für Meteorologie
2000 Hamburg 13 , Bundesstrasse 55 , FRG

March 1988

Abstract

This atlas presents mean fields of surface fluxes of heat, buoyancy and turbulent kinetic energy into the global ocean, for each month averaged over 1950-79. From these basic fluxes we try to estimate the mixed layer Monin-Obukhov length. Finally, we present an alternative to the Newtonian cooling formulation as it is often used in oceanic circulation models.

The main data source for this study is the 'COADS'. Additionally, we take the rainfall analysis from Shea and the surface salinity from Levitus. Fields are left blank in regions where the 'COADS' are uncertain because of too few available measurements. All derived quantities are presented in a spatial resolution of $2^o \times 2^o$ as monthly means and annual means.

In order to calculate the heat fluxes we used bulk parameterizations for the sensible and latent heat flux and parameterizations for incoming short wave radiation and outgoing longwave radiation. From the resulting heat fluxes, the evaporation rate and the rainfall data we derived the buoyancy flux. We also estimated the turbulent kinetic energy input. A mixed layer model allowed us to evaluate the mixed layer Monin-Obukhov length. Finally, we calculated the heat flux coupling coefficients between atmosphere and ocean. Together with the derived net heat flux and the observed SST we propose a formulation of a simple heat forcing similar to the Newtonian cooling one but with much more realism.

With this atlas it is our aim to help ocean modellers in designing their model forcing. We provide a summary of all important fluxes into the ocean which directly influence the ocean dynamics and the underlying formulas.

All basic fields (SST, air temperature, scalar wind and its standard deviation, humidity, cloudiness, rainfall, surface salinity and sea level pressure) as presented by Wright (1988) in a companion atlas and all derived fields shown in this atlas are available on magnetic tape.

Contents

1 Introduction

The seasonal variation in the storage and release of heat and the ability of the ocean to transport heat on much longer time scales are important aspects of the earth's climate. But also the boundary layer at the ocean surface plays a role because it determines the exchange processes between the surface and the deep ocean. Wind stirring and buoyancy fluxes are the key parameters here. In order to estimate all those fluxes we need a good data base and, additionally, well tuned parameterizations. For this purpose we need, as a minimum, data of air temperature, wind, humidity and cloudiness to determine the budget of radiative and turbulent fluxes, and rainfall to obtain an estimate of the buoyancy flux.

A preliminary set of basic fields was prepared by Esbensen and Kushnir (1981) based on an earlier-available data set. However, with the availability of the 'trimmed' (fully quality-controlled) version of the 'Comprehensive Ocean-Atmosphere Data Set ' (COADS), which is based on more observations than was Esbensen and Kushnir's set, it was considered desirable now to prepare a new set of basic fields, based on a standard reference period 1950-79. This work was carried out by Woodruff et al. (1987). Wright (1988) prepared an atlas of mean fields from the COADS. His results justify our hopes that these fields are more detailed than those of Esbensen and Kushnir in many areas, and are more consistent with our expectations of how such fields should look. Since the COADS are presented with a relatively high spatial resolution of $2^o \times 2^o$, we may hope that typical length scales in the atmosphere are better represented than in Esbensen and Kushnir's $4^o \times 5^o$ grid or in the $5^o \times 5^o$ grid of Hsiung (1986) who used a more recent data set. However, the COADS are not of uniform quality spatially. There are large gaps in data coverage in the areas of the northern hemisphere ice edge, the southeast Pacific, and midlatitudes of the southern hemisphere. Data near the Antarctic ice edge are adequate only during the southern summer. Therefore, it is not yet possible to derive a global budget of fluxes at the ocean surface from the COADS with high certainty everywhere. Nevertheless, these fields have been proved to be very useful in numerical experiments on the forcing of the Atlantic ocean circulation carried out with an isopycnal model (Oberhuber,1988). Also Rosati and Miyakoda (1987) showed that a detailed heat flux computation is more appropriate in forcing an oceanic model than the Newtonian formulation.

Because results from models of the general circulation often suffer from insufficiently known forcing, we have endeavoured to make a complete data set available to the community of modellers, prepare parameterizations for the surface fluxes which can be used in models and demonstrate how these parameterizations work with observed data.

The basic fields which were prepared by Wright and used for this study are sea surface temperature (SST), surface air temperature, scalar wind speed, standard deviation of scalar wind speed, cloudiness, humidity and surface pressure. The rainfall analysis is from Shea (1986) and the surface salinity from Levitus (1982).

The derived fields are short-wave, long-wave and net radiation budgets; latent, sensible and net downward heat fluxes; net downward fresh water flux; resulting buoyancy fluxes; fluxes of turbulent kinetic energy; an estimate for the mixed layer Monin-Obukhov length and the ocean-atmosphere coupling coefficient for heat. This atlas presents monthly and annual mean maps of all the derived fields. All these fields are made available on magnetic tape.

2 Data Sources

The data used were the COADS as described by Woodruff et al. (1987). They are quality-controlled. Peter Wright (1988) derived the climatology from the COADS for the years 1950-79. He formed the mean for each calendar month in each 2-degree square, accepting the mean if at least 10 out of the 30 values were present, or at least 9 in the case of SST and air temperature. The data are filtered.

The data set for precipitation was prepared by Dennis Shea (1986) on a $2.5^o \times 2.5^o$ grid and projected on to our $2^o \times 2^o$ grid. It was derived from land or island station records and completed by satellite observations. The buoyancy calculation requires in addition the surface salinity of the world ocean. These data are taken from Levitus (1982) in a spatial resolution of $1^o \times 1^o$ and projected on to our grid.

3 Description of Parameterizations

The data sets required to determine surface fluxes of heat, buoyancy and turbulent kinetic energy are surface air temperature, sea surface temperature, relative humidity, cloudiness, the time averaged absolute wind speed and its standard deviation, surface salinity and sea level pressure. All data are monthly mean climatological values except the surface salinity, which is provided only as an annual mean because of the small variation of the climatological mean surface salinity throughout the year.

The parameterizations for the fluxes are not generally agreed upon. There are some uncertainties. For instance, values for the drag coefficients given in the literature vary from source to source. An unknown in the data is the height above sea level of each measurement. Because the COADS are based on ship observations each measurement is taken at a different height depending on the ship instrumentation. This leads to an inhomogeneous data set. We decided to take a mean height of 10 m. From the later described formula for the drag coefficient we recognize that this choice is rather uncritical. The parameterization for radiative heat fluxes is uncertain because we do not consider effects of atmospheric stratification or of different radiative properties of various cloud types. We have tried to parameterize the fluxes in terms of surface quantities or vertical mean values. The most uncertain quantity in our study is the precipitation. However, we know that in the climatological mean the fresh water flux gives only a second order contribution to the buoyancy flux compared with the heat flux. Therefore, the final results for the buoyancy flux should not be significantly influenced by uncertainties in the precipitation data. Other, possibly better, data sets such as that of Dorman and Bourke (1981) do not give significantly different results in the buoyancy flux in the tropics and midlatitudes.

3.1 Parameterization of Surface Heat Fluxes

The total surface heat flux Q consists of the contribution due to short wave radiation Q_s, long wave radiation Q_l, sensible heat flux Q_H and latent heat flux Q_L. The turbulent surface heat fluxes, namely the sensible and latent heat fluxes, are estimated by the bulk formulations

$$\begin{aligned} Q_H &= \rho_a c_{p,air} c_H V(T_a - T_s) && (1) \\ Q_L &= \rho_a L_w c_L V(q_a - q_s) && (2) \end{aligned}$$

where T_a is the air temperature, T_s the sea surface temperature, q_a the air specific humidity and q_s the specific humidity close to the surface, assumed to be saturated. $c_{p,air} = 1005\ WsKg^{-1}K^{-1}$ is the specific heat of air and $L_w = 2.5 \times 10^6\ WsKg^{-1}$ the latent heat of evaporation. The specific humidity q is given by the vapor pressure e and the atmospheric surface pressure p. Through all following relations e and p are in Pascal and T is in Kelvin.

$$\begin{aligned} e &= 611 \times 10^{(T-273.16)/(T-35.86)*7.5} && (3) \\ q &= \frac{0.622e}{p - 0.378e} && (4) \end{aligned}$$

From this we obtain $q_s = q(p, e(T_s))$ and $q_a = q(p, r \times e(T_a))$. The transfer coefficients c_H and c_L are calculated as proposed by Large and Pond (1982). The formulas are given in the next section.

The net effect of long wave radiation at the surface is taken from Berliand (1952)

$$Q_l = \varepsilon\sigma T_a^4(.39 - .05\sqrt{e/100})(1 - \chi n^2) + 4\varepsilon\sigma T_a^3(T_s - T_a) \qquad (5)$$

where $\varepsilon = 0.97$ is the emissivity of water, $\sigma = 5.67 \times 10^{-8} Wm^{-2}K^{-4}$ the Stefan-Boltzmann constant and n the relative cloud cover. In order to account for various properties of different cloud types, χ is allowed to vary linearly with latitude as Budyko (1974) has proposed.

The insolation is calculated from the daily averaged heat flux at the top of the atmosphere and is then corrected after Zillmann (1972) for relative humidity and inclination. For instance, Parkinson and Washington (1979) already used Zillmann's formula for modelling the sea ice. Hsiung (1985,1986) used the empirical formula of Seckel and Beaudry (1973). However, since it is valid only in a latitudinal band we decided to choose Zillmann's formula. It can be used in global models. Following Reed (1977), the insolation is finally reduced by a cloudiness factor. In contrast to Esbensen and Kushnir (1981) we do not use the cloudiness correction of Berliand (1960) which gives too low insolation at high cloud cover, as already pointed out by Weare et al. (1981). The resulting relations required to compute the daily mean downward short wave radiative flux Q_s are:

$$\begin{aligned} \cos\eta &= \sin\delta\sin\varphi + \cos\delta\cos\varphi\cos t && (6) \\ \sin\eta_{noon} &= \sin\delta\sin\varphi + \cos\delta\cos\varphi && (7) \\ \kappa &= 1 - 0.62n + 0.0019\eta_{noon} && (8) \\ Q_s &= \alpha\frac{\kappa\gamma}{2\pi}\int_{t_1}^{t_2} \frac{S_o\cos^2\eta}{((\cos\eta + 2.7)re(T_a)/p + 1.085\cos\eta + 0.1)}(\frac{\bar{d}}{d})^2 dt && (9) \end{aligned}$$

Here $S_o = 1370 W m^{-2}$ is the solar constant and η the sun elevation. In order to represent an albedo of .06 over sea, we chose $\gamma = .94$. α is a later explained tuning coefficient and is set to 0.9. d denotes the actual distance between the sun and earth and $\bar{d}$ its annual average. Following Paltridge and Platt (1976) the ratio $(\bar{d}/d)^2$ is estimated in terms of the Julian Day β :

$$\begin{aligned}(\frac{\bar{d}}{d})^2 &= 1.00011 + 0.00128\, sin(\beta) + 0.034221\, cos(\beta) \\ &+ 0.000077\, sin(2\beta) + 0.000719\, cos(2\beta) \qquad (10)\end{aligned}$$

The declination δ (in radians) needed to compute η is given by:

$$\begin{aligned}\delta &= 0.006918 + 0.070257\, sin(\beta) - 0.399912\, cos(\beta) \\ &+ 0.000907\, sin(2\beta) - 0.006758\, cos(2\beta) \\ &+ 0.00148\, sin(3\beta) - 0.002697\, cos(3\beta) \qquad (11)\end{aligned}$$

Variations in the distance between sun and earth produce only slightly more than 3 % to variations in the net solar radiation.

3.2 Transfer Coefficient

In order to compute the transfer coefficients by a bulk aerodynamic method we use the parametrization of Large and Pond (1981,1982) as recommended by WOCE. Although the method is discussed in detail in both papers we have to list all relations to make clear which of the equations we have used.

$$\begin{aligned}c_H &= \frac{c_{HN}\sqrt{c_M/c_{MN}}}{1 - c_{HN}\kappa^{-1}c_{MN}^{-1/2}\psi_H(Z/L)} &(12)\\ c_L &= \frac{c_{LN}\sqrt{c_M/c_{MN}}}{1 - c_{LN}\kappa^{-1}c_{MN}^{-1/2}\psi_L(Z/L)} &(13)\\ \sqrt{c_M/c_{MN}} &= (1 - \sqrt{c_{MN}}\kappa^{-1}\psi_M(Z/L))^{-1} &(14)\\ c_{MN} &= \frac{\kappa^2}{ln^2(Z/Z_o)} &(15)\\ c_{HN} &= 0.0327\frac{\kappa}{ln(Z/Z_o)} &(16)\\ c_{LN} &= 0.0346\frac{\kappa}{ln(Z/Z_o)} &(17)\\ Z_o &= c_{char}\frac{u_*^2}{g} &(18)\\ u_*^2 &= c_M u^2 &(19)\\ T_o &= T(1 + 1.7 \times 10^{-6} Tq) &(20)\end{aligned}$$

Here c_M, c_H and c_L are the transfer coefficients for momentum, sensible and latent heat, respectively. The subscript N denotes the transfer coefficient for neutral condition. In order to distinguish between stable and unstable conditions we take the following formulas for ψ and (Z/L), first for stable conditions:

$$\psi_M = \psi_H = \psi_L = -7(Z/L) \tag{21}$$

$$(Z/L) = -\frac{70Z}{u^2 T_o}(\Delta\theta + 2.5 \times 10^{-6} T_o^2 \Delta q) \tag{22}$$

For unstable conditions we take:

$$\psi_M = 2ln[(1+X)/2] + ln[(1+X^2)/2] - 2arctanX + \pi/2 \tag{23}$$

$$\psi_H = \psi_L = 2ln[(1+X^2)/2] \tag{24}$$

$$X = (1 - 16(Z/L))^{1/4} \tag{25}$$

$$(Z/L) = -\frac{100Z}{u^2 T_o}(\Delta\theta + 1.7 \times 10^{-6} T_o^2 \Delta q) \tag{26}$$

Δq is the difference between the specific humidity of air and that at the sea surface, $\Delta\theta$ the potential temperature difference of SST and air temperature. The only difference from Large and Pond's work is that we do not fit c_{MN} against data but take a more theoretical approach. The equations (15), (18) and (19) relate the neutral drag coefficient c_{MN} to the friction velocity u_*, to the Karman constant κ, which was chosen to be .4, to the height of the measurement Z and to Charnock's constant c_{char}. In order to obtain a drag coefficient of about 1.15×10^{-3} for neutral conditions at $10m/s$, c_{char} would have to be set to .0064. Within the accuracy of measurements the resulting dependency of the neutral drag coefficient c_{MN} on the wind speed u is similiar to Large and Pond's approach and within the accuracy of Large and Pond's presented measurements. However, how it is explained in the following section, we chose $c_{char} = .032$.

3.3 Calibration of the Heat Flux

In order to verify the net heat flux and its components it is advisable to compute the meridional heat transport from the annual net heat flux. Surprisingly, we found a severe discrepancy in the estimates for the meridional heat transport when the original transfer coefficients of Large and Pond and $\alpha = 1$ in equation (9) are used. We detected a too strong net heat input. For instance, if the meridional heat transport is set to $\frac{1}{10}$ PW at 60^oN in the Atlantic, we obtain a meridional heat transport of O(-1PW) at the equator. If we want to increase the meridional heat transport in order to obtain a northward transport, then each PW must be balanced by an additional heat loss of about $20W/m^2$ overall the Atlantic.

This mismatch could have two major reasons. Either the heat input by insolation is overestimated or the heat loss by evaporation is underestimated. If we try to tune the parameterization, then we need either an albedo of 0.3, which is unrealistically high, or an increase of the transfer coefficients by 30 %. One possible source of error are the equations for the solar heat flux. However, since Reed (1977) has determined the error of the cloud correction to be below 10% and since our relation for the solar heat flux under clear sky has only a slightly higher transmissivity than the often used harmonic formula of Seckel and Beaudry (1973), the error in the meridional heat transport must have mainly another reason. Incidentally, the empirical formulas of Seckel and Beaudry are not used for this study since they are valid only in a meridional band.

The only other major source of error are the transfer coefficients for latent and sensible heat. Indeed, the coefficients of Large and Pond (1982) are much smaller than those of Bunker (1976), for example. Since Large and Pond's coefficients are based on instantaneous measurements we may argue that, due to their nonlinear dependency on wind speed and stability, they are underestimated if monthly mean values are taken. Indeed, if we analyse the relations (12) to (26) and assume that the occurance of strong winds and highly unstable conditions are correlated then the mean transfer coefficients will become larger if hourly data are used.

Because it was necessary to tune the parametrization to obtain a reasonable heat transport, we decided to increase Charnock's constant c_{char} to .032 as mentioned above. This value is also taken from the operationally working T21-model of the ECMWF at our institute. Furthermore, we decreased the insolation by 10 % to account for possibly existing overestimates of the insolation due to Zillmann's formula. Using these values, we computed the meridional heat transport in the Atlantic, in the Pacific and its zonal average. The resulting curves are presented in figure 1.0. All curves apparently agree with those of Hsiung (1985). The only basic difference is that our analysis shows a stronger northward heat transport in the Pacific than in the Atlantic.

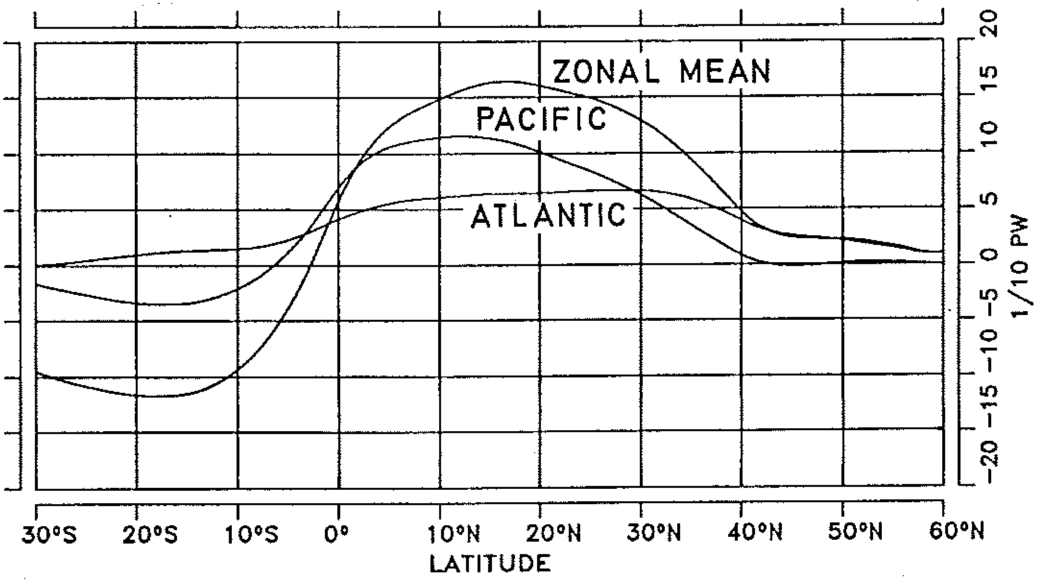

Figure 1.0: Meridional heat transport in the Atlantic, the Pacific and its zonal mean.

We must recognize that the meridional heat transport in the ocean is calculated from the residual of large terms in the heat balance, and each term is uncertain by 10 % or more. Therefore, it is not possible to determine the meridional heat transport with such a parametrization accurately enough. Following our sensitivity study it became apparent that the formulas chosen by Hsiung (1985) fortunately fit very well.

Nevertheless, if the heat transport is known the parameterization can be calibrated or verified. This allows modellers of the oceanic circulation to use a calibrated heat flux scheme. However, the calibration of the meridional heat transport can succeed only if accurate global data are available. The COADS and the data set used by Hsiung (1985) does not contain accurate values south of 30^oS. Therefore, the meridional heat transport can be tuned only towards a reasonable trend which, for instance, can be justified by inverse methods such as that one used by Wunsch (1980) for determining the meridional heat transport in the North Atlantic. Since we have no accurate data available south of 30^oS we cannot examine whether our globally averaged meridional heat transport would vanish at Antarctica if we keep its value fixed at 0.1 PW at 60^oN as done in our study.

3.4 Estimate for Turbulent Kinetic Energy Input

Absolute wind $\overline{V}$ and its standard deviation $\sigma(V)$ were prepared by Wright (1988). The standard deviation is required for evaluating the third power of the time averaged friction velocity u_* occuring in the energy flux relation more accurately. If we assume that the wind fluctuates sinusoidally about a mean value $\bar{V}$ then we obtain:

$$V(t) = \overline{V} + \sqrt{2}\sigma(V)\sin(2\pi t) \qquad with \qquad \overline{V} = \int_0^1 V dt \tag{27}$$

The mean u_*^3 can be estimated after integrating $V(t)^3$ over one period if we assume that the amplitude of the fluctuations is smaller than that of the mean wind:

$$u_*^3 = \sqrt{\frac{c_d\rho_a}{\rho}}^{\,3}\,\overline{V}(\overline{V}^2 + 3\sigma^2(V)) \tag{28}$$

The standard deviation of the wind is generally of the order of half of the mean wind strength, so that the expression (28) yields roughly twice as much kinetic energy as would result from the mean wind alone. Oceanic circulation models used for climatological studies do not in general contain fluctuations of the forcing explicitly, so that equation (28) is useful in providing an estimate for the turbulent kinetic energy input expressed in terms of mean quantities only.

3.5 Estimate for Buoyancy Flux

The buoyancy flux at the sea surface is the result of fluxes of heat and fresh water and is a measure of the input of mean potential energy at the ocean surface. Both fluxes affect the density at the surface. The buoyancy flux is calculated from

$$B = \frac{g}{\rho}(\frac{\alpha}{c_{p,water}\rho}Q + S\beta(E-P)) \qquad with \qquad E = \frac{\rho_a}{\rho_o}c_L V(q_a - q_s) \tag{29}$$

Here g=9.8 m/s^2 is the gravitational constant, ρ the surface density of sea water and $c_{p,water} = 4180 Ws/KgK$. P is the precipitation and E the evaporation rate in units of ms^{-1}. The expansion coefficients α for temperature and β for salinity are defined by:

$$\alpha = \frac{\partial \rho}{\partial T}|_{P,S} \tag{30}$$

$$\beta = \frac{\partial \rho}{\partial S}|_{T,S} \tag{31}$$

Both expansion coefficients are derived from the UNESCO formula (1981) for the equation of state of sea water by analytic differentiation with respect to temperature and salinity, respectively.

Because solar radiation is not totally absorbed at the surface but penetrates into the ocean with some decay length scale h_s, we have to modify the above relation slightly. First we ignore the fact that h_s is dependent on the frequency. We choose a constant value of 5m. The total surface heat flux Q may be divided into these fluxes $Q_{surface}$ which act directly on the surface, consisting of the sensible and latent heat and the long wave radiation, and the solar radiative heat flux Q_{solar}:

$$Q = Q_{surface} + Q_{solar} \tag{32}$$

To determine the buoyancy flux due to solar radiation, we need to consider only that fraction which does not penetrate through the mixed layer but is absorbed there. If h is the mixed layer thickness, then following Denman and Miyake (1973) the effective buoyancy flux into the mixed layer may be written

$$B^* = \frac{g}{\rho}\{S\beta(R-E) + \frac{\alpha}{c_p\rho}(Q_{surface} + Q_{solar}((1 + exp(-\frac{h}{h_s})) - 2\frac{h_s}{h}(1 - exp(-\frac{h}{h_s}))))\} \tag{33}$$

We recognize from this formula that with increasing h_s the buoyancy flux due to solar radiation increases, or, in other words, the stabilizing effect of the surface heating due to solar radiation decreases. As a result we get a deeper mixed layer during summer. If it were assumed that solar radiation is totally absorbed at the ocean surface then the summer mixed layer would be systematically too shallow.

3.6 Estimate of Mixed Layer Monin-Obukhov Length

The estimate of the turbulent kinetic energy input into the ocean and the buoyancy flux allows the evaluation of the mixed layer Monin-Obukhov length. However, this estimate is dependent on the chosen mixed layer theory. For simplicity we chose the simplest mixed layer theory which says that kinetic energy is totally converted into potential energy. The Monin-Obukhov length is defined as the mixed layer depth in the equilibrium case of no entrainment

$$2m_0u_*^3 + hB^*(h, ...) = 0 \tag{34}$$

The solution of the equation yields h. From various papers we know that this equation must be modified to match observations by including further damping terms which make the mixed layer shallower. For instance, Martin (1985) compared the Mellor-Yamada, Niiler and Garwood models. Thus our equation for h yields an upper estimate for the equilibrium mixed layer thickness. We chose $m_0 = 1.25$. The actual mixed layer thickness is then equal to the Monin-Obukhov length in the retreat phase and shallower in the entrainment phase.

4 Newtonian Cooling in an OGCM

Heat flux schemes as outlined above are more and more used for forcing an OGCM. If we take into account the fact that a large data set for atmospheric quantities has to be made available to an OGCM we should ask whether there are simplifications possible. Indeed, if we linearize the heat flux Q around the observed $SST|_{obs}$, then we find:

$$Q = Q|_{obs} - \frac{\partial Q}{\partial T}|_{obs}(SST|_{obs} - SST|_{model}) \tag{35}$$

Here $Q|_{obs}$ is the observed heat flux, $(\partial Q)/(\partial T)|_{obs}$ the coupling coefficient and $SST|_{model}$ the model SST.

In order to derive the Newtonian cooling formulation it is assumed that the observed heat flux $Q|_{obs}$ at the observed $SST|_{obs}$ vanishes and additionally that the coupling coefficient $(\partial Q)/(\partial T)|_{obs}$ is constant. Both assumptions are unrealistic.

To compute the heat flux Q from the linearized heat flux scheme only three data sets are needed. It are $Q|_{obs}$, $(\partial Q)/(\partial T)|_{obs}$ and $SST|_{obs}$, respectively. A further simplification can be made by introducing an equilibrium temperature $SST|_{equ}$ defined by:

$$SST|_{equ} = SST|_{obs} - Q|_{obs}(\frac{\partial Q}{\partial T}|_{obs})^{-1} \tag{36}$$

With this definition we obtain:

$$Q = -\frac{\partial Q}{\partial T}|_{obs}(SST|_{equ} - SST|_{model}) \tag{37}$$

Apparently, we now have to prepare only the coupling coefficient $(\partial Q)/(\partial T)|_{obs}$ and the equilibrium temperature $SST|_{equ}$ to compute the actual heat flux in an OGCM.

If we consider the extreme case of a heat loss of about $400 W/m^2$ in the Gulf stream region during winter and assume a coupling coefficient of $(\partial Q)/(\partial T)|_{obs} = -50 W/(m^2 K)$ then equation (36) yields an equilibrium temperature $SST|_{equ}$ which is 8 $Kelvin$ less than the observed $SST|_{obs}$. Although equation (37) is as simple as the Newtonian cooling formulation, it should lead to a better simulation of the observed SST at the correct heat flux.

5 Discussion of Results

5.1 Layout of Pictures

All derived quantities are plotted as monthly mean values and their annual average. The second part in the figure number denotes the n-th month of the year; n=13 stands for annual mean. The contour interval is indicated in the lower panel together with the level of the reference line, shown as an extra thick solid line. Land points are marked as blank areas surrounded by the coastline. All ocean regions where not enough data are available are shaded. In regions of only a few missing data points we eliminate the gaps by interpolation. The spatial distribution of the number of observations of the COADS are presented by Woodruff et al. (1987) at some examples. On the right hand side of each spatial distribution the zonal average of the quantity is plotted. The curve stops at $61°N$ and $45°S$, respectively.

Since the originally determined fields were rather noisy, we filtered all fields for plotting. For this purpose we used a nonlinear filter which removes only two-dimensional small-scale chess-board patterns but does not modify one-dimensional small-scale patterns. Fields which are needed for further calculations are left unfiltered.

In order to remove chess-board patterns out of a two-dimensional field we determine for each grid point the mixed derivative in all four surrounding cells and their spatial average. From the ratio of the actual and the mean mixed derivative we determine for each surrounding cell a coefficient which reflects how strong the actual mixed derivative differs from its spatially averaged value. Consequently, these coefficients are a measure of the noise amplitude. Finally, these coefficients determine the ratio of how much is taken from the original value and how much from the average in each cell.

5.2 Table of figures

5.3 Comments on Heat Fluxes

5.3.1 Solar Radiation

The net solar radiative flux into the ocean is essentially a function of cloud cover and daily averaged sun elevation. The seasonal cycle is mainly defined by the change in the declination angle, which decreases going from lower to higher latitudes with some modification by the spatially and seasonally dependent cloud cover. Near the equator a narrow region of reduced solar heat flux reflects the ITCZ, and in the subtropics higher values result from less cloudiness.

5.3.2 Outgoing Long Wave Radiation

The OLR is influenced by the atmospheric water vapor content and the cloud cover. Consequently, we find weaker heat loss in lower latitudes due to the high humidity and higher heat loss in the subtropics, which has typically dry and cloud free air. However, the range of heat loss due to OLR is only from $40W/m^2$ to $60W/m^2$ in low and midlatitudes. Thus it does not contribute significantly to the patterns in the net heat flux.

5.3.3 Sensible Heat Flux

Because sea surface and air temperature do not differ significantly, the sensible heat flux is generally small. Exceptions are those regions where mostly rather cold air of continental origin flows over warm water with rather high velocity. In our data set this is only the case in the Gulf stream and Kuroshio region. Heat fluxes then achieve $140W/m^2$ in the Kuroshio and $120W/m^2$ in the Gulf stream region in January but are still small compared to the latent heat flux at the same time there.

5.3.4 Latent Heat Flux

The latent heat flux is controlled by the wind speed, the air humidity and the temperature. Therefore, we get systematically higher values at lower latitudes due to the higher temperature and resultant higher absolute humidity there. Because relative humidity varies only between .75 to .85 in low- and midlatitudes with typically higher values in areas of high cloud cover, the final patterns of latent heat release are dominated by the wind speed patterns and by the difference between SST and air temperature. Consequently, areas of strong winds like the trades or at the oceanic western boundary currents give maxima in the latent heat flux.

5.3.5 Net Downward Heat Flux

The net downward heat flux is mainly the residual of solar radiation and latent heat flux. The long wave radiation contributes a heat loss of typically $-50W/m^2$. The sensible heat flux is negligible except for the area of the western boundary currents, where the heat loss can exceed $150W/m^2$ due to the big difference between air and sea surface temperatures. In the annual mean, a strong heat loss appears in regions of the western boundary currents. Areas of strong heat gain exist at the equator in the eastern Pacific and the Atlantic. Typical values for the heat input are $100W/m^2$ for the equatorial eastern Pacific and $75W/m^2$ for the equatorial Atlantic. Surface cooling results in the strong equatorial upwelling which is initiated by the strong trade winds. Also along the west coast of South and North America, along the west coast of Africa and in the Arabic Sea we find regions of net heat input in the mean. This also is associated with upwelling processes. In the zonal mean this results in a heat gain of slightly more than $60W/m^2$ at the equator, but only in a narrow band with a width typical for oceanic upwelling areas. The highest values of heat loss occur during January in the Gulf stream region with more than $450W/m^2$ and in the Kuroshio with more than $500W/m^2$.

5.4 Comments on Buoyancy Flux

Buoyancy fluxes are fluxes of potential energy. They reflect changes of density due to heat and fresh water fluxes. The evaporation rate required for the total fresh water flux is quickly derived from the latent heat flux Q_L by the relation $E = Q_L/(\rho_a L_w)$. Above the freezing point of water the thermal expansion coefficient becomes rather large. Therefore, fresh water fluxes dominate only in regions of water at temperatures close to the freezing point. There the thermal expansion coefficient is small but still high in respect to salinity. However, since ice-covered regions are not part of our analysis and because we consider only climatological mean values for the fresh water flux, which are generally small at higher latitudes, patterns in the heat flux reappear also in the buoyancy flux.

5.5 Comments on Flux of Turbulent Kinetic Energy

The mean friction velocity u_* used as an estimate of the turbulent kinetic energy input into the mixed layer has pronounced maxima in the North Pacific and North Atlantic during the winter season. Strong mean absolute winds and their strong fluctuations due to the midlatitude eddy activity are the reasons for these. Although the trade winds are also quite intense their high persistence expressed in terms of a low standard deviation of the scalar wind does not lead to pronounced maxima in the effective friction velocity. In the tropics values are quite small throughout the year.

5.6 Comments on Mixed Layer Monin-Obukhov Length

The estimates, given for the mixed layer Monin-Obukhov length should not be misinterpreted as observation. Since the results are highly model dependent our intent is only to illustrate the response to the diagnostically determined surface fluxes. Because the Monin-Obukhov length is only identical to the actual mixed layer thickness during the detrainment phase, which takes place during spring and early summer, it can be compared with observed mixed layer thicknesses only in these seasons. During autumn and winter we must expect the diagnostically determined Monin-Obukhov length to be larger than the actual mixed layer thickness. In this sense we can only try to find out whether the estimated Monin-Obukhov length does not contradict observed mixed layer thicknesses.

5.7 Comments on Newtonian Cooling

Since the solar radiative heat input into the ocean has a negligible feedback with the SST, the only important contribution comes from the latent heat. A typical value is $-50W/m^2K$. Sensible heat contributes with about $-10W/m^sK$ and the longwave radiation with about $-5W/m^2K$ to the total coupling coefficient. By differentiation of the formula for latent heat we recognize that the coupling coefficient is controlled by the wind strength, the absolute temperature and the relative humidity. The last two quantities are responsible for the difference between the water vapor content of air and the saturated water vapor content at the surface. Thus, it is not surprising that the coupling coefficient decreases systematically from the subtropics to midlatitudes due to the connection between absolute temperature and water vapor content. Also regions of stronger winds show increased coupling coefficients. At the equator they are systematically lower.

6 Conclusion

The goal of this study was to present a complete set of derived surface fluxes of heat, buoyancy and turbulent kinetic energy and to show estimates for them. Furthermore, we determined the meridional heat transport and found a surprisingly high sensitivity to changes in the heat flux parametrizations. Therefore, it is one of our conclusions that the naturally existing uncertainty of the heat flux parametrizations does not allow an accurate estimate of the meridional heat transport. We also found that the latent heat flux estimated from climatological atmospheric quantities seems to be underestimated if transfer coefficients derived from instantaneous measurements are used. Since the difference between the coefficients of Large and Pond and those needed to obtain a reasonable meridional heat transport in the ocean are too large to be explained by the general uncertainty we conclude that we need a differently derived data set for the transfer coefficients used in connection with climatological mean fields. One possibility would be to compute the mean heat fluxes by taking hourly data. In comparison to the heat fluxes obtained with climatological data one could determine the transfer coefficients needed to achieve comparable heat fluxes with climatological data sets by an inverse method.

Since the COADS are collected from ship observations, ice covered regions and areas in the southern hemisphere as well as in the circumpolar current appear as large gaps. Therefore, it is not possible in this study to calibrate the heat flux schemes by achieving a vanishing meridional heat transport at Antartica and the North Pole. However, since our heat flux parametrization is tuned toa reasonable meridional heat transport, we can offer a complete scheme which is sufficiently accurate for the usage in a global OGCM.

Dennis Shea has combined the COADS with station data over land and over ice in the northern hemisphere. Unfortunately, he has not done this work for wind speed, cloudiness and humidity. The results presented in this study, however, should give enough motivation to continue the efforts in collecting data for a complete overview of the global surface climatology of ocean and atmosphere. Analyses prduced by the ECMWF could be used to derive the climatology. To our knowledge, this has just started at various locations but results not yet available.

Because it was one of our efforts to prepare a scheme for calculating global heat fluxes we offer it together with all basic and derived fields. These fields are available on magnetic tape.

ACKNOWLEDGEMENT

We would like to thankPeter Wright (Max-Planck-Institute for Meteorology/Hamburg) for his review of this report and for getting the COADS to an immediately usable form, and Dennis Shea (NCAR, Boulder) for his precipitation data. We also thank Klaus Hasselmann and Dick Reynolds for their very helpful comments. The work was carried out on the computer of the Max-Planck-Institute for Meteorology in Hamburg with the help of Bernd Appasamy who has done parts of the programming work.

7 References

Berliand, M.E. and T.G. Berliand, 1952: Determining the net long-wave radiation of the Earth with consideration of the effect of cloudiness. Isv. Akad. Nauk. SSSR Ser. Geofis, No. 1.

Berliand, T., 1960: Methods of climatological computation of total incoming solar radiation. Meteorol. Gidrol., 5, 9-12. MGA 12:1486.

Budyko, M.I., 1974: Climate and Life. Academic Press. 508 pp.

Bunker, A.F., 1976: Computations of surface energy flux and annual air-sea interaction cycles of the North Atlantic Ocean, Mon. Weath. Rev., 104, 1122-1140.

Denman, K.L. and M. Miyake, 1973; Upper Layer Modification at Ocean Station Papa: Observations and Simulations. J. Phys. Oceanogr., 3, 185-196.

Dorman and Bourke, 1978: Precipitation over the Atlantic Ocean, $30^oS - 70^oN$. Quart. J. Roy. Meteor. Soc., 104, 756-773.

Esbensen, S.K. and Y. Kushnir, 1981: The heat budget of the global ocean: an atlas based on estimates from surface marine observations. Climate Research Institute, Oregon State University, Report No. 29.

Hsiung, J., 1985: Estimates of global oceanic meridional heat transport, J. Phys. Oceanogr., 15, 1405-1413.

Hsiung, J., 1986: Mean Surface Energy Fluxes over the Global Ocean. J. Geophys. Res., 91, 10,585-10,606.

Large, W.G., and S. Pond, 1981: Open Ocean Momentum Measurements in Moderate to Strong Winds. J. Phys. Oceanogr., 11, 324-336.

Large, W.G., and S. Pond, 1982: Sensible and Latent Heat Flux Measurements over the Sea. J. Phys. Oceanogr., 12, 464-482.

Levitus, S., 1982: Climatological Atlas of the World Ocean. NOAA Prof. Pap. No. 13, U.S. Gov't. Printing Office, 173pp., 17 fiche.

Martin, P.J., 1985: Simulation of the Mixed Layer at OWS November and Papa With Several Models. J. Geoph. Res., 90, 903-916.

Oberhuber, J.M., 1988: Atlantic Circulation simulated with an Isopycnal Coordinate General Circulation Model. Max-Planck-Institute for Meteorology/Hamburg, Report.

Paltridge, G.W., and C.M.R. Platt, 1976: Radiative Processes in Meteorology and Climatology. Elsevier Sc. Publ. Comp., New York.

Parkinson, C.L., and W.M. Washington, 1979: A large-scale Numerical Model of Sea Ice. *J. Geophys. Res.*, 84, 311 – 337.

Reed, R.K., 1977: On estimating insolation over the ocean. J. Phys. Oceanogr., 6, 781-800.

Rosati, A. and K. Miyakoda, 1987: A GCM for upper ocean simulation. To be submitted to J. Phys. Oceanogr.

Seckel, G.R., and F.H. Beaudry, 1973: The radiation from sun and sky over the North Pacific Ocean (abstract), Trans. Amer. Geophys. Union, 54, 1114.

Shea, D.J., 1986: Climatological Atlas: 1950-1979, National Center for Atmospheric Research, Boulder, Colorado.

UNESCO, 1981: The Practical Salinity scale 1978 and the International Equation of State of Seawater 1980. Unesco Techn. Pap. in Mar. Sci., No. 36, 13-21.

Weare, B.C., P.T. Strub and M.D. Samuel, 1981: Annual mean surface heat fluxes in the Tropical Pacific Ocean. J. Phys. Oceanogr., 11, 705-717.

Wright, P., 1988: An Atlas based on the 'COADS' data set: Fields of mean wind, cloudiness and humidity at the surface of the global ocean. Max-Planck-Institute for Meteorology/Hamburg, Report 14.

Woodruff, S.D., R.J. Slutz, R.L. Jenne and P.M. Steurer, 1987: A Comprehensive Ocean-Atmosphere Data Set. Bull. Amer. Met. Soc., 68, 1239-1250.

Wunsch, C., 1980: Meridional heat flux of the North Atlantic Ocean, Proc. Natl. Acad. Sci. U.S.A., 77, 5043-5047.

Zillmann, J.W., 1972: A study of some aspects of the radiation and the heat budgets of the southern hemisphere oceans. Meteorol. Stud., 26, 562pp, Bur. of Meteorol., Dep. of the Interior, Canberra, Australia.

SHORT WAVE RADIATION BUDGET

FIG. 1.1 SHORT WAVE RADIATION BUDGET JANUARY

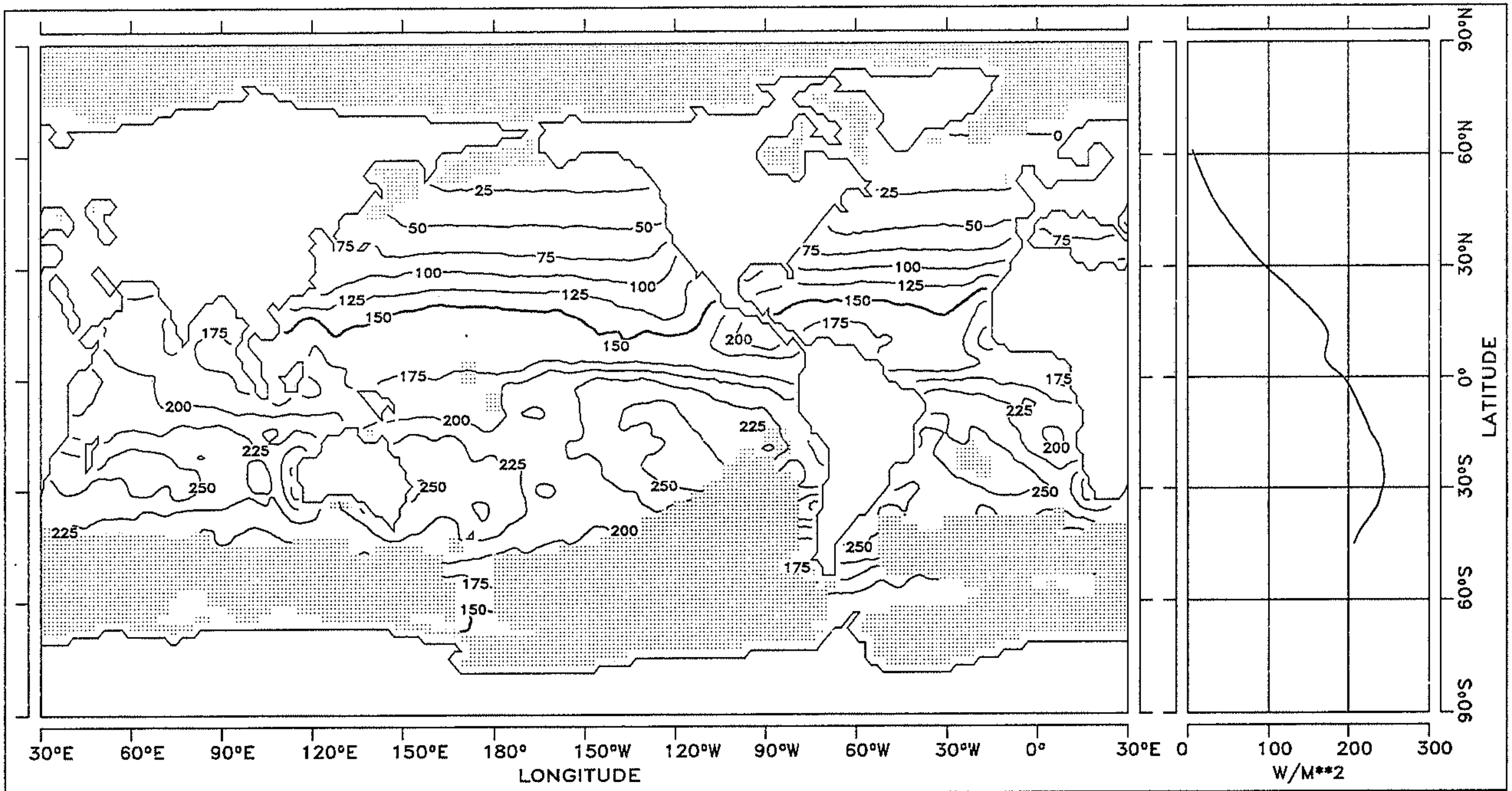

CONTOUR INTERVAL: 25 W/M**2 REFERENCE LINE : 150 W/M**2

FIG. 1.2 SHORT WAVE RADIATION BUDGET FEBRUARY

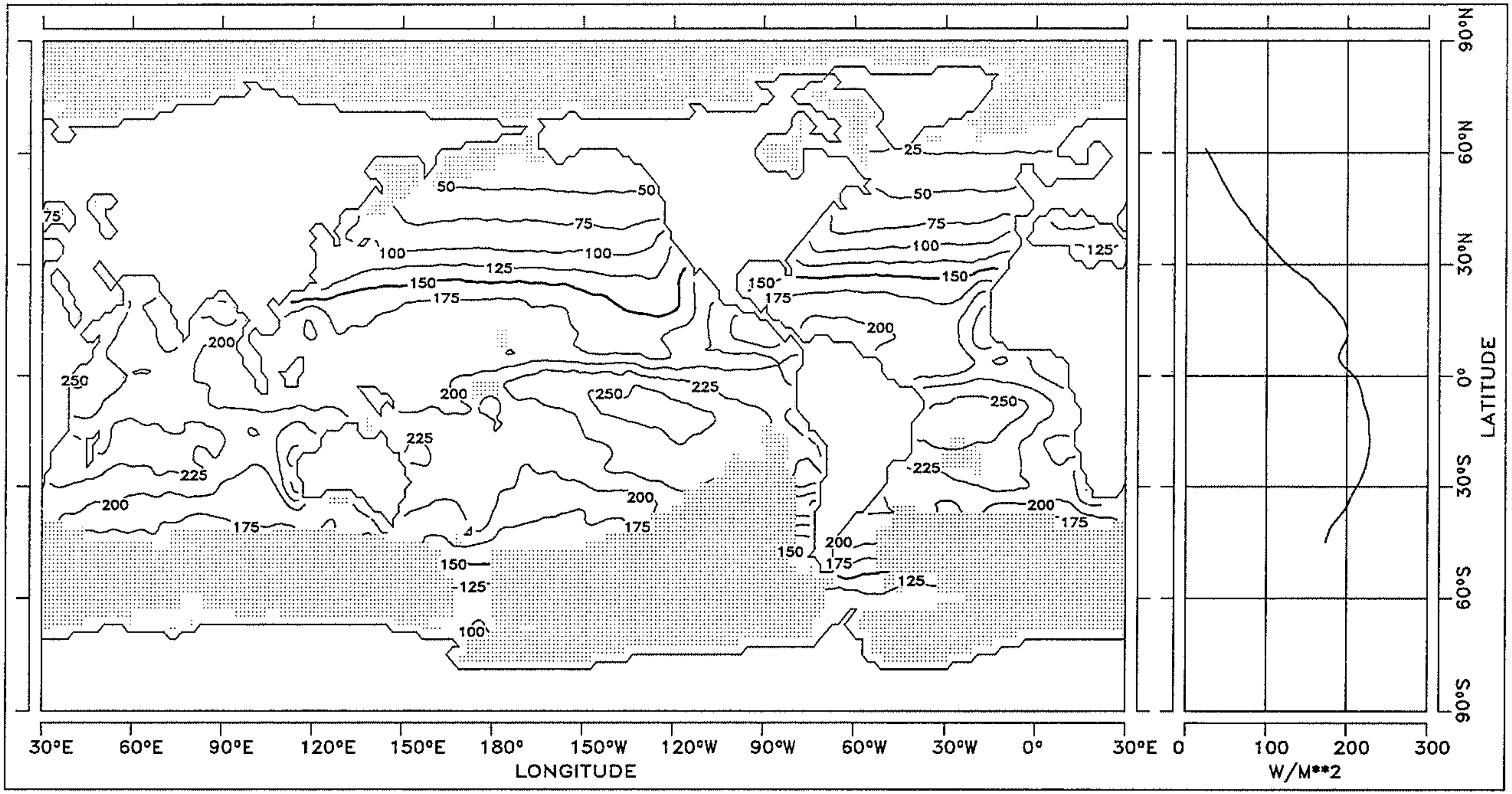

CONTOUR INTERVAL: 25 W/M**2 REFERENCE LINE : 150 W/M**2

FIG. 1.3 SHORT WAVE RADIATION BUDGET MARCH

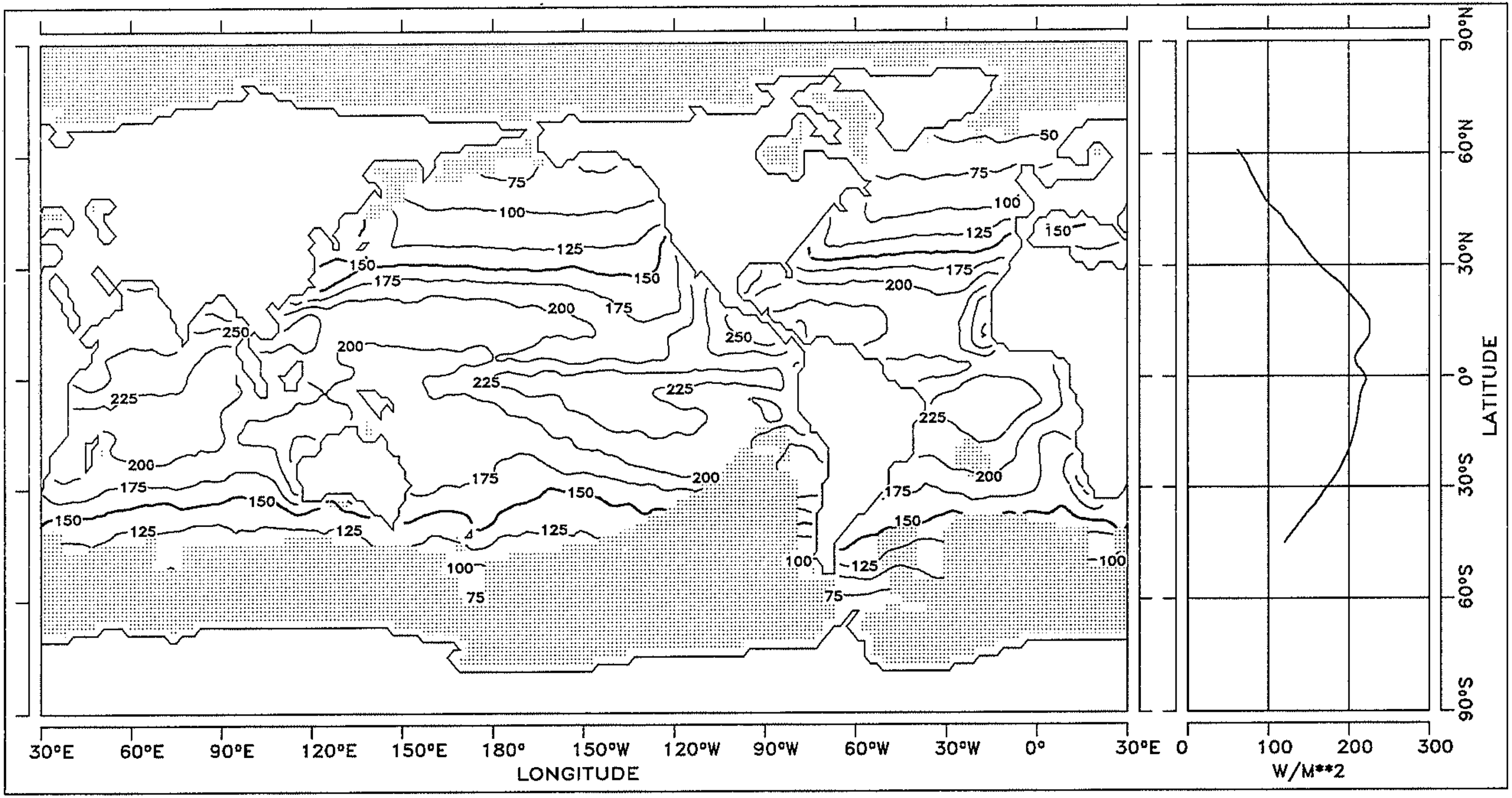

CONTOUR INTERVAL: 25 W/M**2 REFERENCE LINE : 150 W/M**2

FIG. 1.4 SHORT WAVE RADIATION BUDGET APRIL

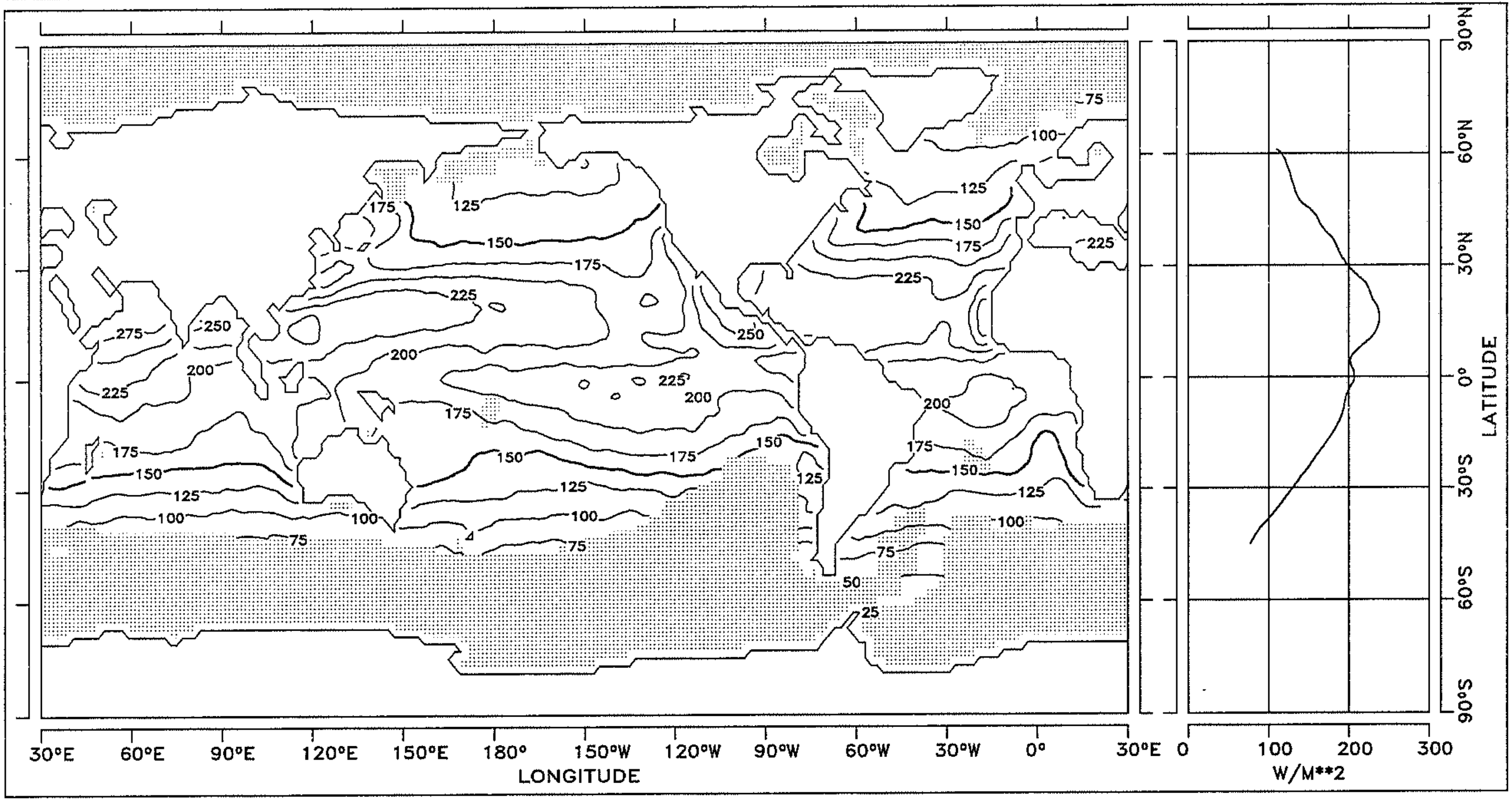

CONTOUR INTERVAL: 25 W/M**2 REFERENCE LINE : 150 W/M**2

FIG. 1.5 SHORT WAVE RADIATION BUDGET MAY

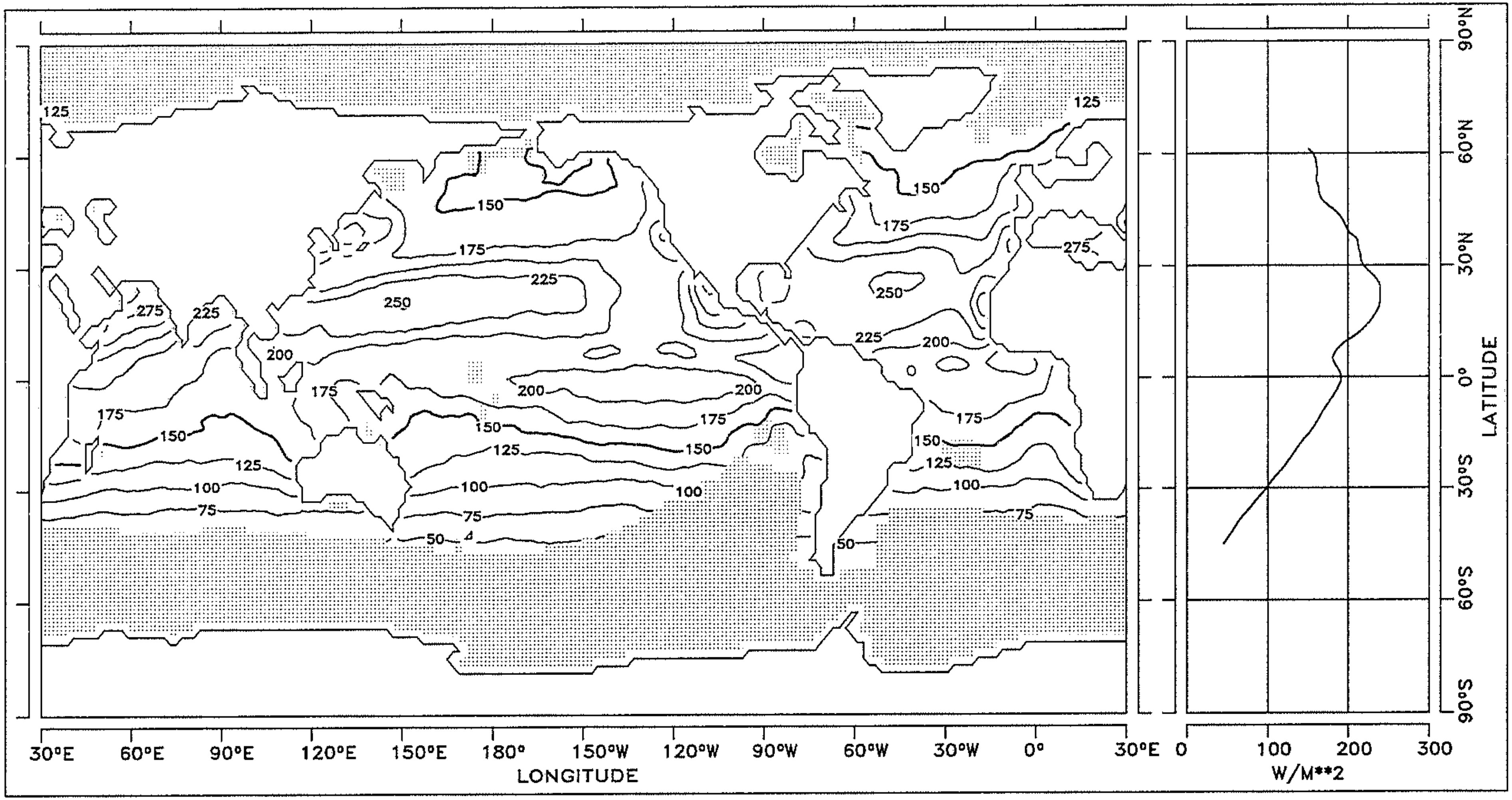

CONTOUR INTERVAL: 25 W/M**2 REFERENCE LINE : 150 W/M**2

FIG. 1.6 SHORT WAVE RADIATION BUDGET JUNE

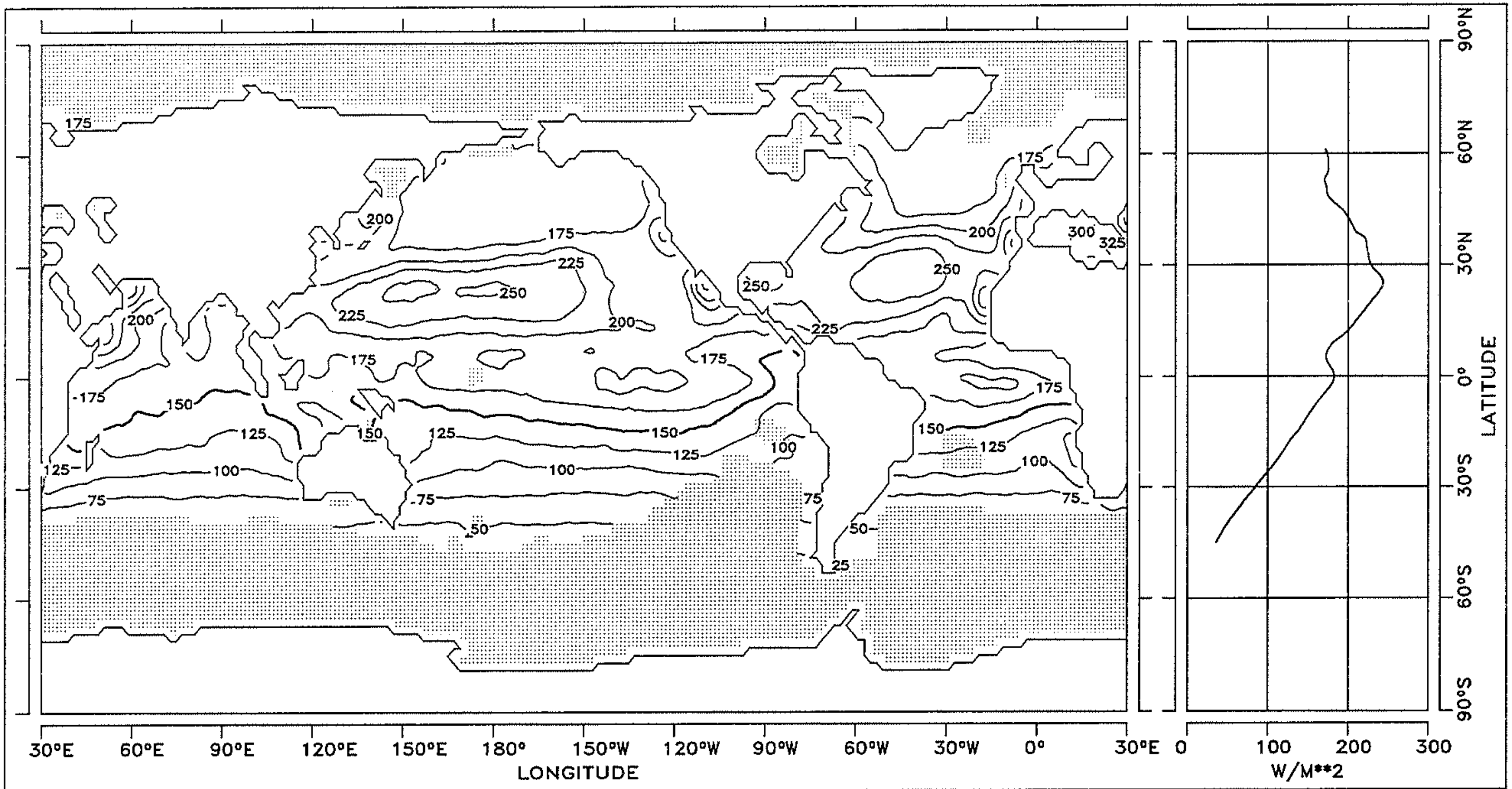

CONTOUR INTERVAL: 25 W/M**2 REFERENCE LINE : 150 W/M**2

FIG. 1.7 SHORT WAVE RADIATION BUDGET JULY

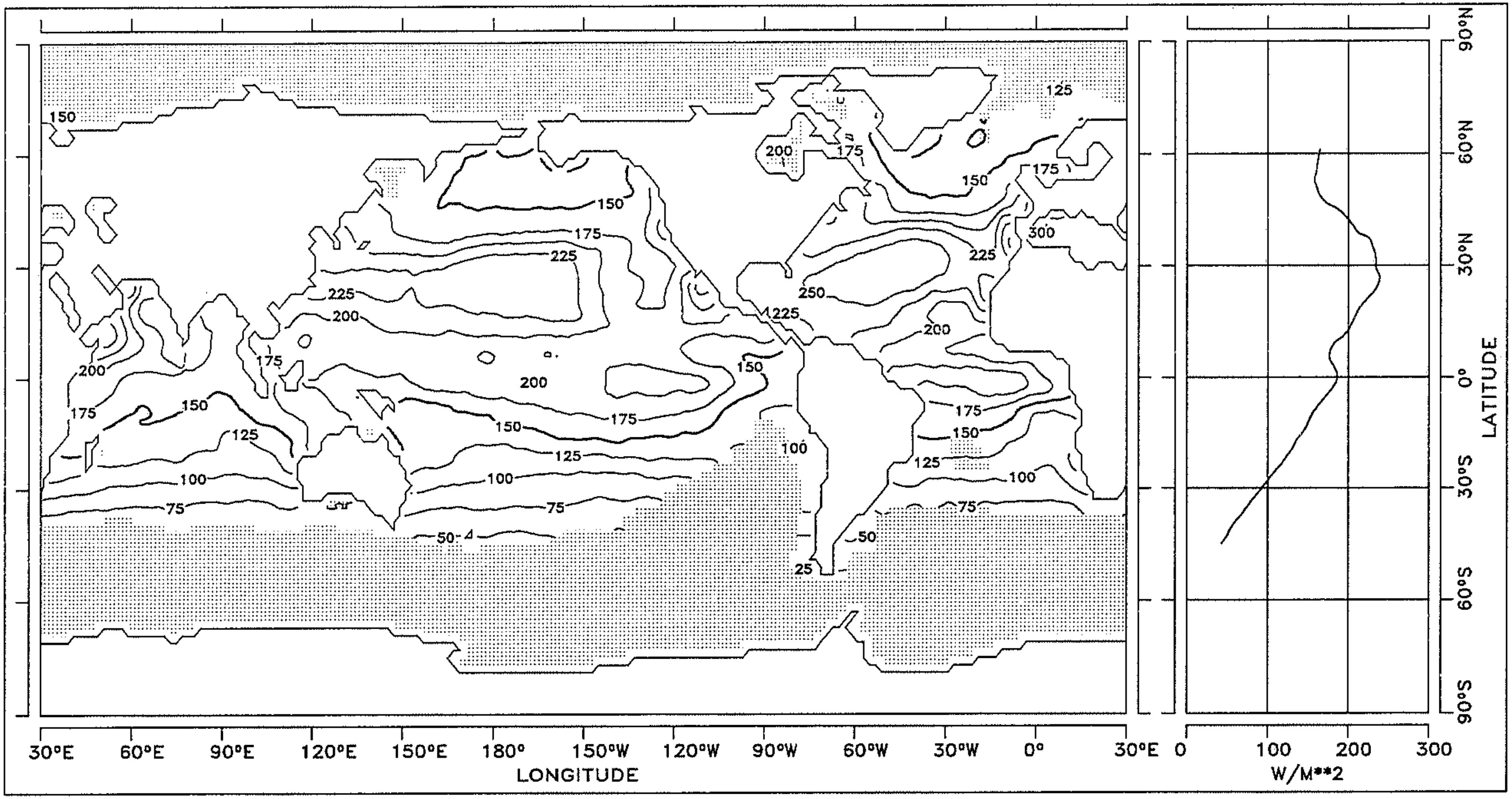

CONTOUR INTERVAL: 25 W/M**2 REFERENCE LINE : 150 W/M**2

FIG. 1.8 SHORT WAVE RADIATION BUDGET AUGUST

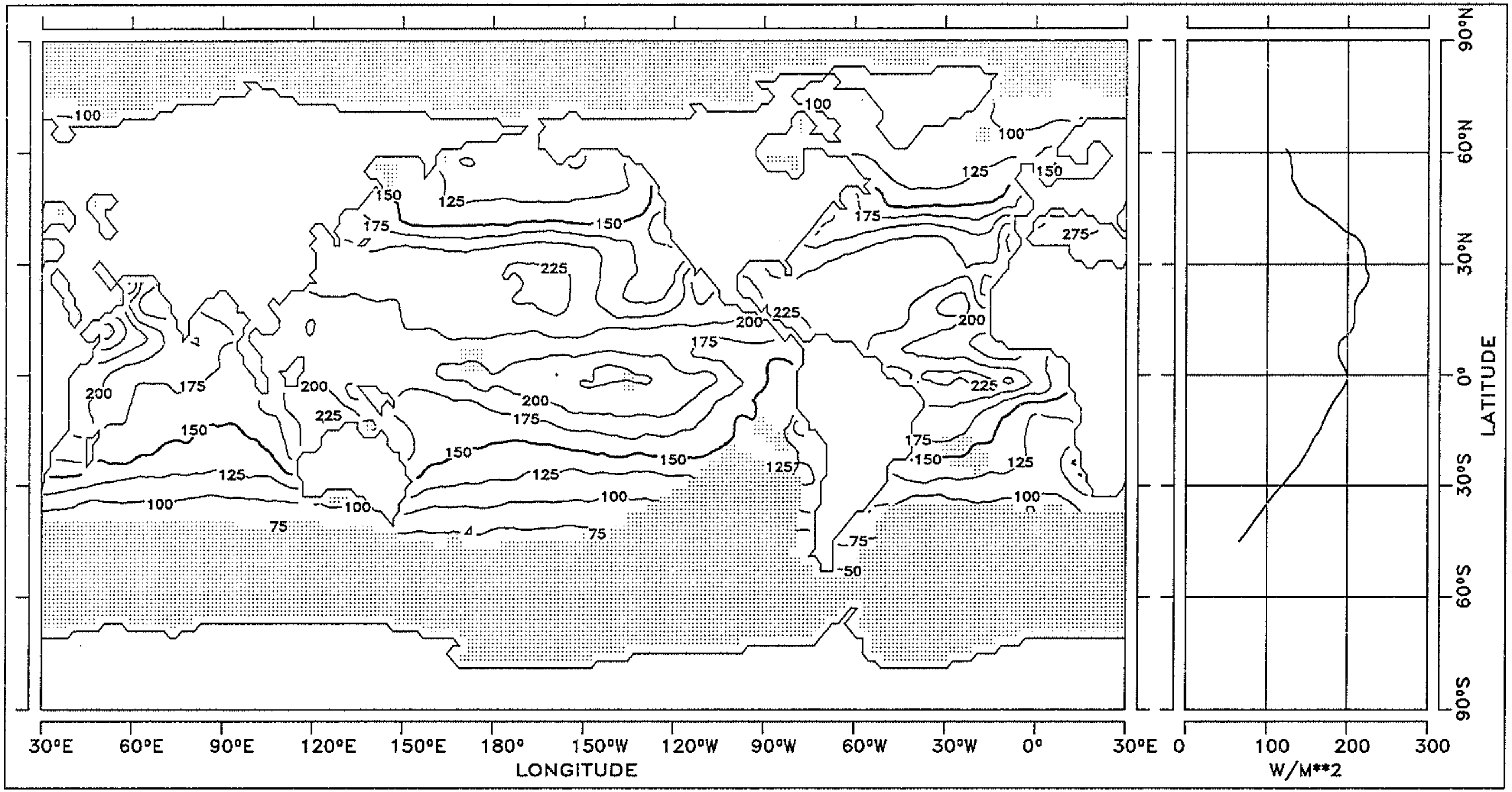

CONTOUR INTERVAL: 25 W/M**2 REFERENCE LINE : 150 W/M**2

FIG. 1.9 SHORT WAVE RADIATION BUDGET SEPTEMBER

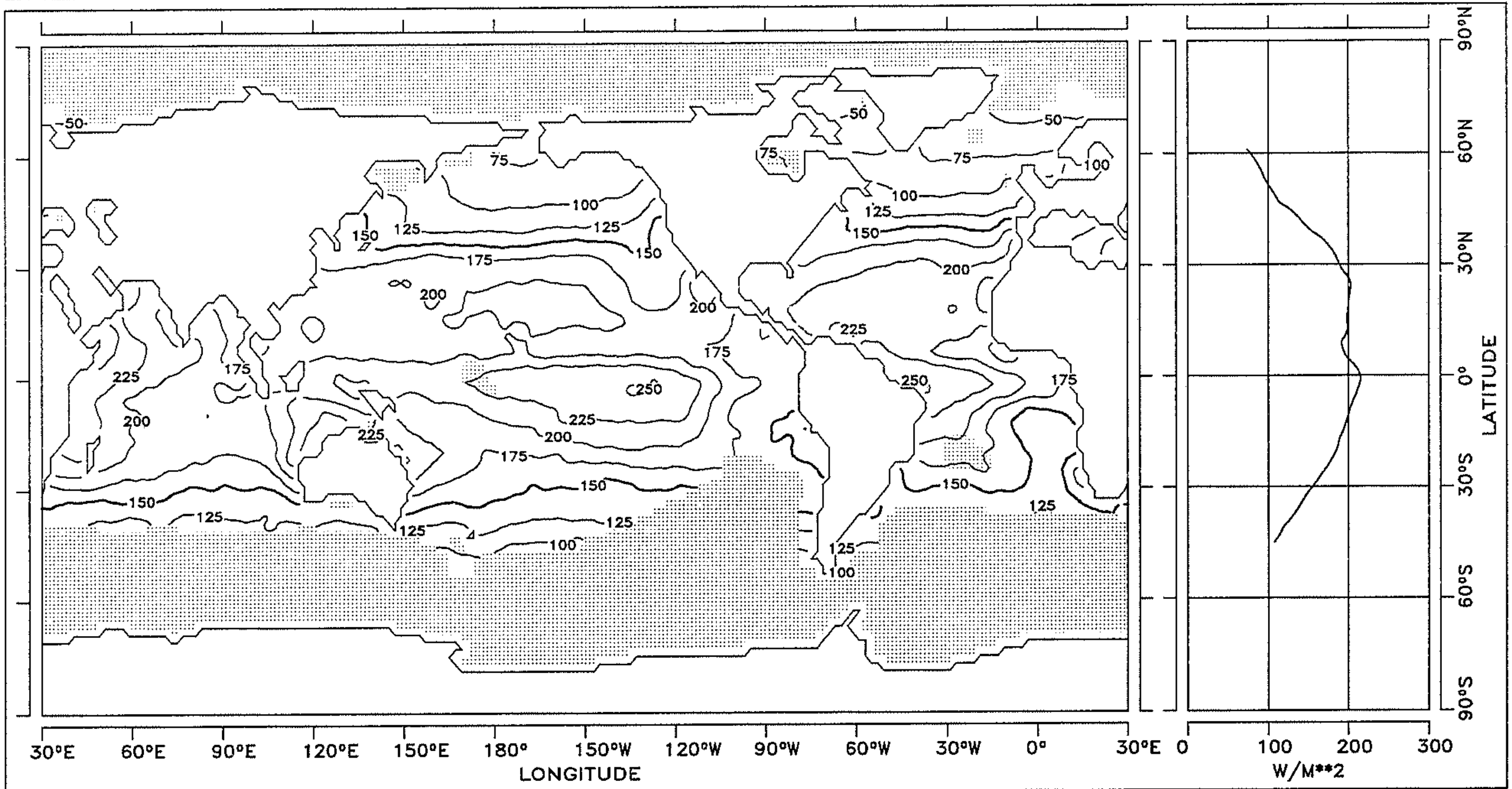

CONTOUR INTERVAL: 25 W/M**2 REFERENCE LINE : 150 W/M**2

FIG. 1.10 SHORT WAVE RADIATION BUDGET OCTOBER

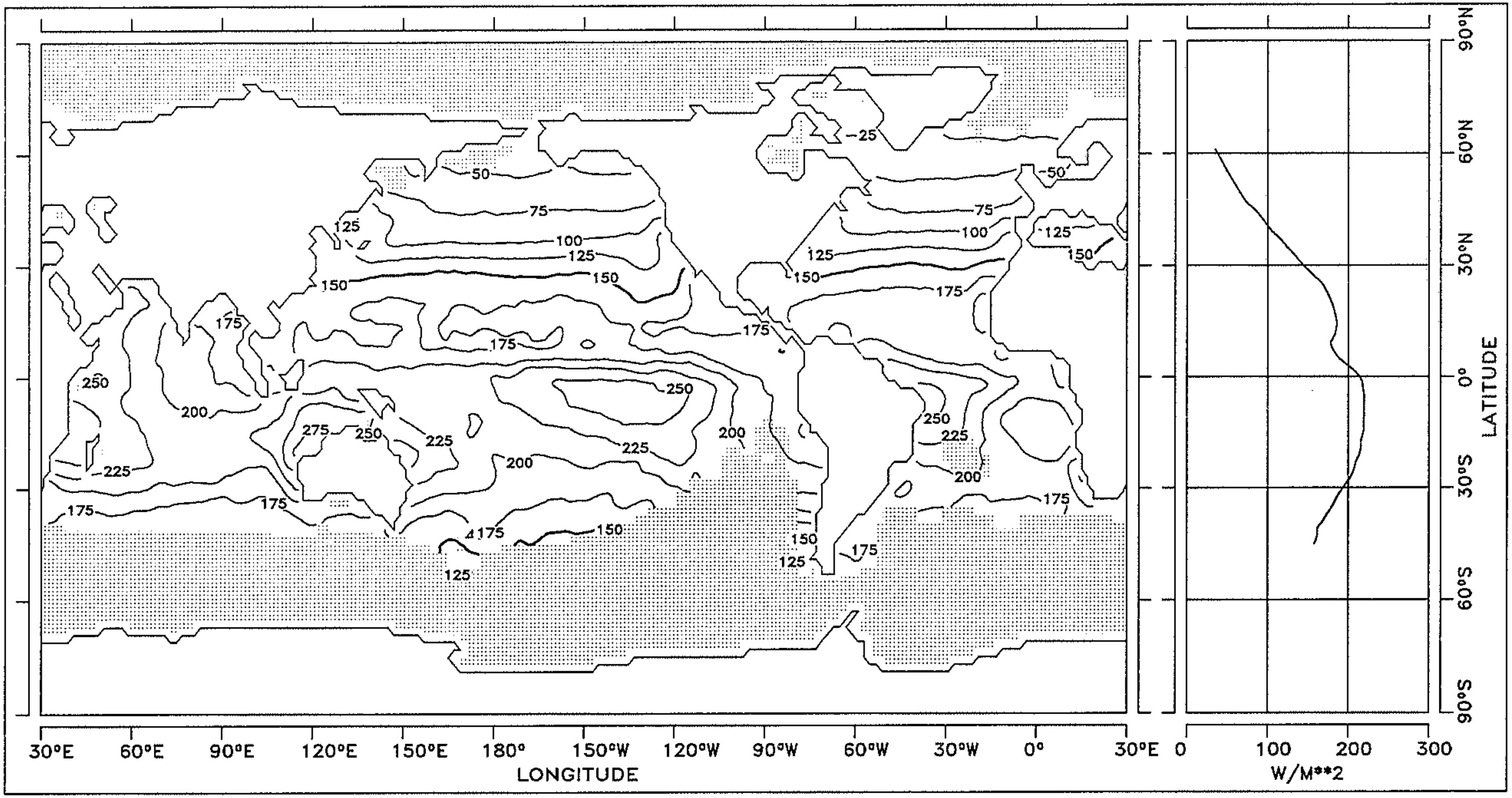

CONTOUR INTERVAL: 25 W/M**2 REFERENCE LINE : 150 W/M**2

FIG. 1.11 SHORT WAVE RADIATION BUDGET NOVEMBER

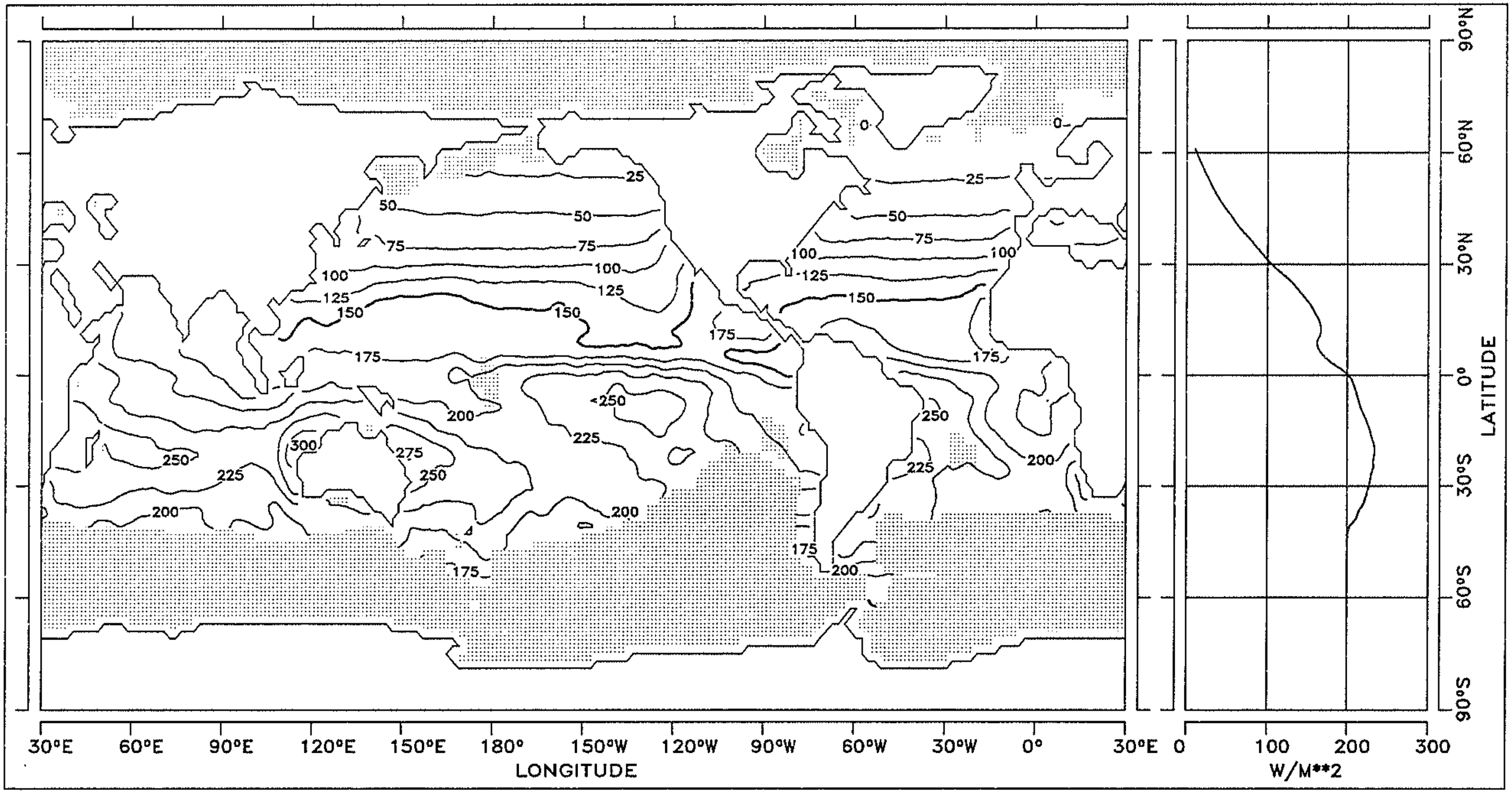

CONTOUR INTERVAL: 25 W/M**2 REFERENCE LINE : 150 W/M**2

FIG. 1.12 SHORT WAVE RADIATION BUDGET DECEMBER

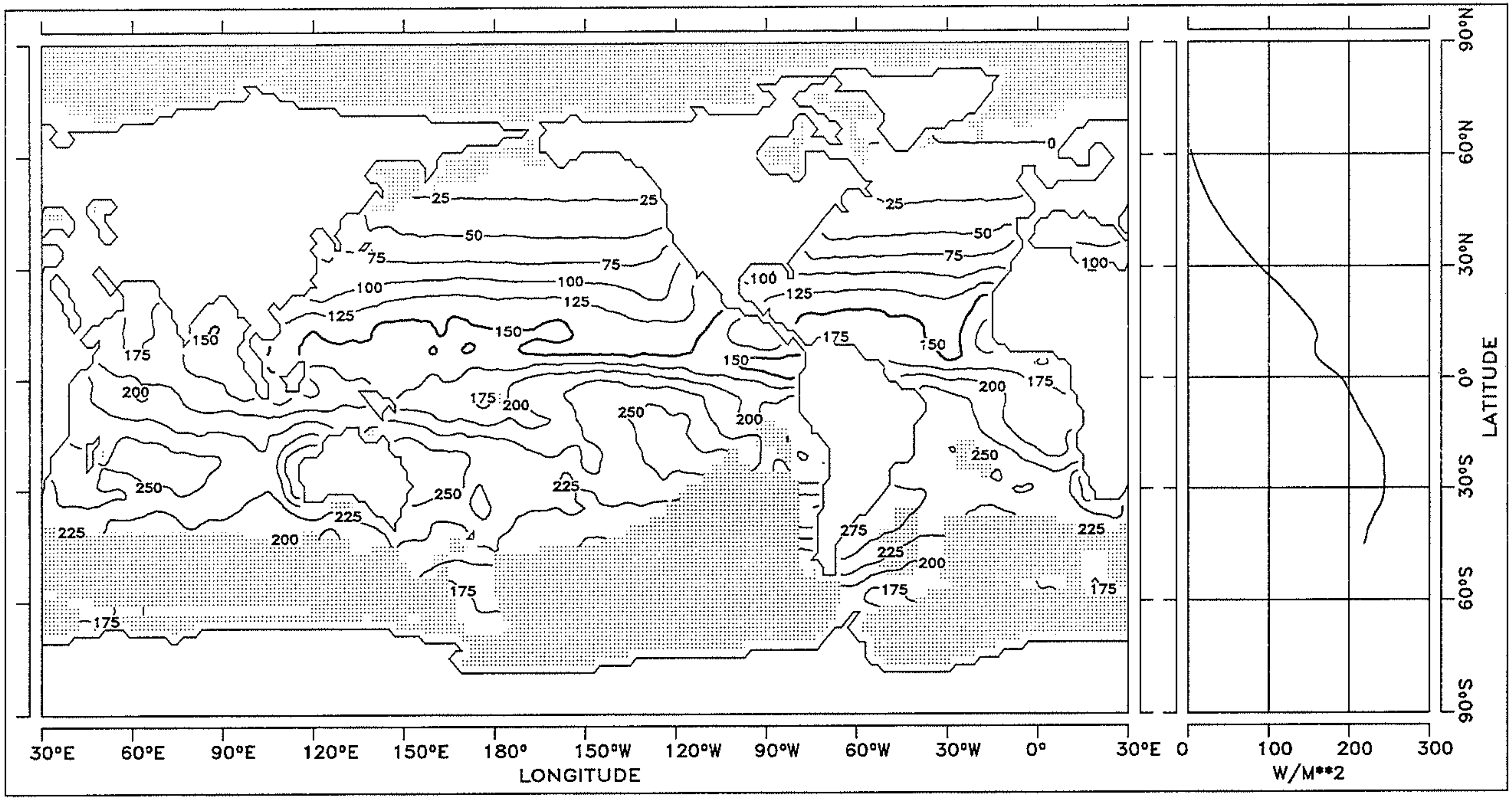

CONTOUR INTERVAL: 25 W/M**2 REFERENCE LINE : 150 W/M**2

FIG. 1.13 SHORT WAVE RADIATION BUDGET ANNUAL MEAN

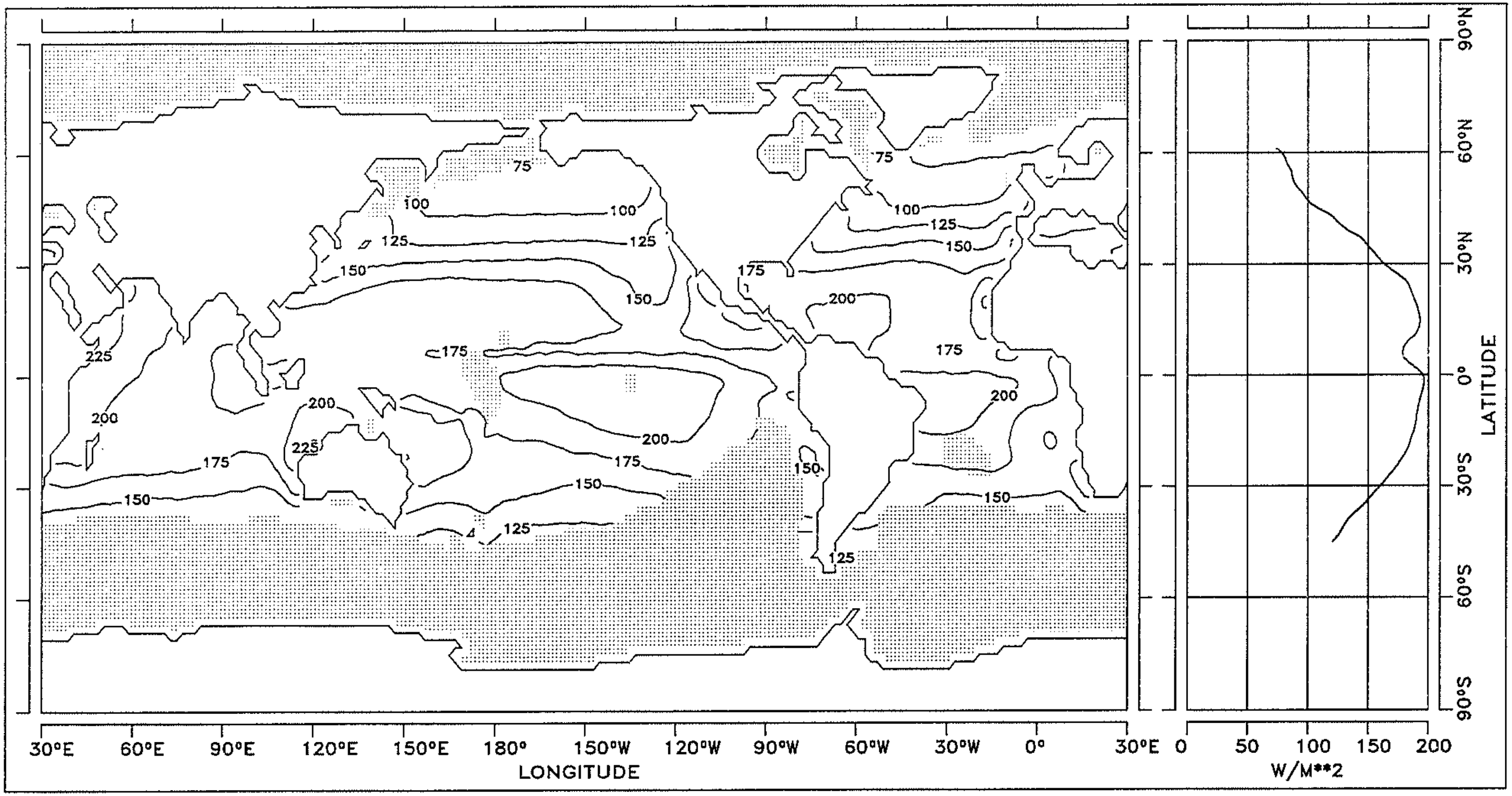

CONTOUR INTERVAL: 25 W/M**2 REFERENCE LINE : 0 W/M**2

LONG WAVE RADIATION BUDGET

FIG. 2.1 LONG WAVE RADIATION BUDGET JANUARY

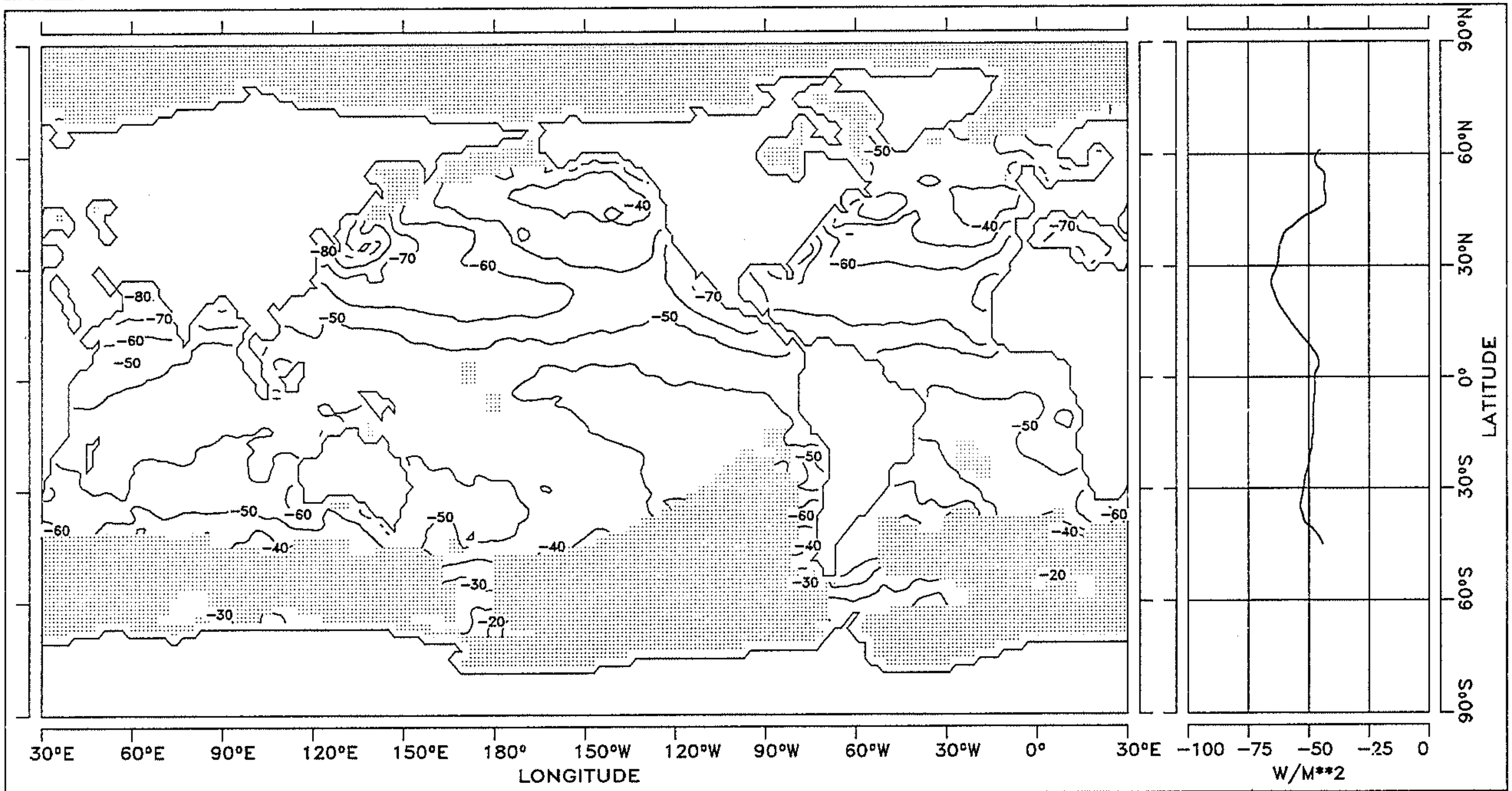

CONTOUR INTERVAL: 10 W/M**2 REFERENCE LINE : 0 W/M**2

FIG. 2.2 LONG WAVE RADIATION BUDGET

FEBRUARY

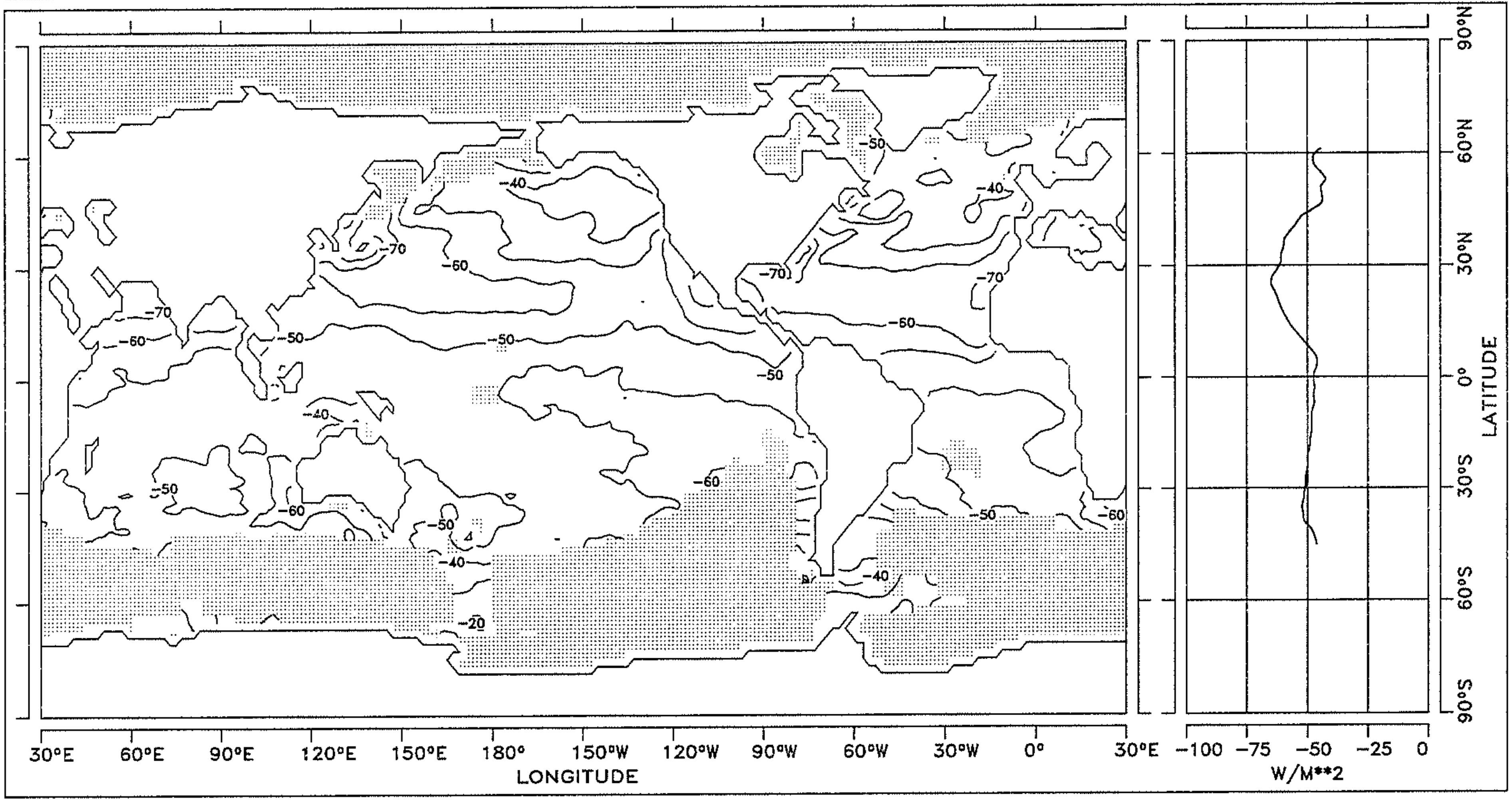

CONTOUR INTERVAL: 10 W/M**2   REFERENCE LINE : 0 W/M**2

FIG. 2.3 LONG WAVE RADIATION BUDGET MARCH

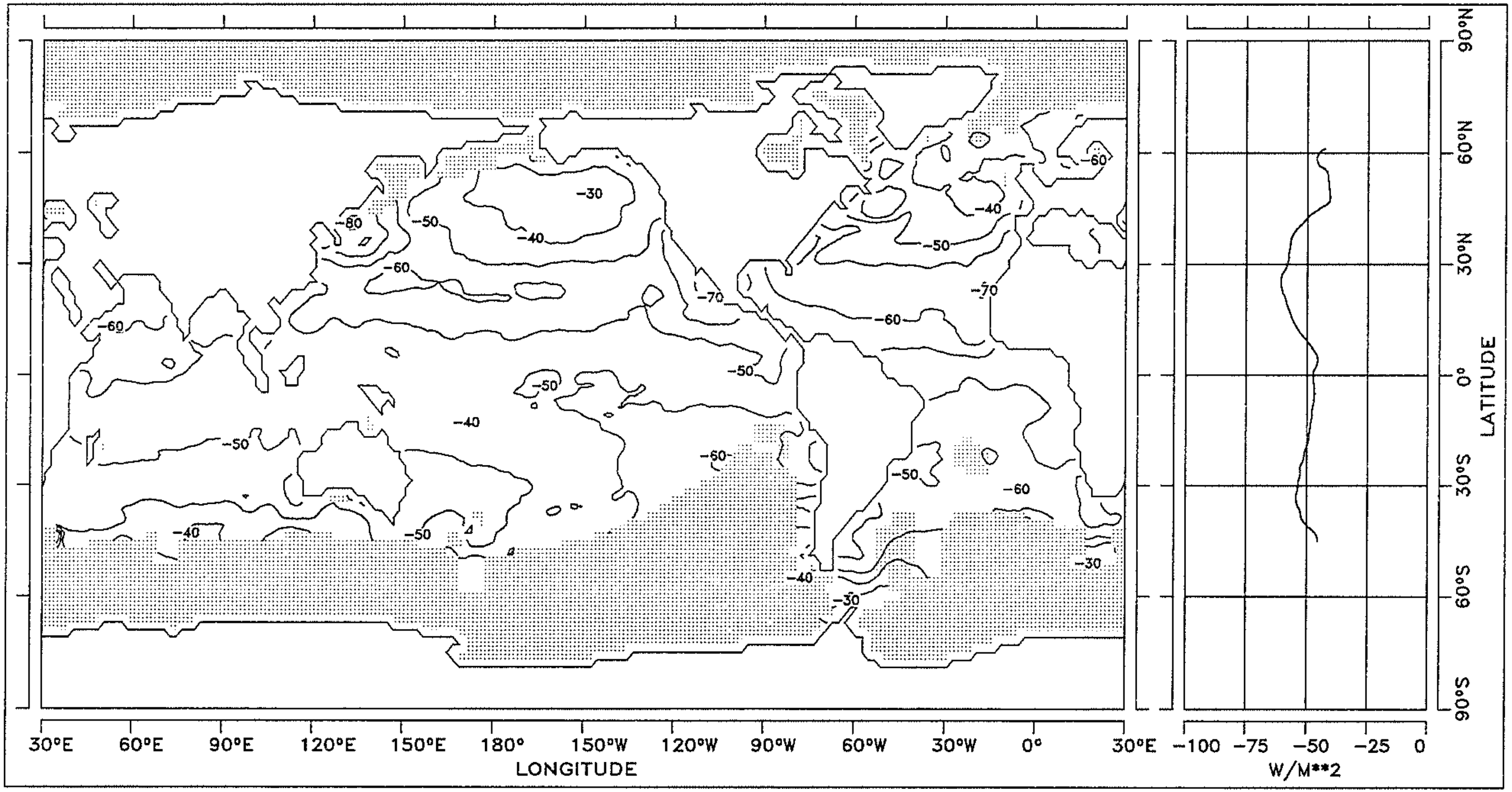

CONTOUR INTERVAL: 10 W/M**2 REFERENCE LINE : 0 W/M**2

FIG. 2.4 LONG WAVE RADIATION BUDGET APRIL

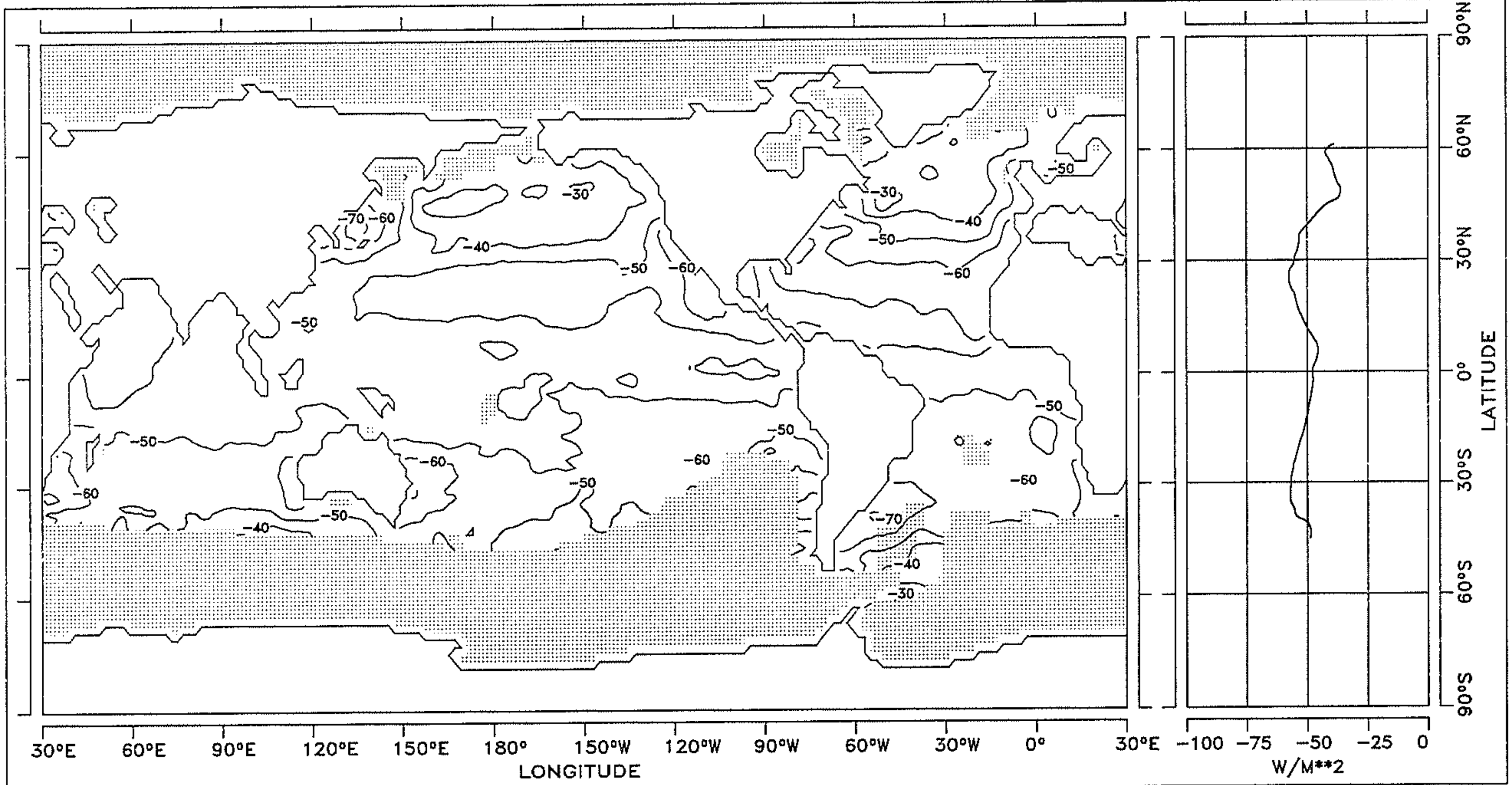

CONTOUR INTERVAL: 10 W/M**2 REFERENCE LINE : 0 W/M**2

FIG. 2.5 LONG WAVE RADIATION BUDGET MAY

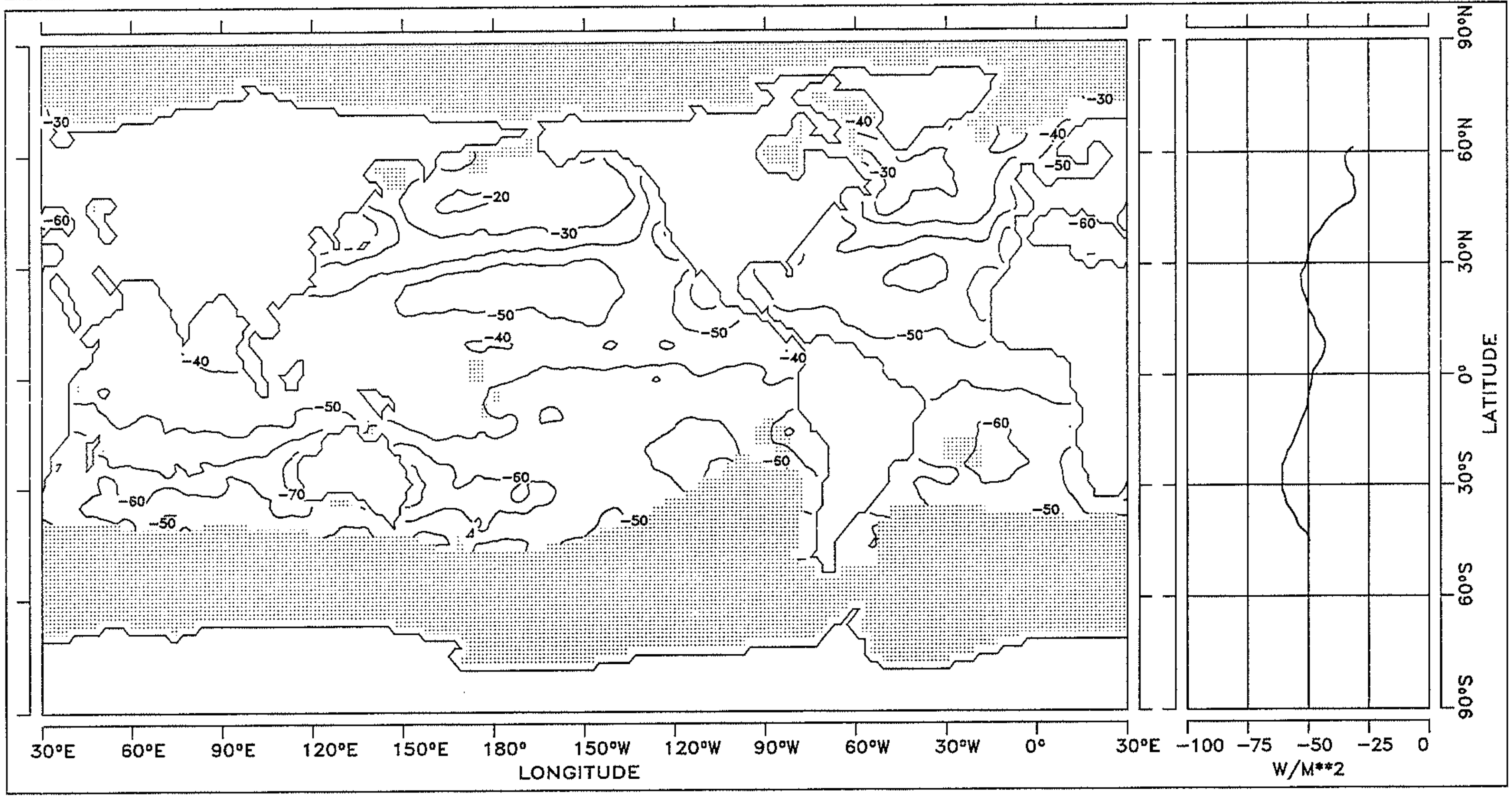

CONTOUR INTERVAL: 10 W/M**2 REFERENCE LINE : 0 W/M**2

FIG. 2.6 LONG WAVE RADIATION BUDGET JUNE

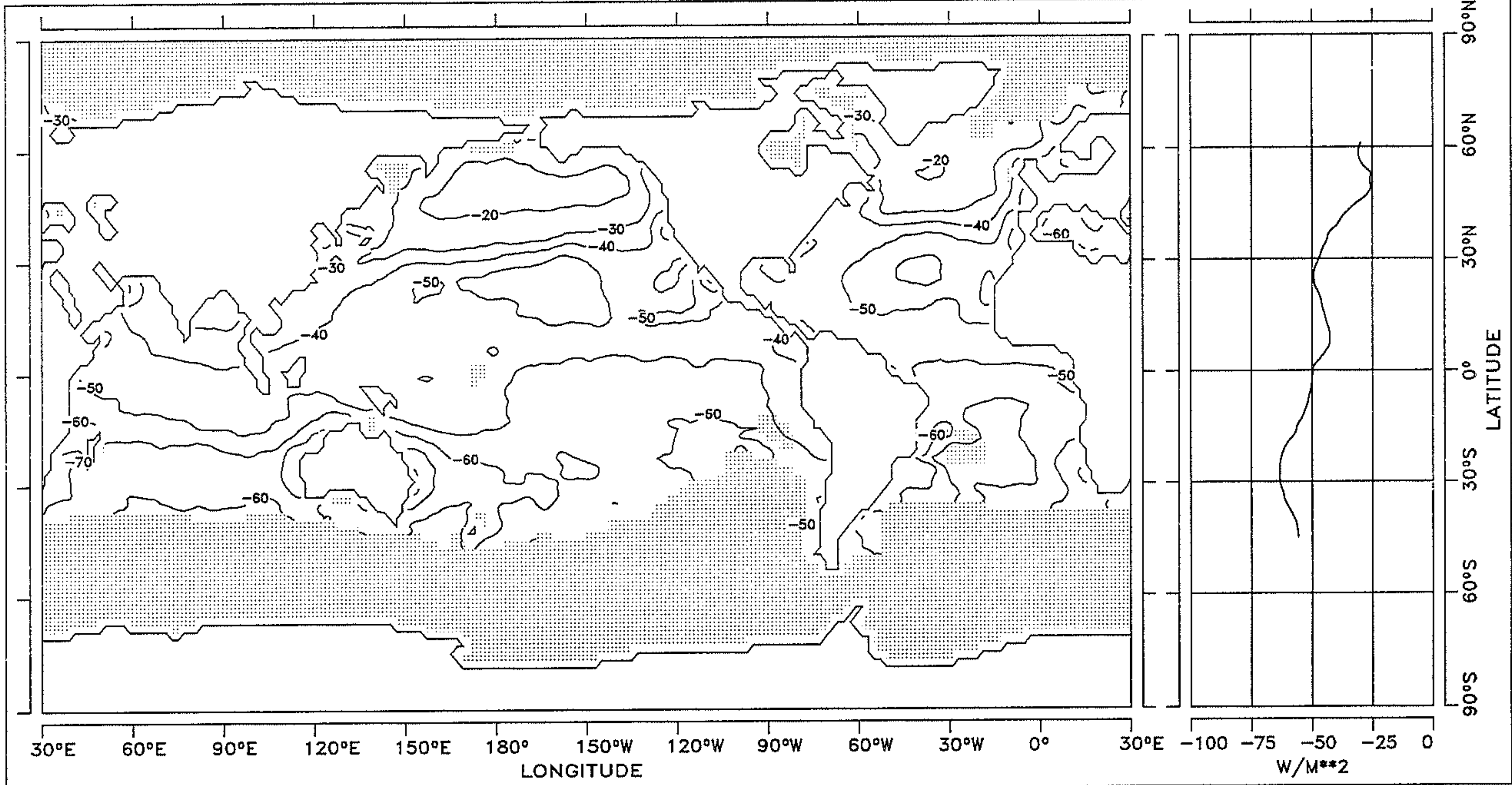

CONTOUR INTERVAL: 10 W/M**2 REFERENCE LINE : 0 W/M**2

FIG. 2.7 LONG WAVE RADIATION BUDGET JULY

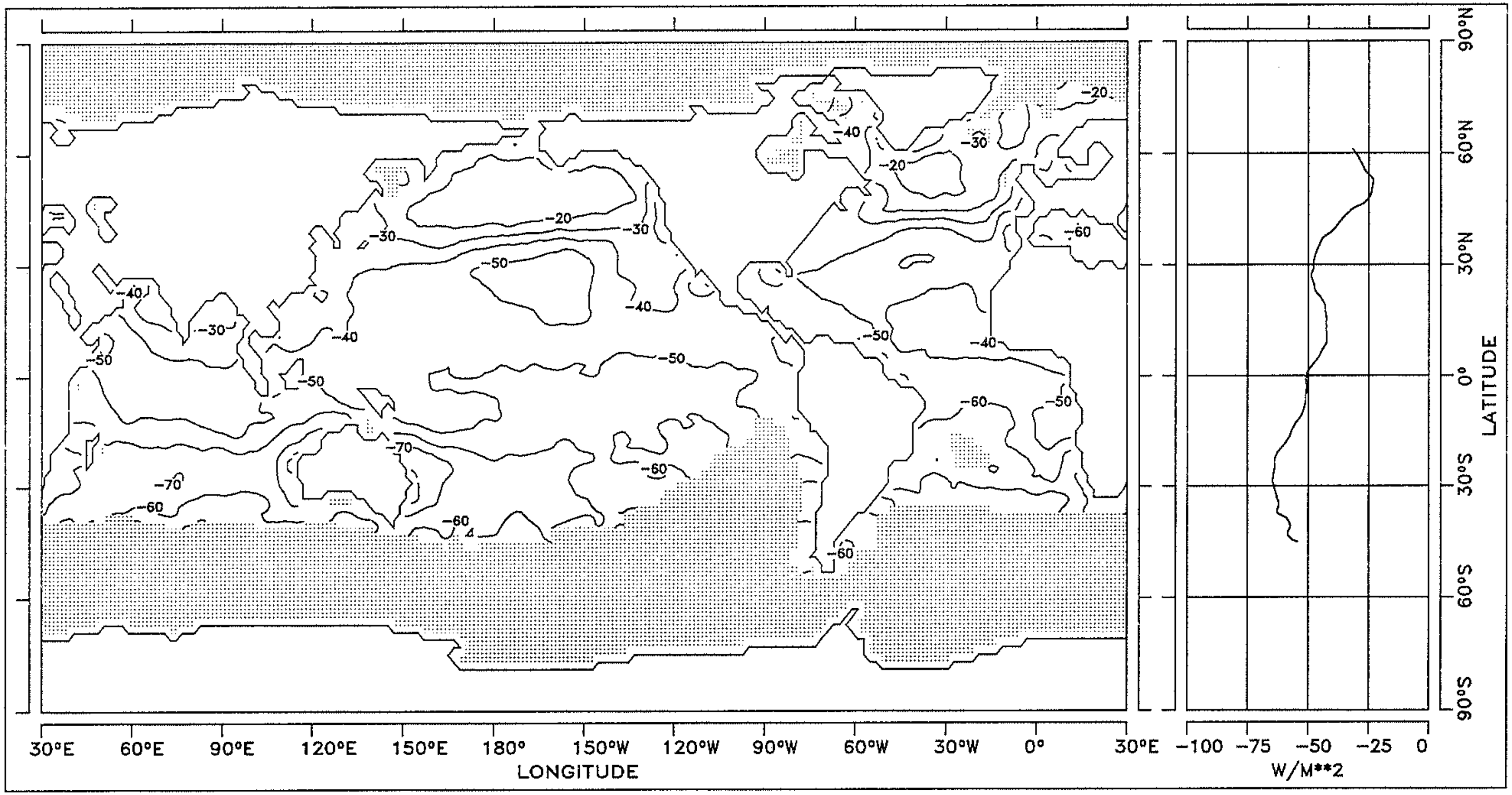

CONTOUR INTERVAL: 10 W/M**2 REFERENCE LINE : 0 W/M**2

FIG. 2.8 LONG WAVE RADIATION BUDGET AUGUST

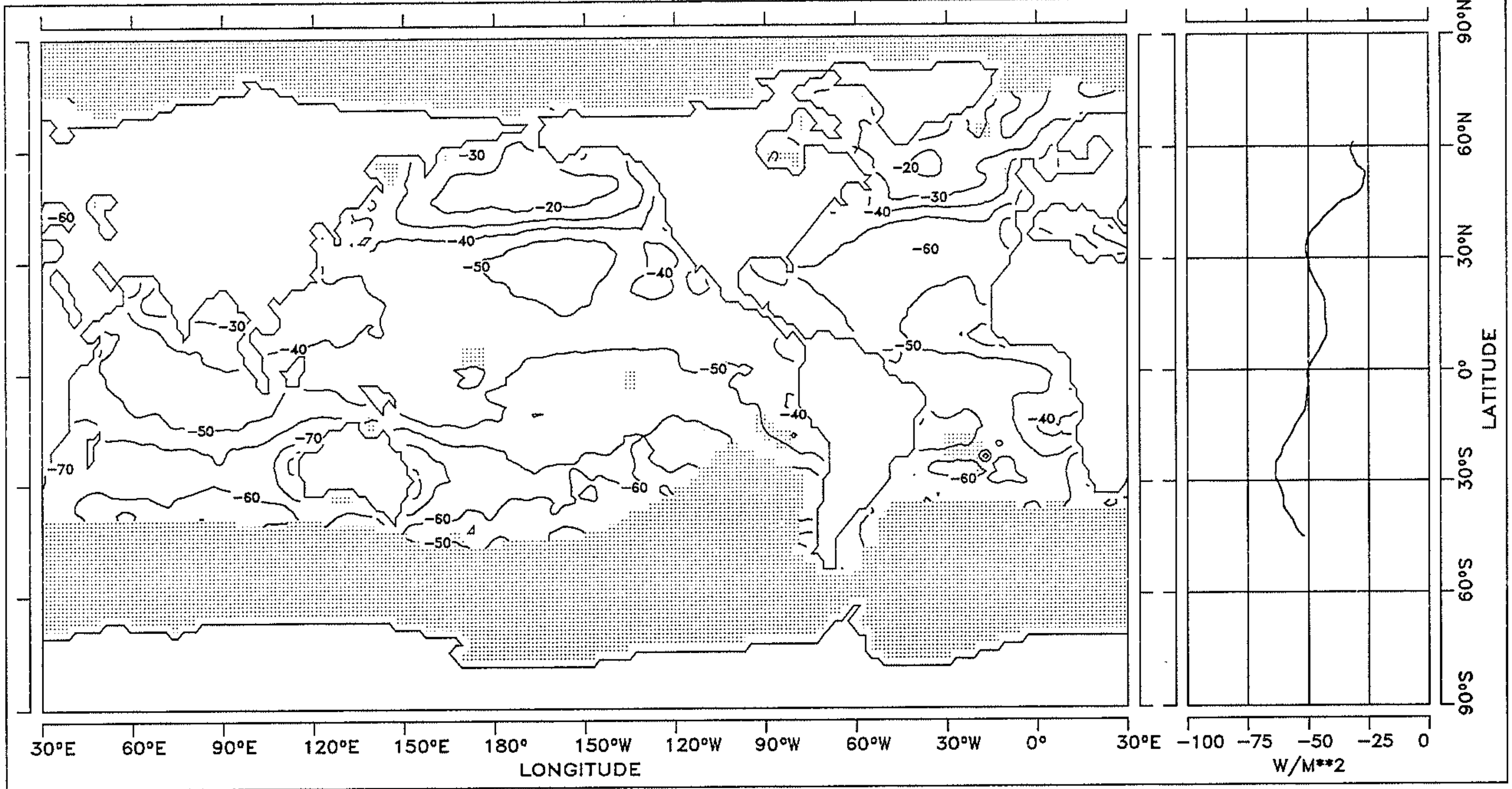

CONTOUR INTERVAL: 10 W/M**2 REFERENCE LINE : 0 W/M**2

FIG. 2.9 LONG WAVE RADIATION BUDGET SEPTEMBER

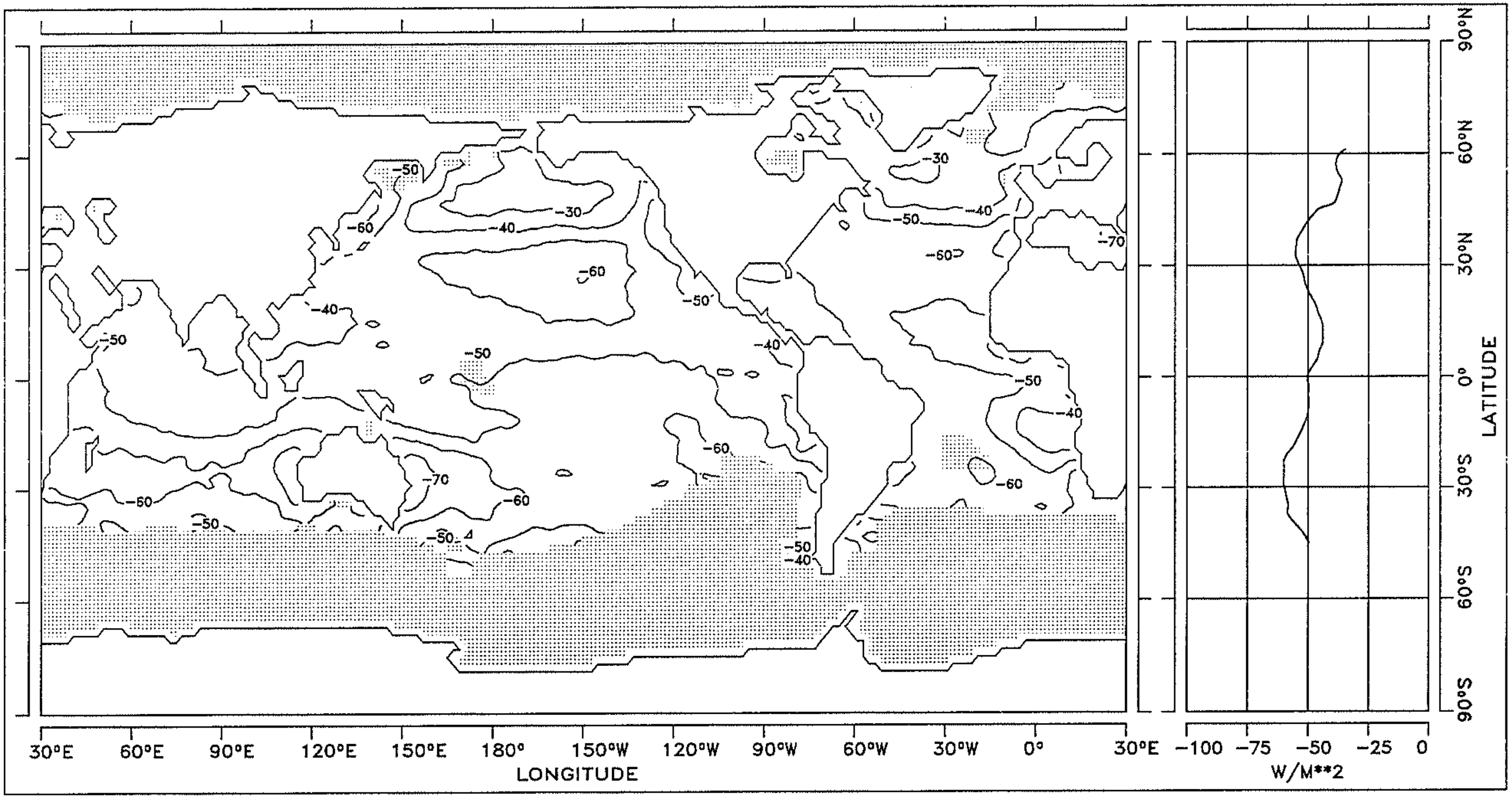

CONTOUR INTERVAL: 10 W/M**2 REFERENCE LINE : 0 W/M**2

FIG. 2.10 LONG WAVE RADIATION BUDGET OCTOBER

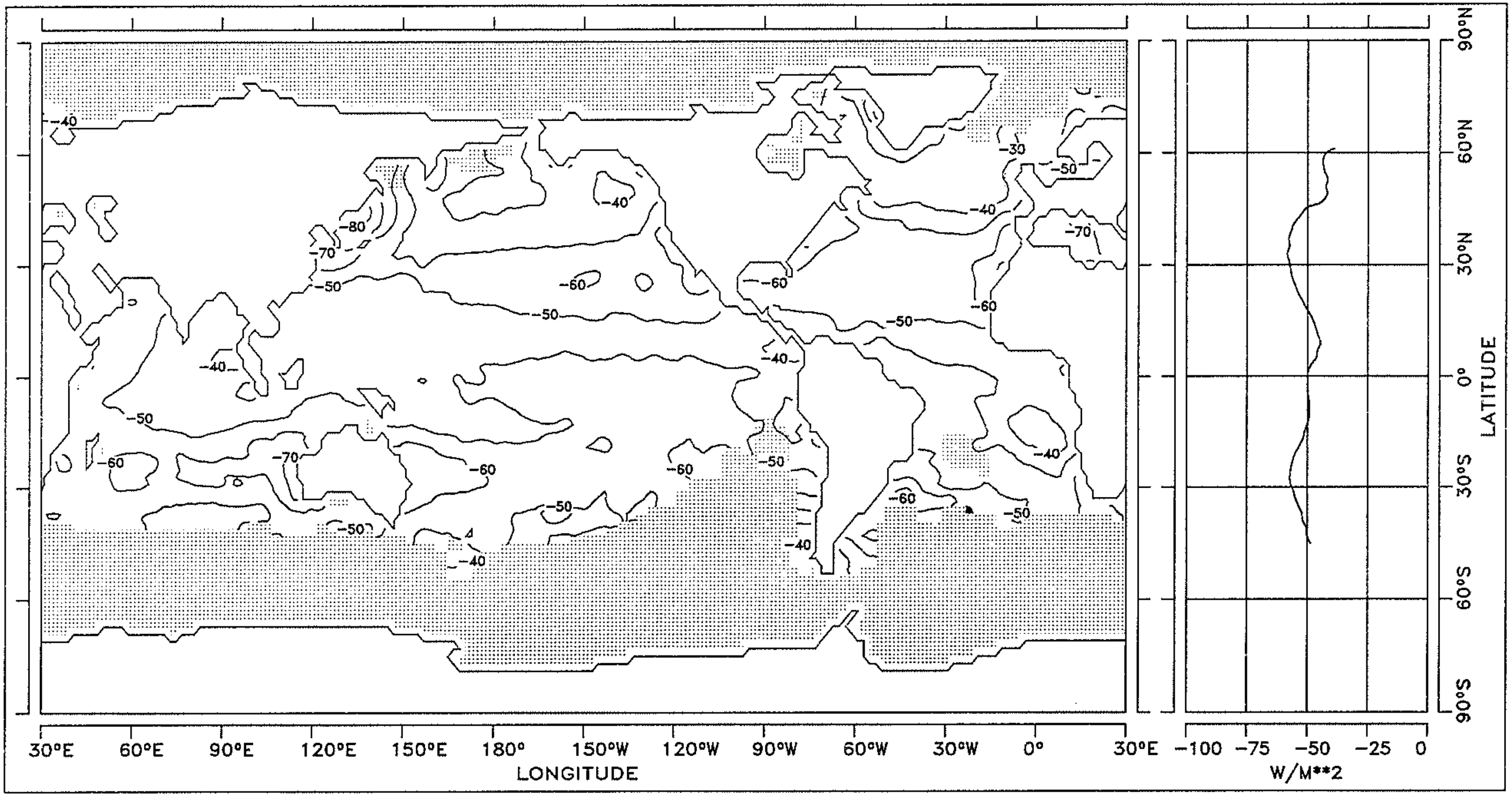

CONTOUR INTERVAL: 10 W/M**2 REFERENCE LINE : 0 W/M**2

FIG. 2.11 LONG WAVE RADIATION BUDGET NOVEMBER

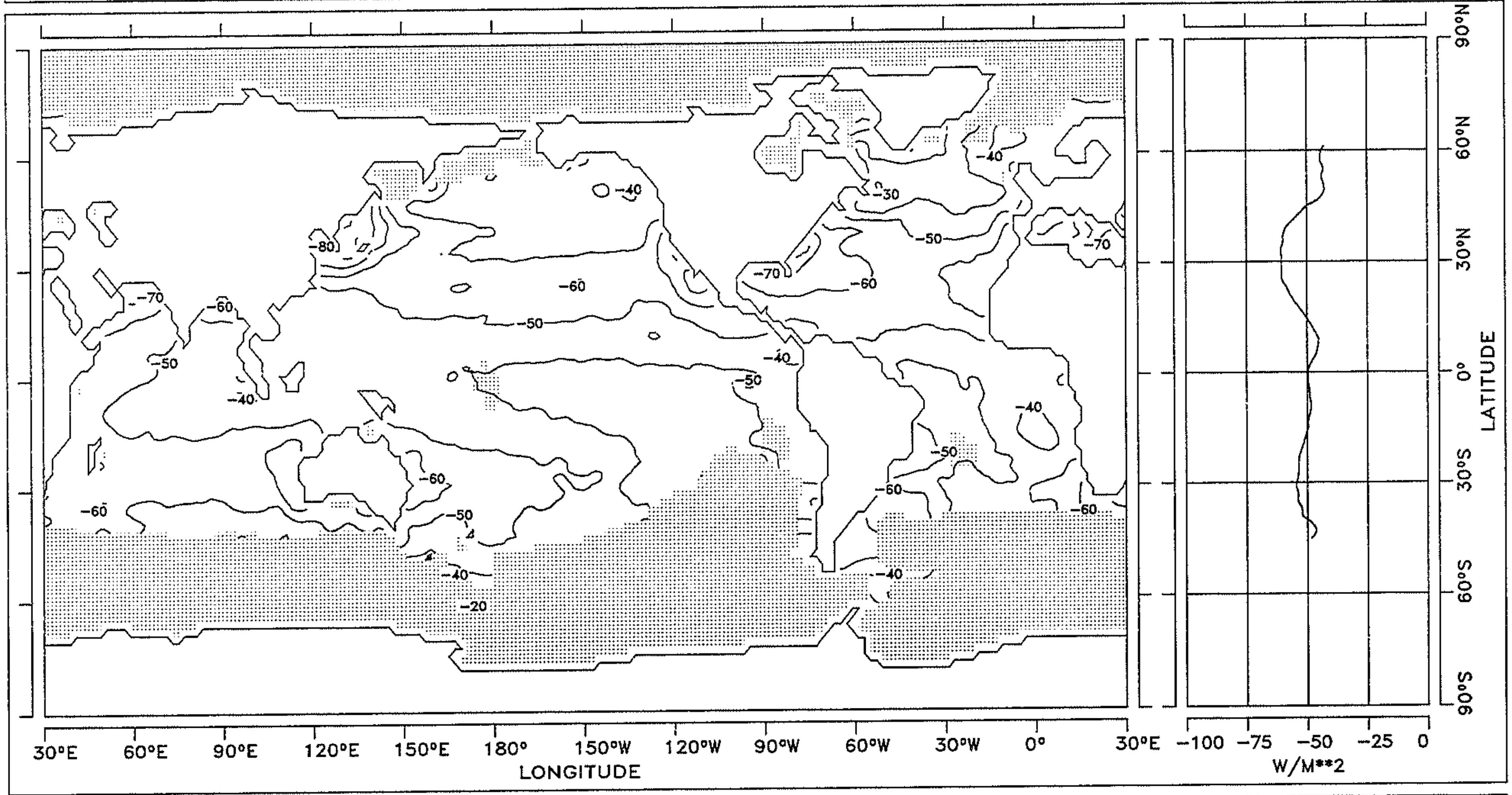

CONTOUR INTERVAL: 10 W/M**2 REFERENCE LINE : 0 W/M**2

FIG. 2.12 LONG WAVE RADIATION BUDGET DECEMBER

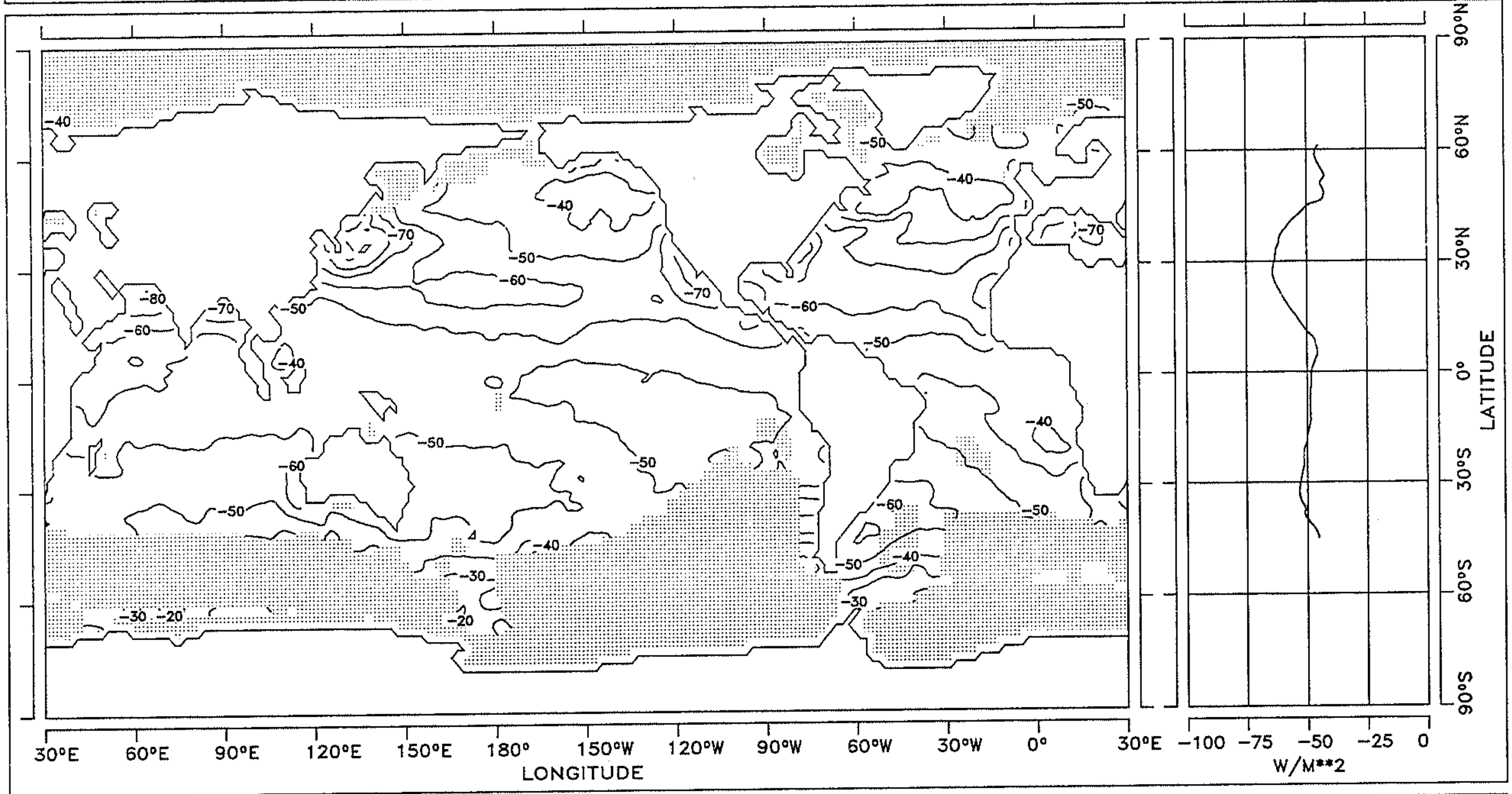

CONTOUR INTERVAL: 10 W/M**2 REFERENCE LINE : 0 W/M**2

FIG. 2.13 LONG WAVE RADIATION BUDGET ANNUAL MEAN

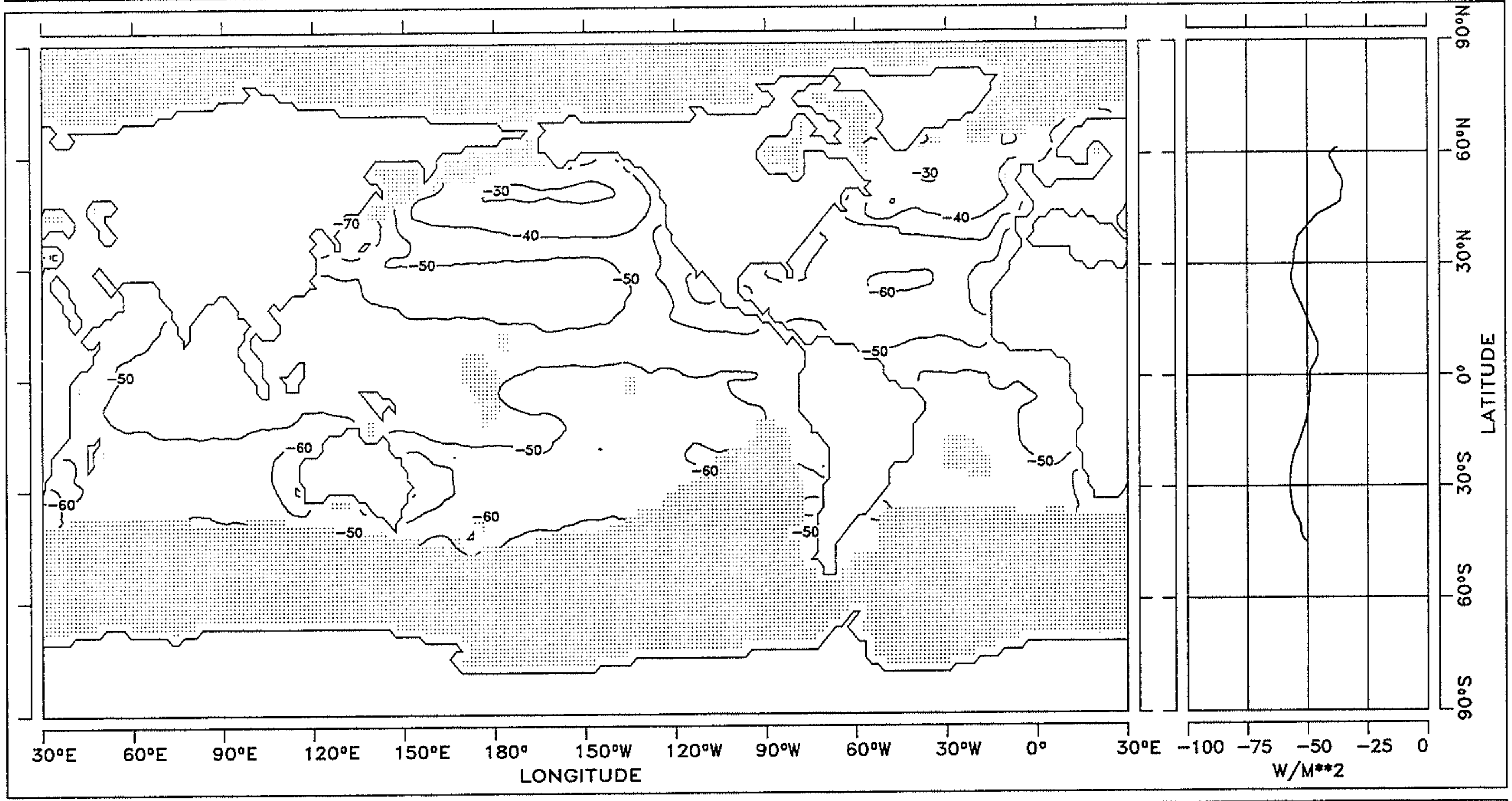

CONTOUR INTERVAL: 10 W/M**2 REFERENCE LINE : 0 W/M**2

NET RADIATION BUDGET

FIG. 3.1 NET RADIATION BUDGET JANUARY

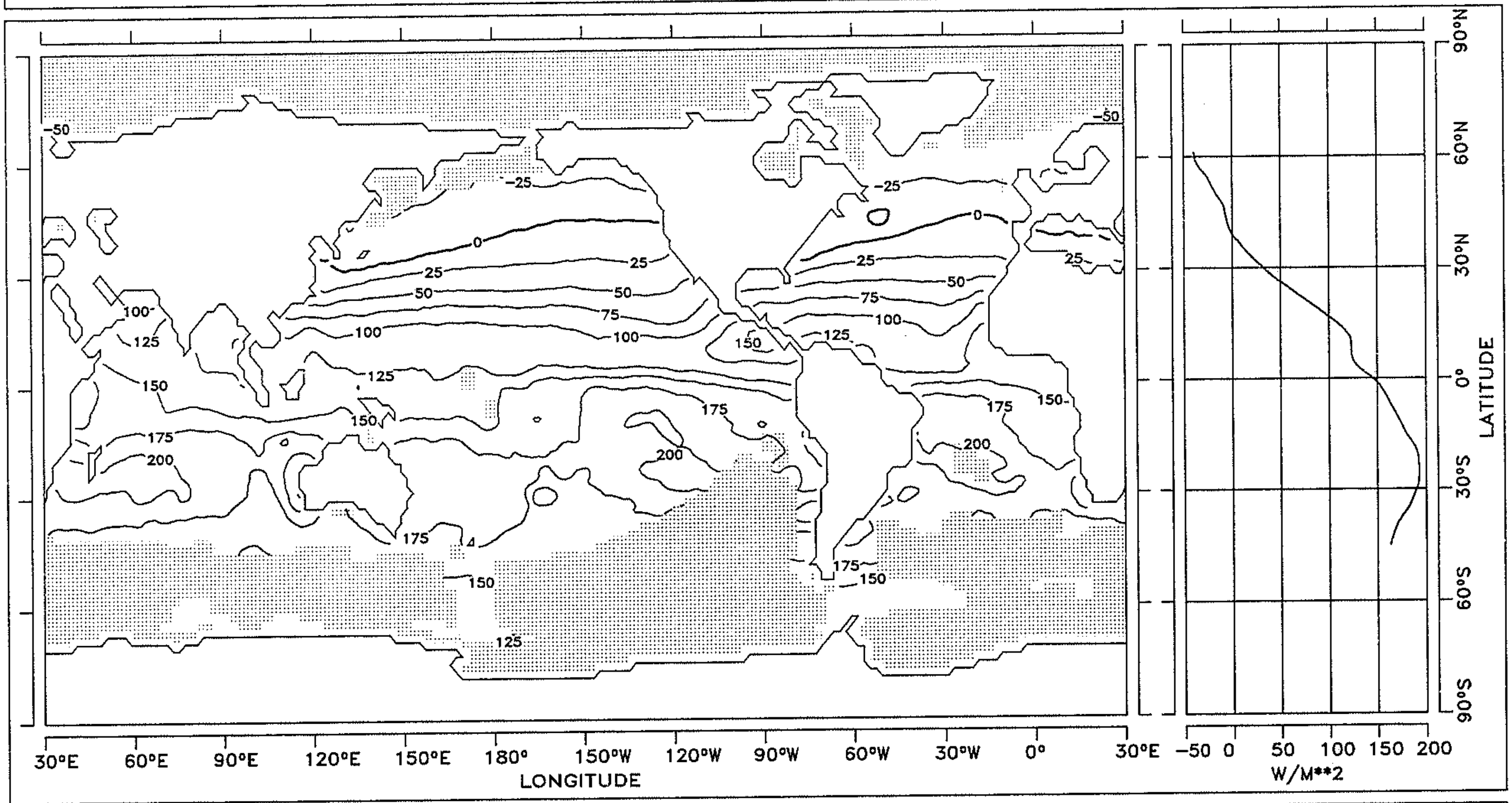

CONTOUR INTERVAL: 25 W/M**2 REFERENCE LINE : 0 W/M**2

FIG. 3.2 NET RADIATION BUDGET FEBRUARY

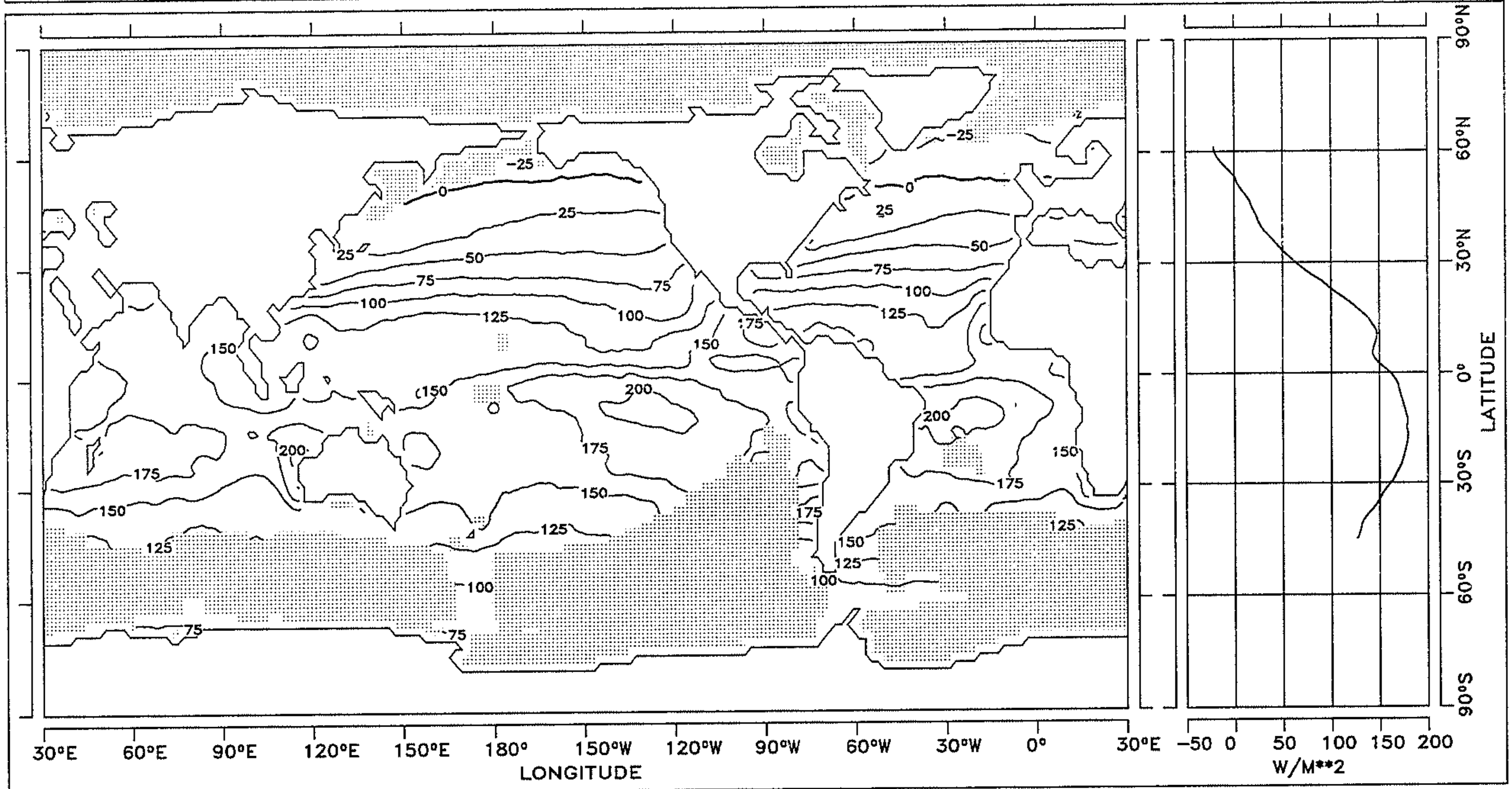

CONTOUR INTERVAL: 25 W/M**2 REFERENCE LINE : 0 W/M**2

FIG. 3.3 NET RADIATION BUDGET MARCH

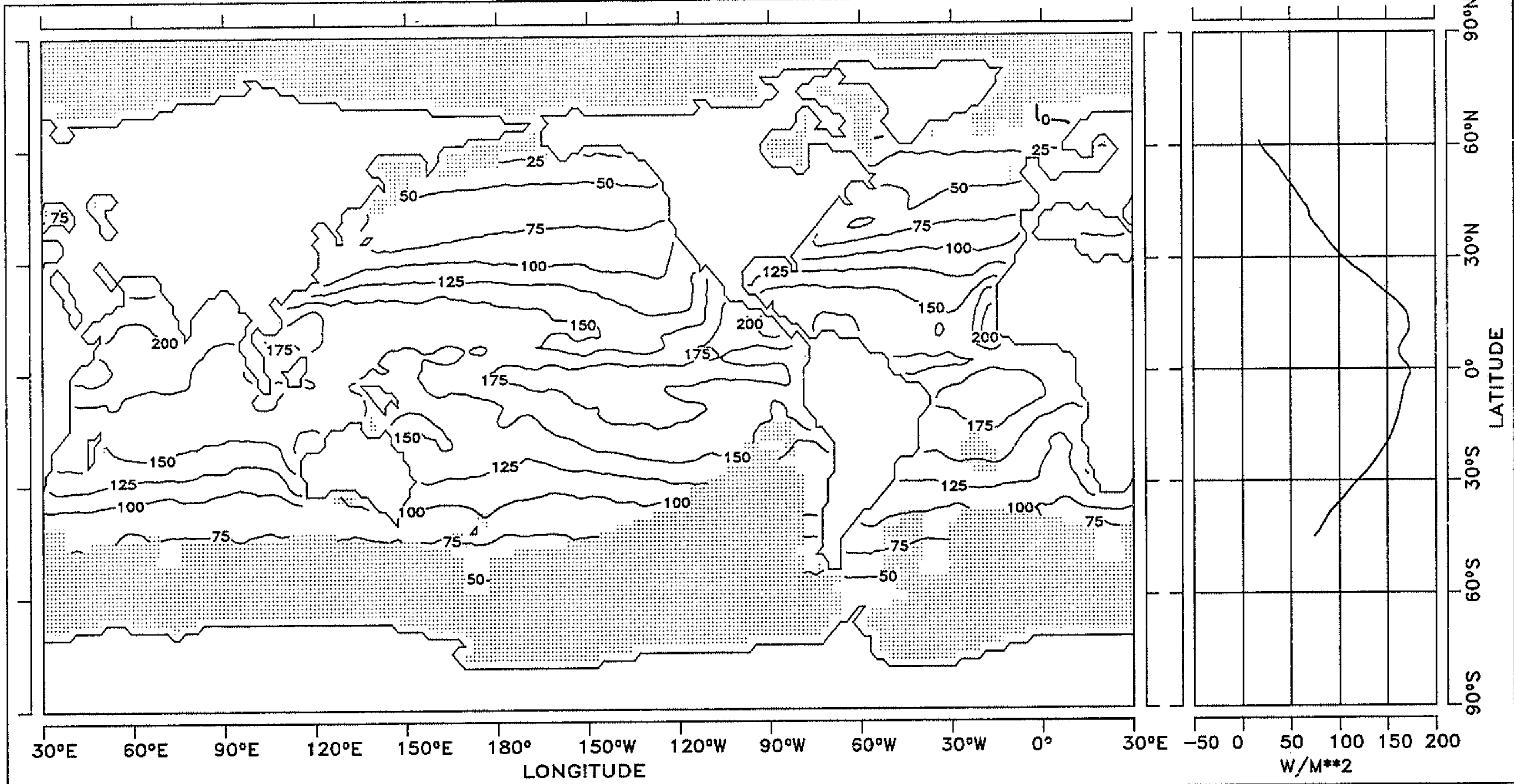

CONTOUR INTERVAL: 25 W/M**2 REFERENCE LINE : 0 W/M**2

FIG. 3.4 NET RADIATION BUDGET APRIL

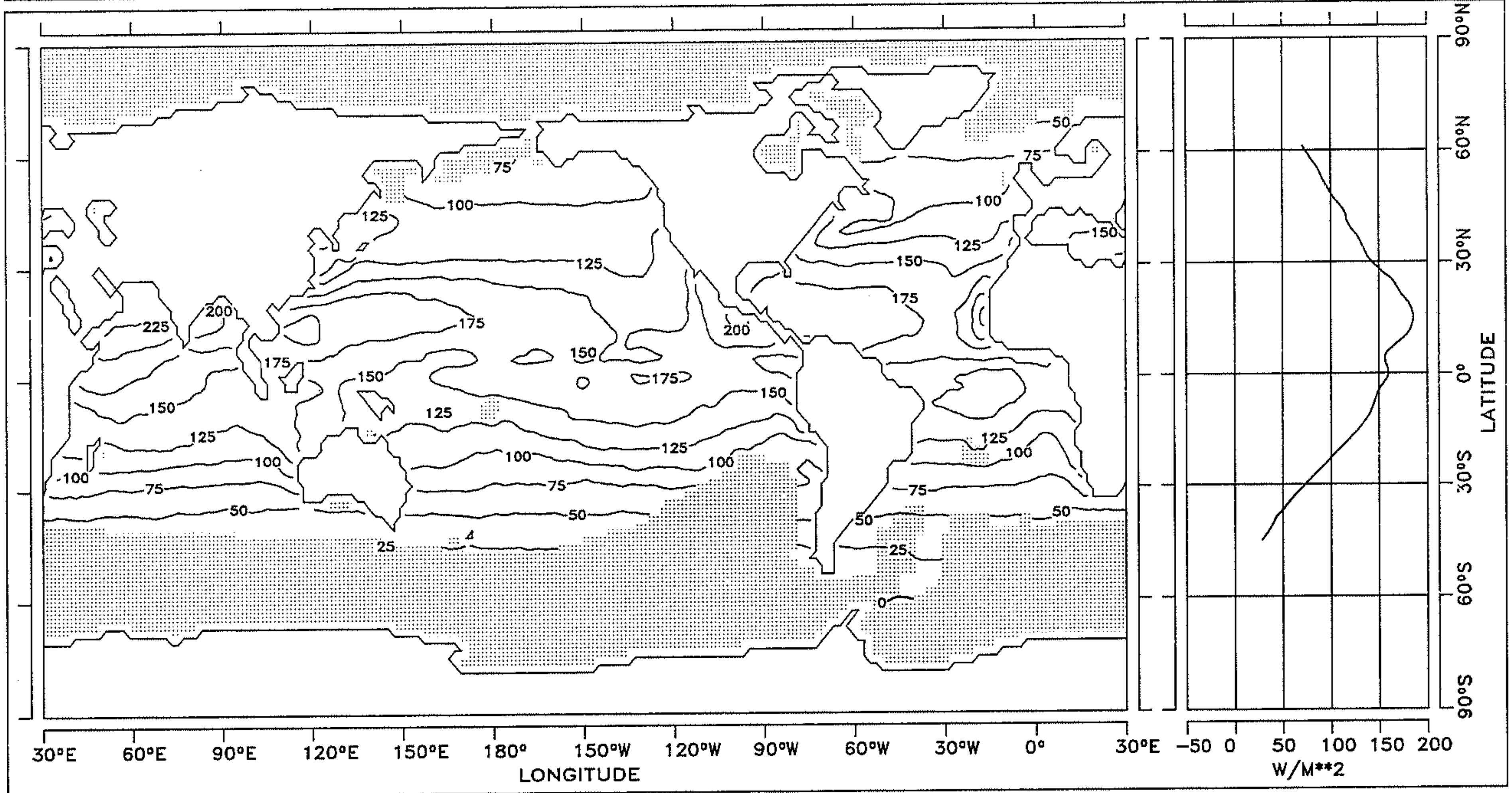

CONTOUR INTERVAL: 25 W/M**2 REFERENCE LINE : 0 W/M**2

FIG. 3.5 NET RADIATION BUDGET MAY

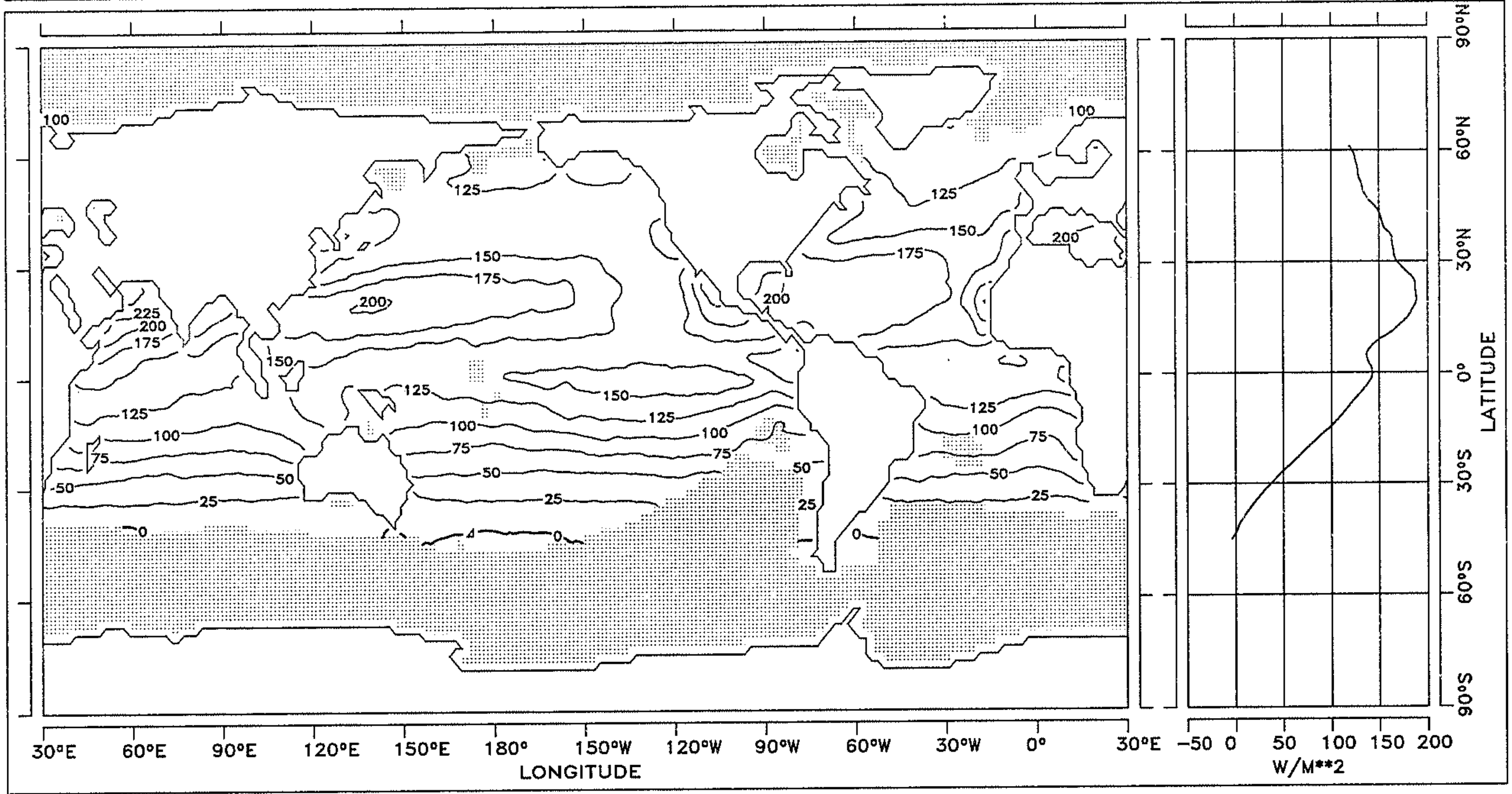

CONTOUR INTERVAL: 25 W/M**2 REFERENCE LINE : 0 W/M**2

FIG. 3.6 NET RADIATION BUDGET JUNE

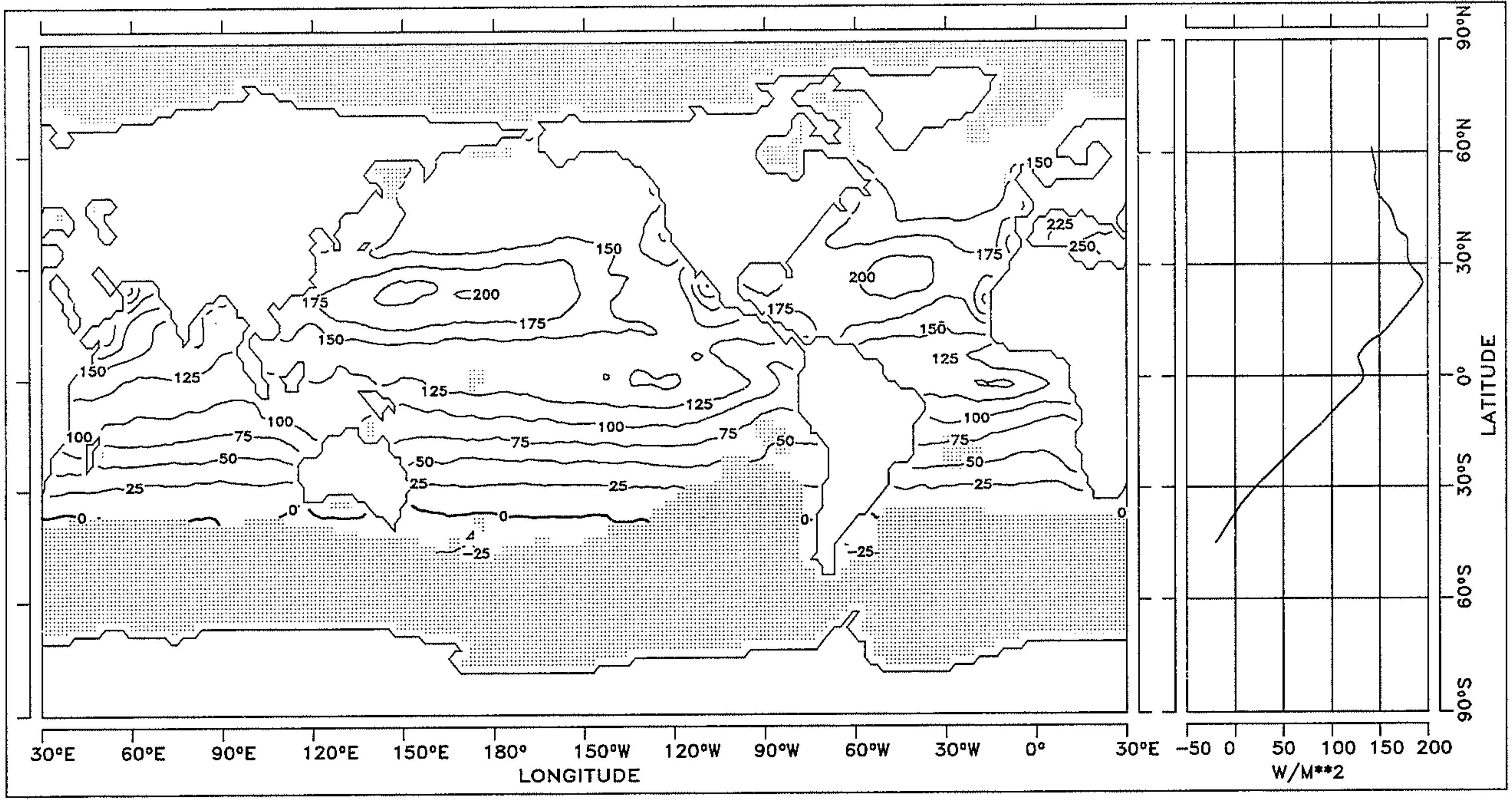

CONTOUR INTERVAL: 25 W/M**2 REFERENCE LINE : 0 W/M**2

FIG. 3.7 NET RADIATION BUDGET JULY

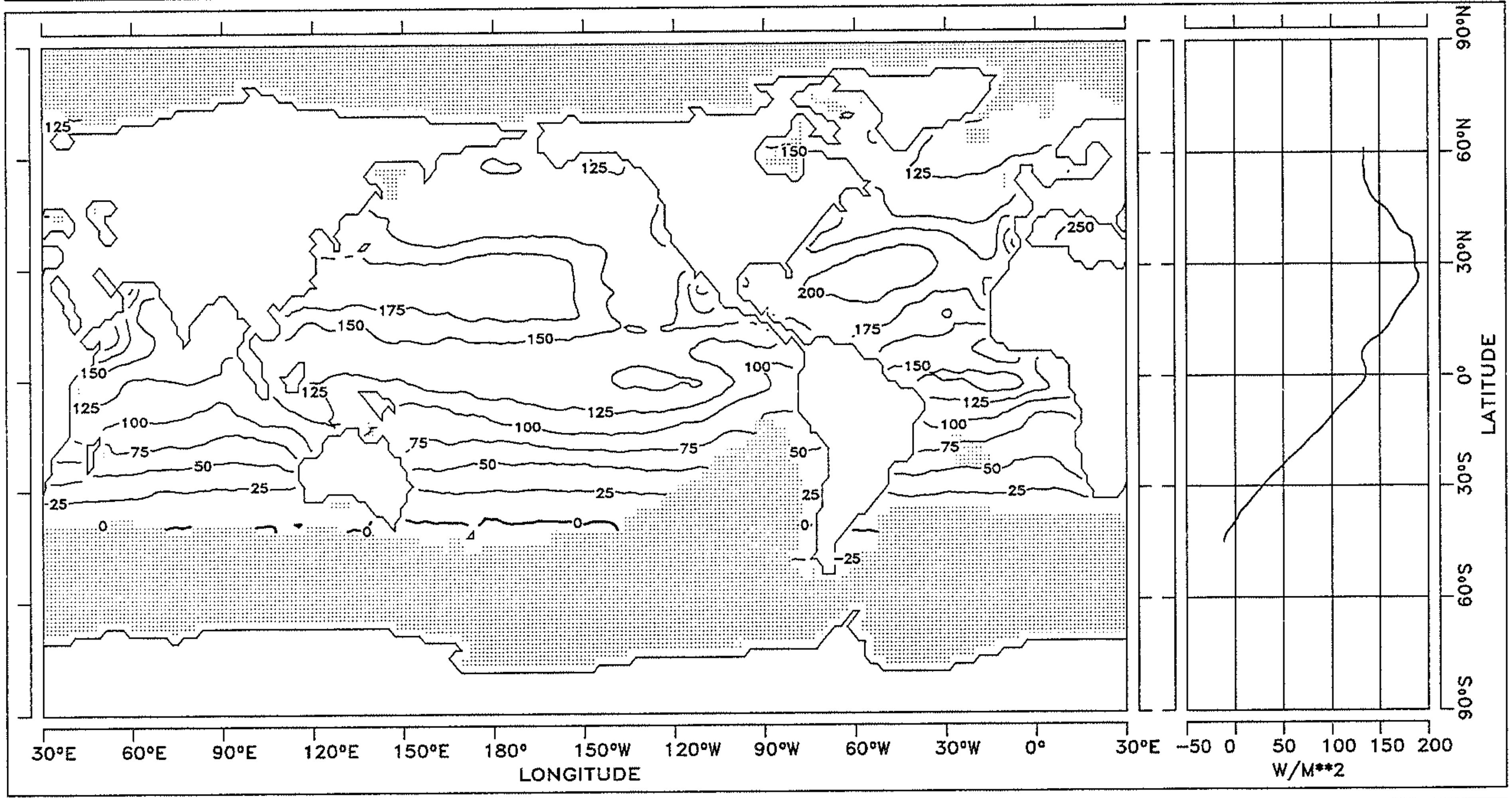

CONTOUR INTERVAL: 25 W/M**2 REFERENCE LINE : 0 W/M**2

FIG. 3.8 NET RADIATION BUDGET AUGUST

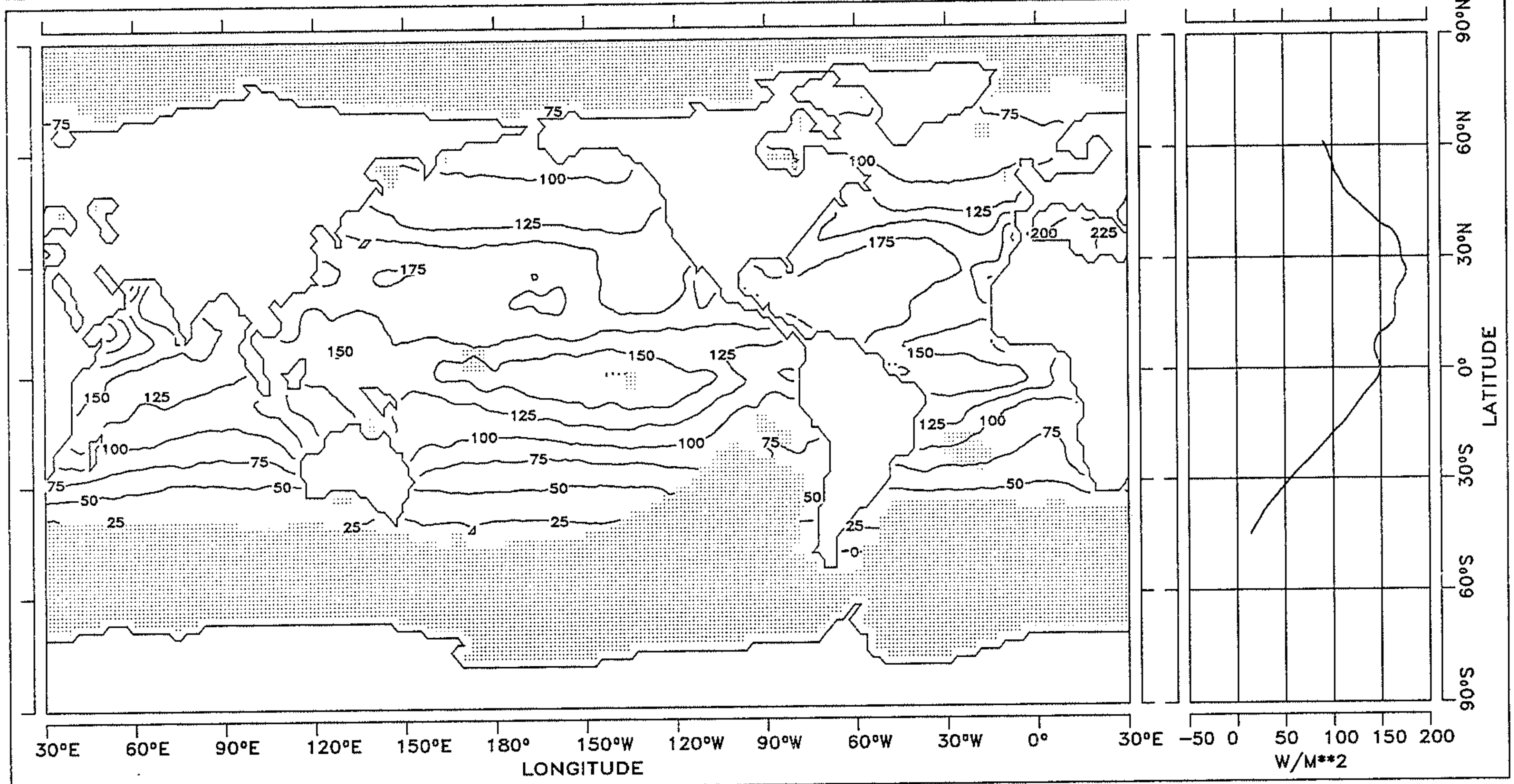

CONTOUR INTERVAL: 25 W/M**2 REFERENCE LINE : 0 W/M**2

FIG. 3.9 NET RADIATION BUDGET

SEPTEMBER

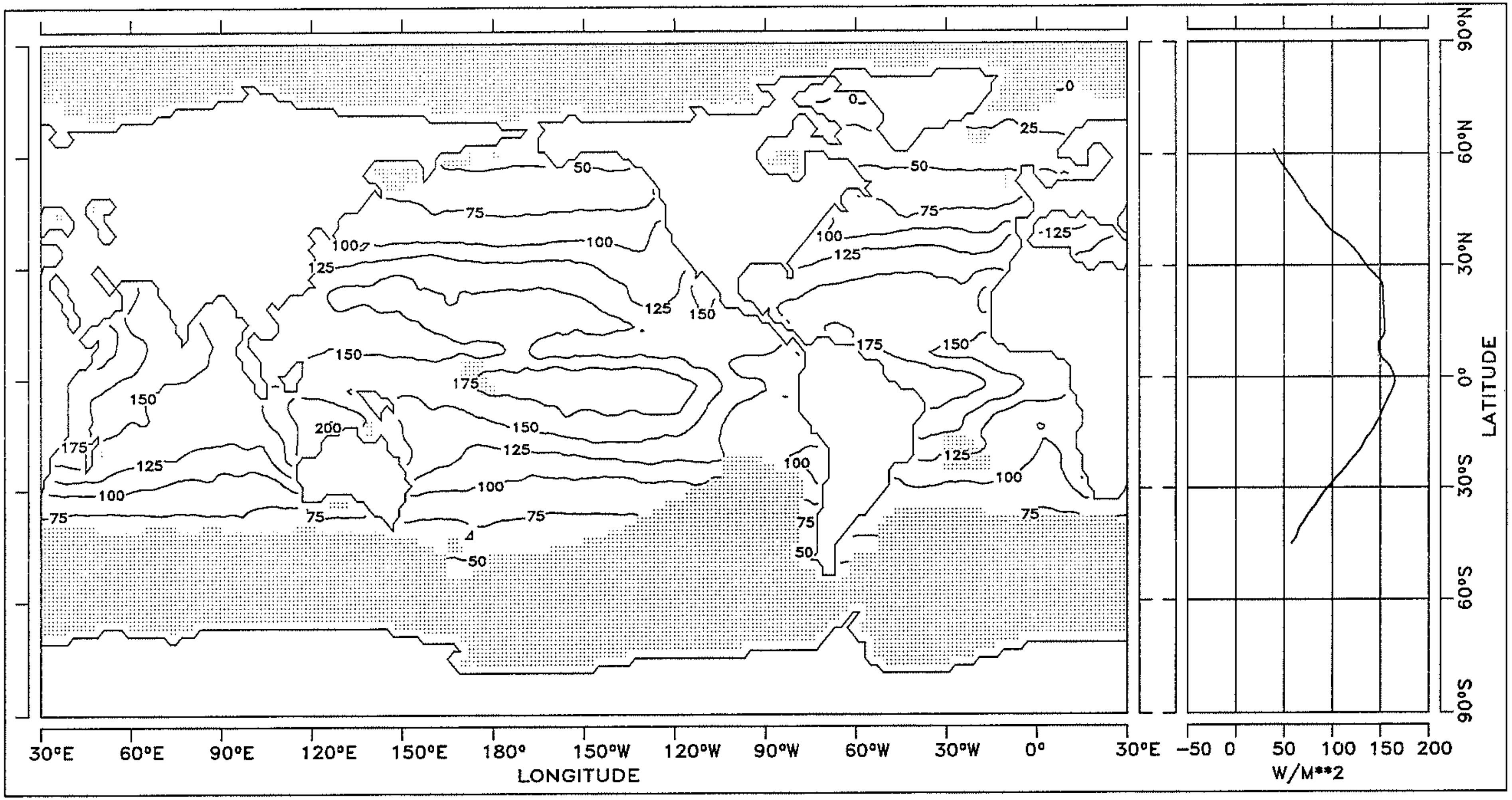

CONTOUR INTERVAL: 25 W/M**2 REFERENCE LINE : 0 W/M**2

FIG. 3.10 NET RADIATION BUDGET OCTOBER

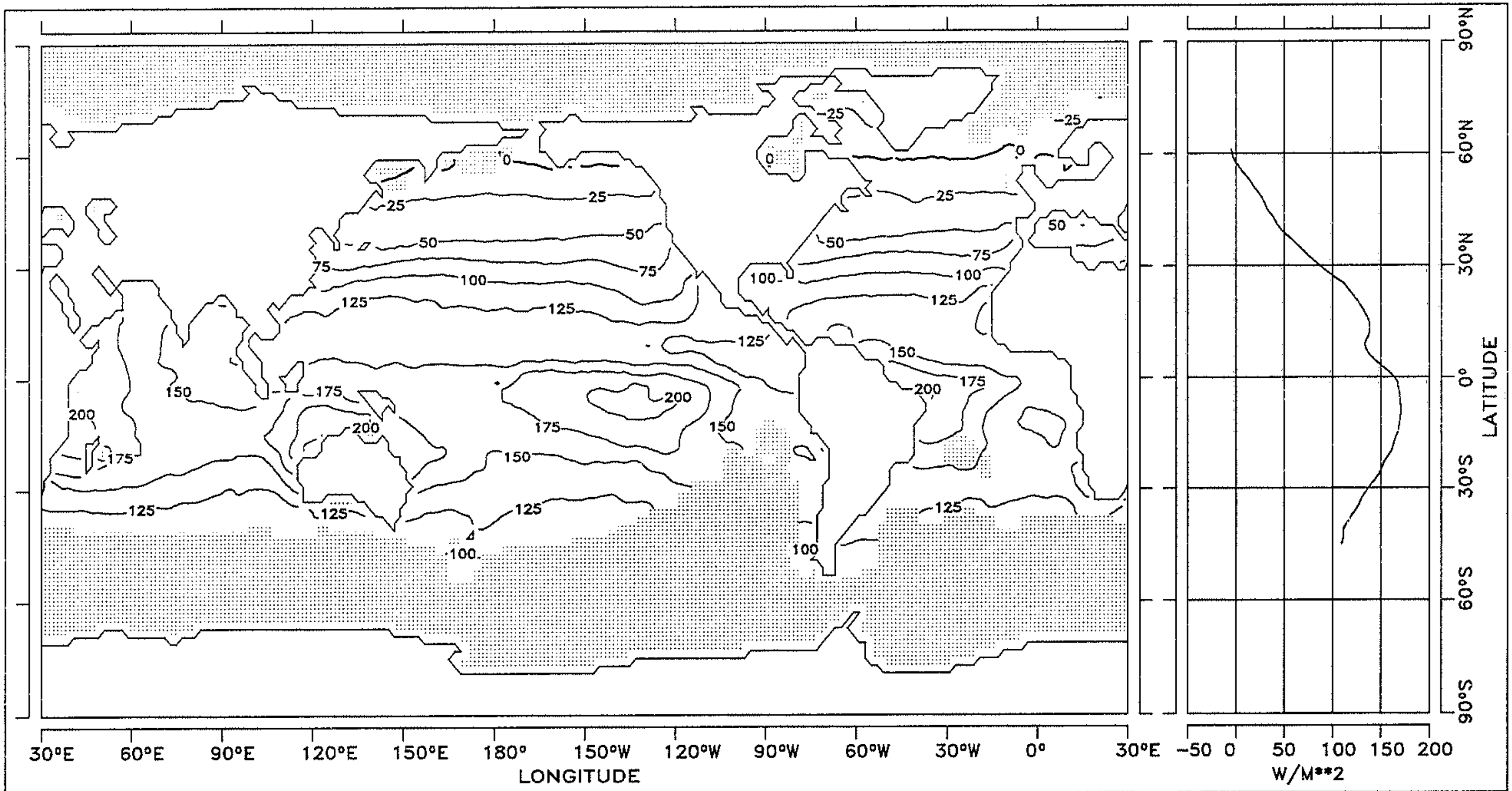

CONTOUR INTERVAL: 25 W/M**2 REFERENCE LINE : 0 W/M**2

FIG. 3.11 NET RADIATION BUDGET NOVEMBER

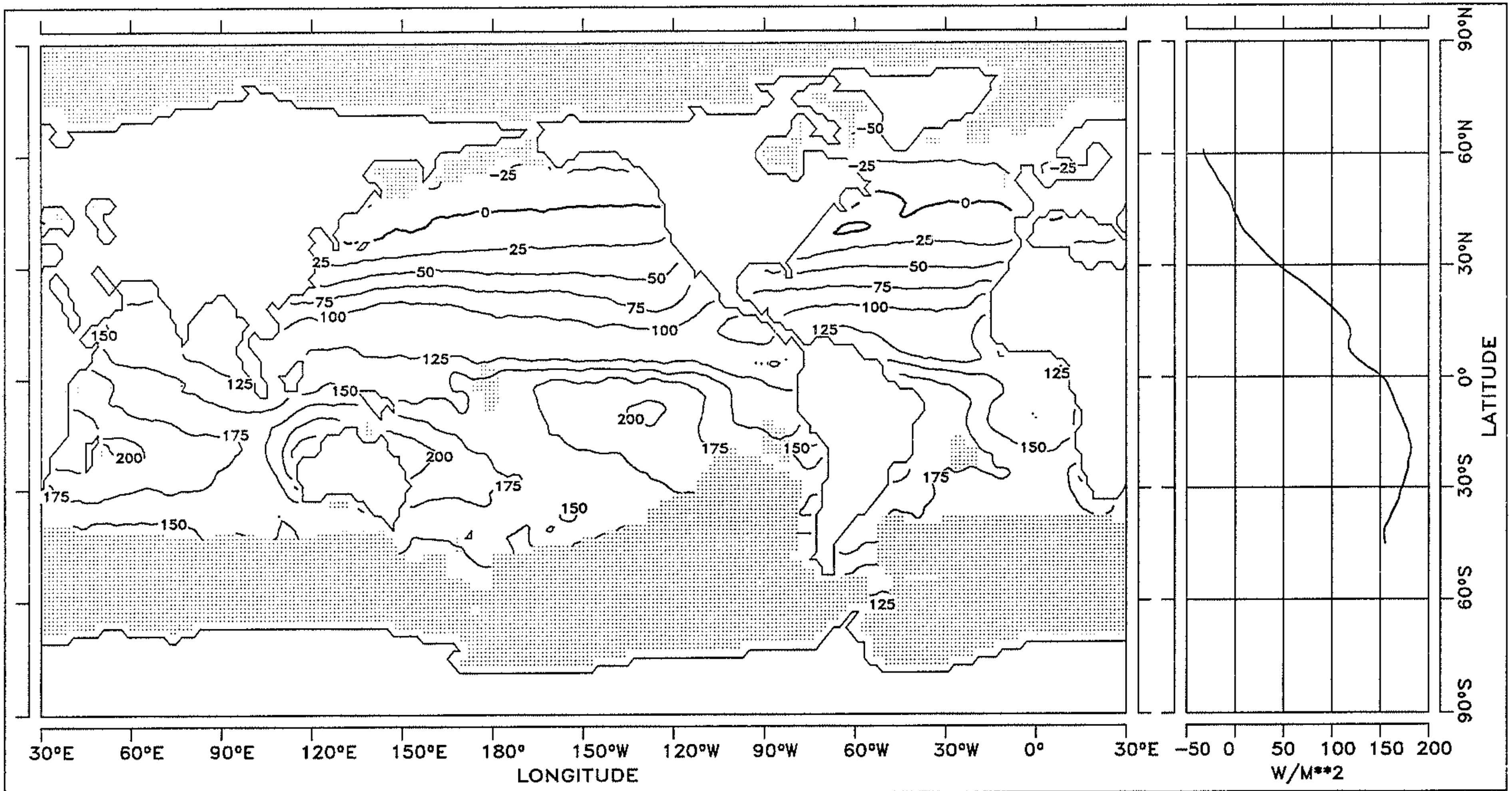

CONTOUR INTERVAL: 25 W/M**2 REFERENCE LINE : 0 W/M**2

FIG. 3.12 NET RADIATION BUDGET DECEMBER

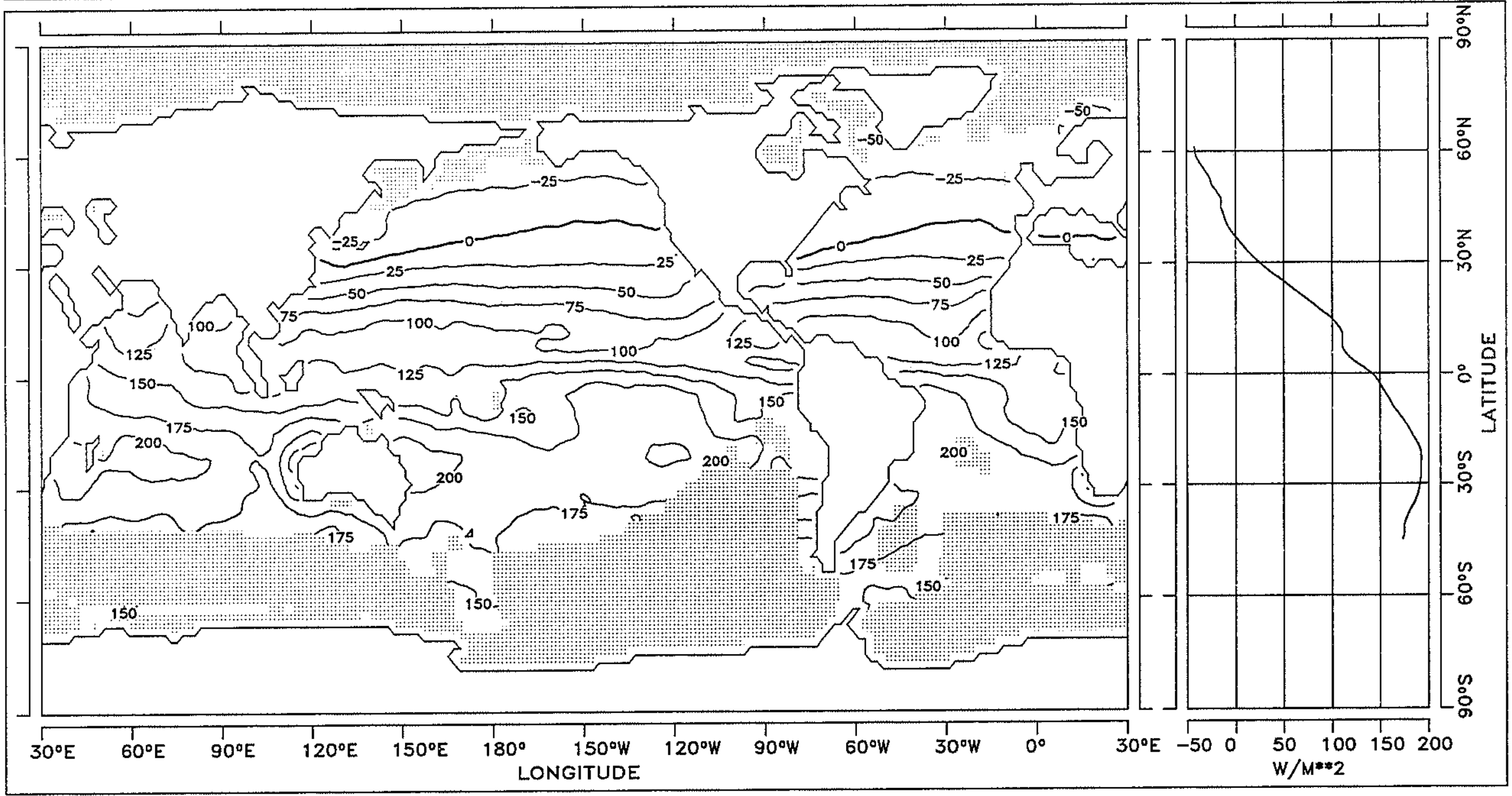

CONTOUR INTERVAL: 25 W/M**2   REFERENCE LINE : 0 W/M**2

FIG. 3.13 NET RADIATION BUDGET

ANNUAL MEAN

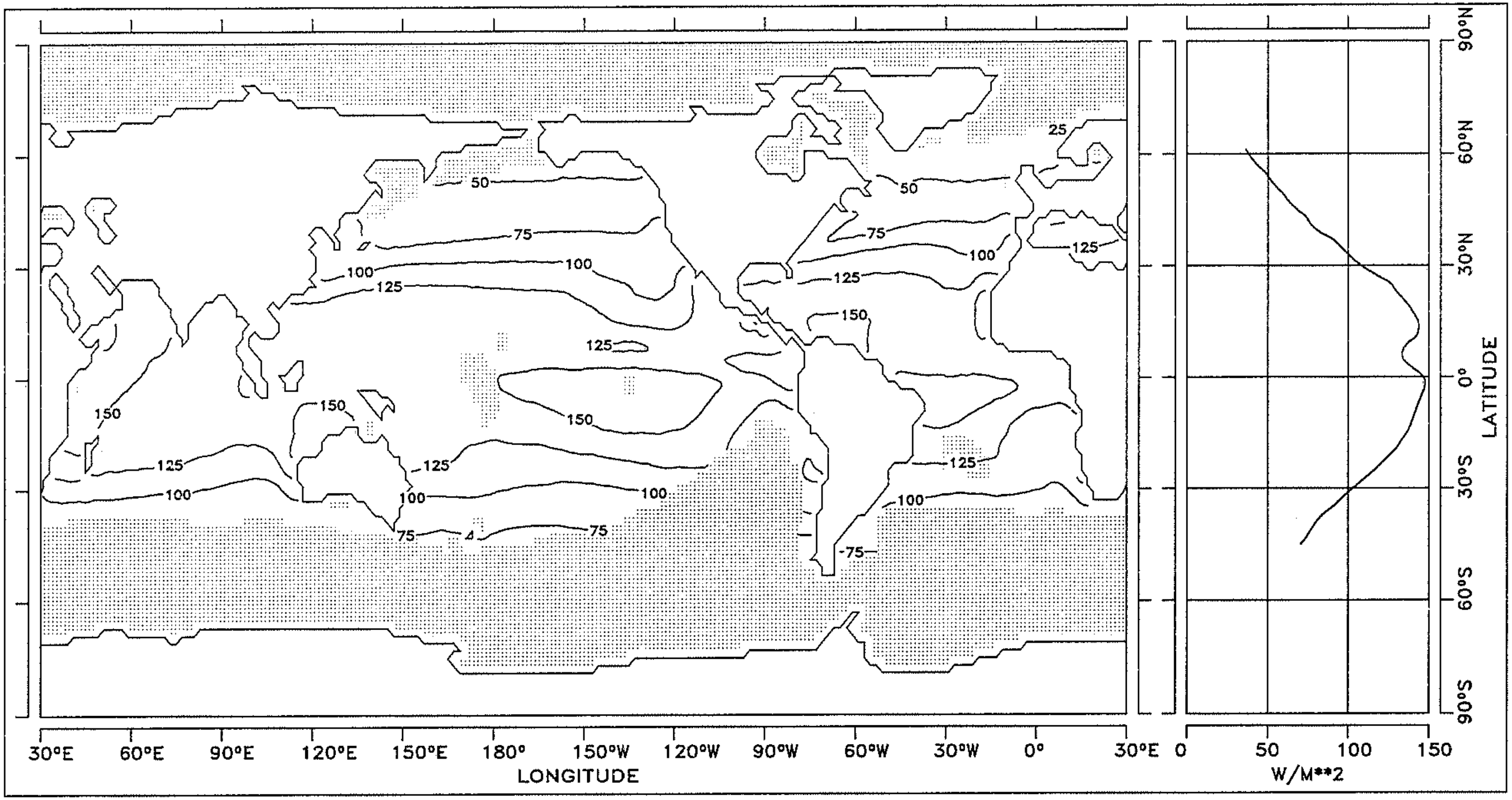

CONTOUR INTERVAL: 25 W/M**2 REFERENCE LINE : 0 W/M**2

LATENT HEAT FLUX

FIG. 4.1 LATENT HEAT FLUX JANUARY

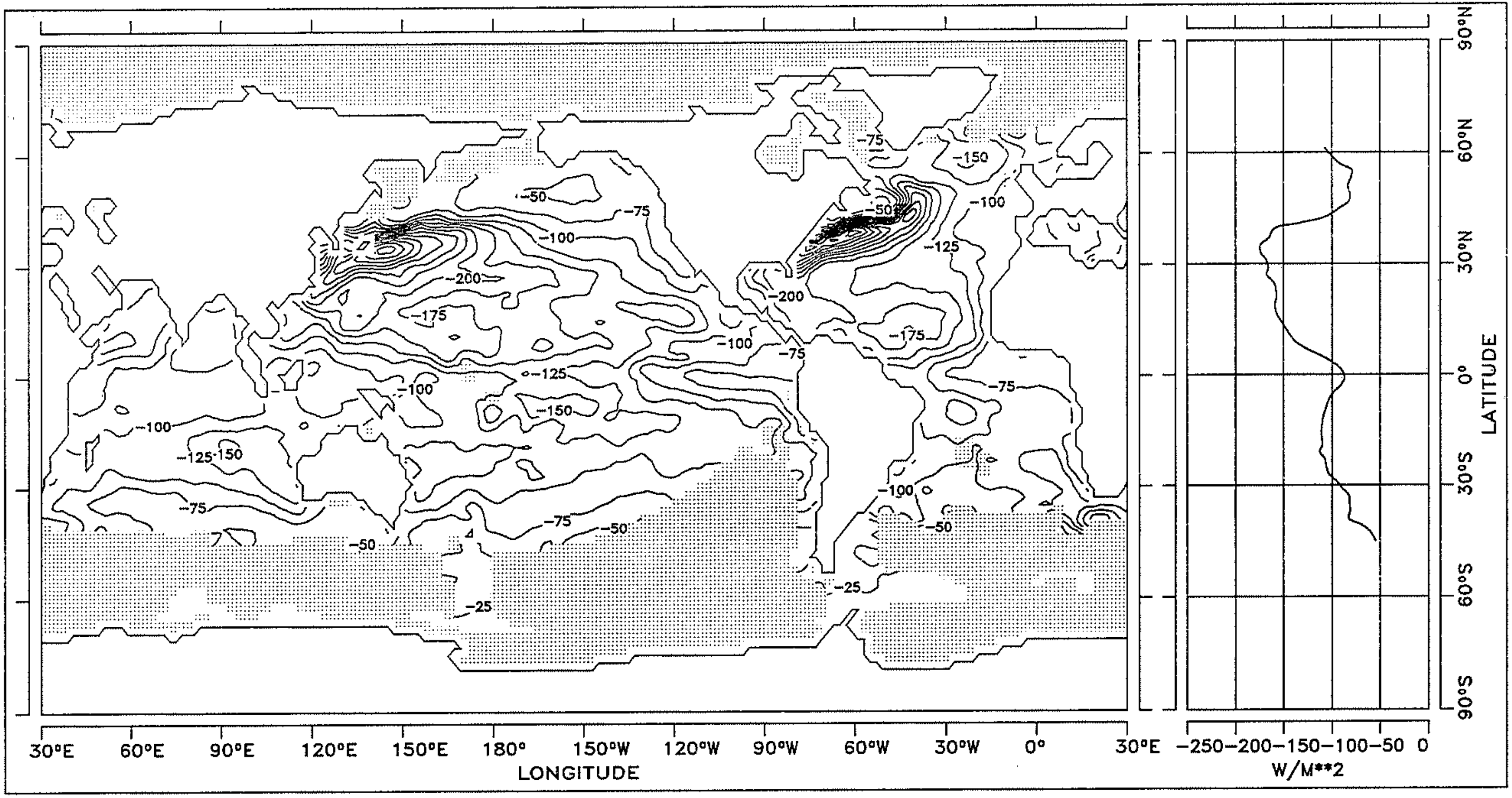

CONTOUR INTERVAL: 25 W/M**2 REFERENCE LINE : 0 W/M**2

FIG. 4.2 LATENT HEAT FLUX FEBRUARY

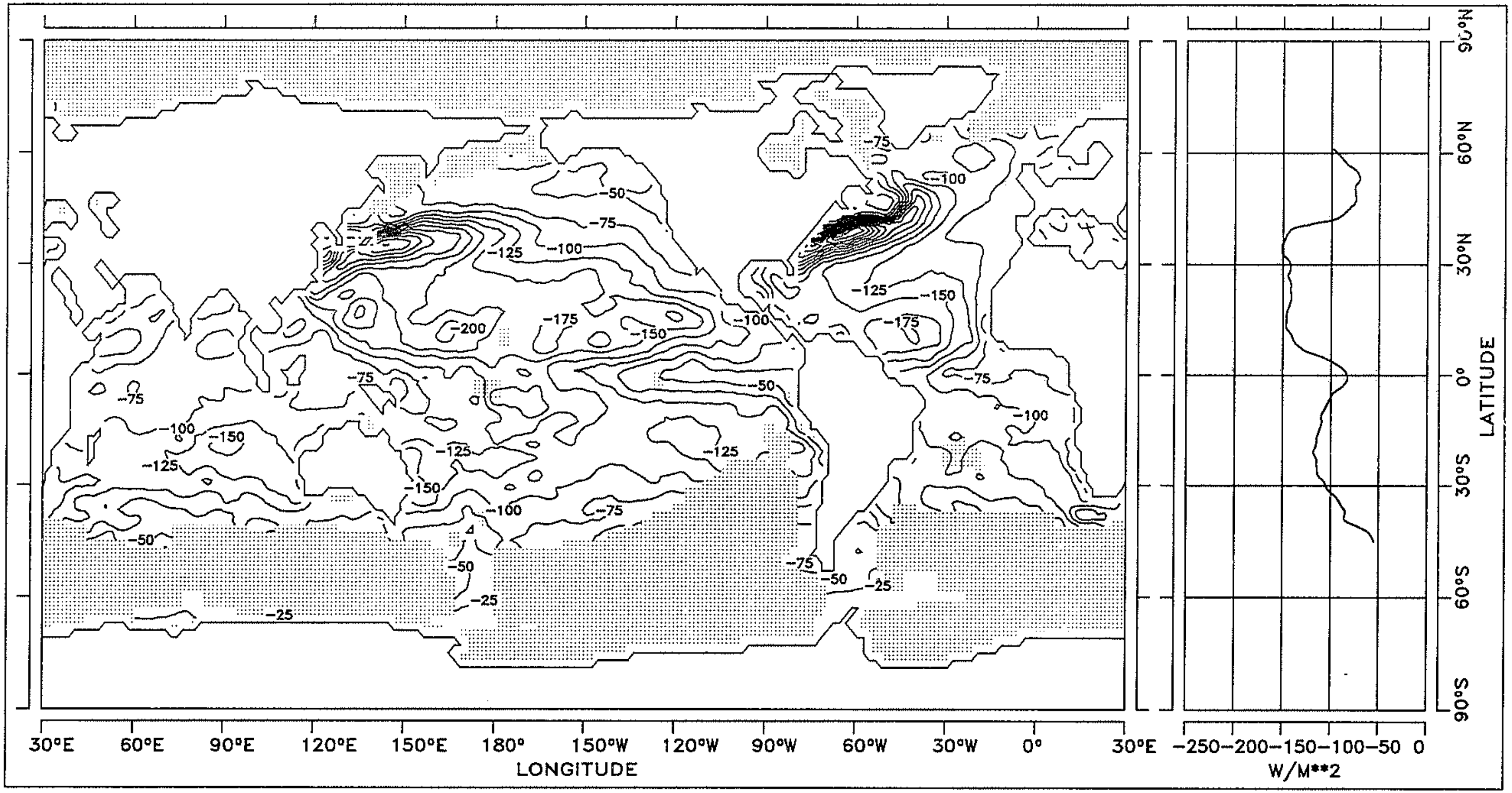

CONTOUR INTERVAL: 25 W/M**2 REFERENCE LINE : 0 W/M**2

FIG. 4.3 LATENT HEAT FLUX MARCH

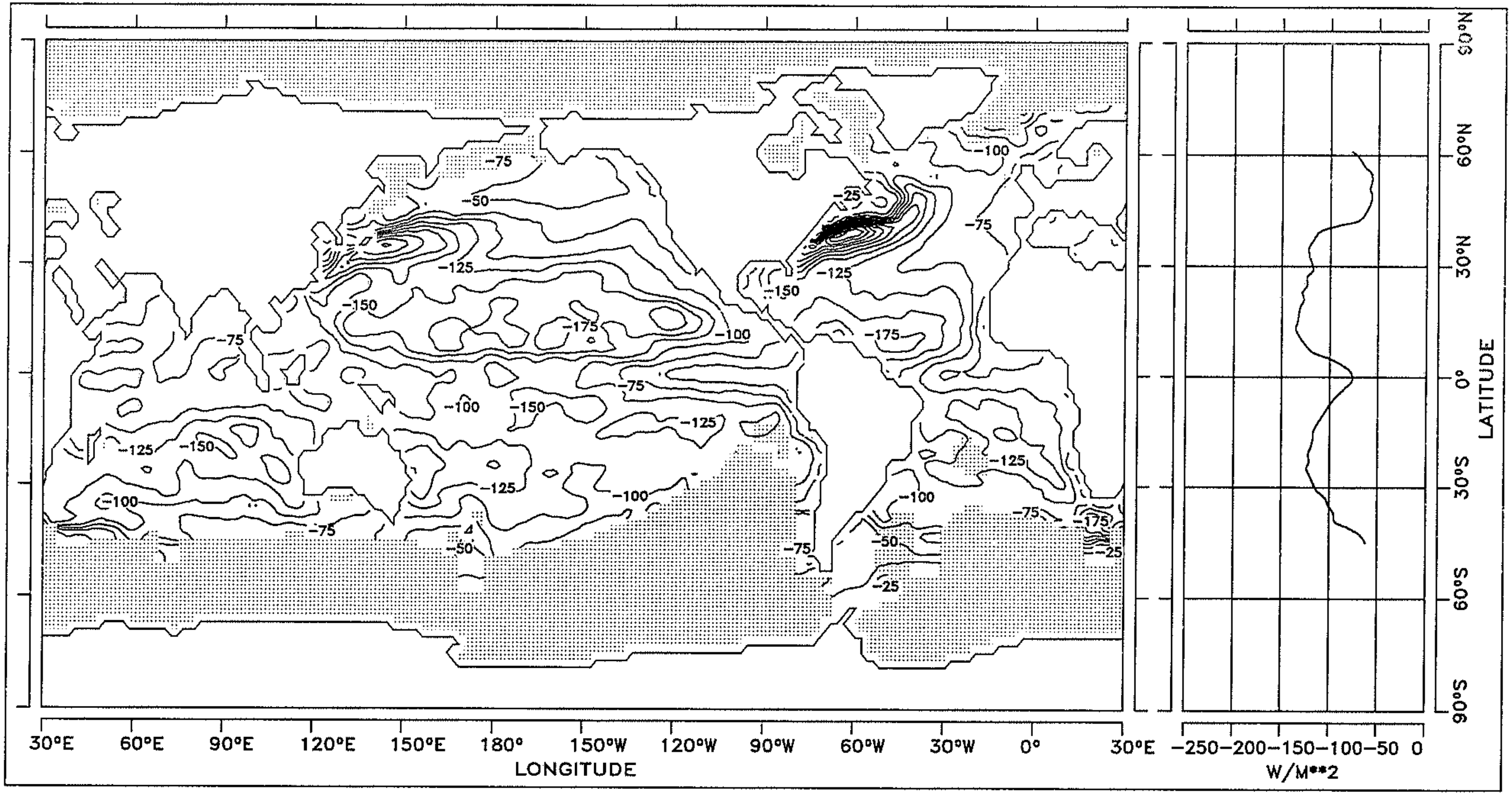

CONTOUR INTERVAL: 25 W/M**2 REFERENCE LINE : 0 W/M**2

FIG. 4.4 LATENT HEAT FLUX APRIL

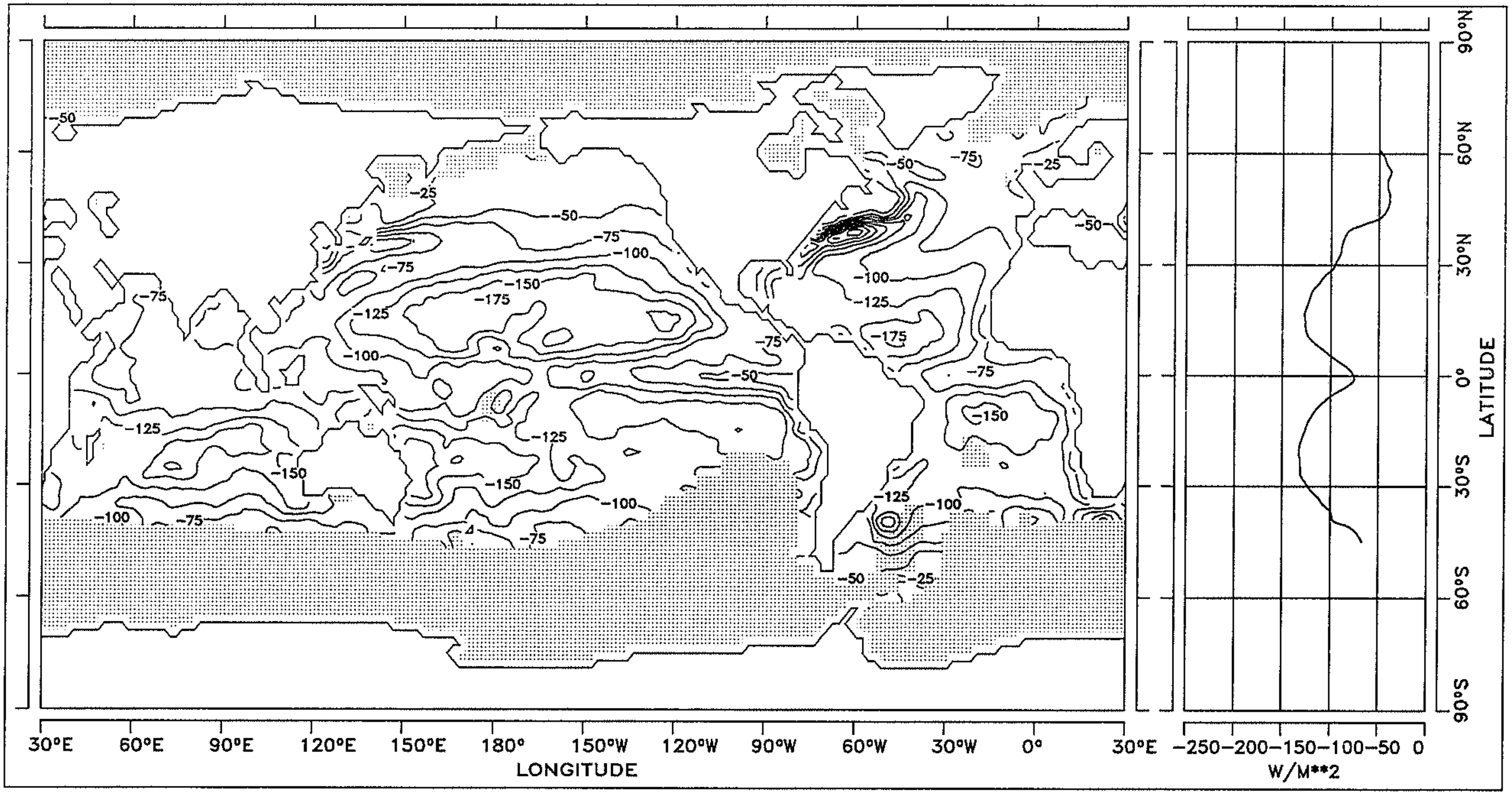

CONTOUR INTERVAL: 25 W/M**2 REFERENCE LINE : 0 W/M**2

FIG. 4.5 LATENT HEAT FLUX MAY

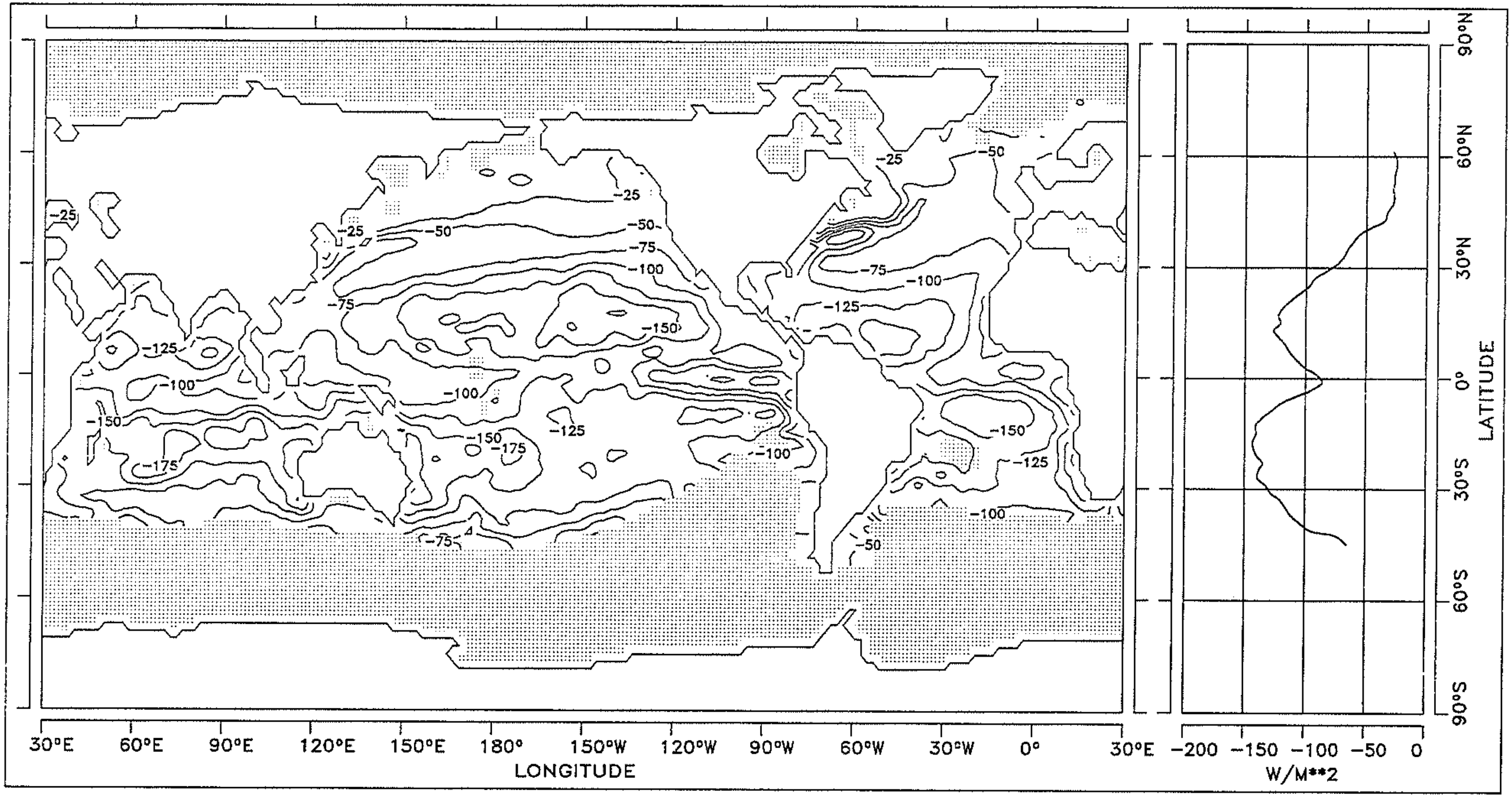

CONTOUR INTERVAL: 25 W/M**2 REFERENCE LINE : 0 W/M**2

FIG. 4.6 LATENT HEAT FLUX JUNE

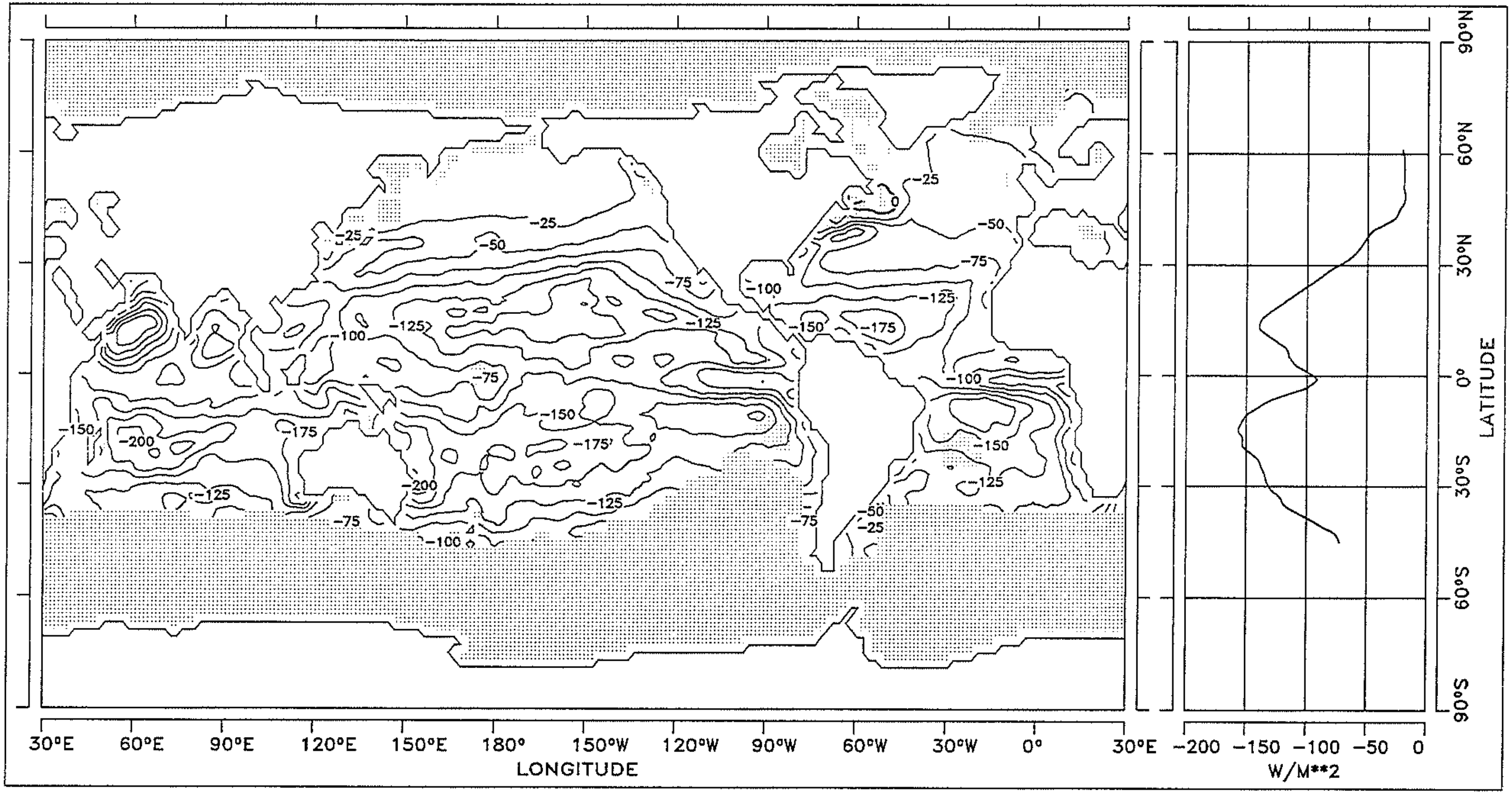

CONTOUR INTERVAL: 25 W/M**2 REFERENCE LINE : 0 W/M**2

FIG. 4.7 LATENT HEAT FLUX JULY

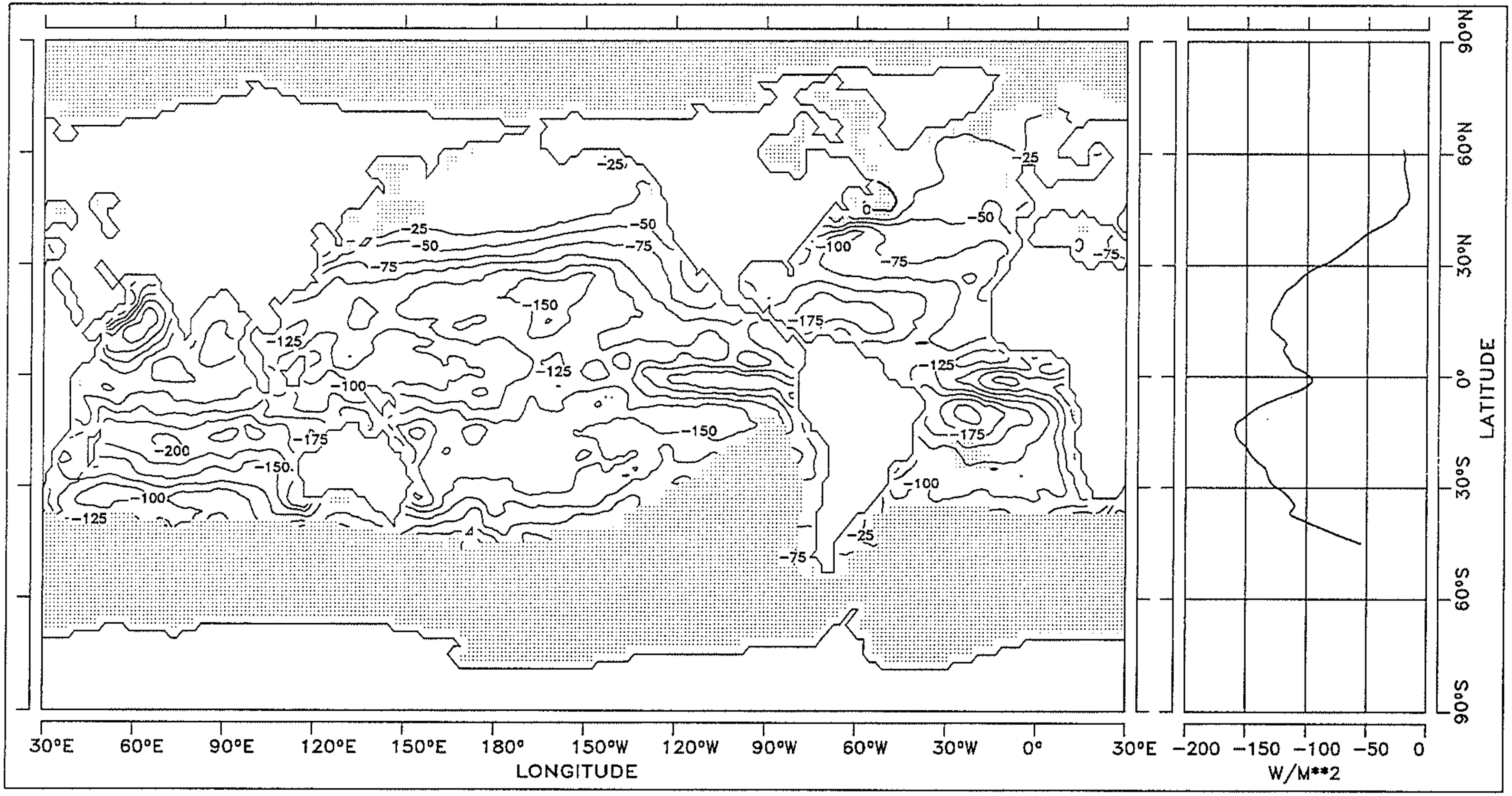

CONTOUR INTERVAL: 25 W/M**2 REFERENCE LINE : 0 W/M**2

FIG. 4.8 LATENT HEAT FLUX AUGUST

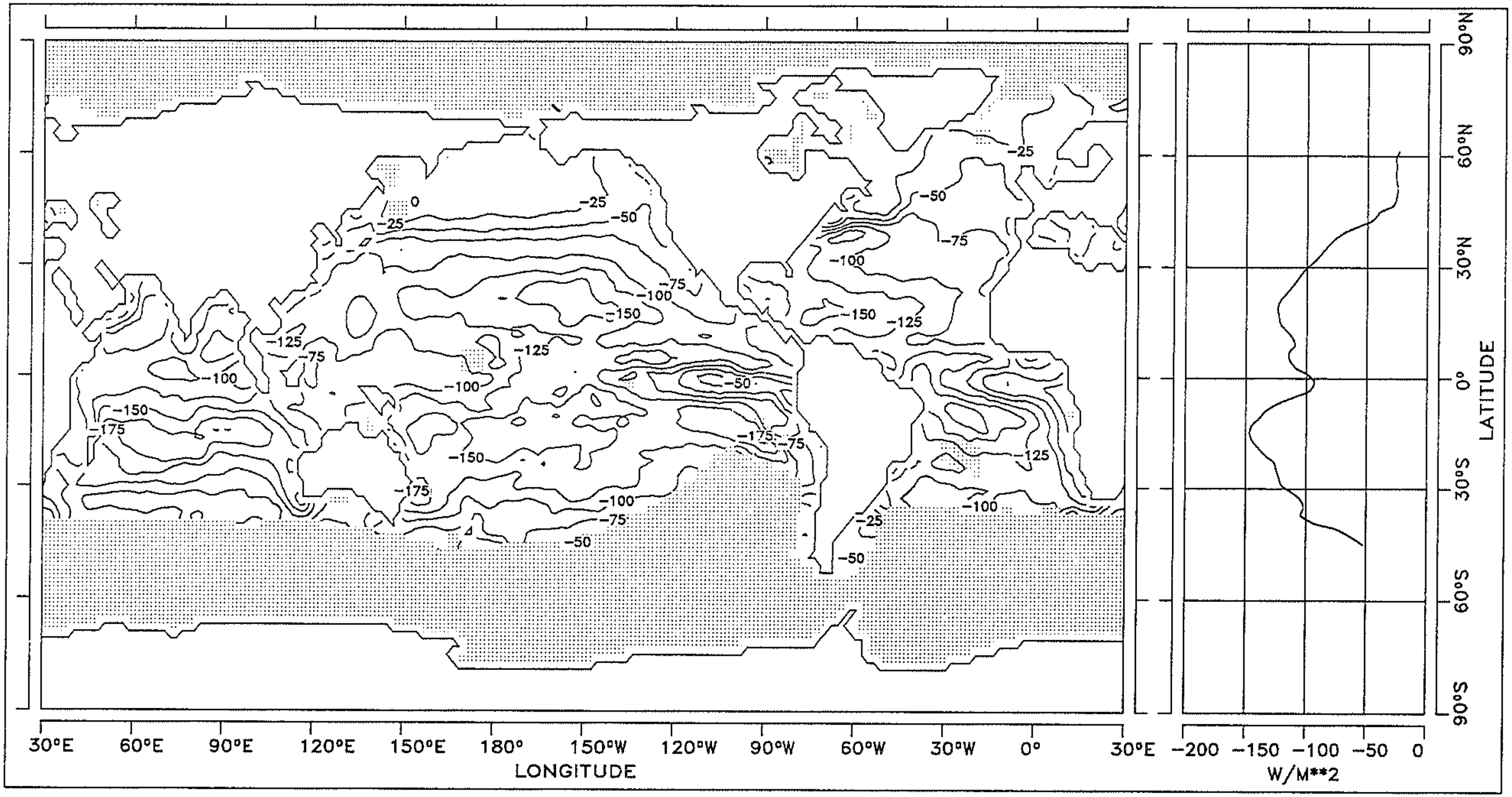

CONTOUR INTERVAL: 25 W/M**2 REFERENCE LINE : 0 W/M**2

FIG. 4.9 LATENT HEAT FLUX SEPTEMBER

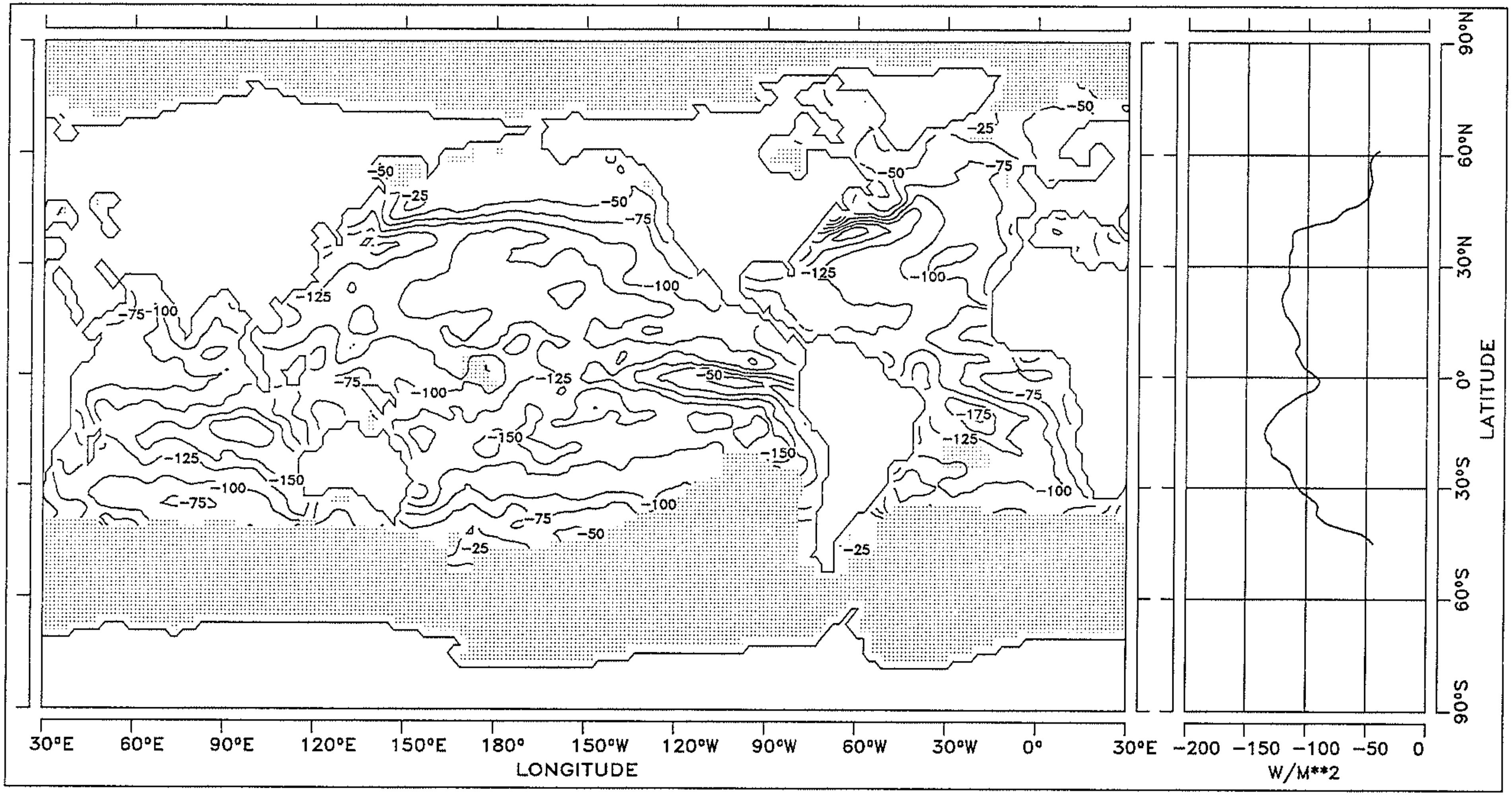

CONTOUR INTERVAL: 25 W/M**2 REFERENCE LINE : 0 W/M**2

FIG. 4.10 LATENT HEAT FLUX OCTOBER

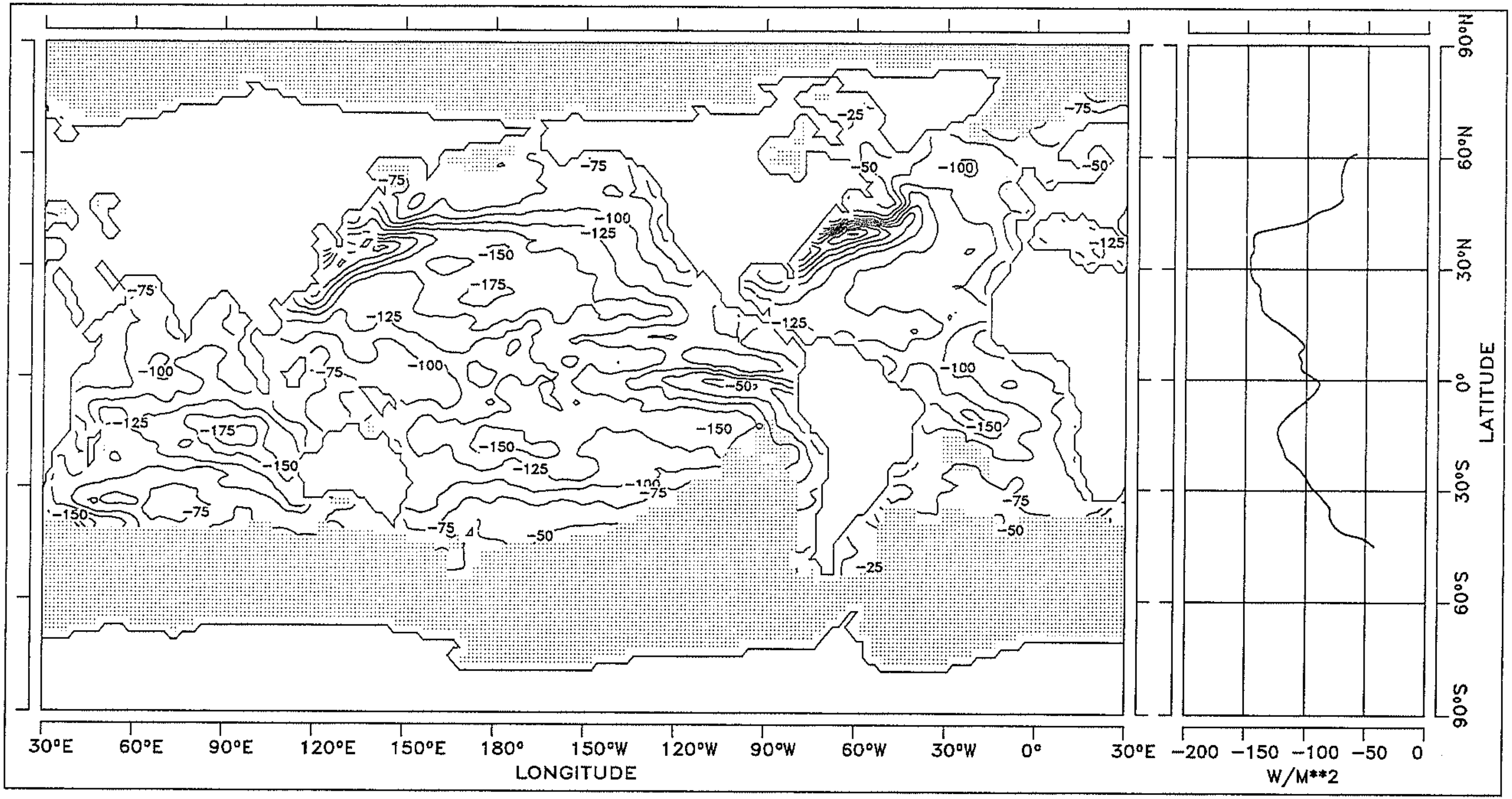

CONTOUR INTERVAL: 25 W/M**2 REFERENCE LINE : 0 W/M**2

FIG. 4.11 LATENT HEAT FLUX NOVEMBER

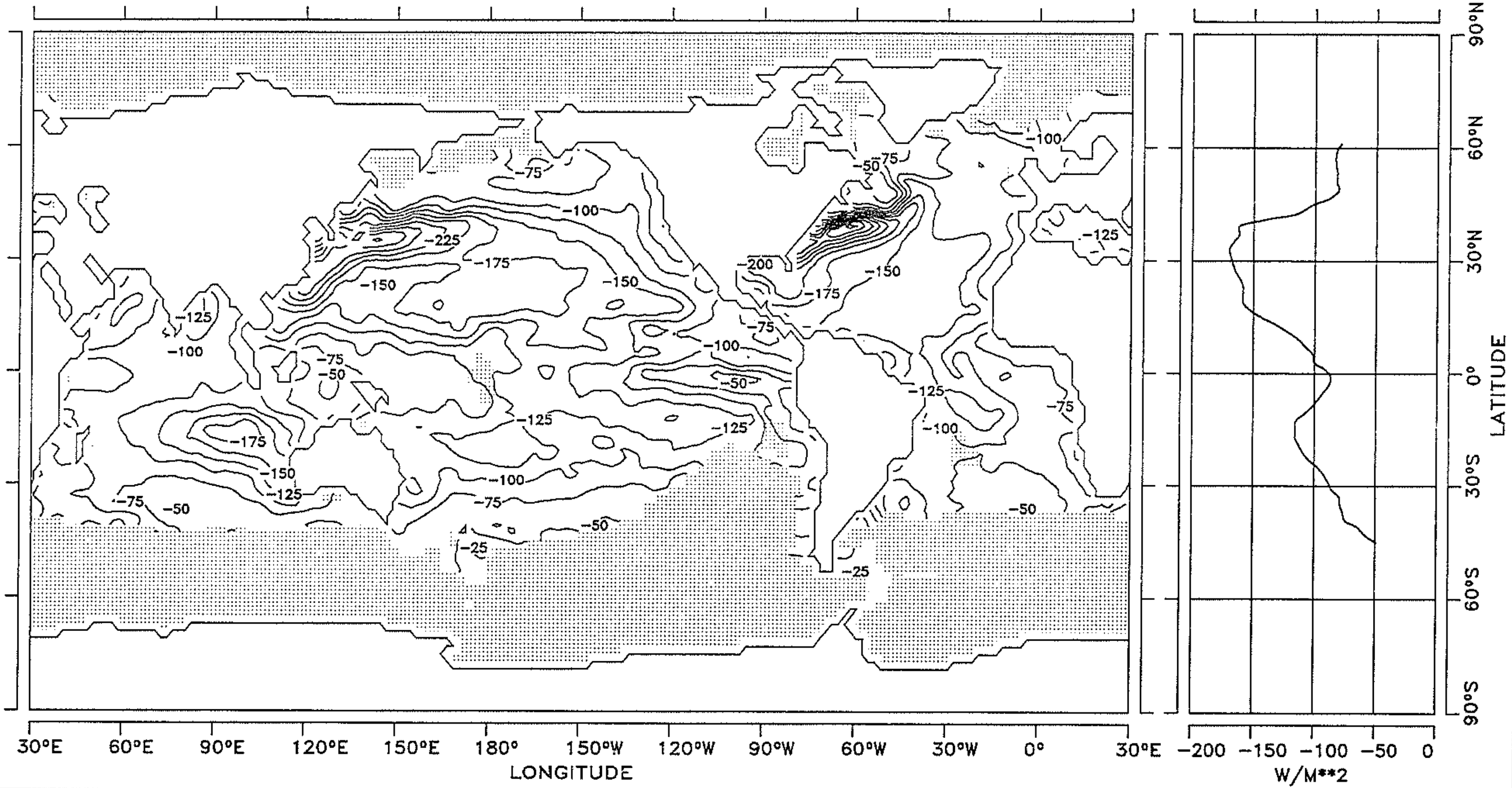

CONTOUR INTERVAL: 25 W/M**2 REFERENCE LINE : 0 W/M**2

FIG. 4.12 LATENT HEAT FLUX DECEMBER

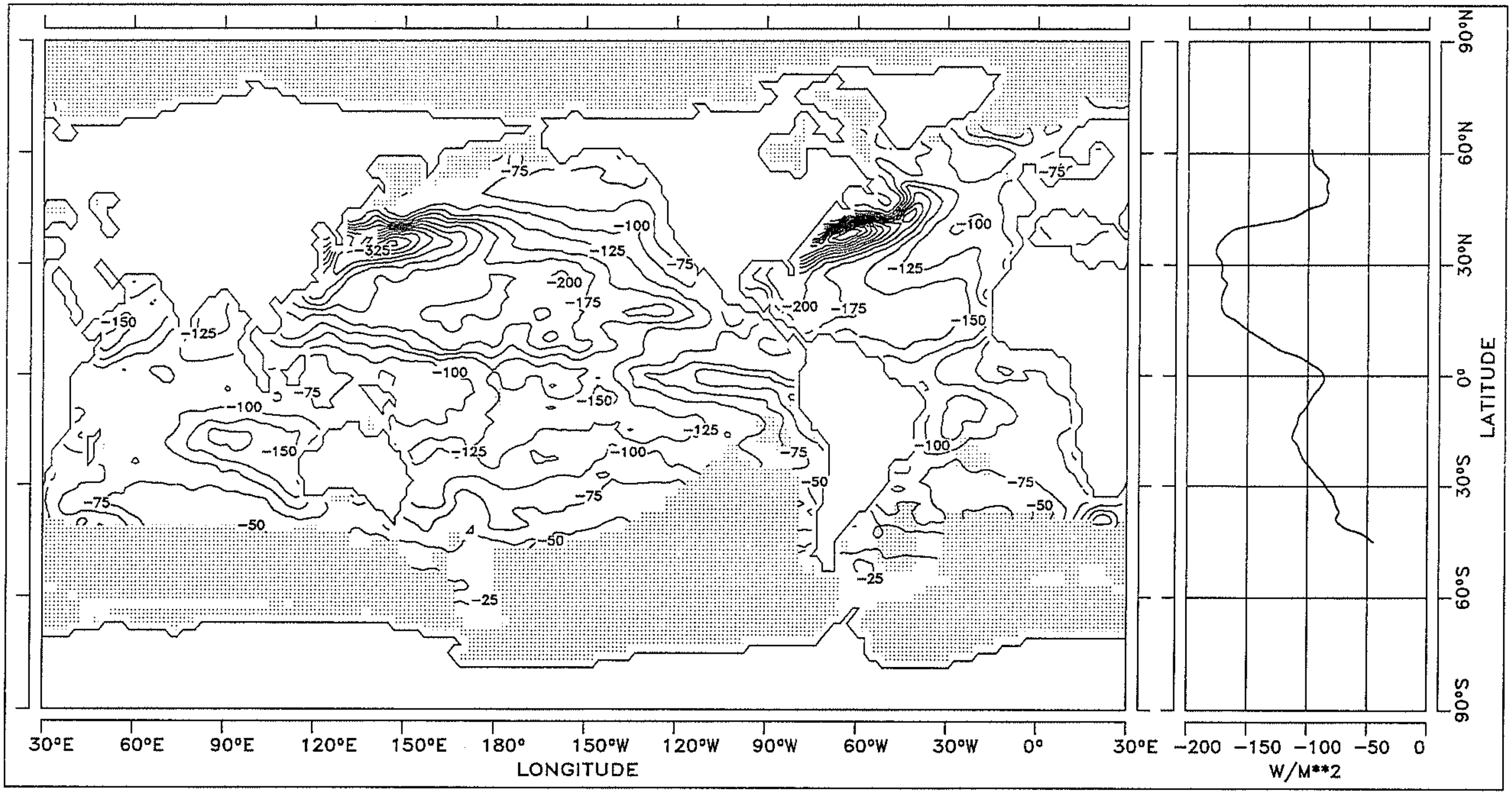

CONTOUR INTERVAL: 25 W/M**2 REFERENCE LINE : 0 W/M**2

FIG. 4.13 LATENT HEAT FLUX

ANNUAL MEAN

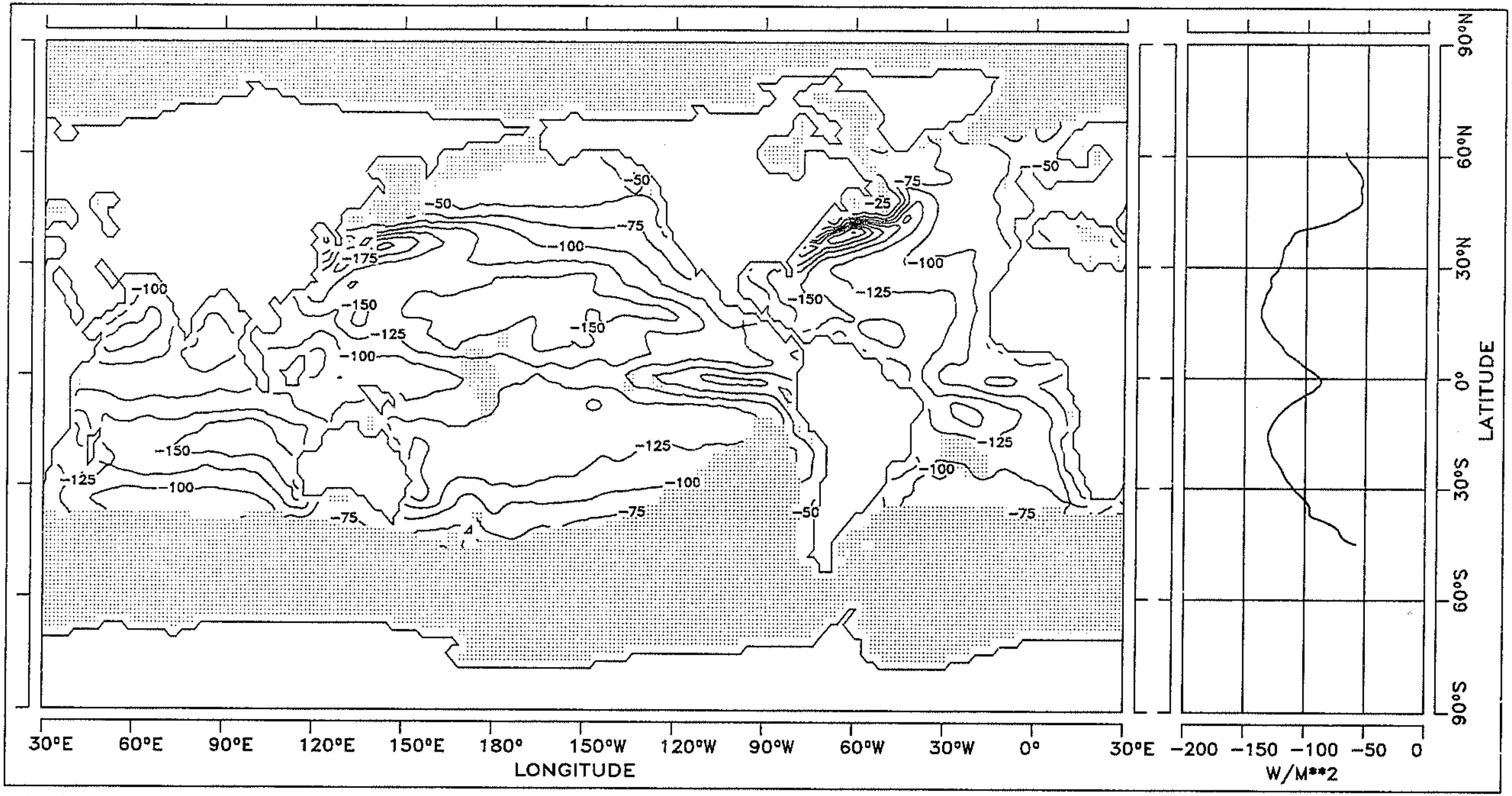

CONTOUR INTERVAL: 25 W/M**2

REFERENCE LINE : 0 W/M**2

SENSIBLE HEAT FLUX

FIG. 5.1 SENSIBLE HEAT FLUX JANUARY

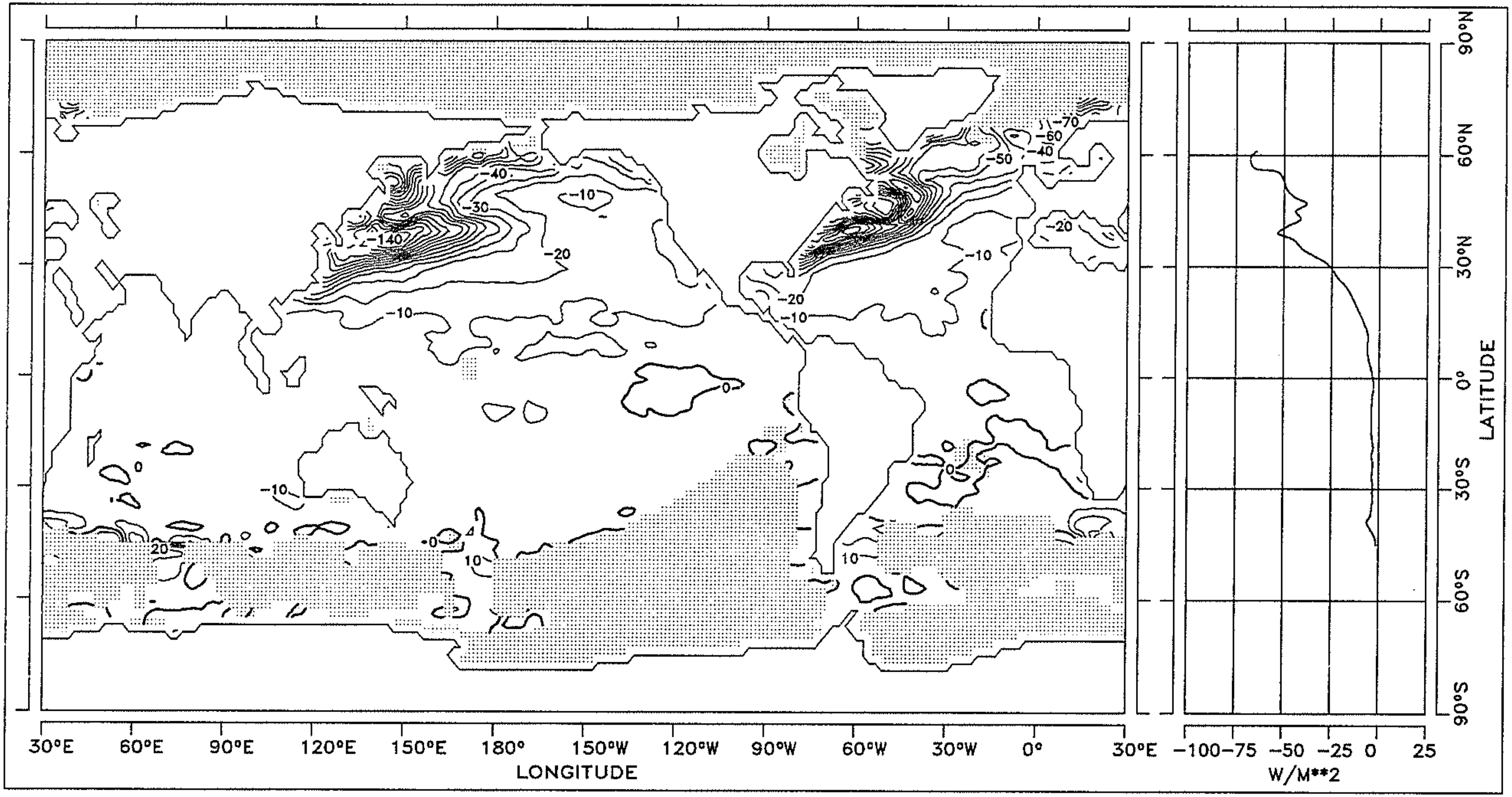

CONTOUR INTERVAL: 10 W/M**2 REFERENCE LINE : 0 W/M**2

FIG. 5.2 SENSIBLE HEAT FLUX FEBRUARY

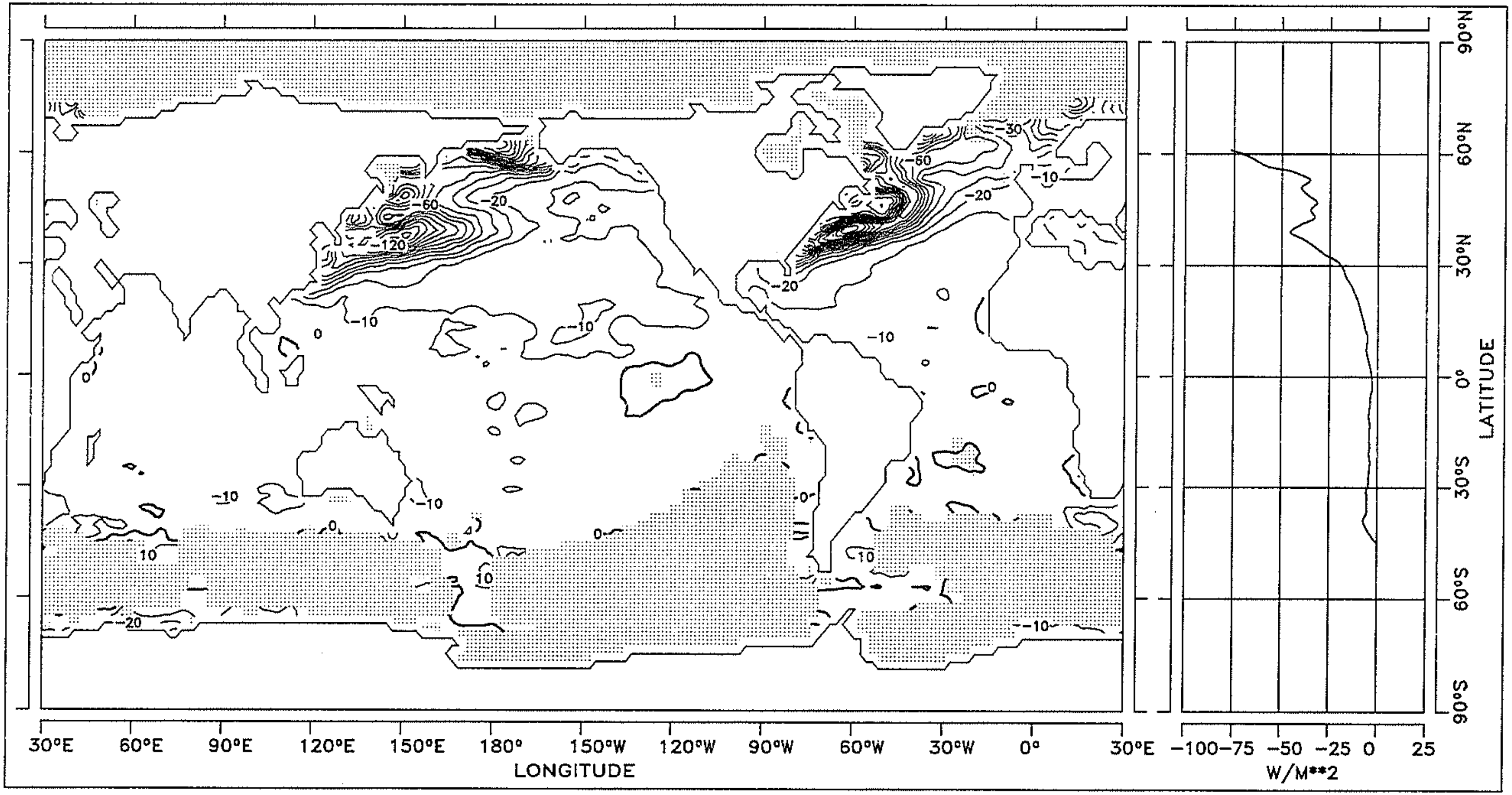

CONTOUR INTERVAL: 10 W/M**2 REFERENCE LINE : 0 W/M**2

FIG. 5.3 SENSIBLE HEAT FLUX MARCH

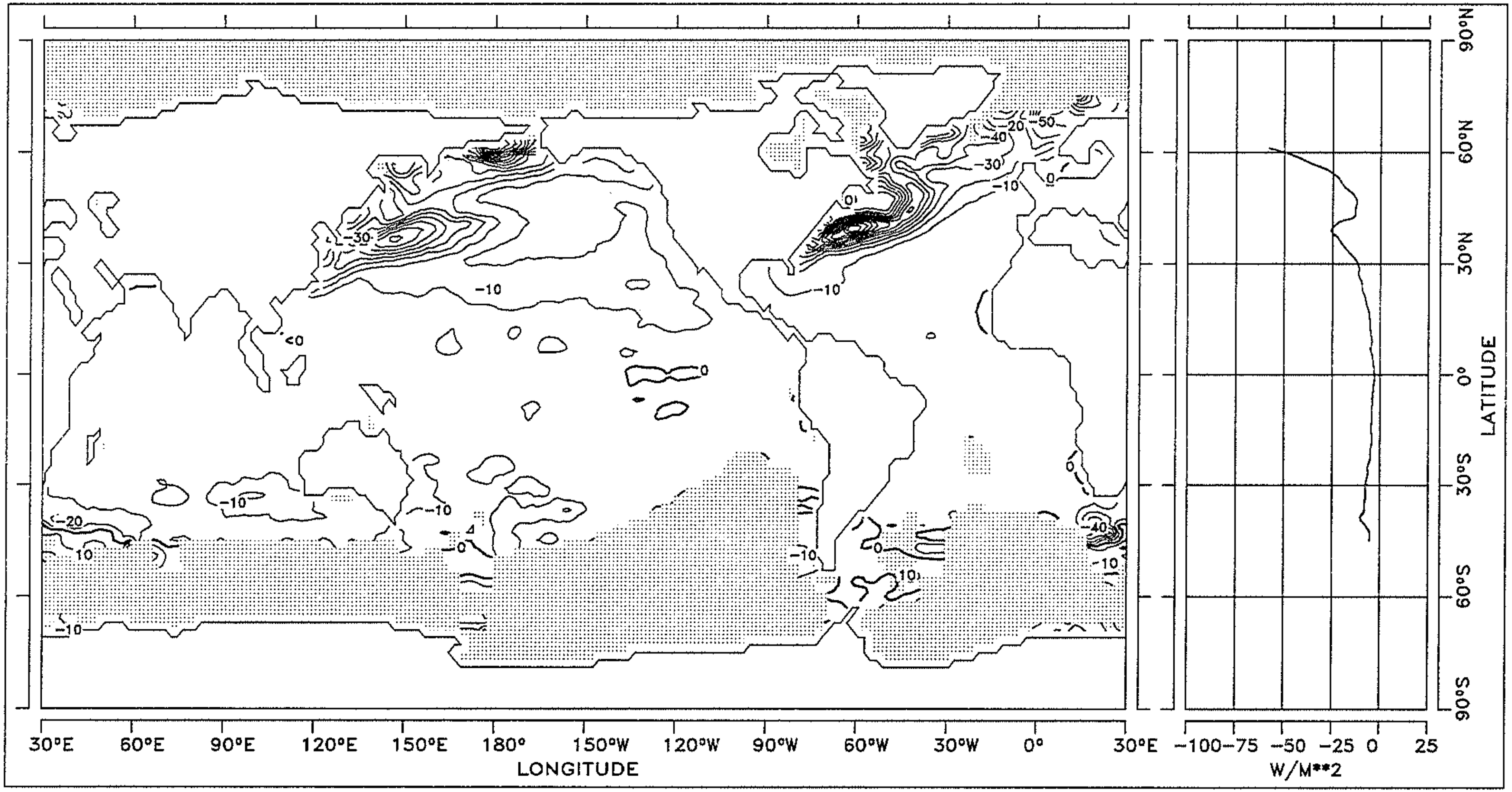

CONTOUR INTERVAL: 10 W/M**2 REFERENCE LINE : 0 W/M**2

FIG. 5.4 SENSIBLE HEAT FLUX APRIL

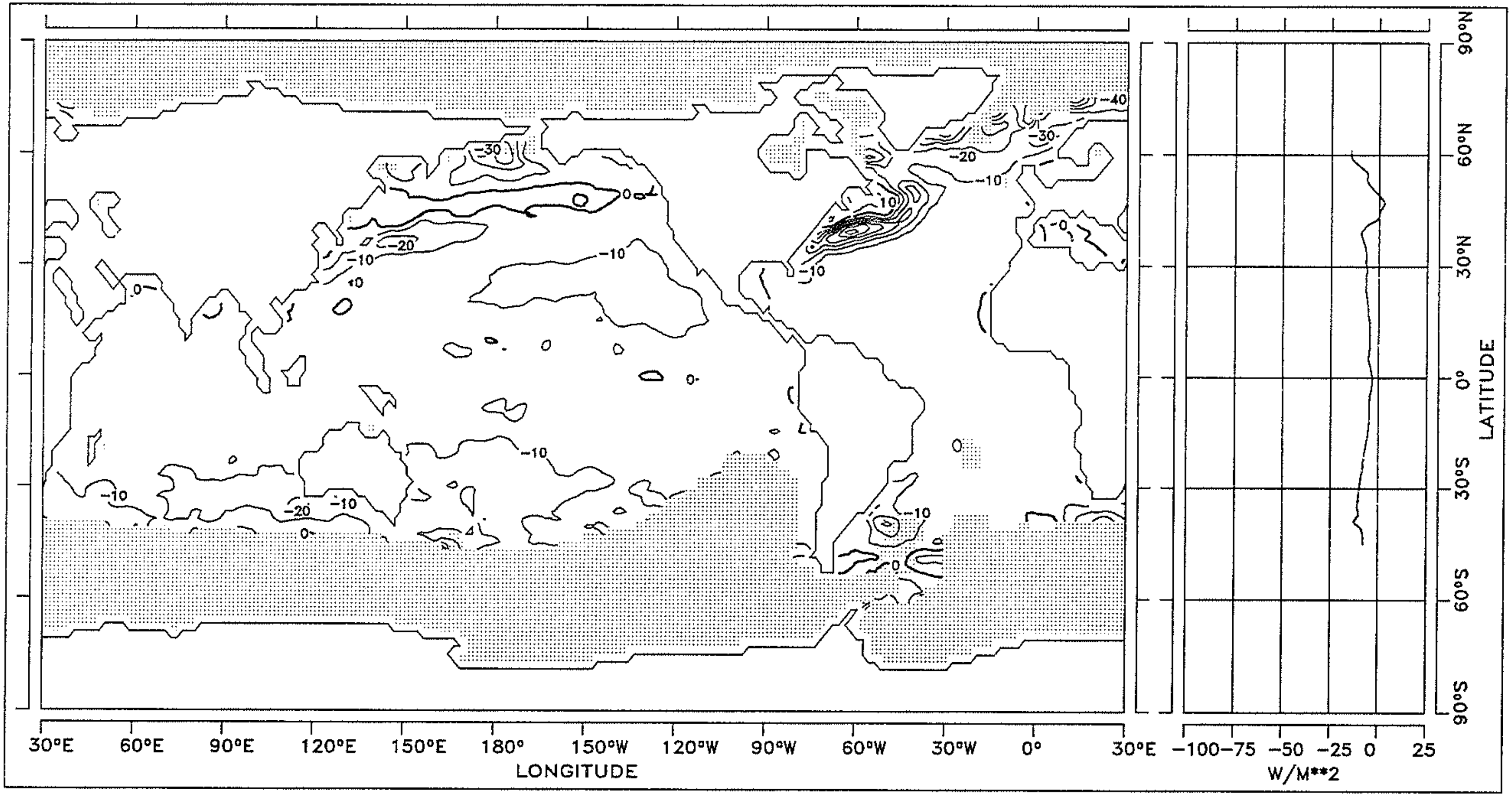

CONTOUR INTERVAL: 10 W/M**2 REFERENCE LINE : 0 W/M**2

FIG. 5.5 SENSIBLE HEAT FLUX MAY

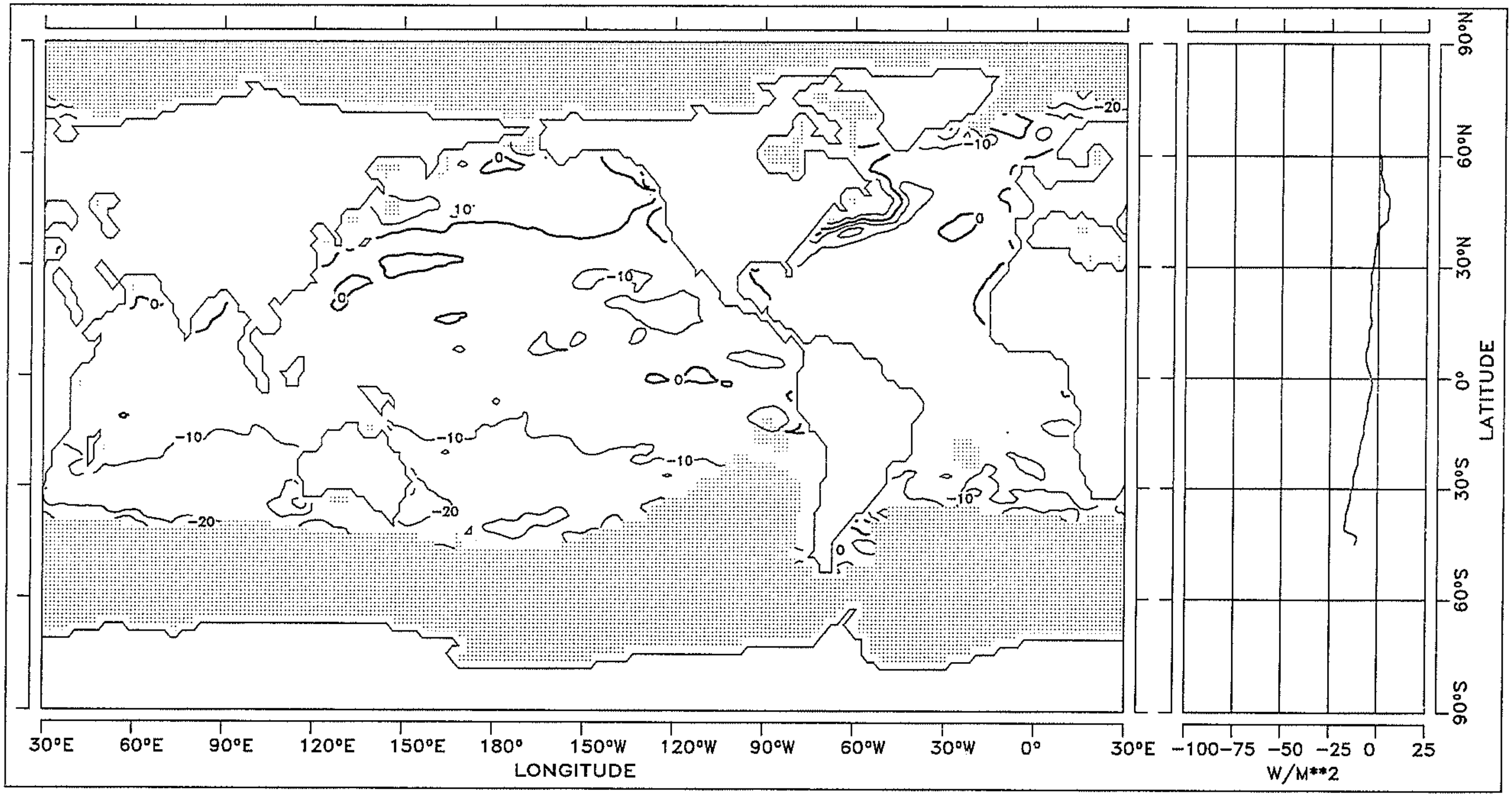

CONTOUR INTERVAL: 10 W/M**2 REFERENCE LINE : 0 W/M**2

FIG. 5.6 SENSIBLE HEAT FLUX JUNE

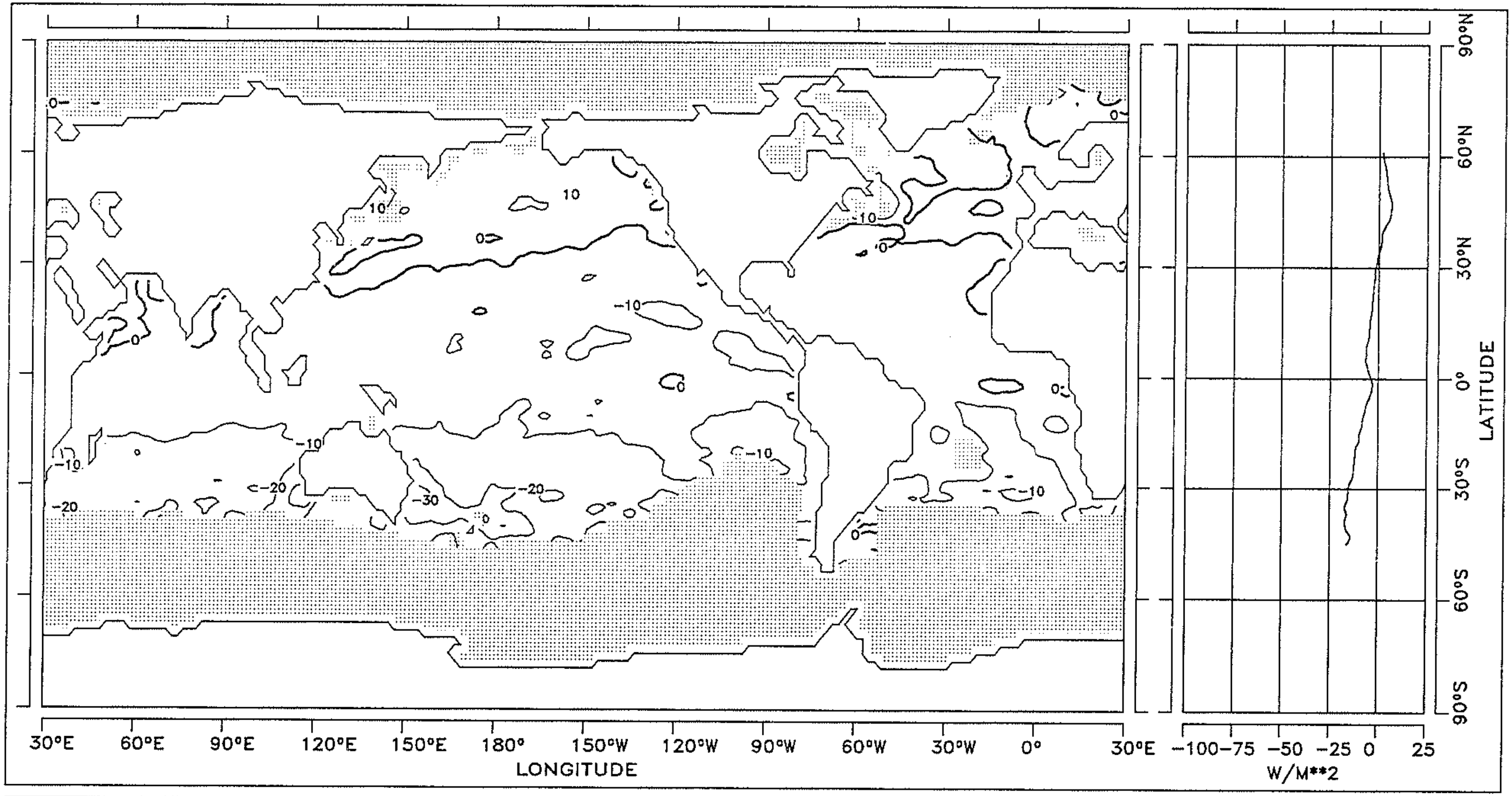

CONTOUR INTERVAL: 10 W/M**2 REFERENCE LINE : 0 W/M**2

FIG. 5.7 SENSIBLE HEAT FLUX JULY

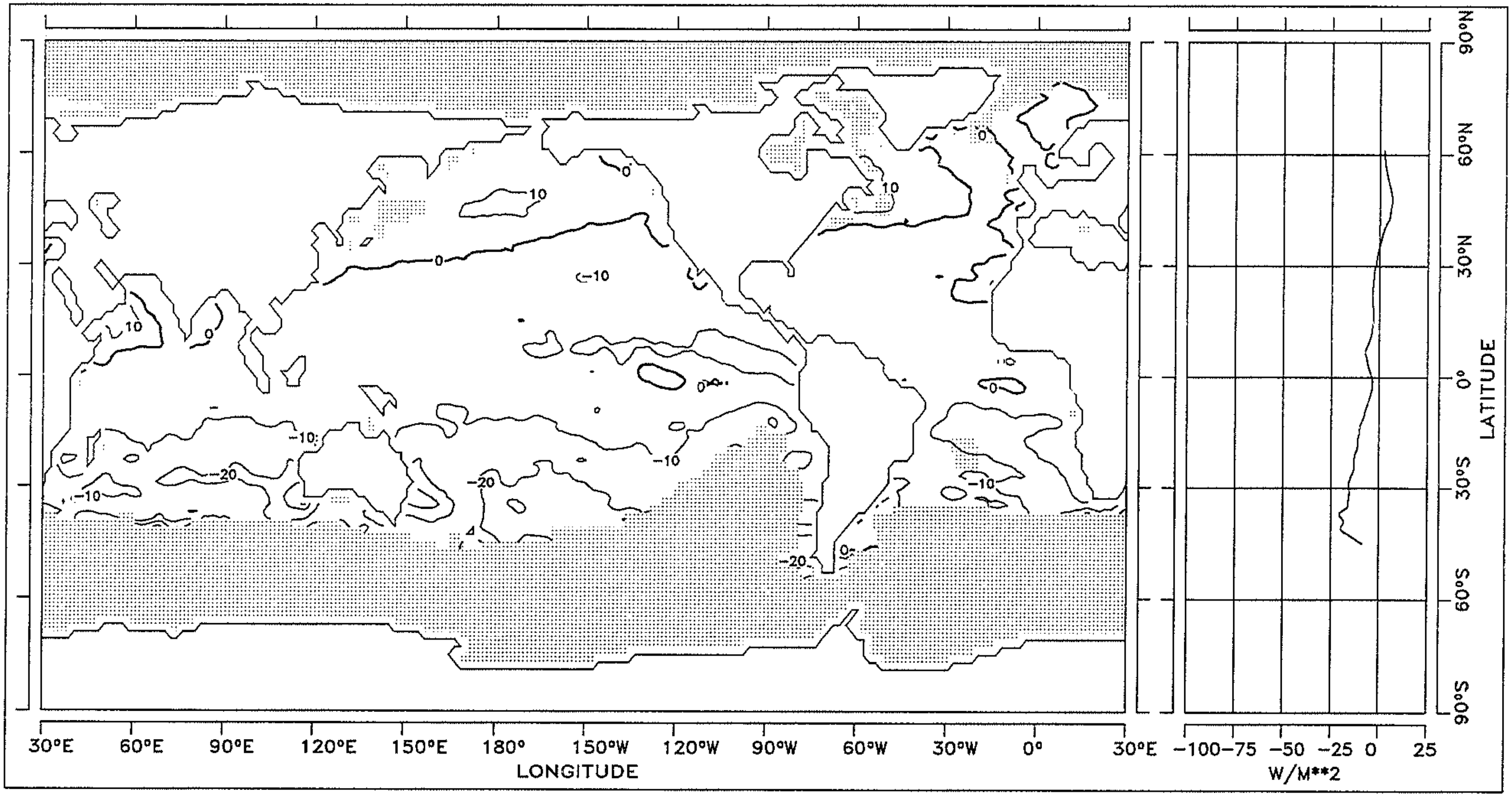

CONTOUR INTERVAL: 10 W/M**2 REFERENCE LINE : 0 W/M**2

FIG. 5.8 SENSIBLE HEAT FLUX AUGUST

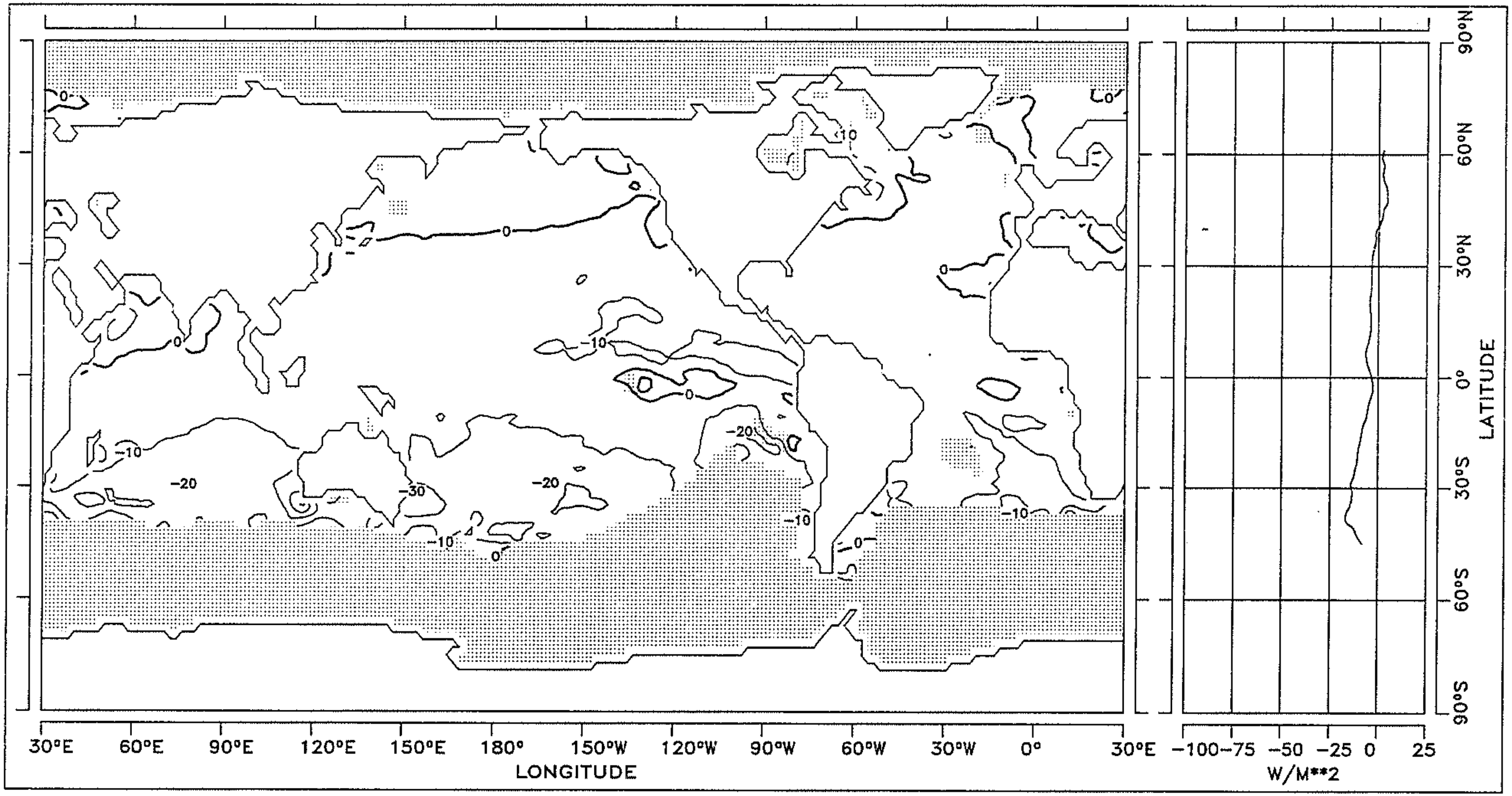

CONTOUR INTERVAL: 10 W/M**2 REFERENCE LINE : 0 W/M**2

FIG. 5.9 SENSIBLE HEAT FLUX SEPTEMBER

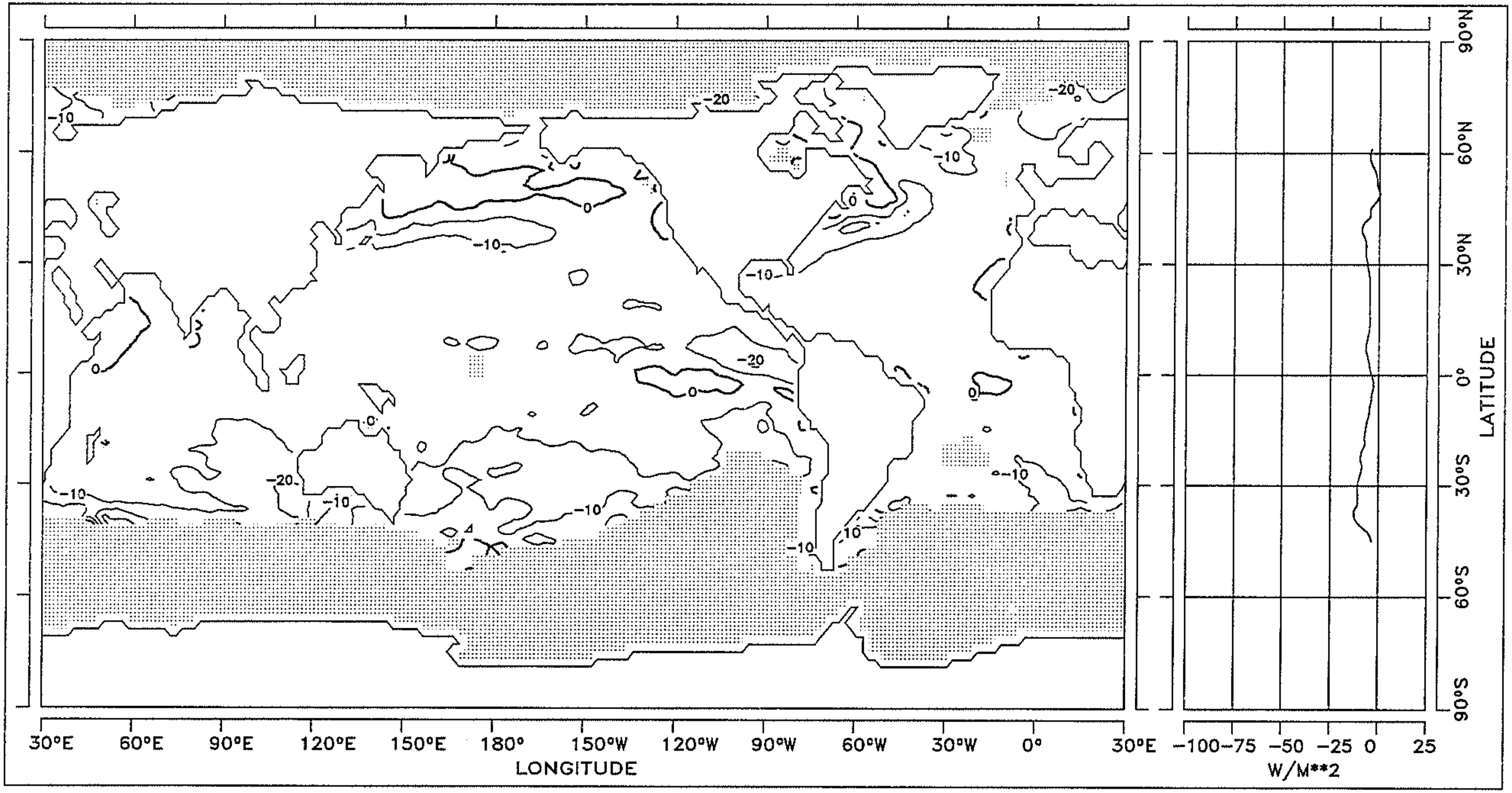

CONTOUR INTERVAL: 10 W/M**2 REFERENCE LINE : 0 W/M**2

FIG. 5.10 SENSIBLE HEAT FLUX OCTOBER

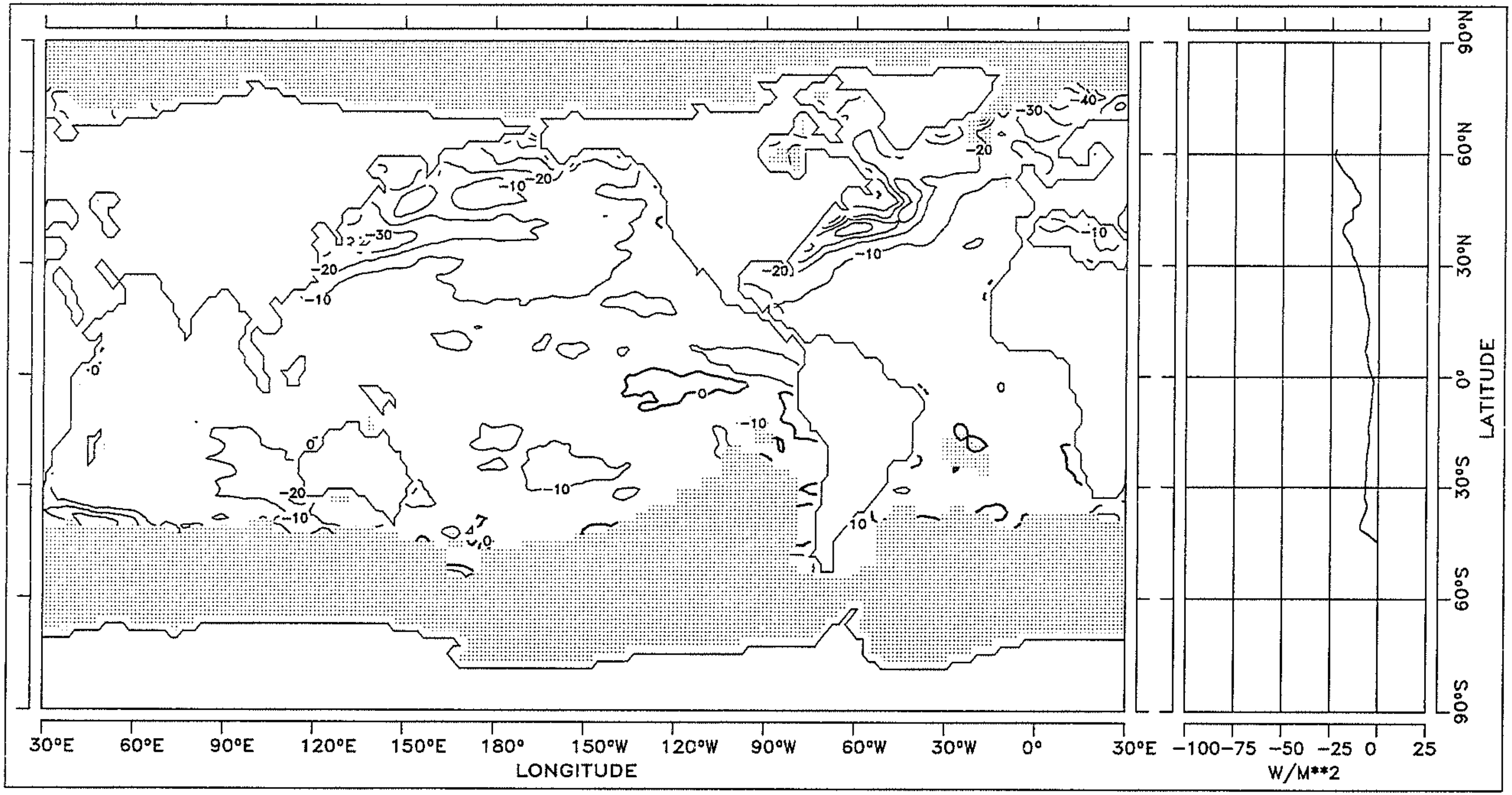

CONTOUR INTERVAL: 10 W/M**2 REFERENCE LINE : 0 W/M**2

FIG. 5.11 SENSIBLE HEAT FLUX NOVEMBER

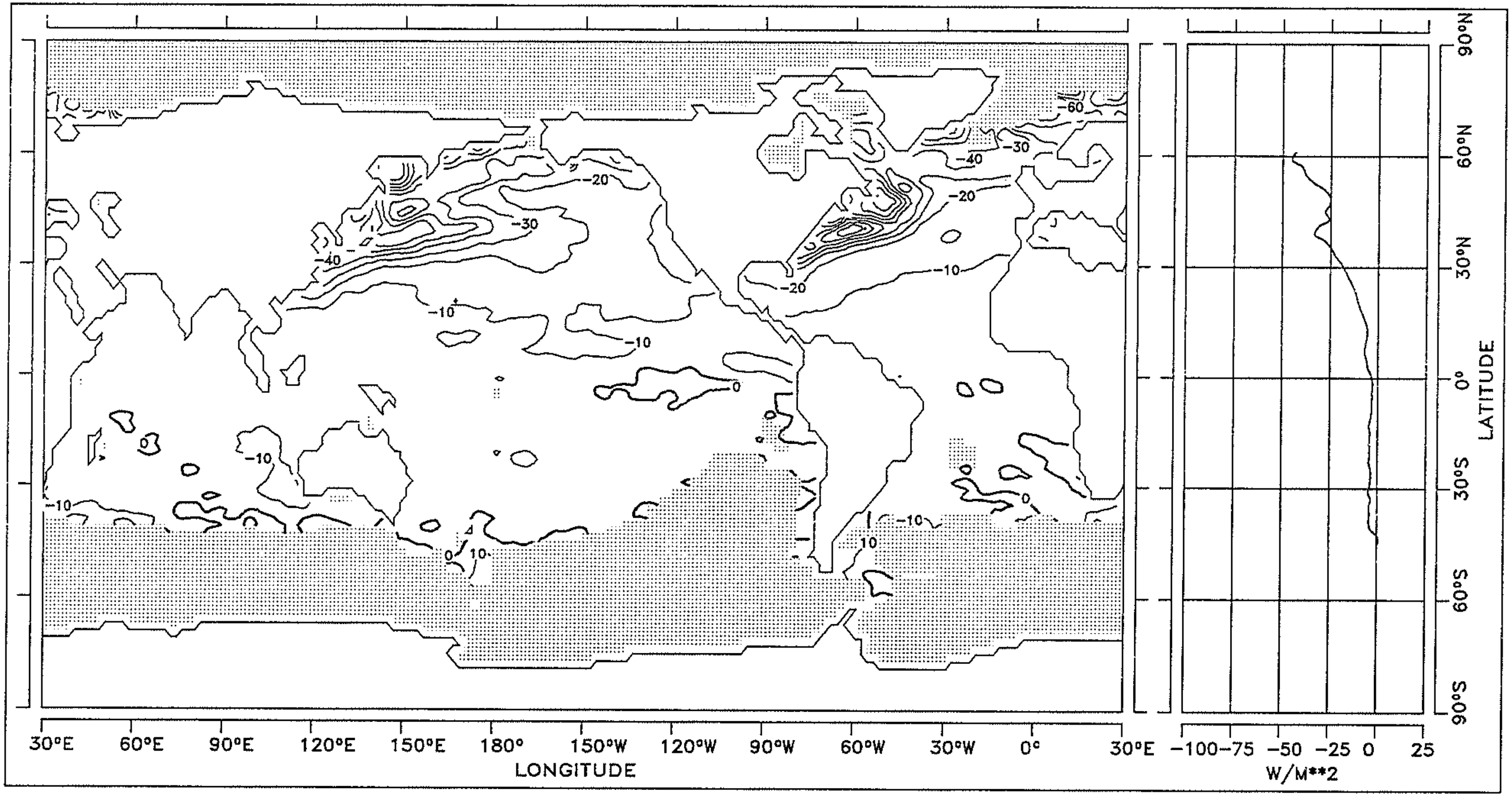

CONTOUR INTERVAL: 10 W/M**2 REFERENCE LINE : 0 W/M**2

FIG. 5.12 SENSIBLE HEAT FLUX DECEMBER

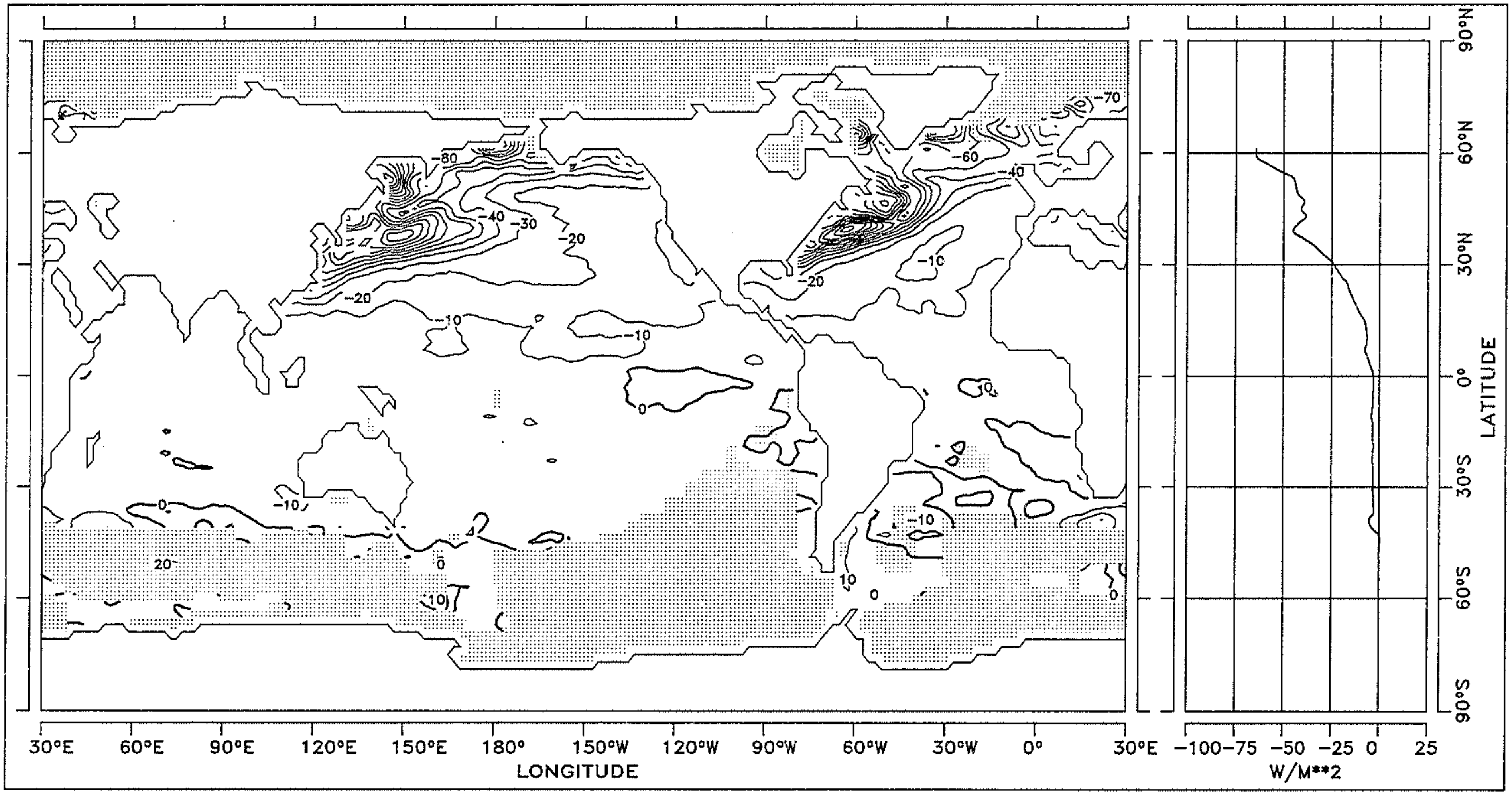

CONTOUR INTERVAL: 10 W/M**2 REFERENCE LINE : 0 W/M**2

FIG. 5.13 SENSIBLE HEAT FLUX ANNUAL MEAN

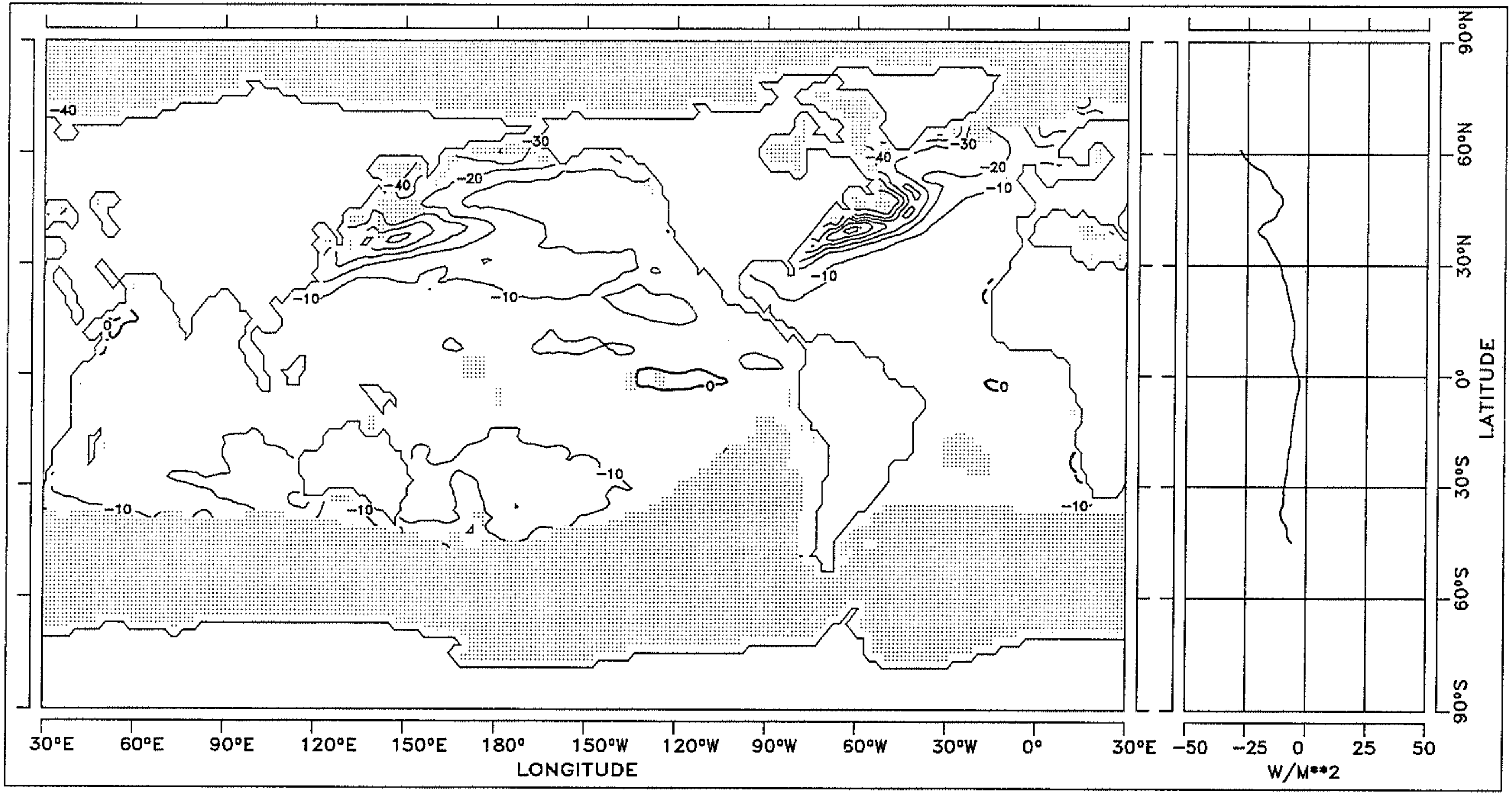

CONTOUR INTERVAL: 10 W/M**2 REFERENCE LINE : 0 W/M**2

NET DOWNWARD HEAT FLUX

FIG. 6.1 NET DOWNWARD HEAT FLUX JANUARY

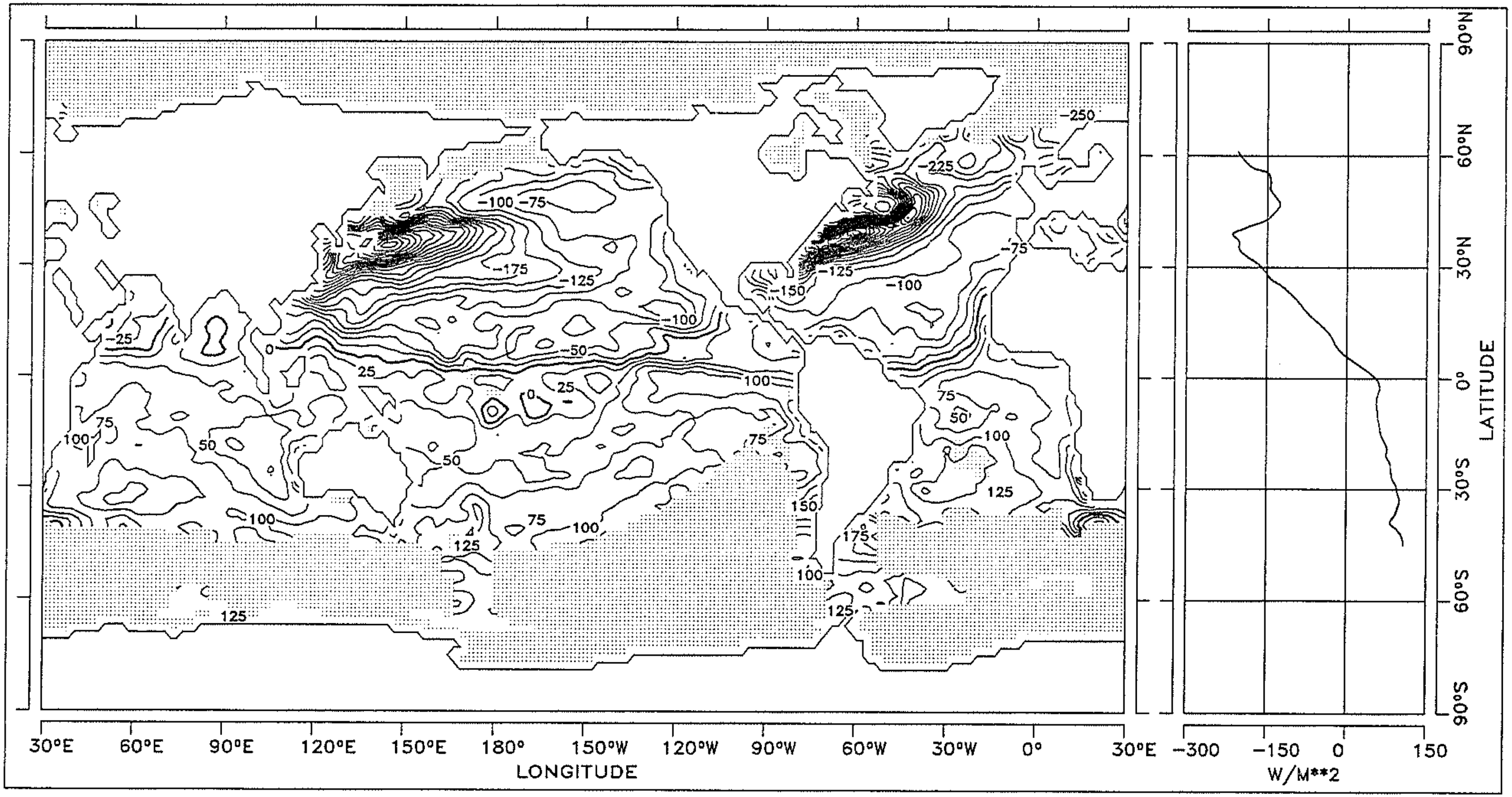

CONTOUR INTERVAL: 25 W/M**2 REFERENCE LINE : 0 W/M**2

FIG. 6.2 NET DOWNWARD HEAT FLUX FEBRUARY

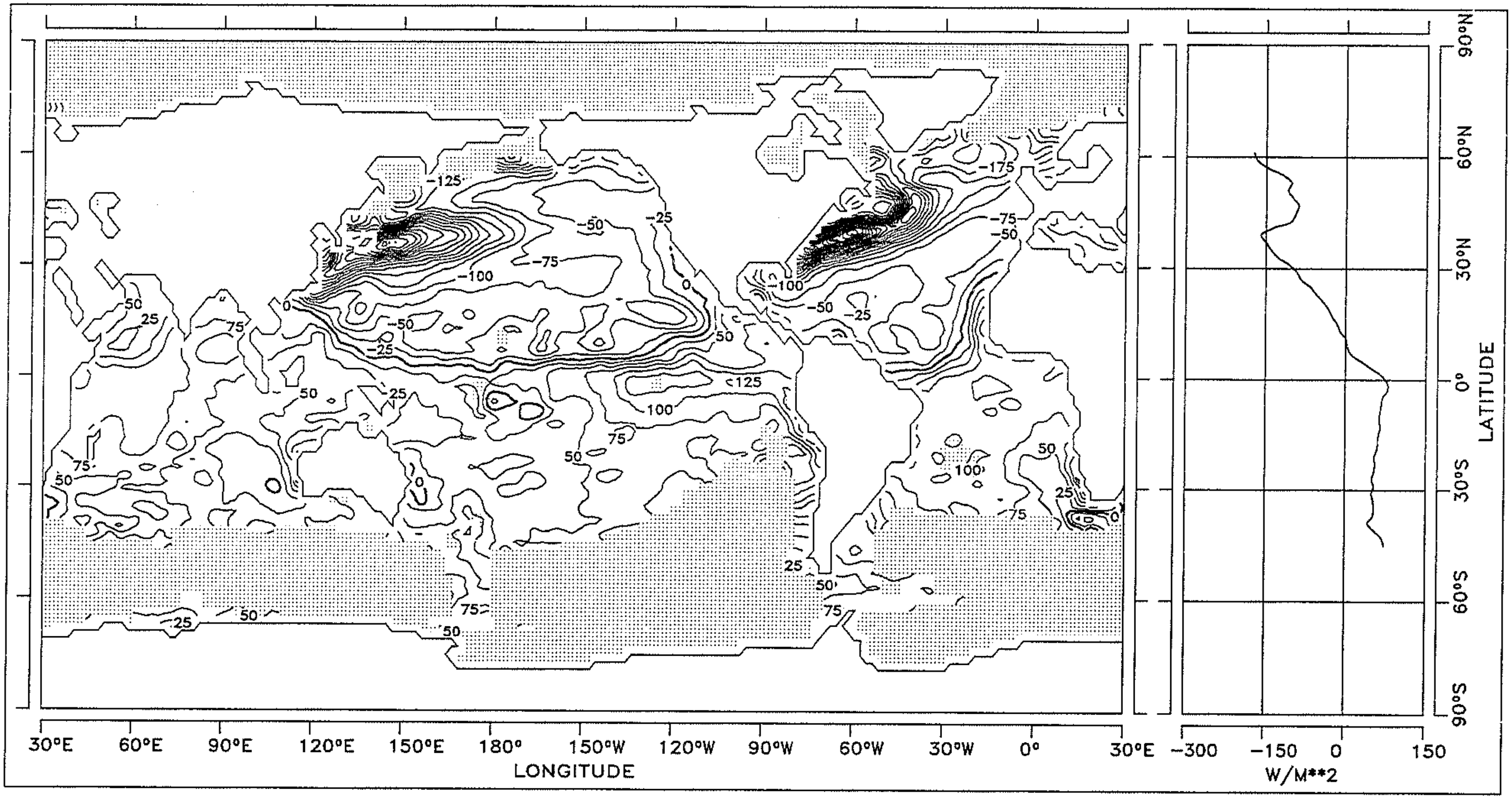

CONTOUR INTERVAL: 25 W/M**2 REFERENCE LINE : 0 W/M**2

FIG. 6.3 NET DOWNWARD HEAT FLUX

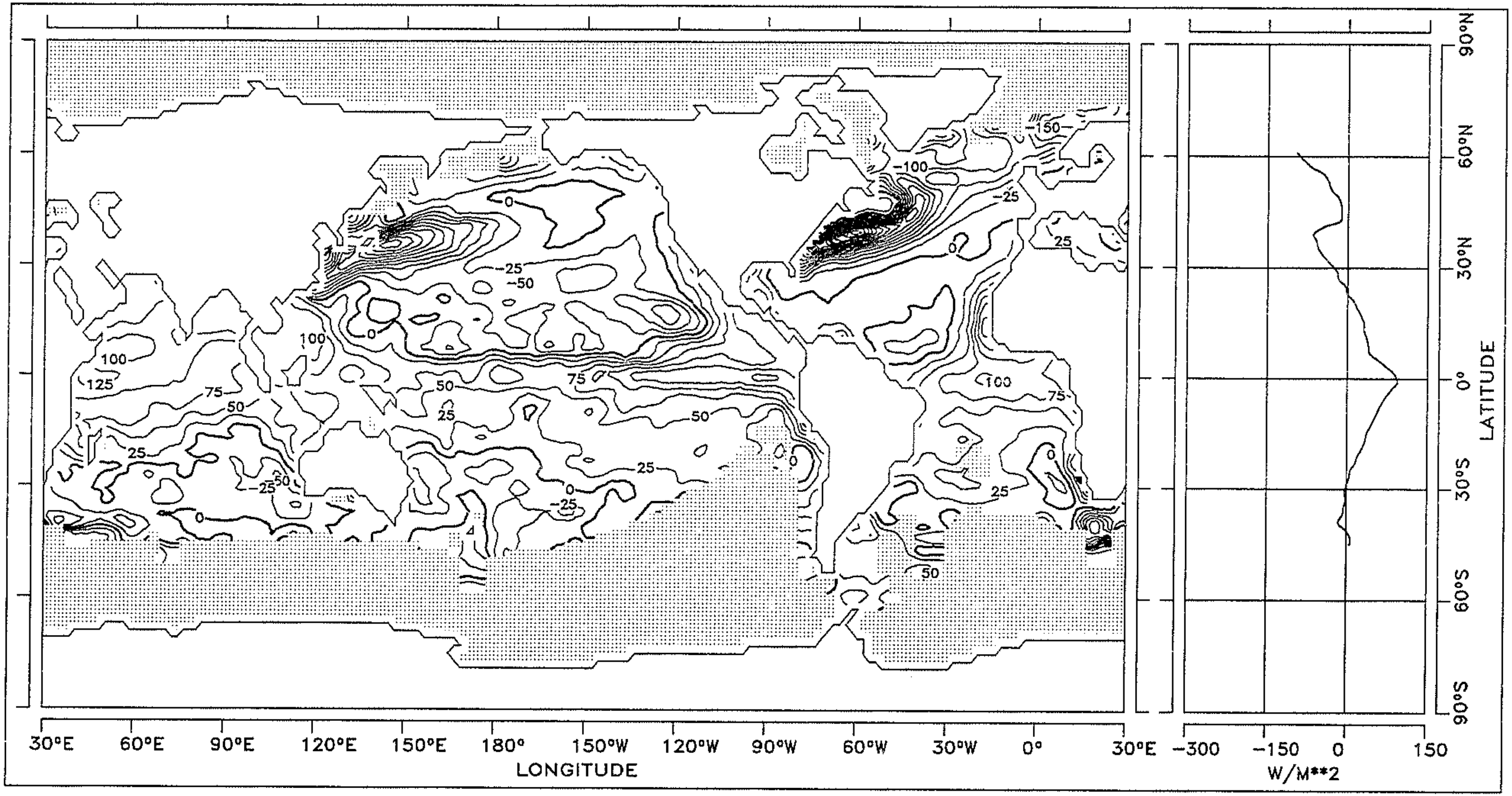

CONTOUR INTERVAL: 25 W/M**2 REFERENCE LINE : 0 W/M**2

FIG. 6.4 NET DOWNWARD HEAT FLUX APRIL

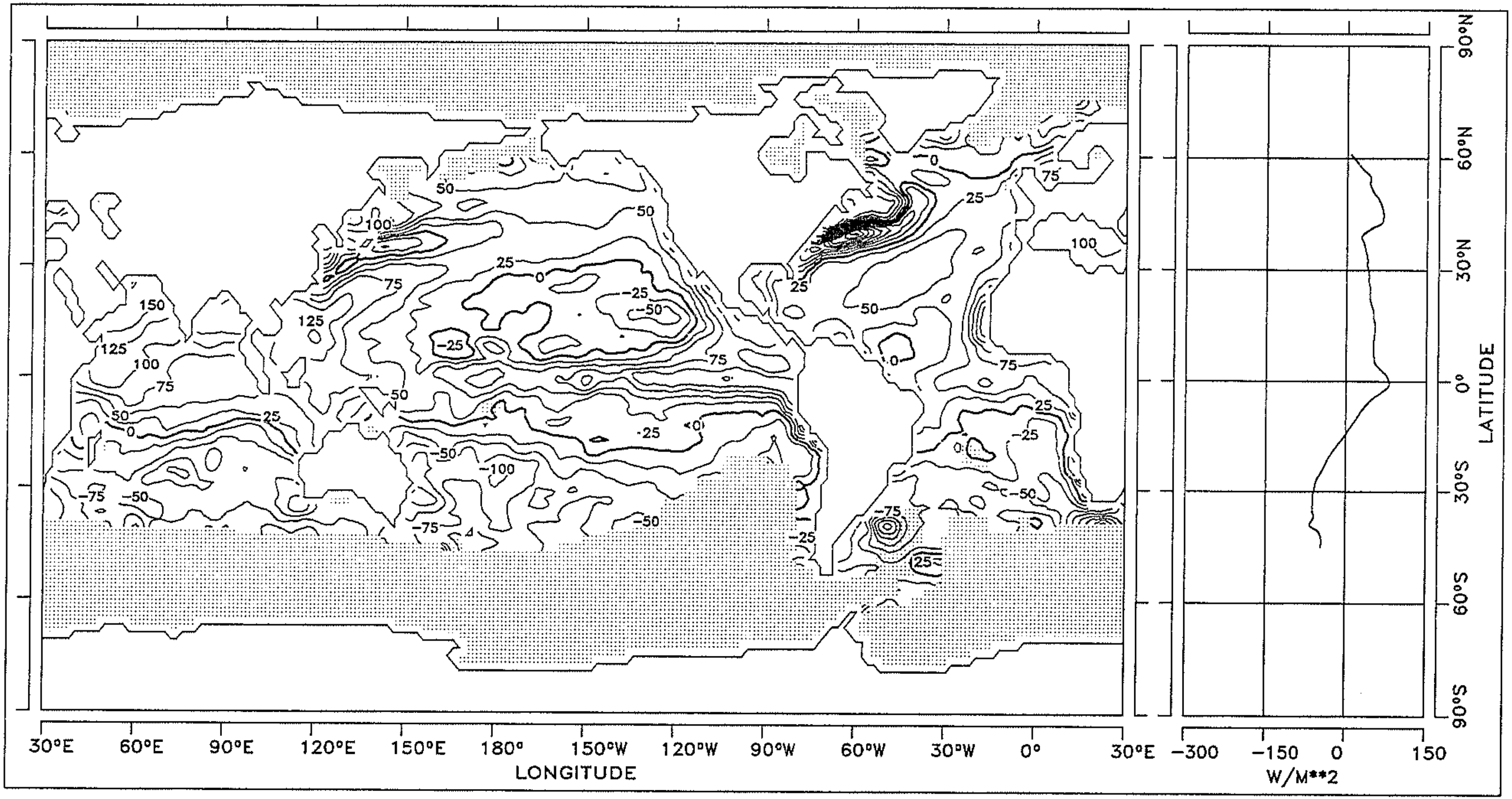

CONTOUR INTERVAL: 25 W/M**2 REFERENCE LINE : 0 W/M**2

FIG. 6.5 NET DOWNWARD HEAT FLUX MAY

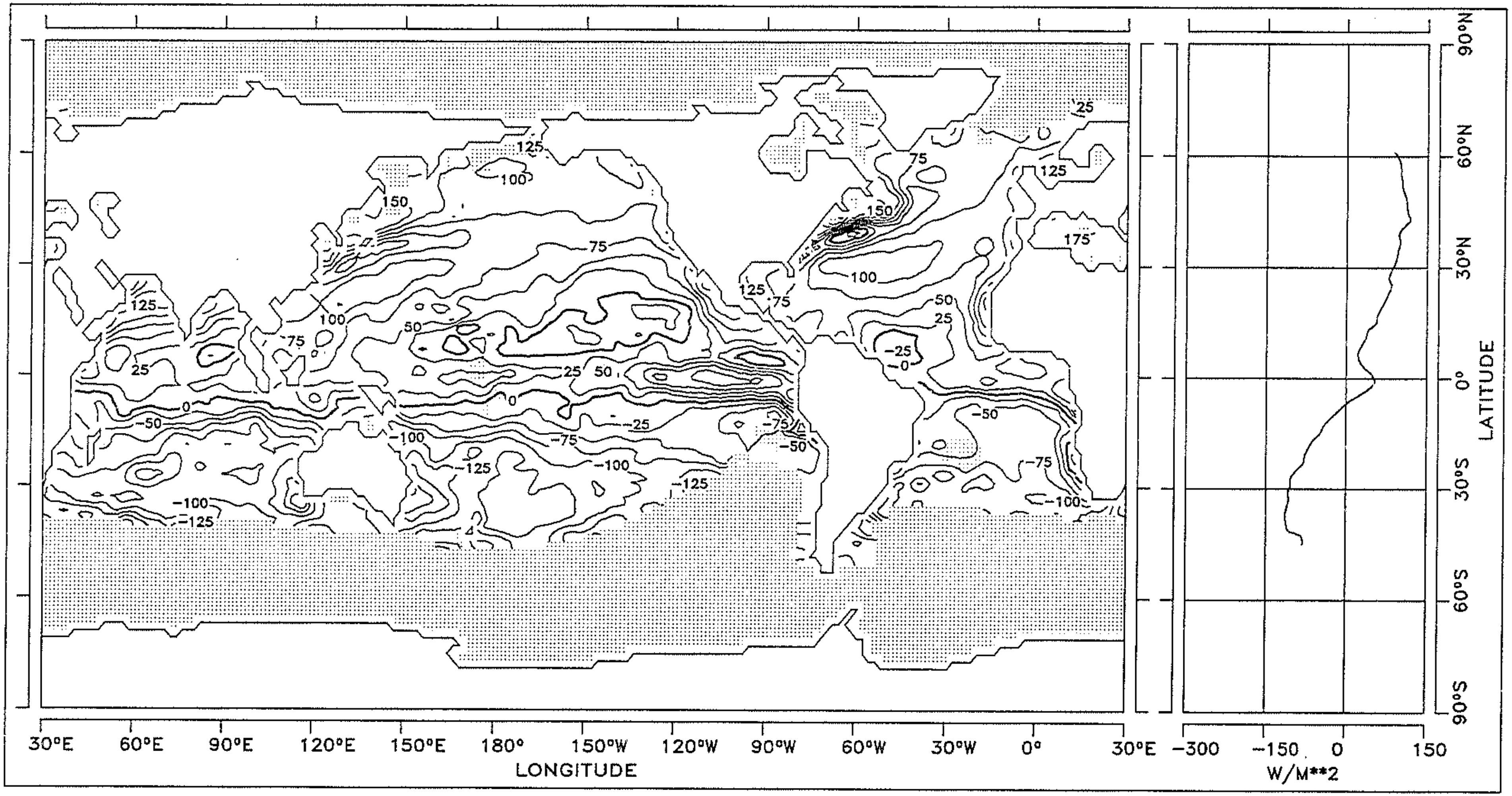

CONTOUR INTERVAL: 25 W/M**2 REFERENCE LINE : 0 W/M**2

FIG. 6.6 NET DOWNWARD HEAT FLUX JUNE

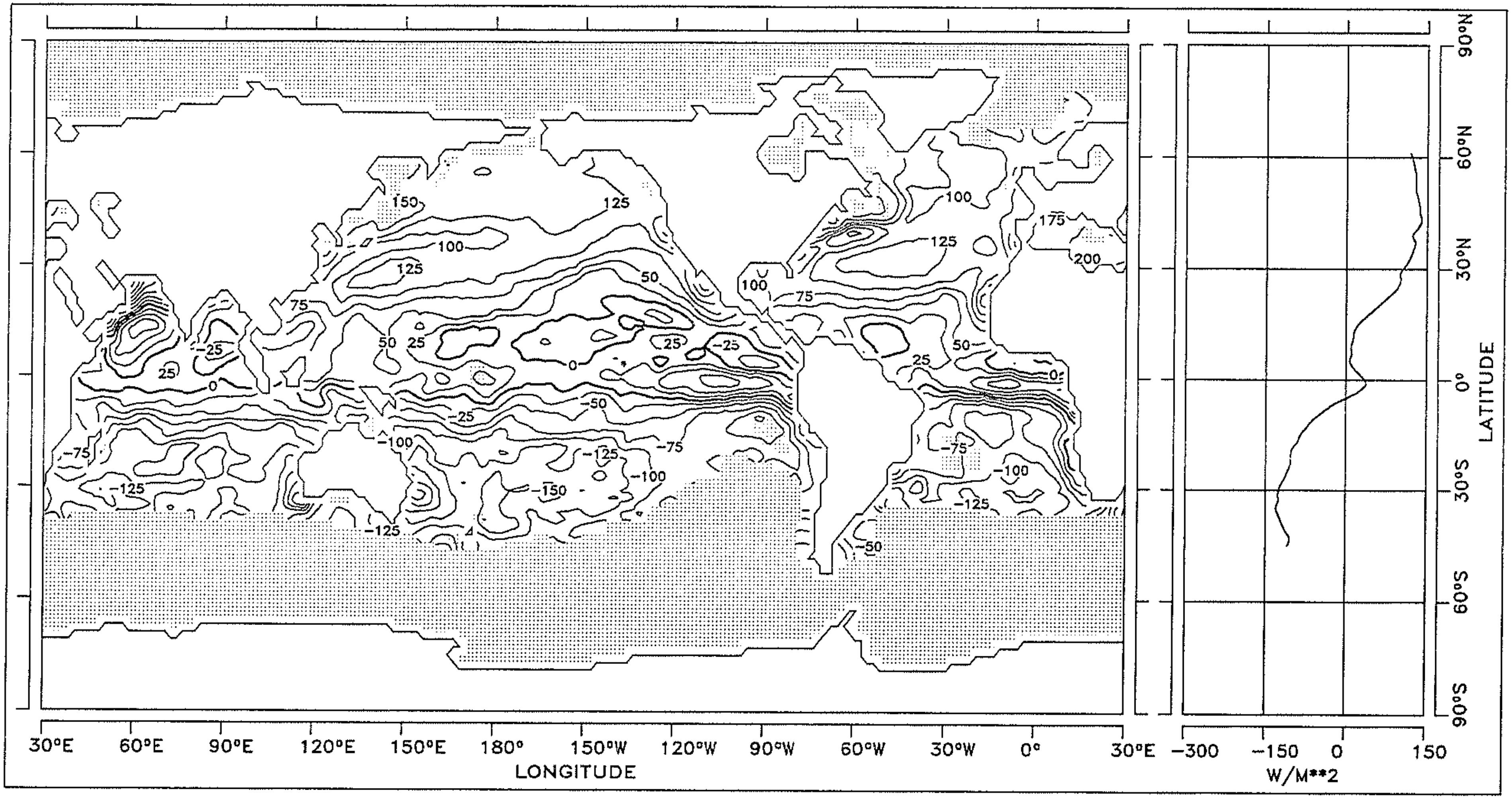

CONTOUR INTERVAL: 25 W/M**2 REFERENCE LINE : 0 W/M**2

FIG. 6.7 NET DOWNWARD HEAT FLUX JULY

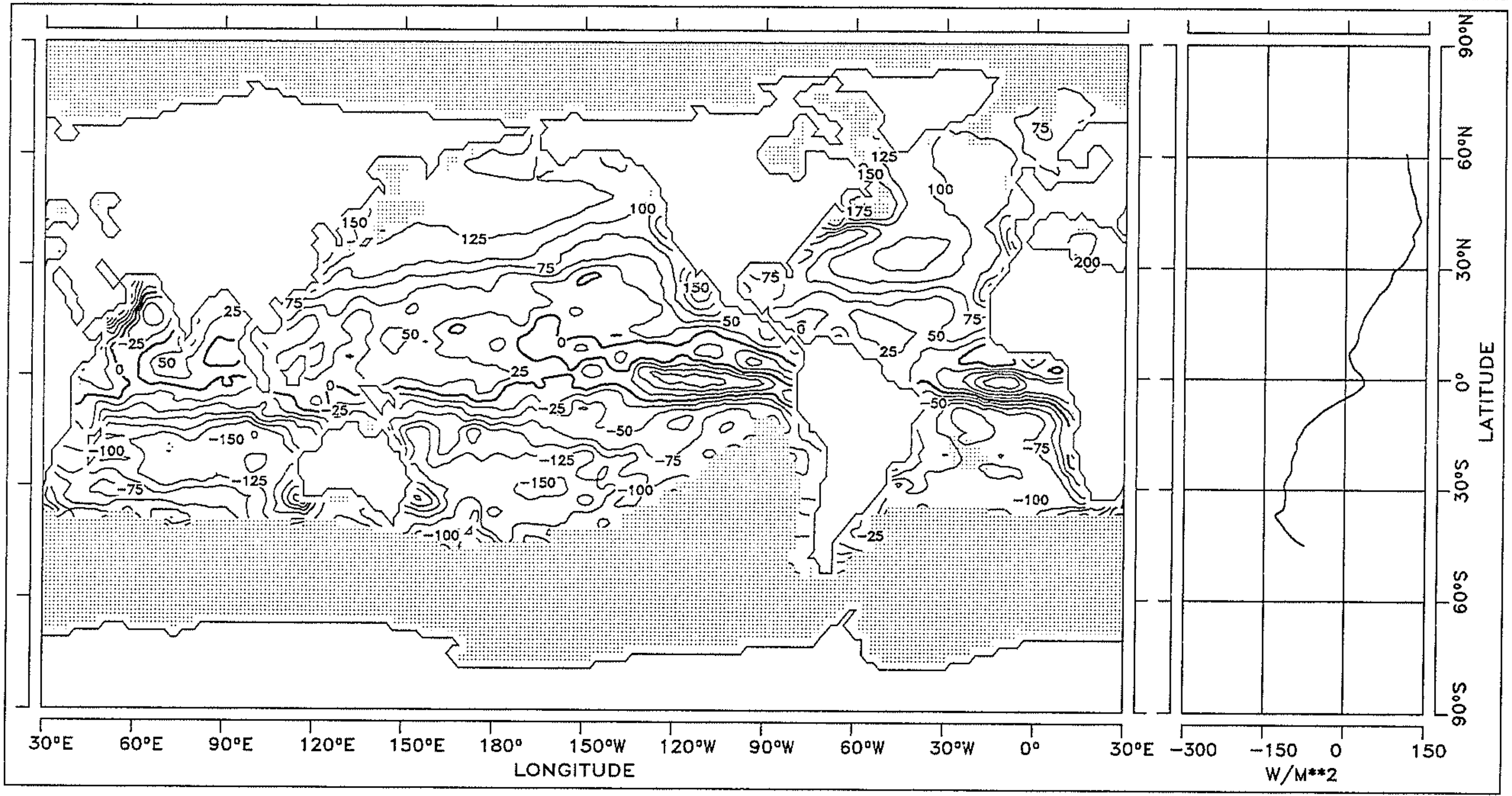

CONTOUR INTERVAL: 25 W/M**2 REFERENCE LINE : 0 W/M**2

FIG. 6.8 NET DOWNWARD HEAT FLUX AUGUST

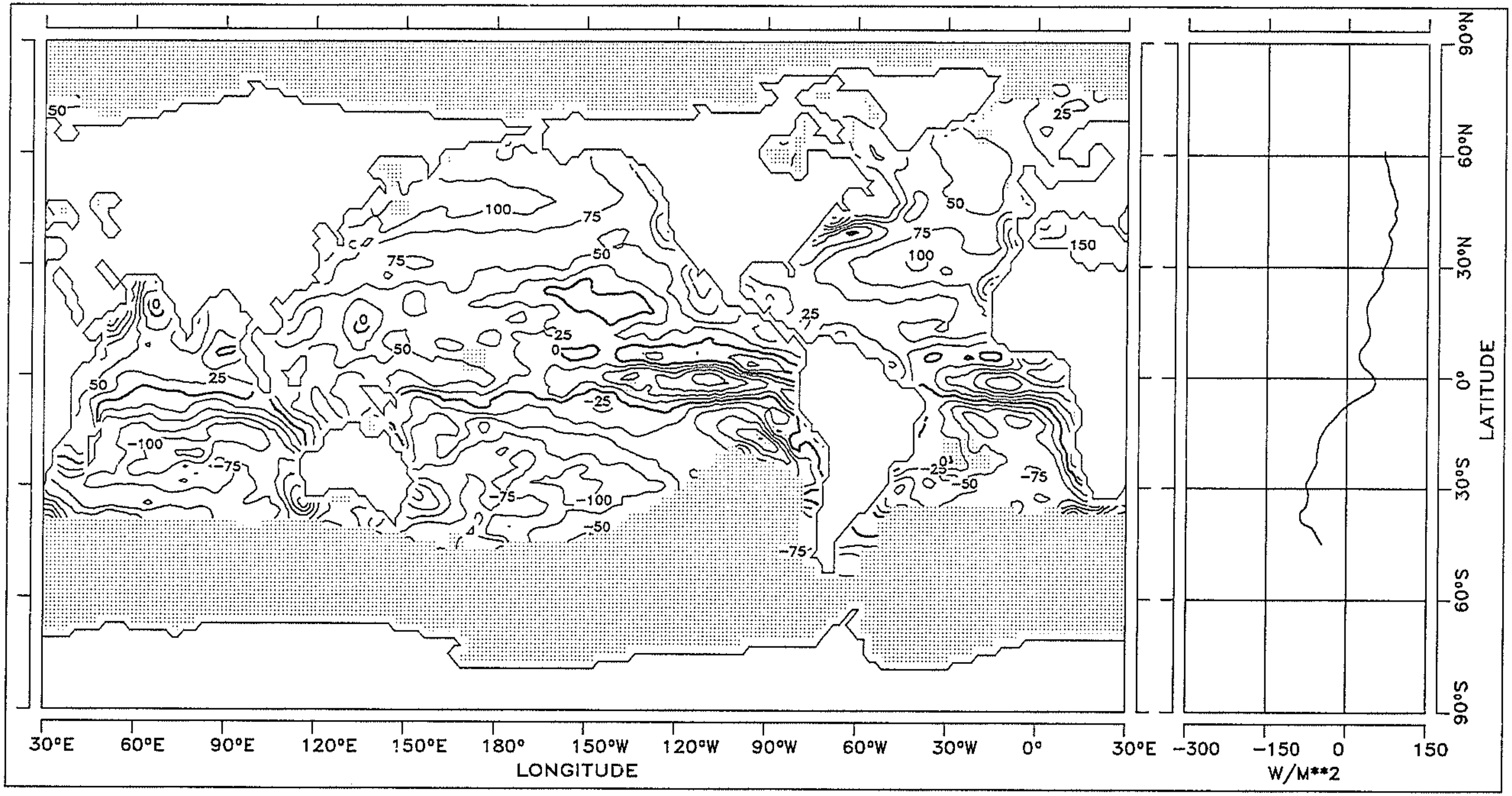

CONTOUR INTERVAL: 25 W/M**2 REFERENCE LINE : 0 W/M**2

FIG. 6.9 NET DOWNWARD HEAT FLUX SEPTEMBER

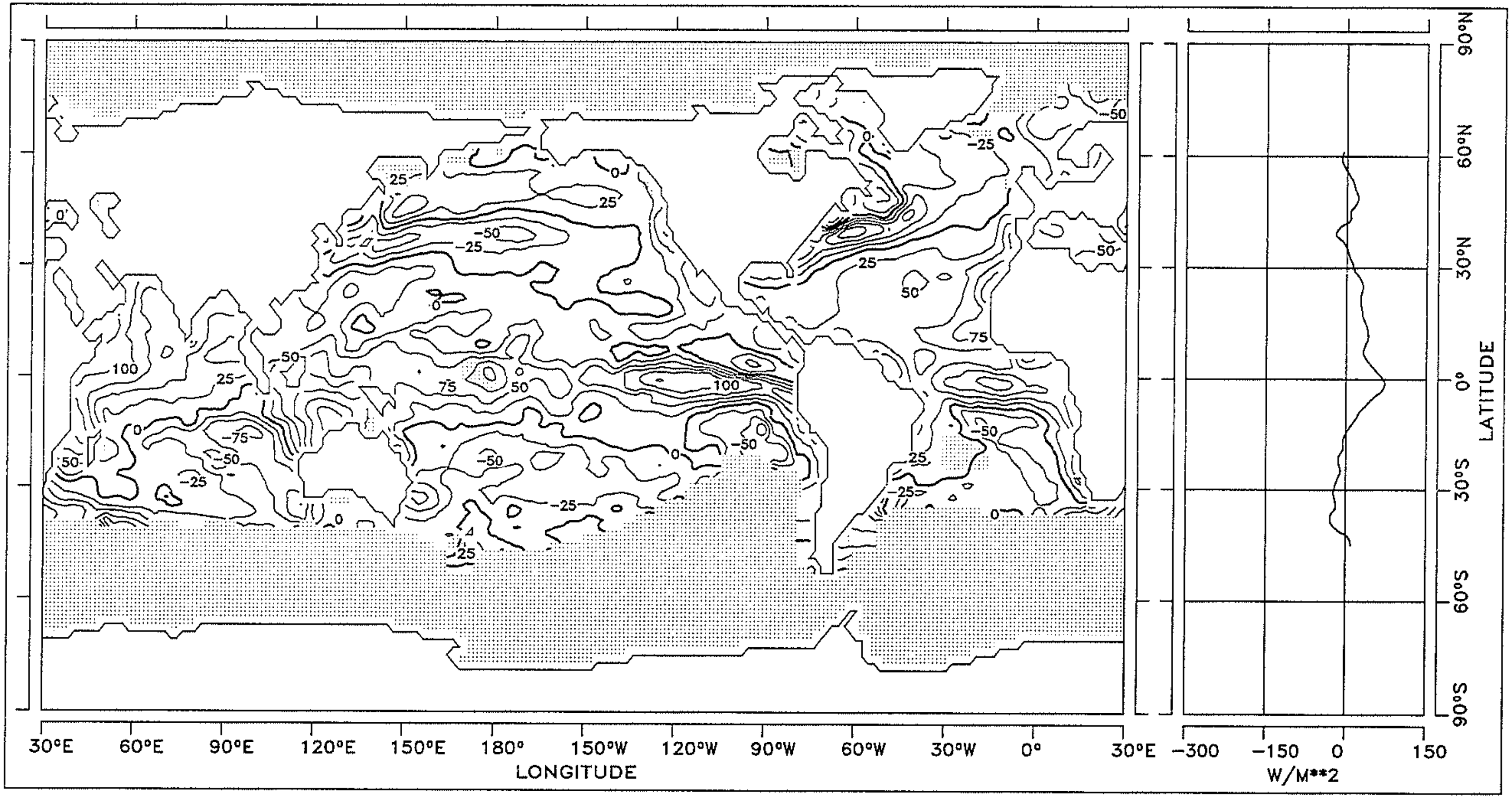

CONTOUR INTERVAL: 25 W/M**2 REFERENCE LINE : 0 W/M**2

FIG. 6.10 NET DOWNWARD HEAT FLUX OCTOBER

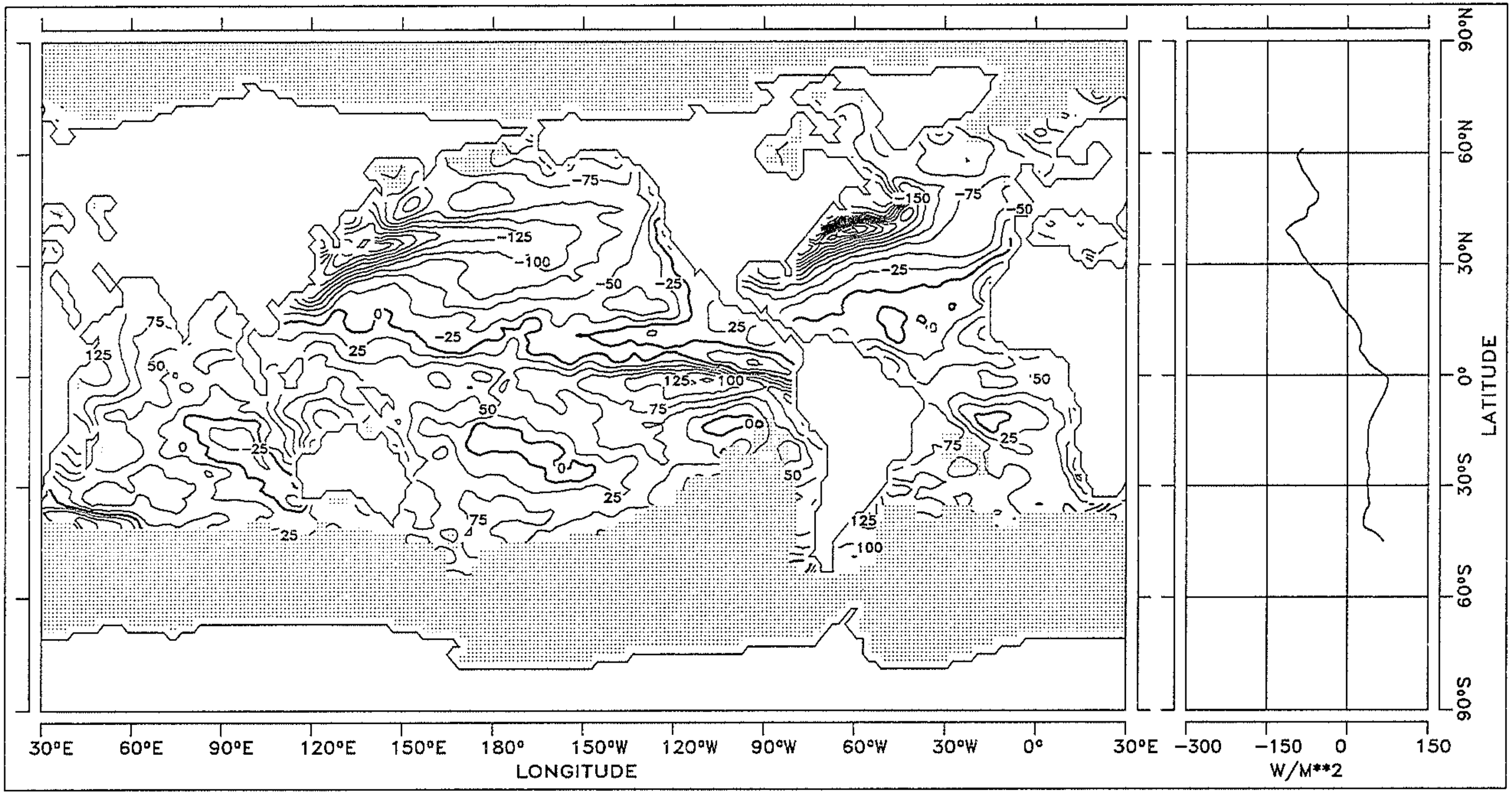

CONTOUR INTERVAL: 25 W/M**2 REFERENCE LINE : 0 W/M**2

FIG. 6.11 NET DOWNWARD HEAT FLUX NOVEMBER

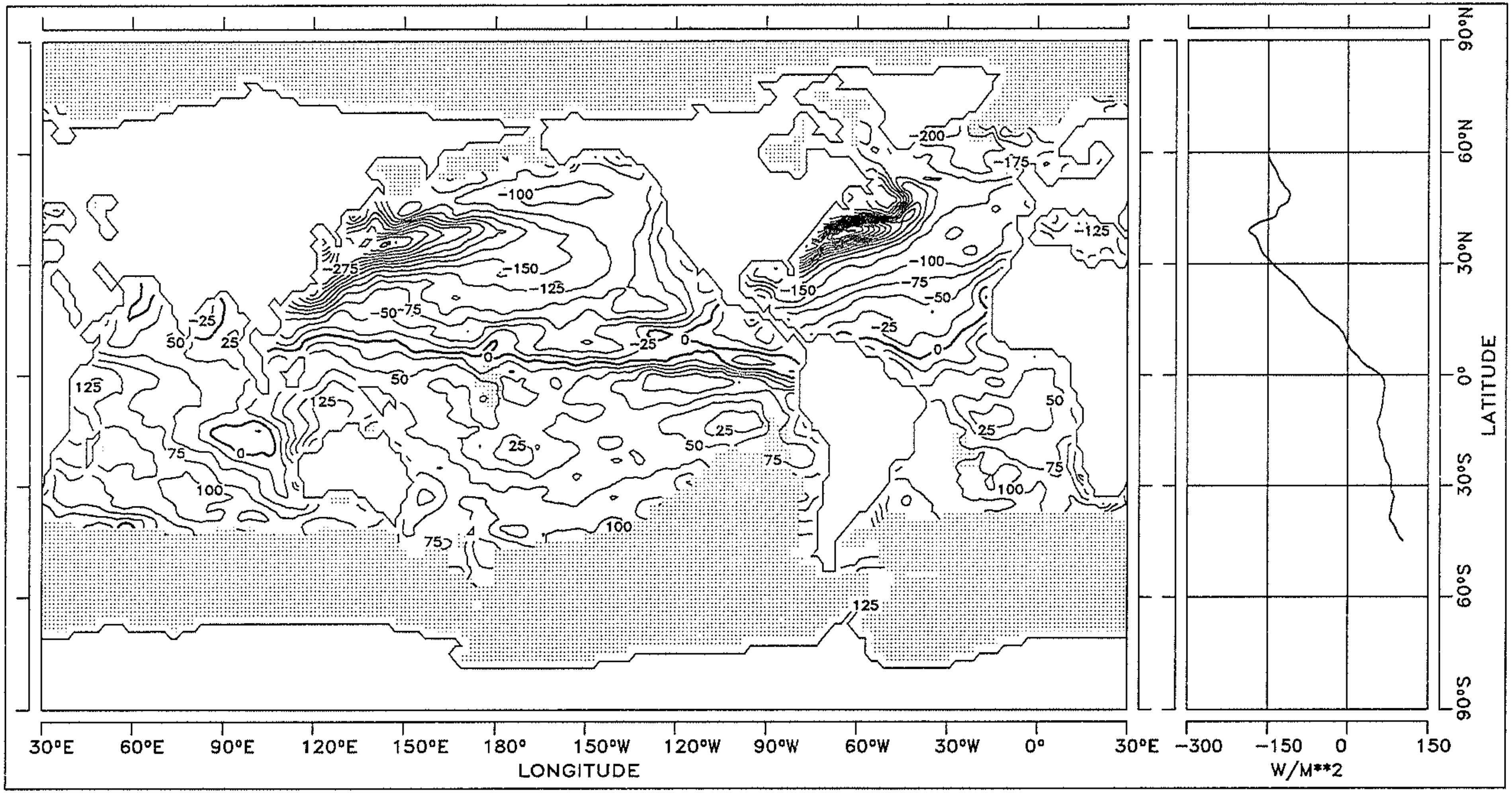

CONTOUR INTERVAL: 25 W/M**2 REFERENCE LINE : 0 W/M**2

FIG. 6.12 NET DOWNWARD HEAT FLUX DECEMBER

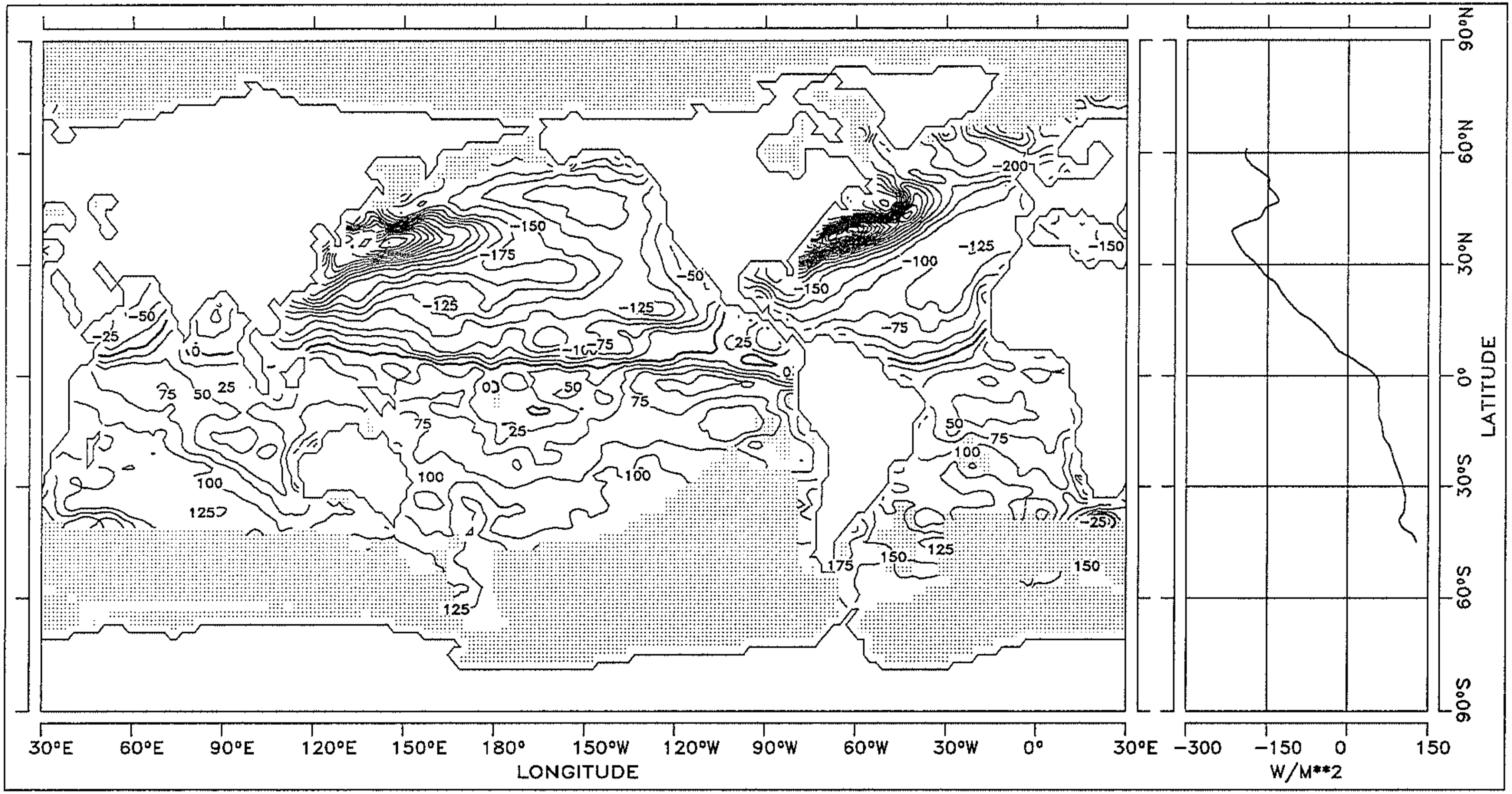

CONTOUR INTERVAL: 25 W/M**2 REFERENCE LINE : 0 W/M**2

FIG. 6.13 NET DOWNWARD HEAT FLUX

ANNUAL MEAN

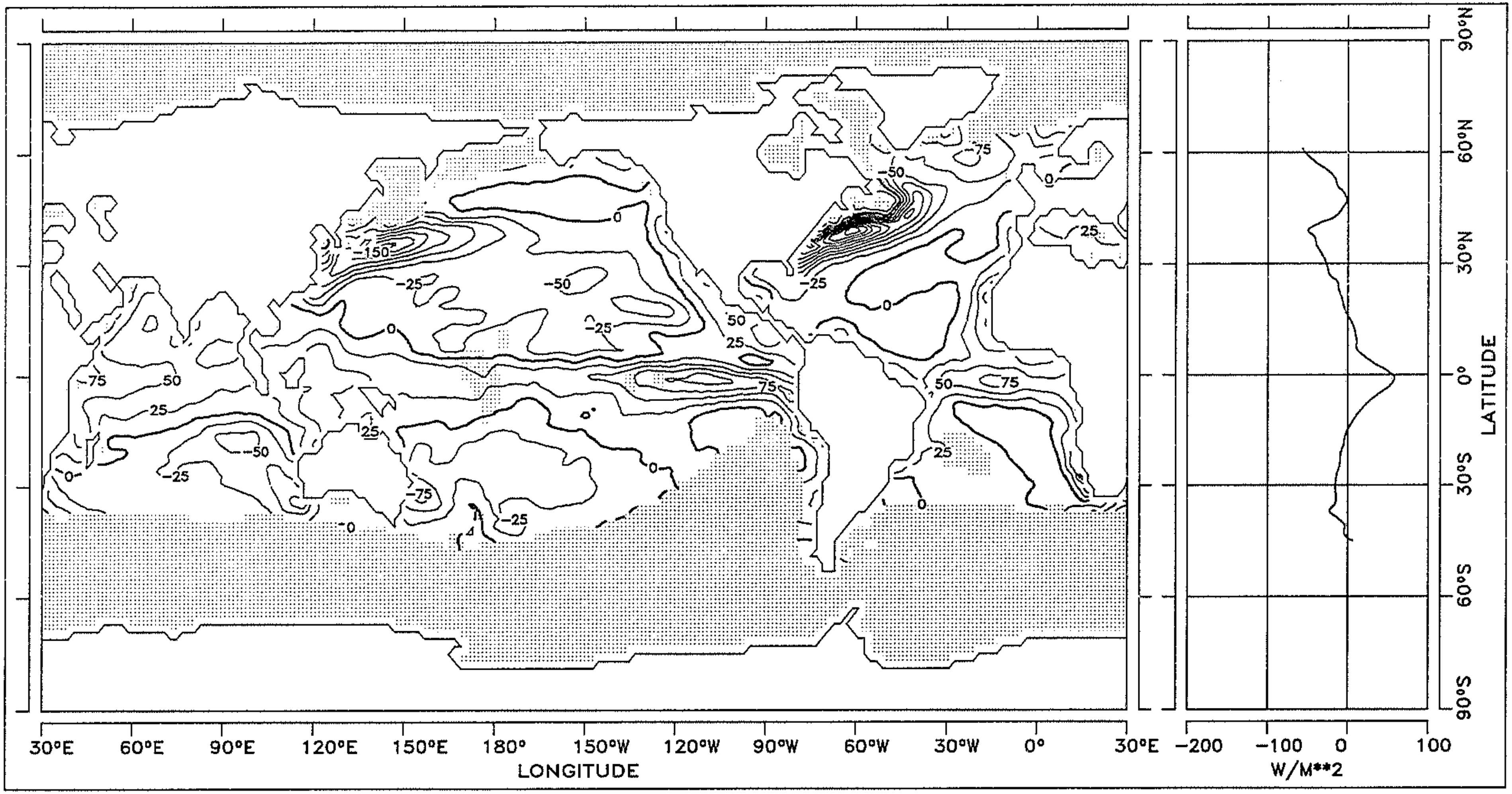

CONTOUR INTERVAL: 25 W/M**2   REFERENCE LINE : 0 W/M**2

TIME CROSS-SECTIONS OF HEAT FLUXES

FIG. 7 TIME CROSS SECTION OF ZONALLY AVERAGED SHORT WAVE RADIATION BUDGET

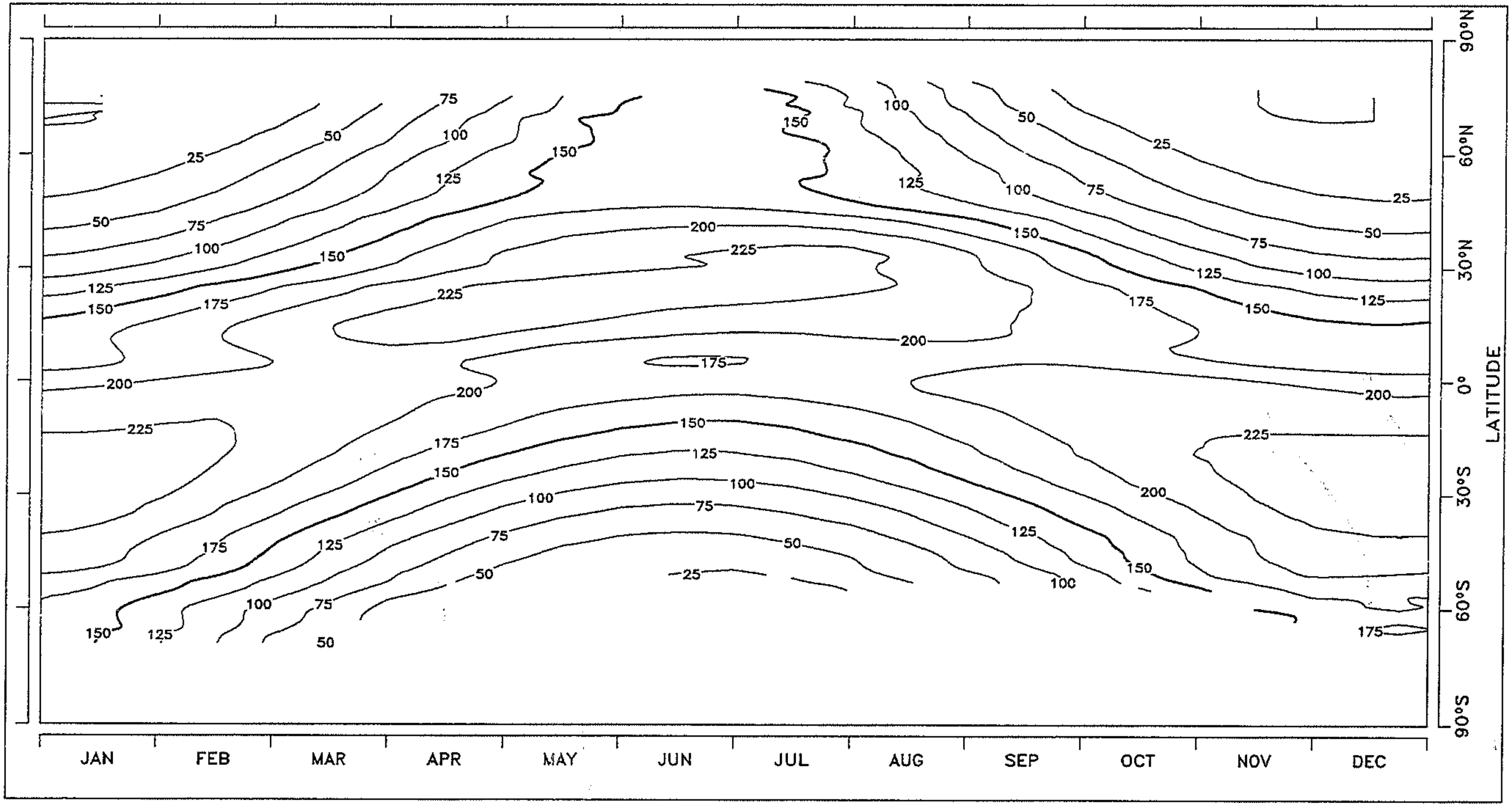

CONTOUR INTERVAL: 25 W/M**2 REFERENCE LINE : 150 W/M**2

FIG. 8 TIME CROSS SECTION OF ZONALLY AVERAGED LONG WAVE RADIATION BUDGET

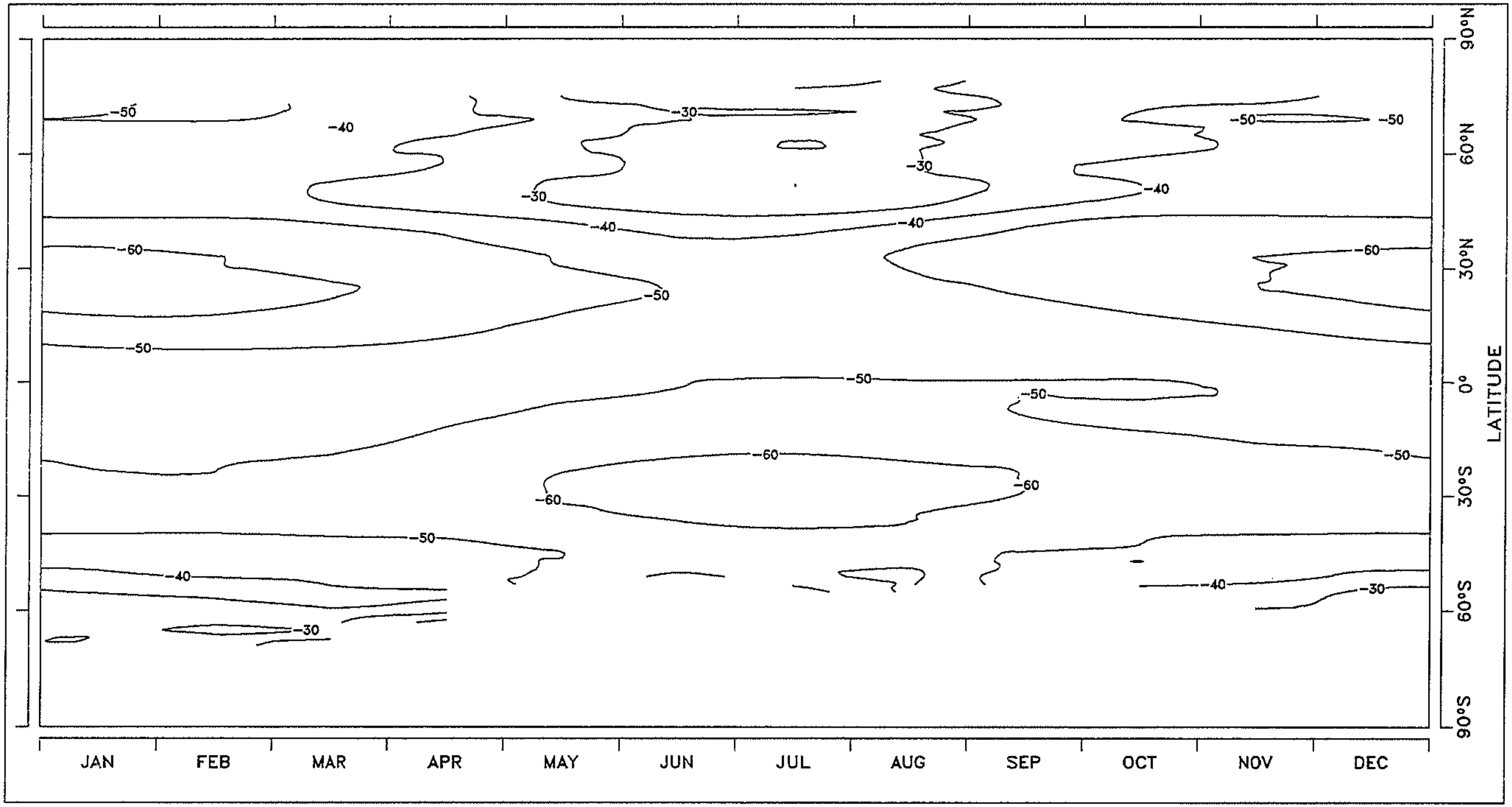

CONTOUR INTERVAL: 10 W/M**2 REFERENCE LINE : 0 W/M**2

FIG. 9 TIME CROSS SECTION OF ZONALLY AVERAGED NET RADIATION BUDGET

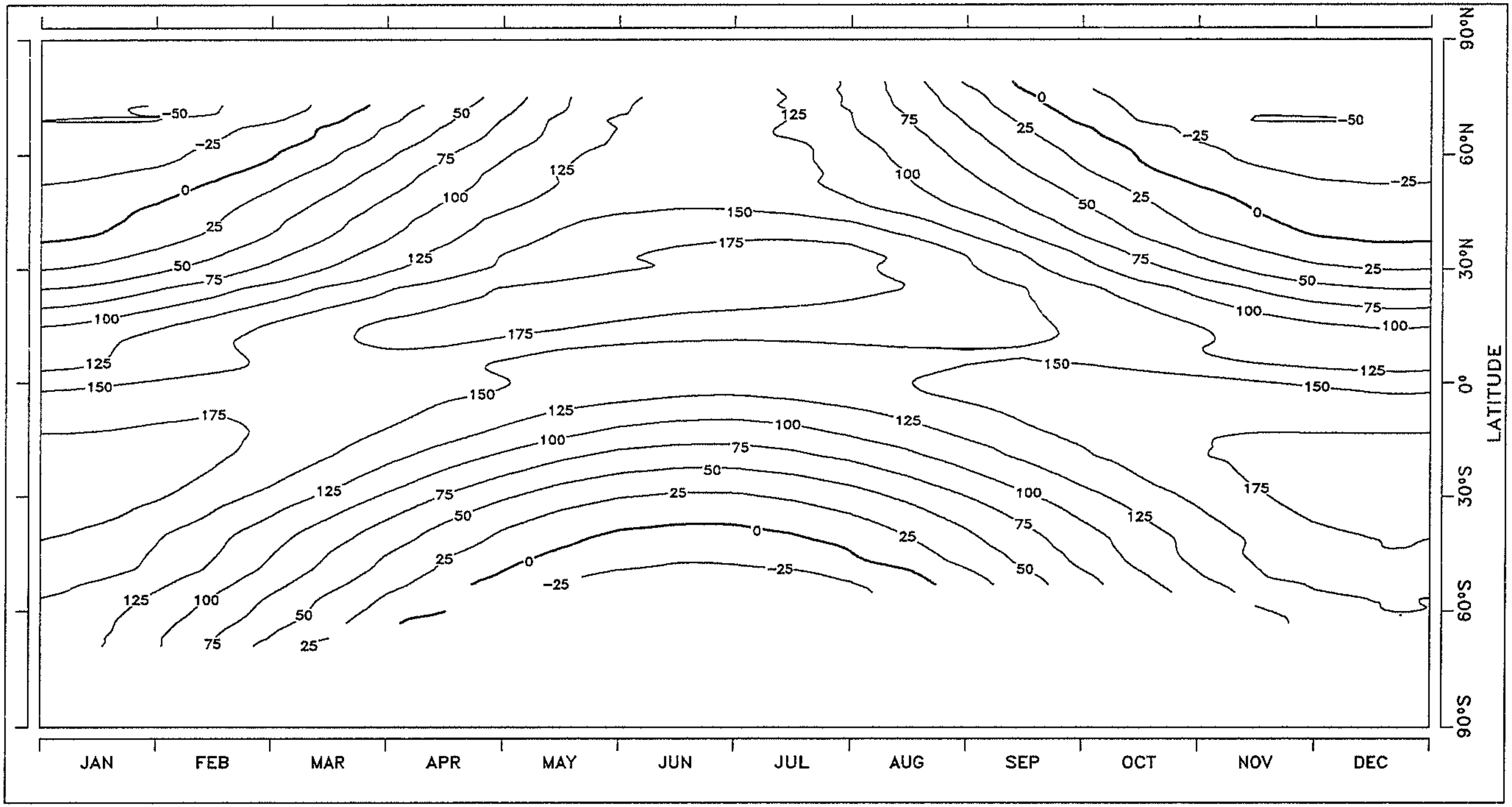

CONTOUR INTERVAL: 25 W/M**2 REFERENCE LINE : 0 W/M**2

FIG. 10 TIME CROSS SECTION OF ZONALLY AVERAGED LATENT HEAT FLUX

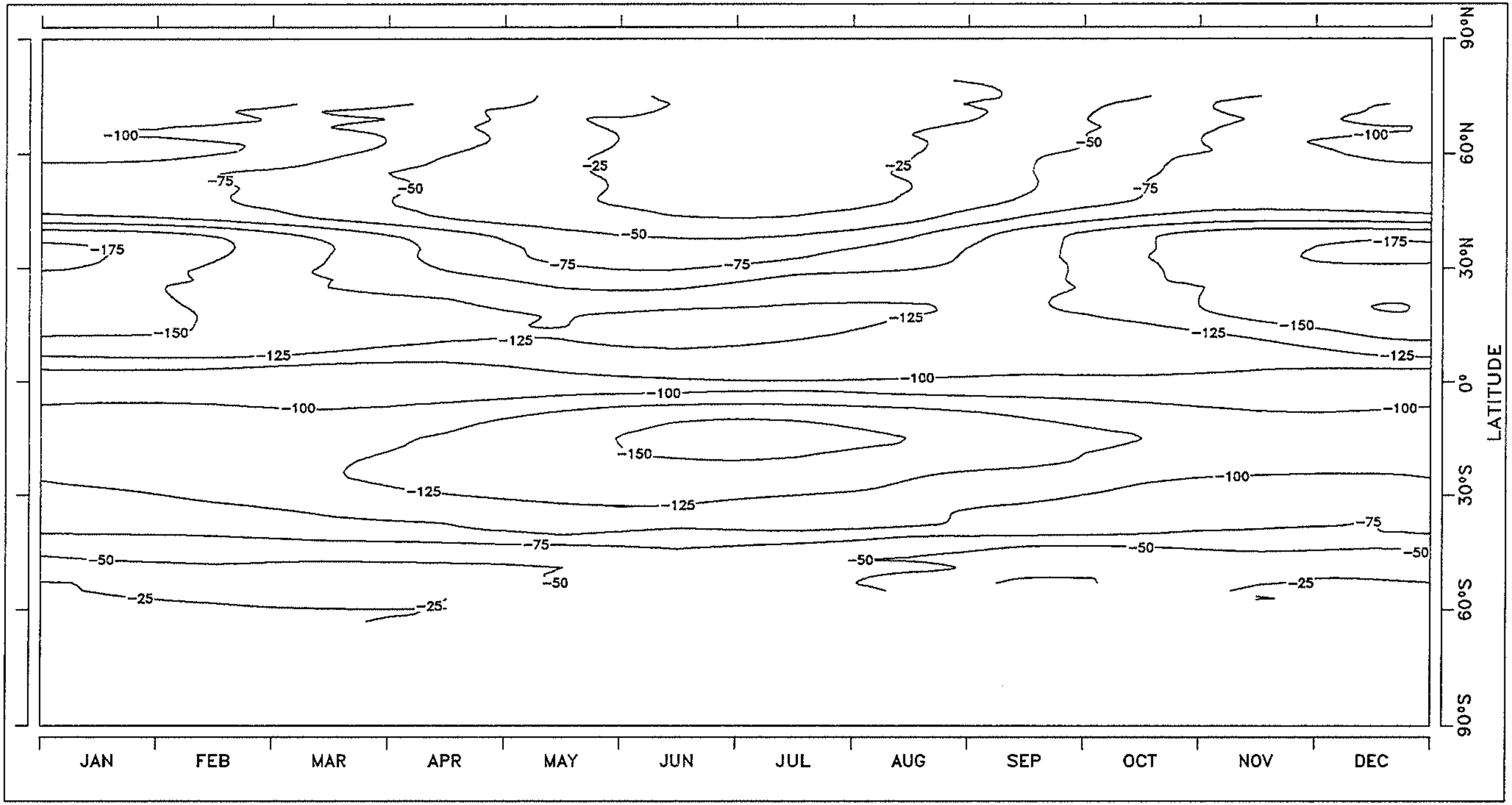

CONTOUR INTERVAL: 25 W/M**2 REFERENCE LINE : 0 W/M**2

FIG. 11 TIME CROSS SECTION OF ZONALLY AVERAGED SENSIBLE HEAT FLUX

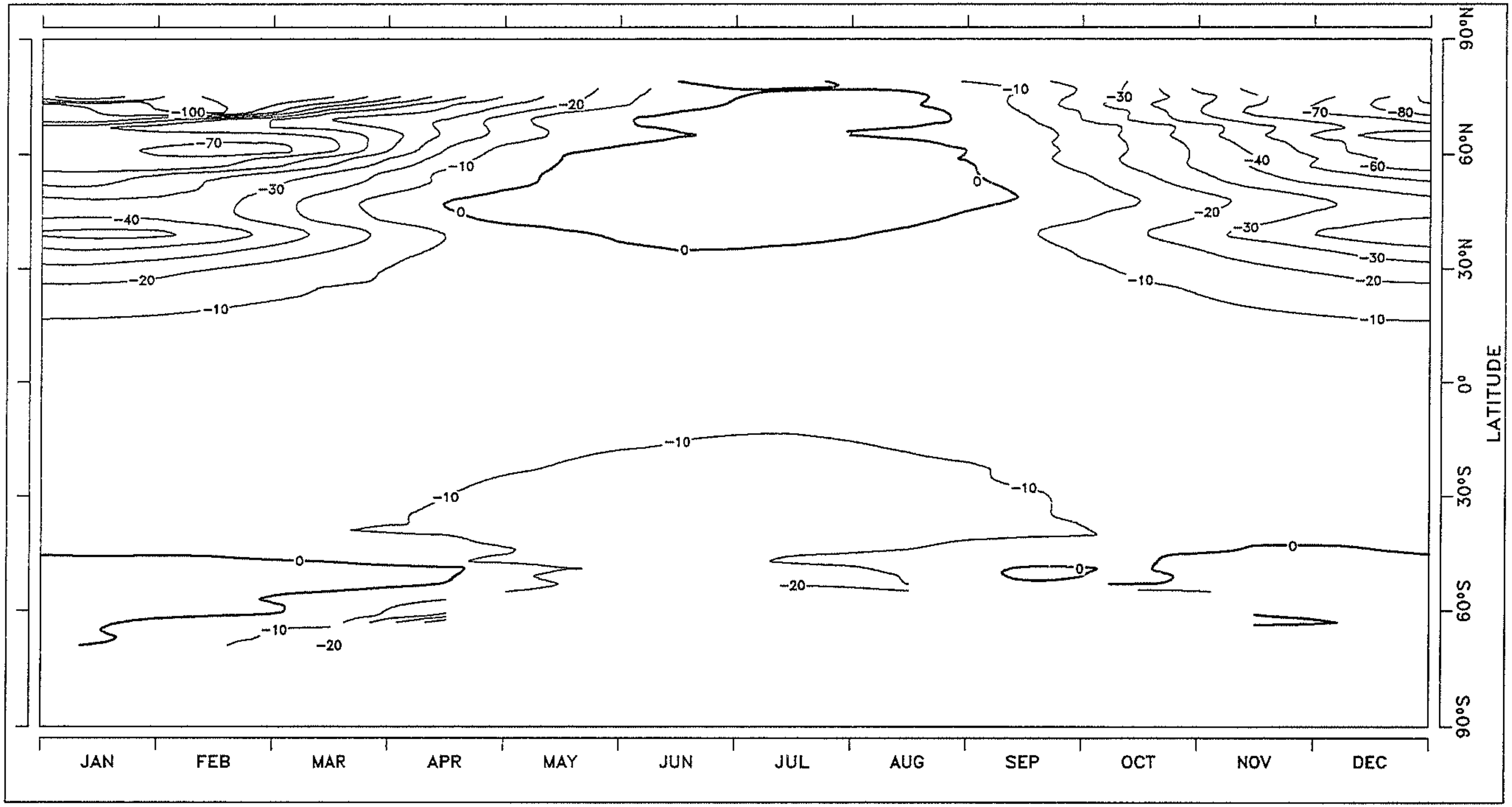

CONTOUR INTERVAL: 10 W/M**2 REFERENCE LINE : 0 W/M**2

FIG. 12 TIME CROSS SECTION OF ZONALLY AVERAGED NET DOWNWARD HEAT FLUX

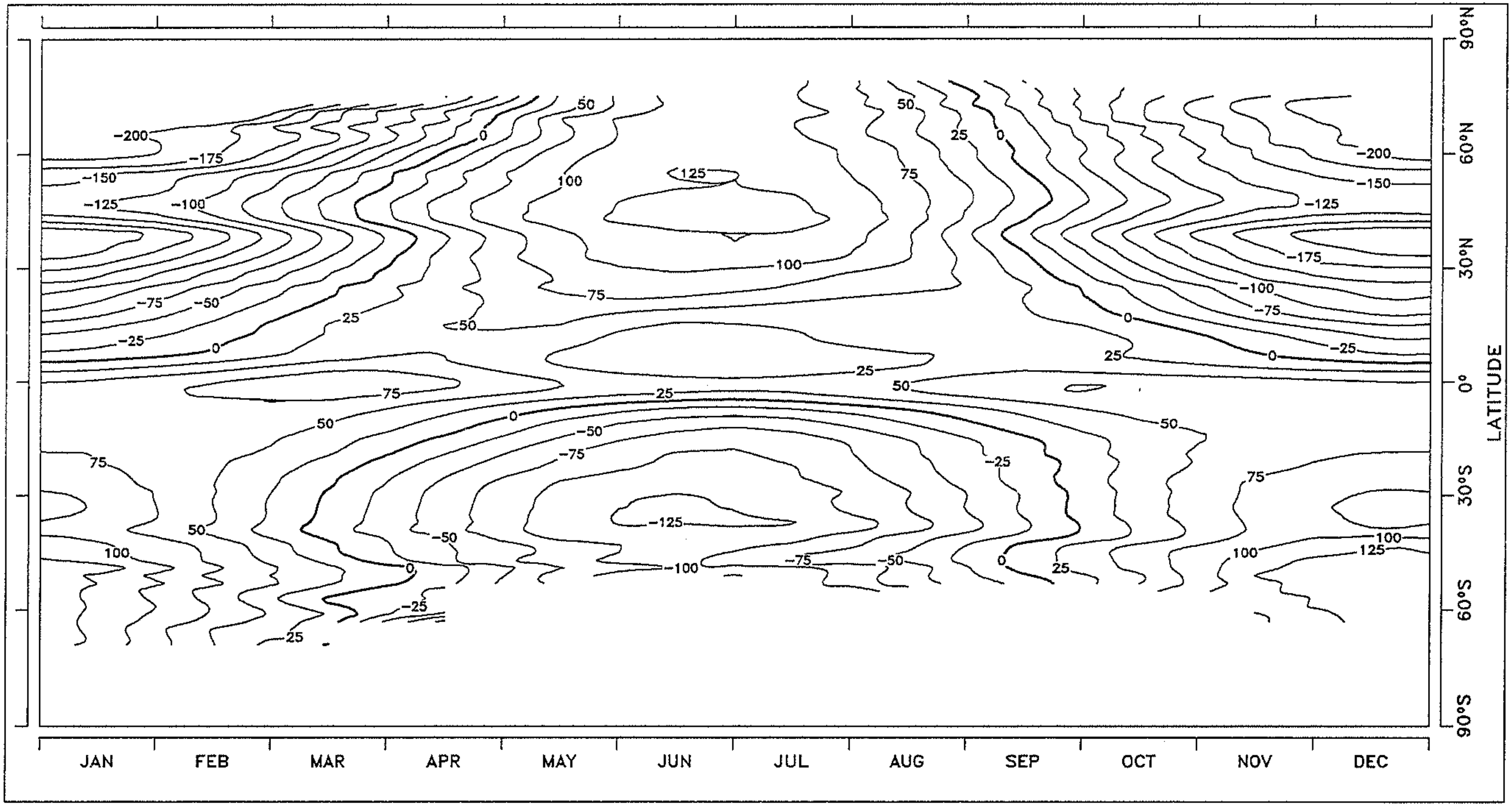

CONTOUR INTERVAL: 25 W/M**2 REFERENCE LINE : 0 W/M**2

FIG. 13 MERIDIONAL PROFILES OF ANNUAL HEAT BUDGET COMPONENTS

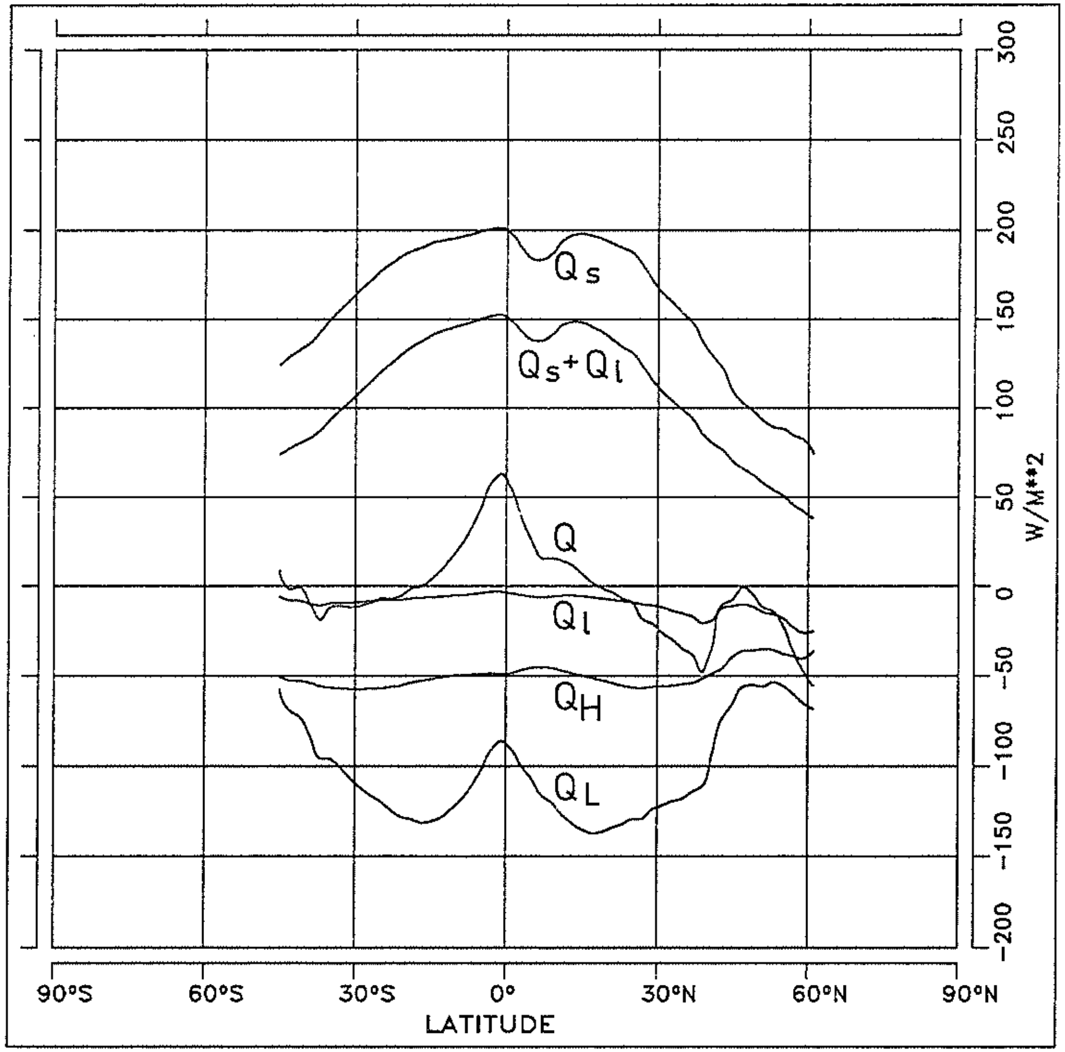

NET DOWNWARD FRESH WATER FLUX

FIG. 14.1 NET DOWNWARD FRESH WATER FLUX JANUARY

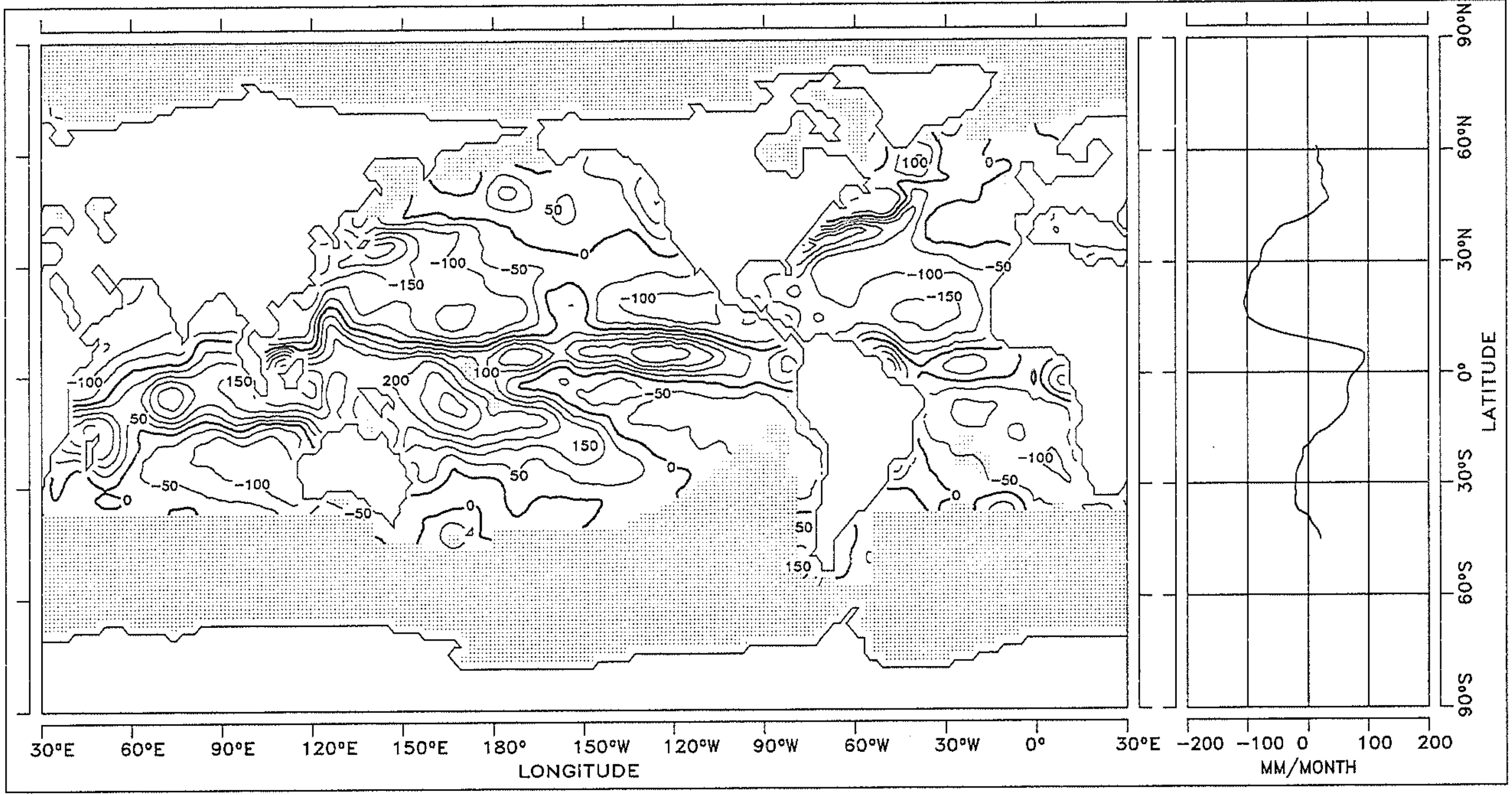

CONTOUR INTERVAL: 50 MM/MONTH REFERENCE LINE : 0 MM/MONTH

FIG. 14.2 NET DOWNWARD FRESH WATER FLUX FEBRUARY

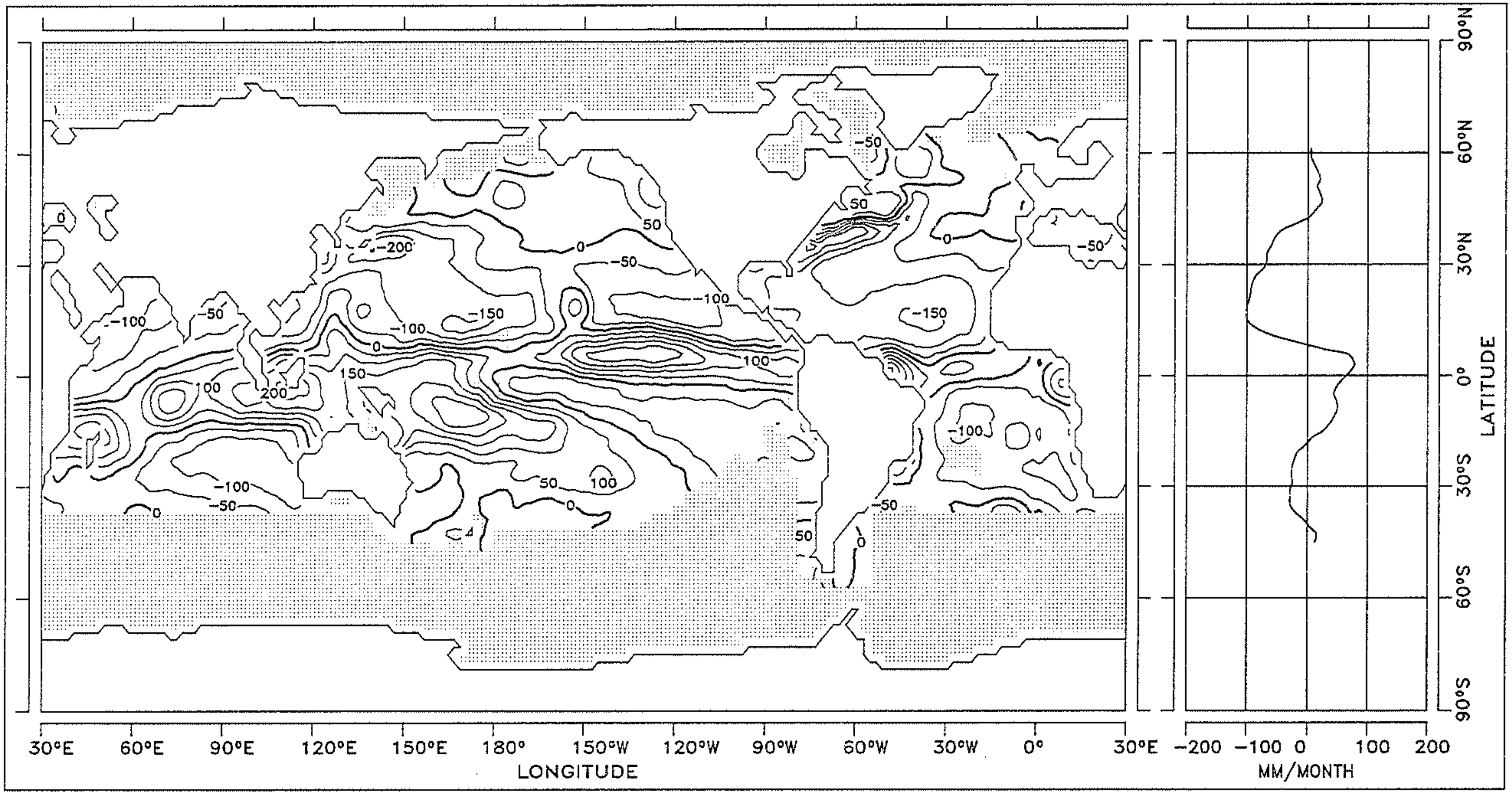

CONTOUR INTERVAL: 50 MM/MONTH REFERENCE LINE : 0 MM/MONTH

FIG. 14.3 NET DOWNWARD FRESH WATER FLUX MARCH

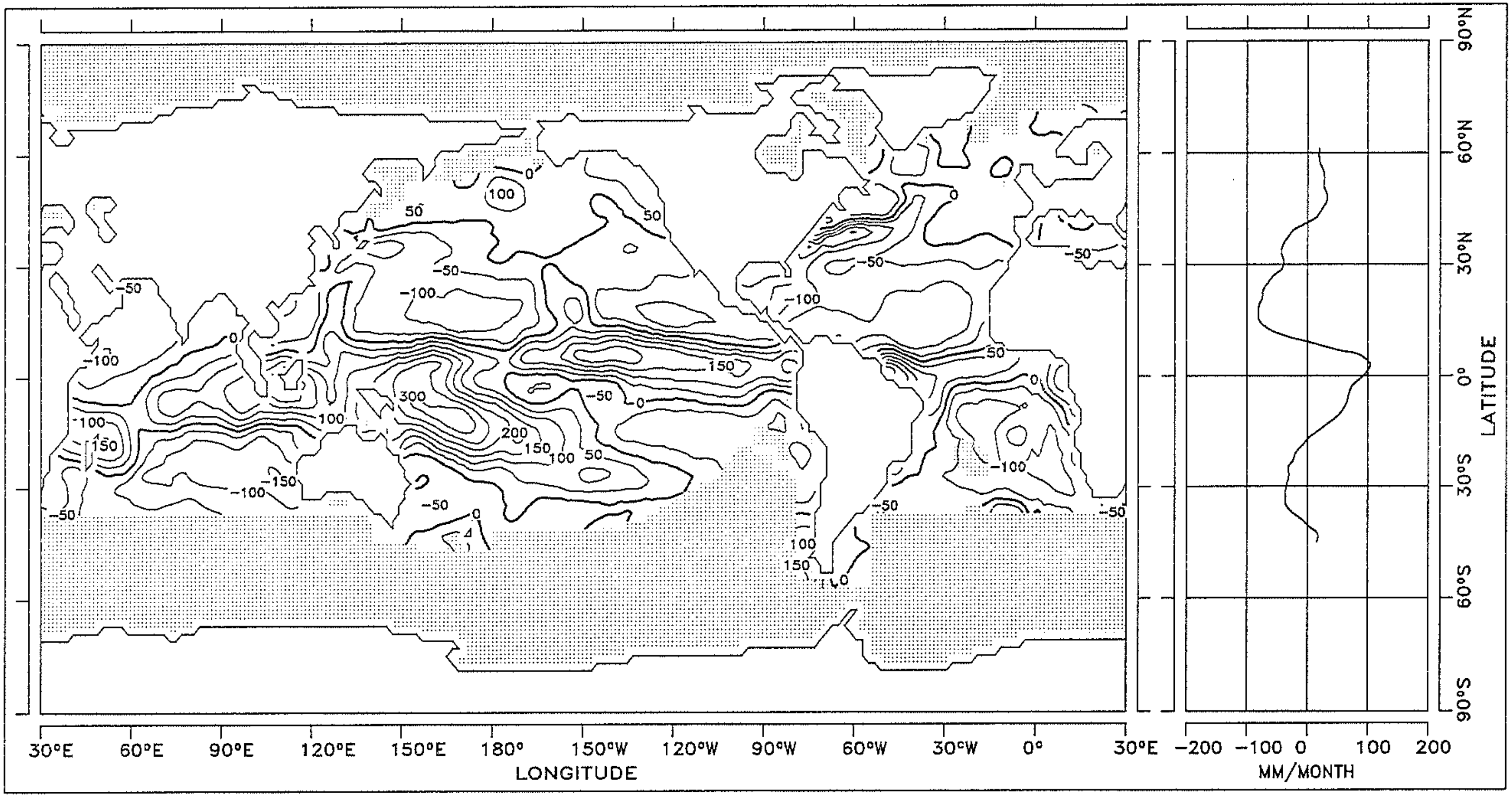

CONTOUR INTERVAL: 50 MM/MONTH REFERENCE LINE : 0 MM/MONTH

FIG. 14.4 NET DOWNWARD FRESH WATER FLUX APRIL

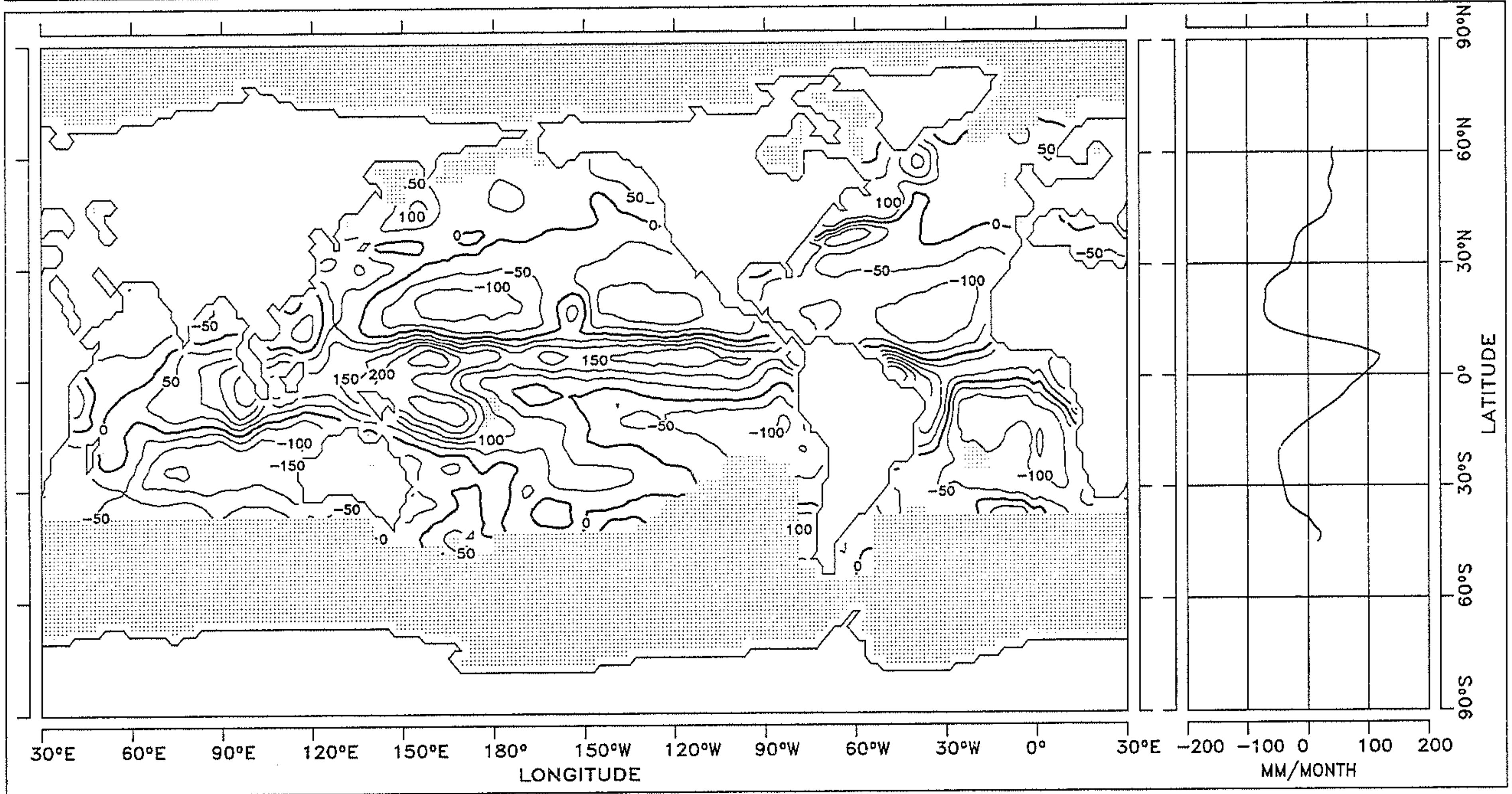

CONTOUR INTERVAL: 50 MM/MONTH REFERENCE LINE : 0 MM/MONTH

FIG. 14.5 NET DOWNWARD FRESH WATER FLUX MAY

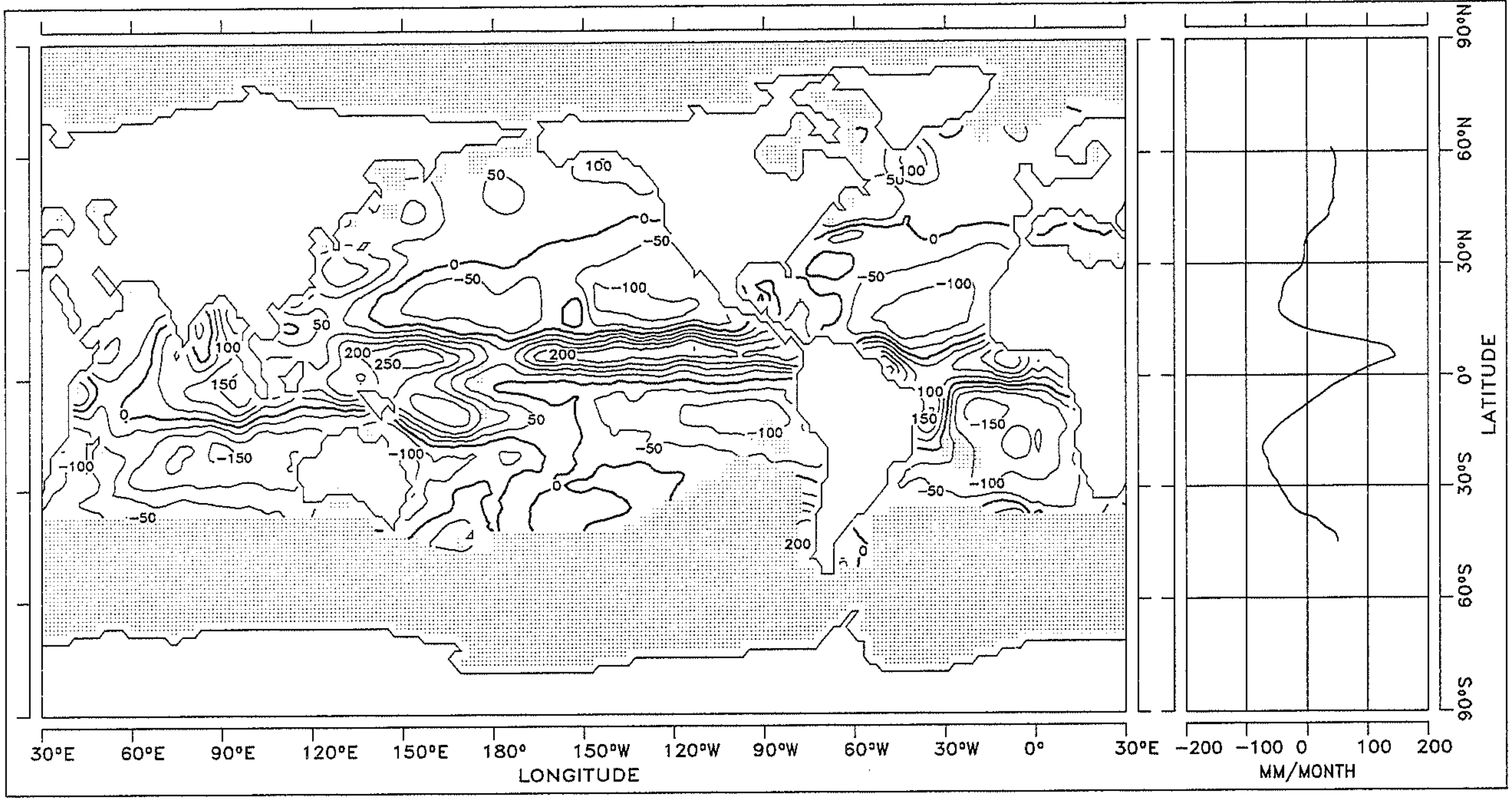

CONTOUR INTERVAL: 50 MM/MONTH REFERENCE LINE : 0 MM/MONTH

FIG. 14.6 NET DOWNWARD FRESH WATER FLUX JUNE

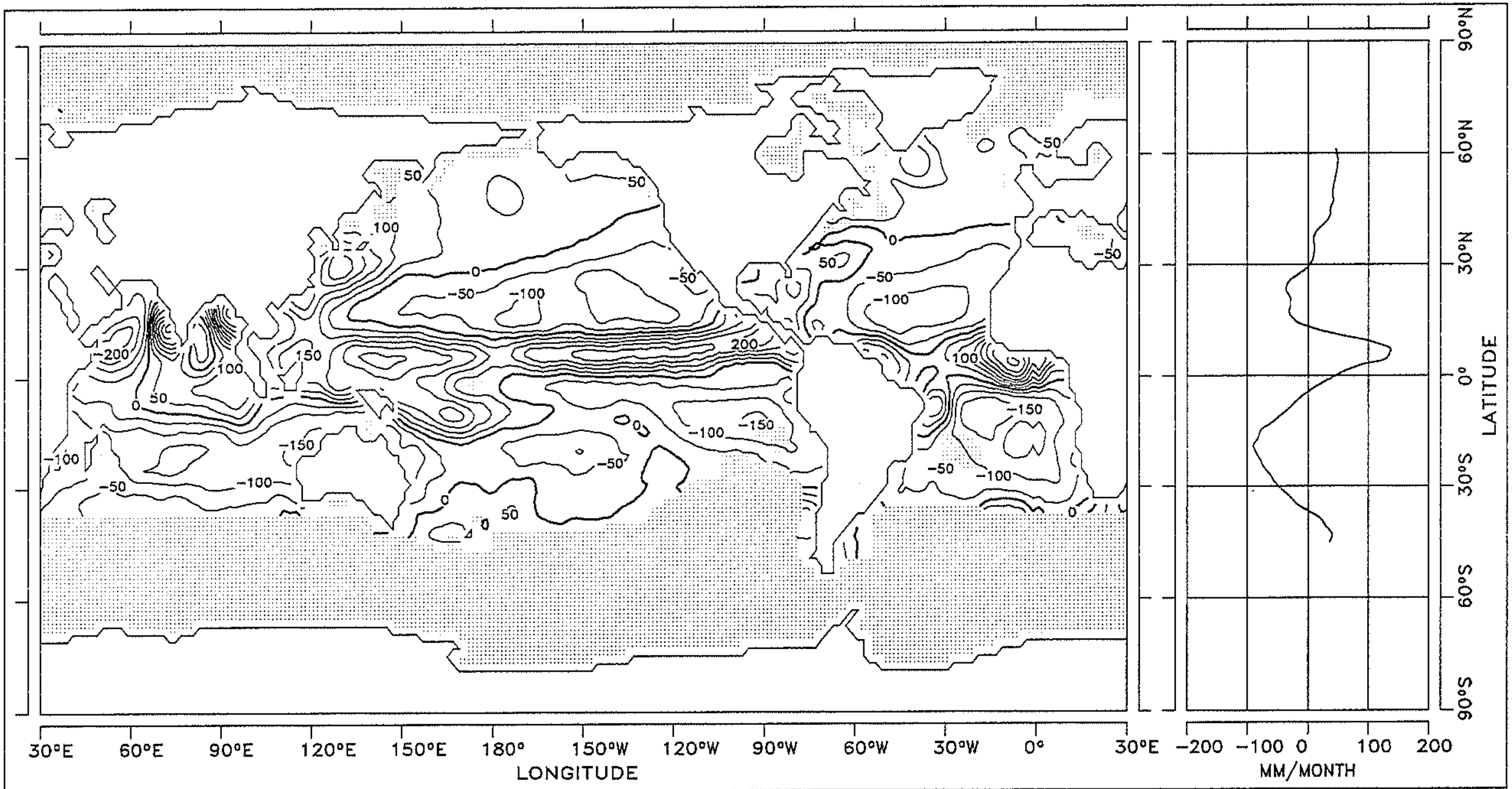

CONTOUR INTERVAL: 50 MM/MONTH REFERENCE LINE : 0 MM/MONTH

FIG. 14.7 NET DOWNWARD FRESH WATER FLUX JULY

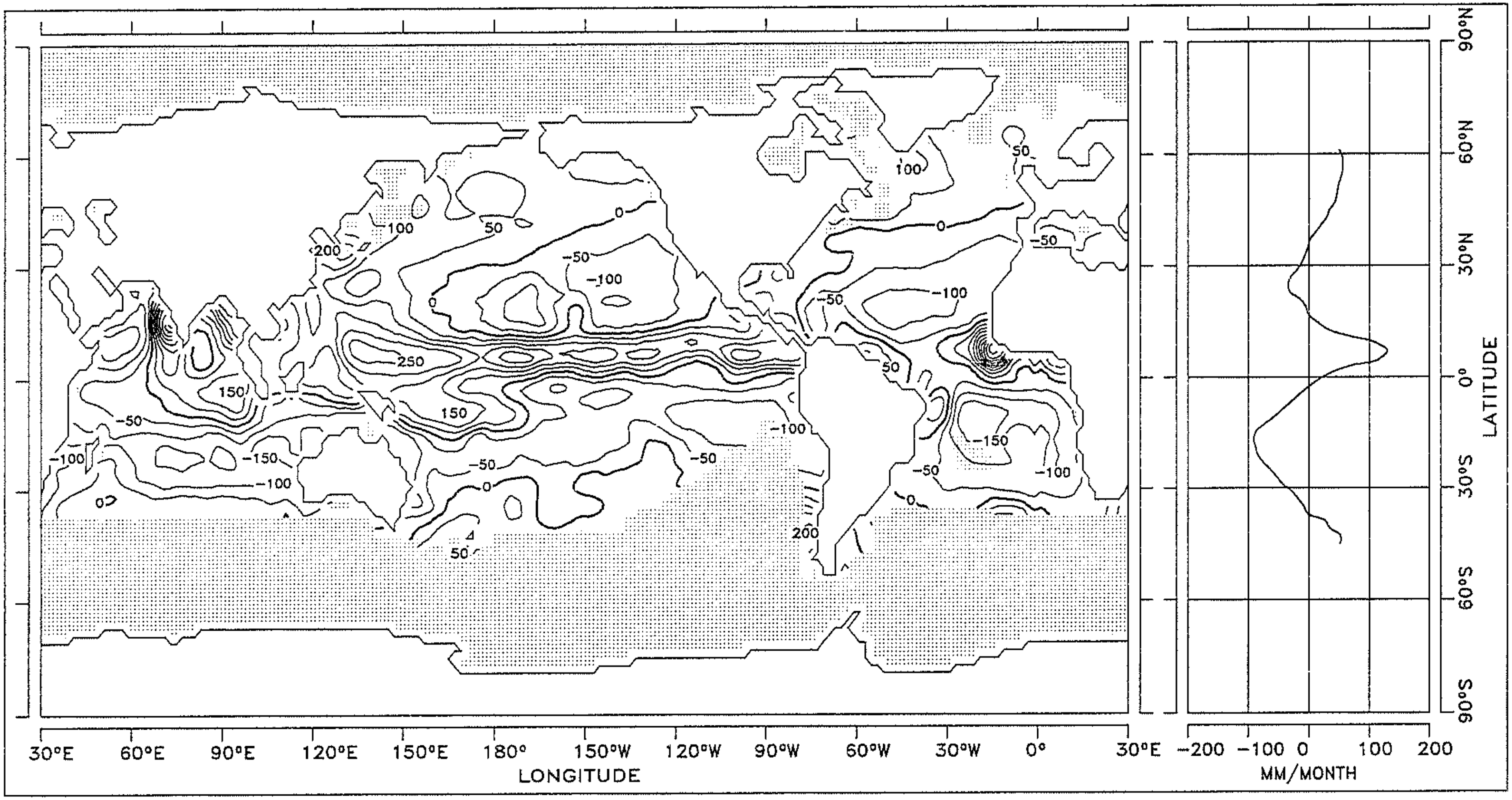

CONTOUR INTERVAL: 50 MM/MONTH REFERENCE LINE : 0 MM/MONTH

FIG. 14.8 NET DOWNWARD FRESH WATER FLUX AUGUST

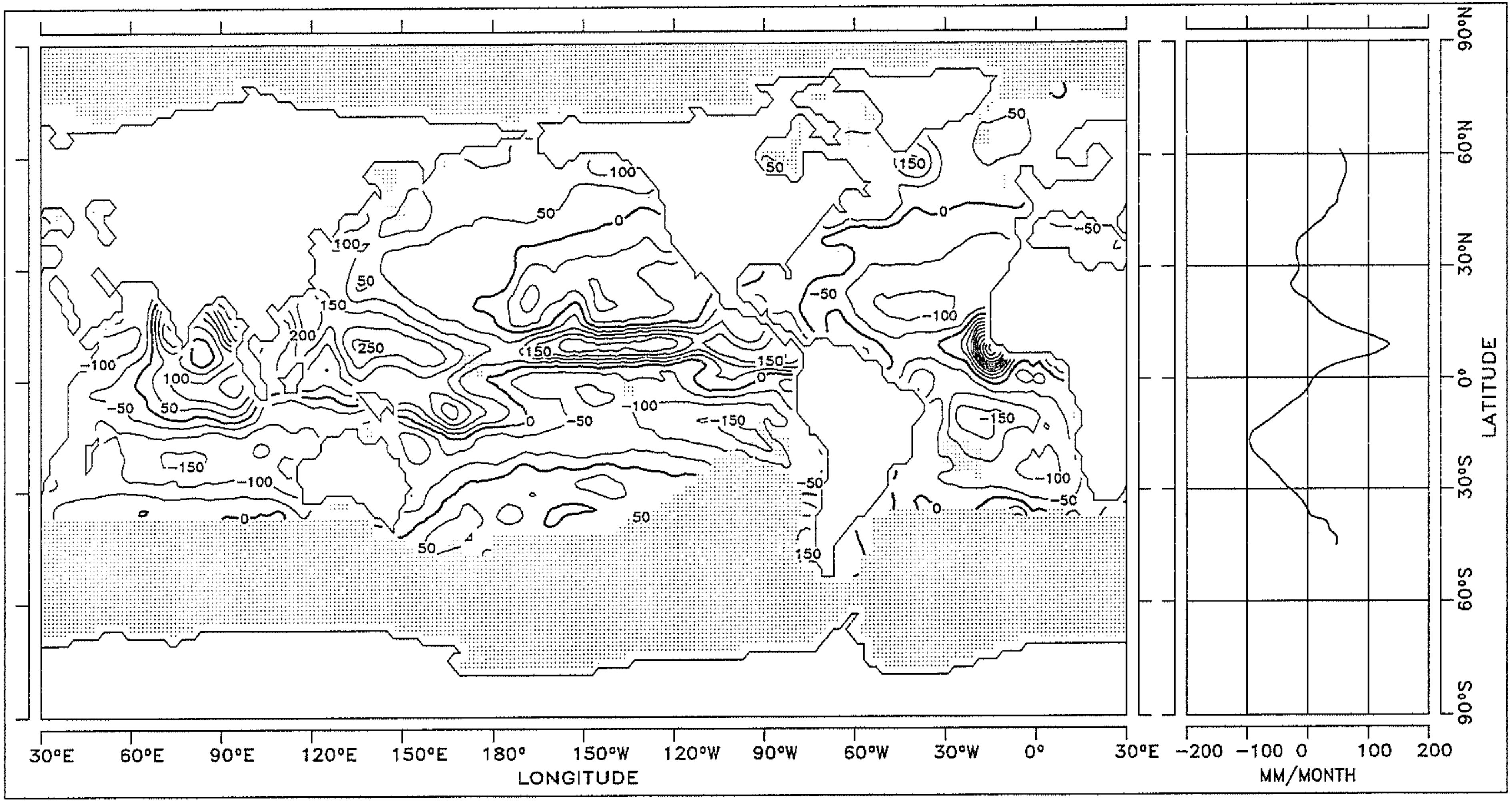

CONTOUR INTERVAL: 50 MM/MONTH REFERENCE LINE : 0 MM/MONTH

FIG. 14.9 NET DOWNWARD FRESH WATER FLUX SEPTEMBER

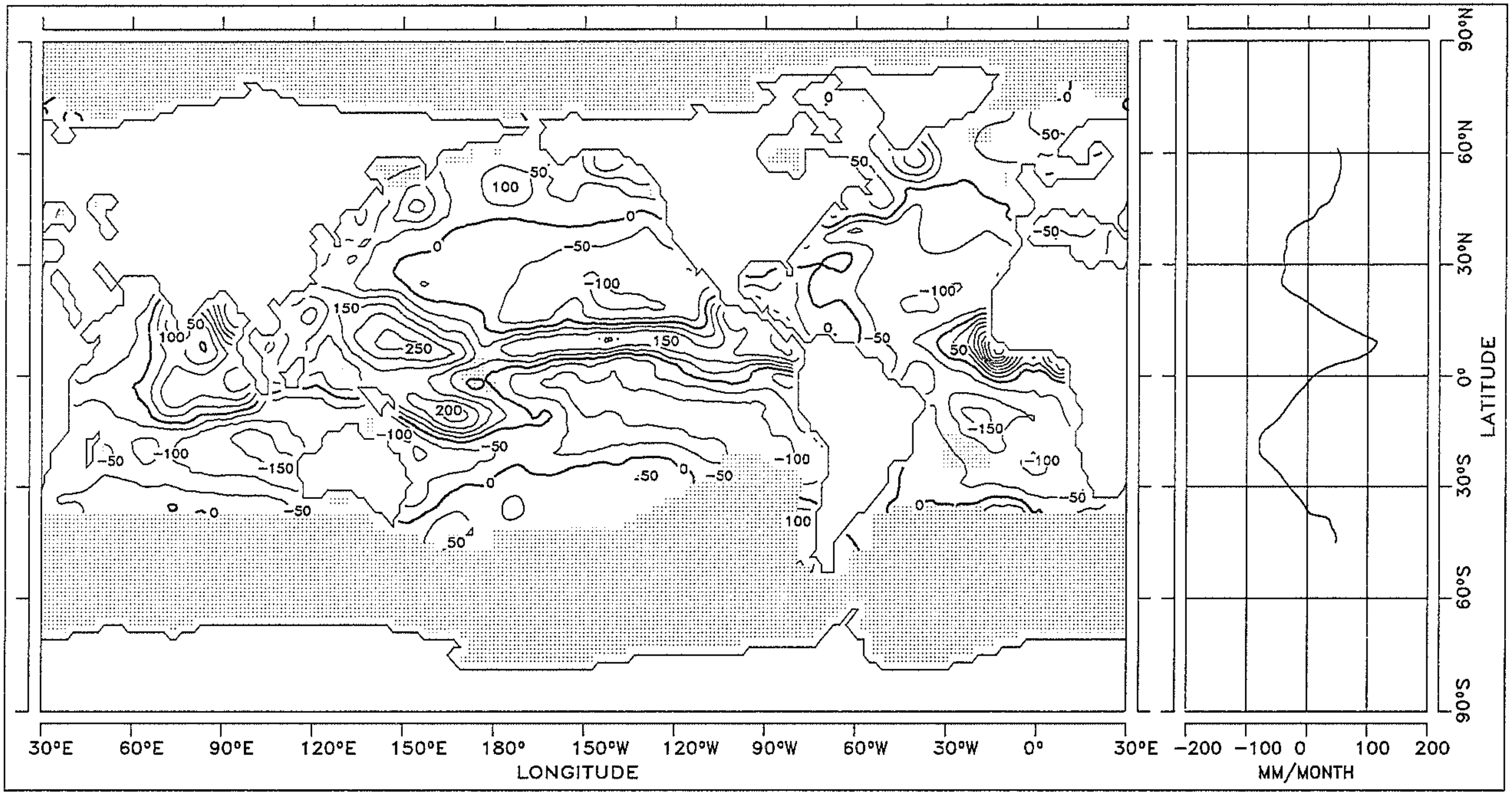

CONTOUR INTERVAL: 50 MM/MONTH REFERENCE LINE : 0 MM/MONTH

FIG. 14.10 NET DOWNWARD FRESH WATER FLUX OCTOBER

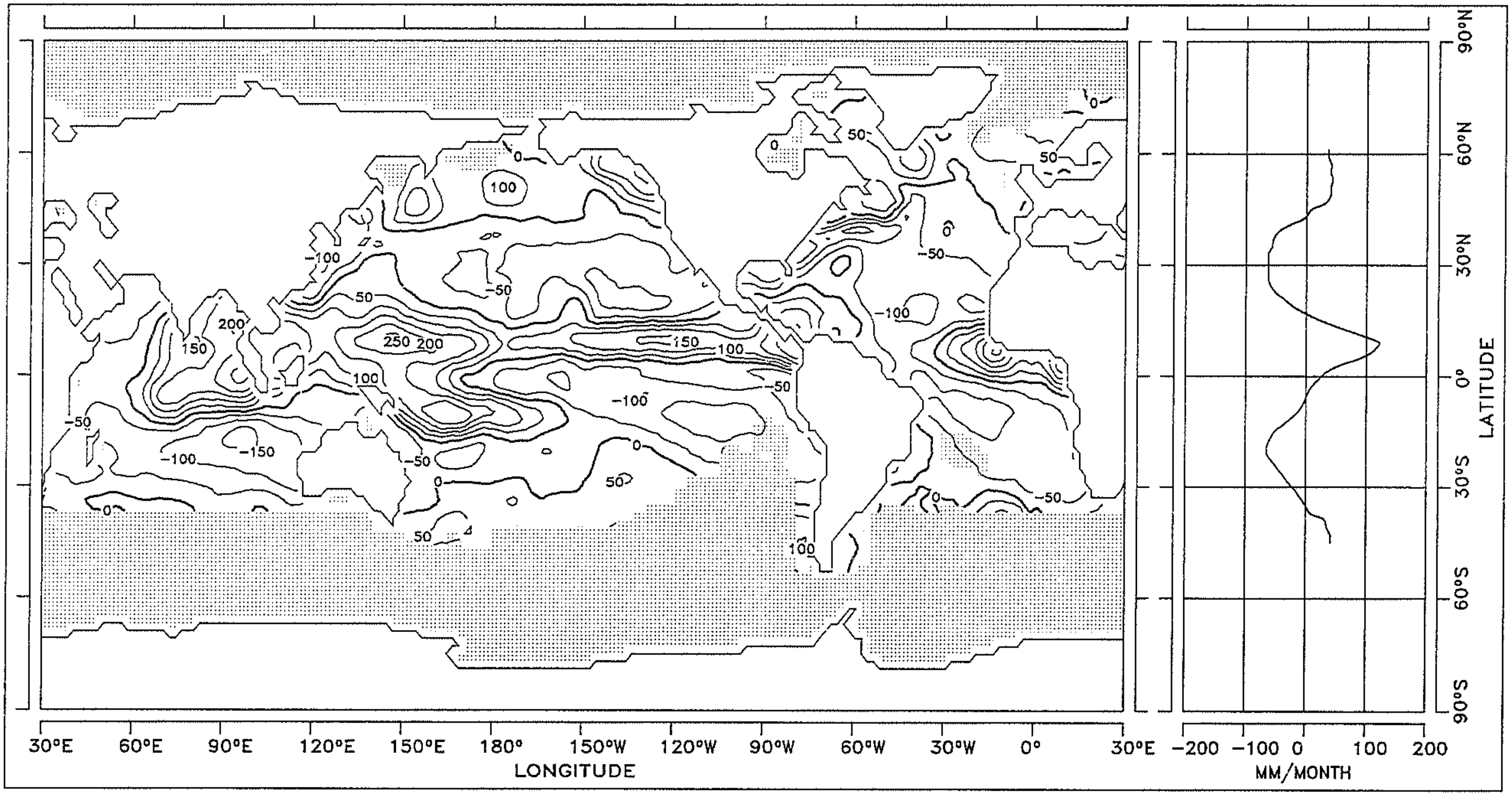

CONTOUR INTERVAL: 50 MM/MONTH REFERENCE LINE : 0 MM/MONTH

FIG. 14.11 NET DOWNWARD FRESH WATER FLUX NOVEMBER

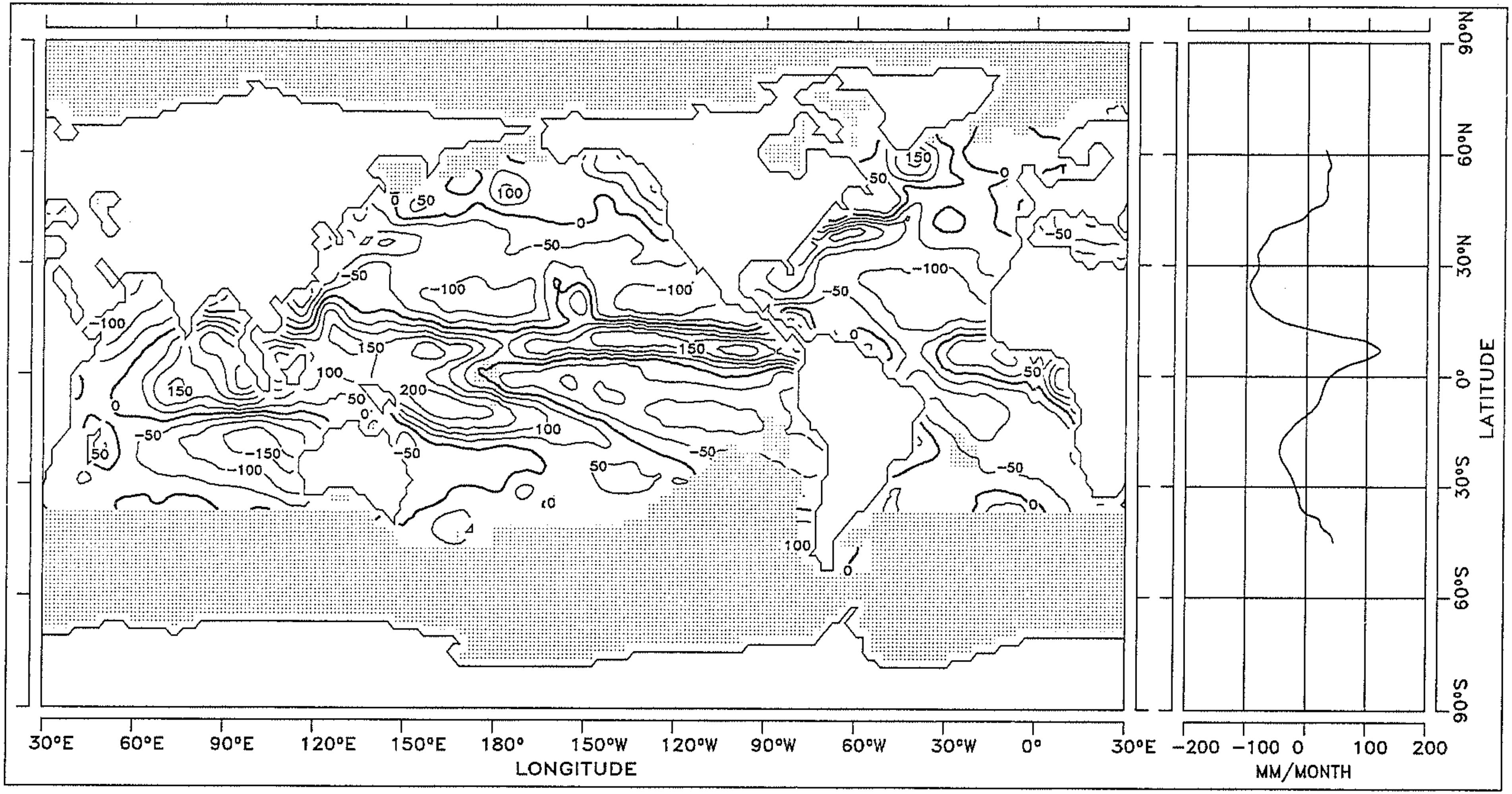

CONTOUR INTERVAL: 50 MM/MONTH REFERENCE LINE : 0 MM/MONTH

FIG. 14.12 NET DOWNWARD FRESH WATER FLUX DECEMBER

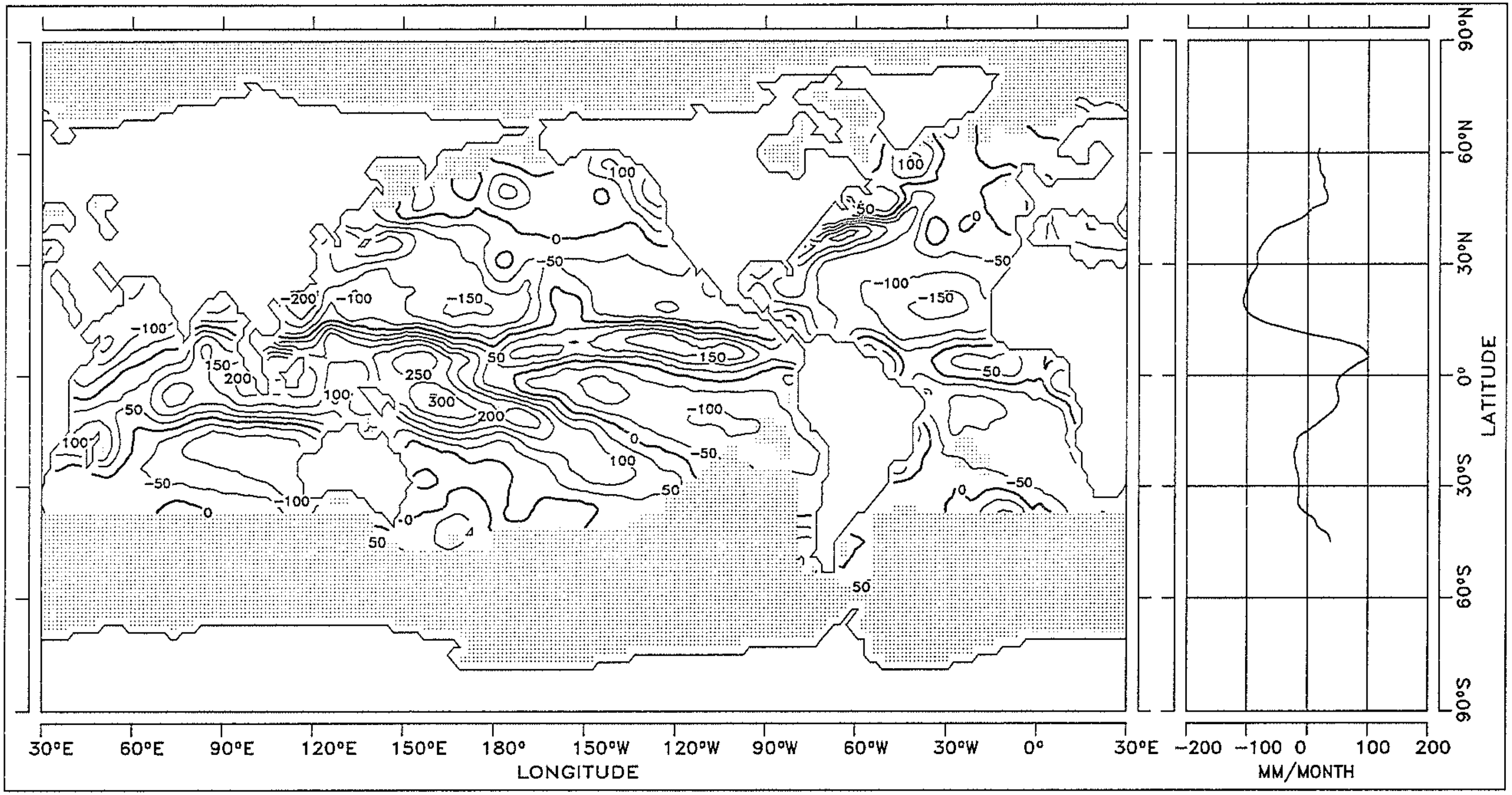

CONTOUR INTERVAL: 50 MM/MONTH REFERENCE LINE : 0 MM/MONTH

FIG. 14.13 NET DOWNWARD FRESH WATER FLUX ANNUAL MEAN

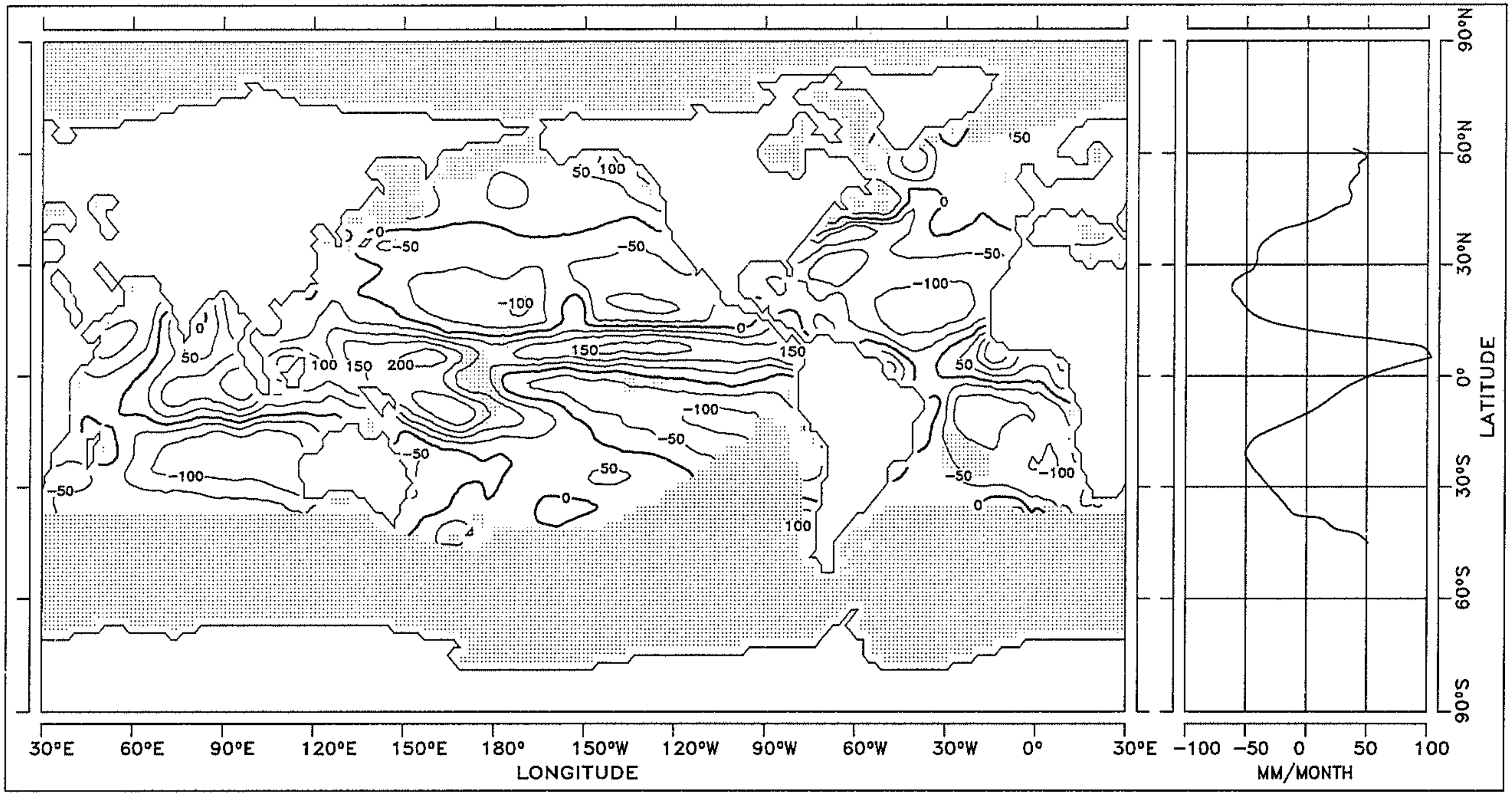

CONTOUR INTERVAL: 50 MM/MONTH REFERENCE LINE : 0 MM/MONTH

BUOYANCY FLUX

FIG. 15.1 BUOYANCY FLUX JANUARY

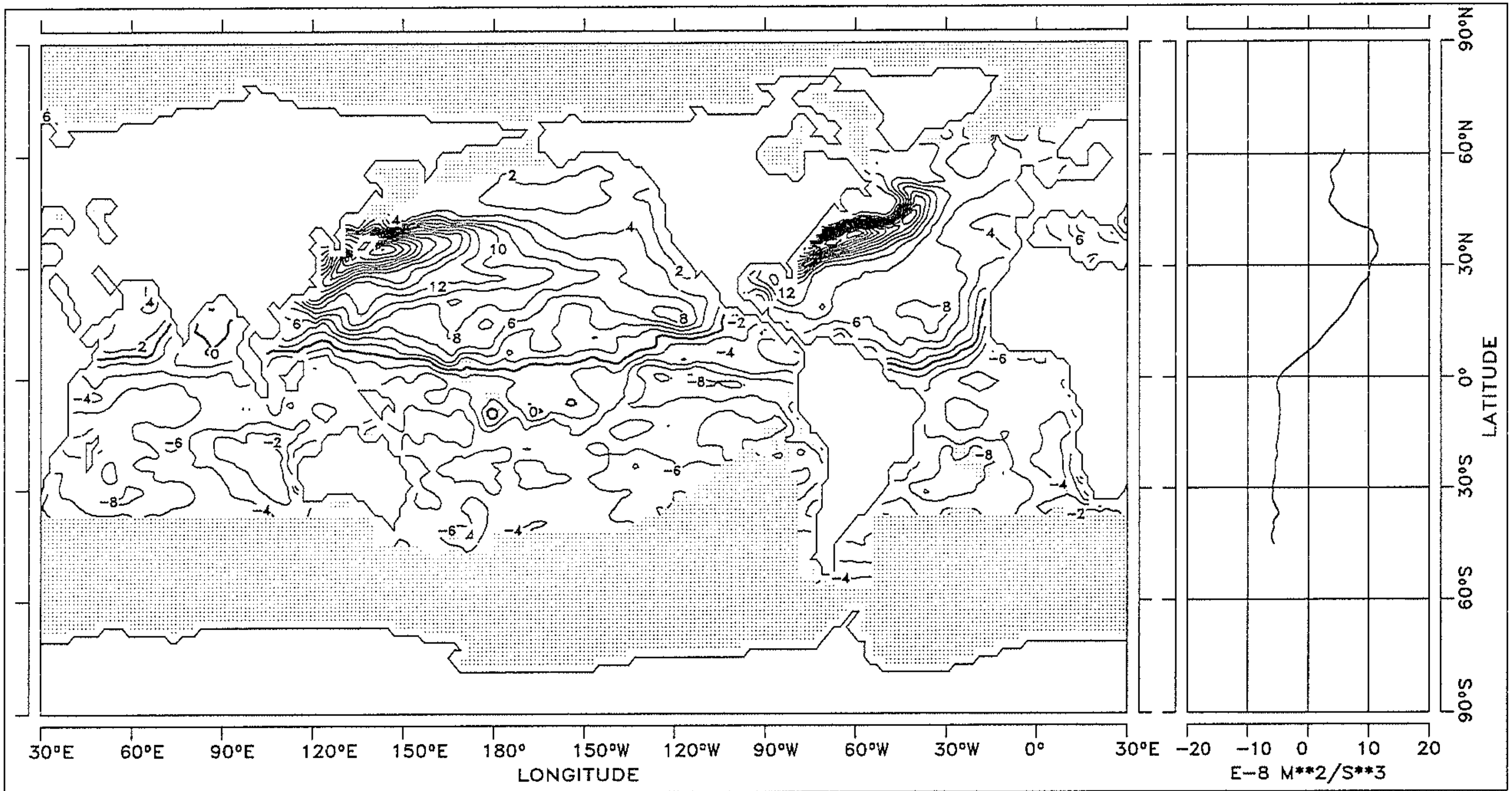

CONTOUR INTERVAL: 2.E-8 M**2/S**3 REFERENCE LINE : 0 M**2/S**3

FIG. 15.2 BUOYANCY FLUX

FEBRUARY

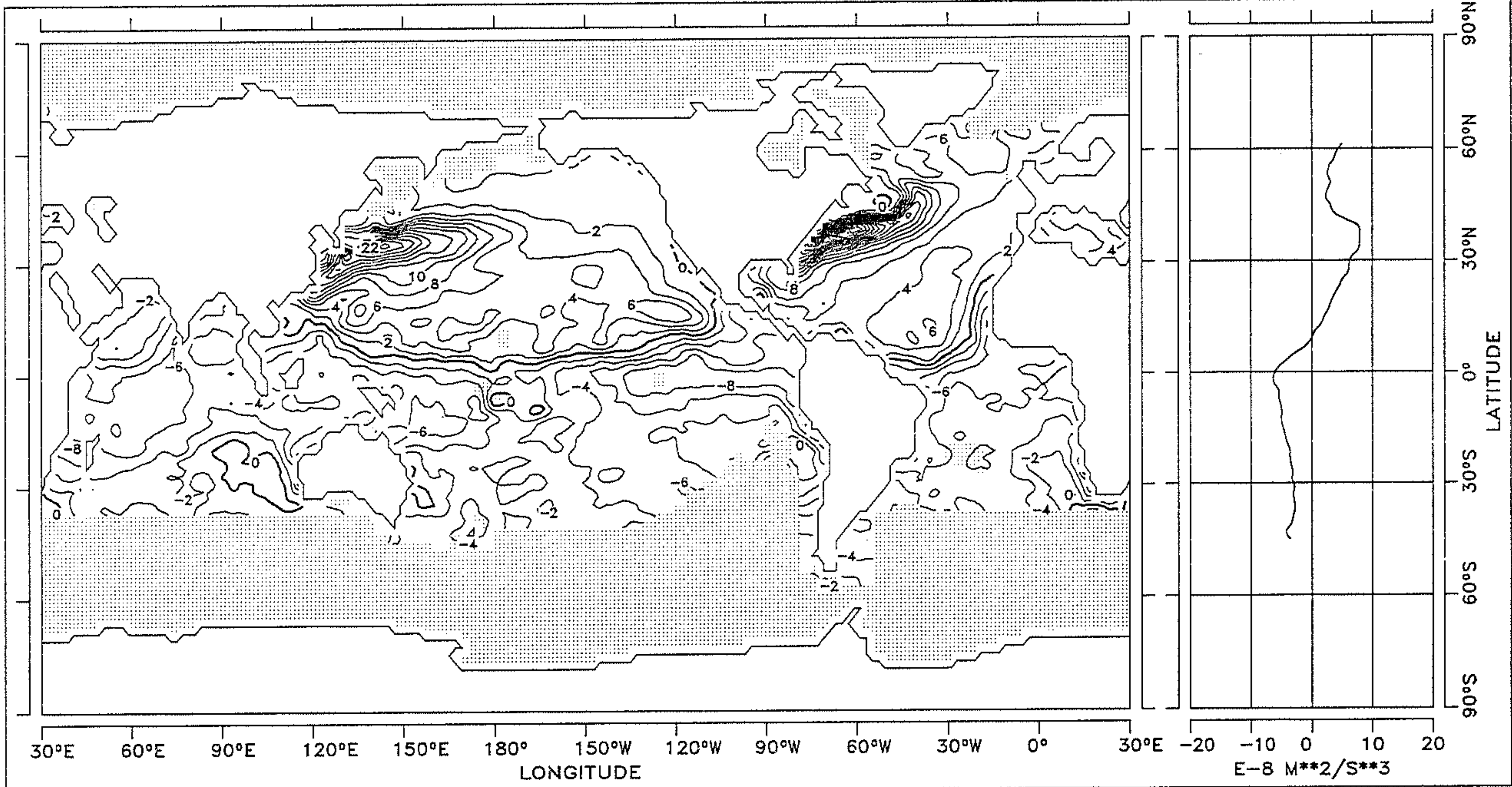

CONTOUR INTERVAL: 2.E-8 M**2/S**3 REFERENCE LINE : 0 M**2/S**3

FIG. 15.3 BUOYANCY FLUX MARCH

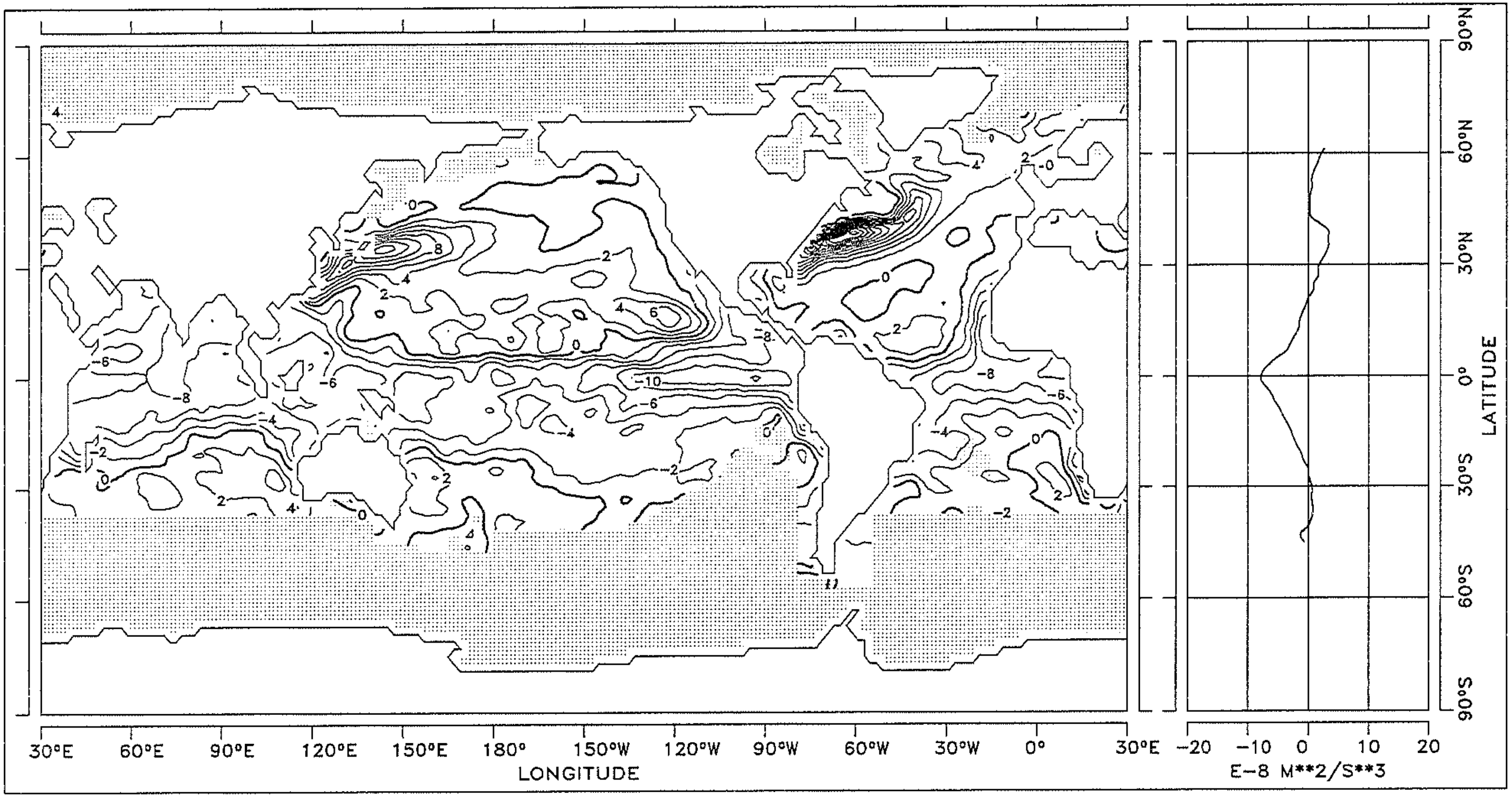

CONTOUR INTERVAL: 2.E-8 M**2/S**3 REFERENCE LINE : 0 M**2/S**3

FIG. 15.4 BUOYANCY FLUX APRIL

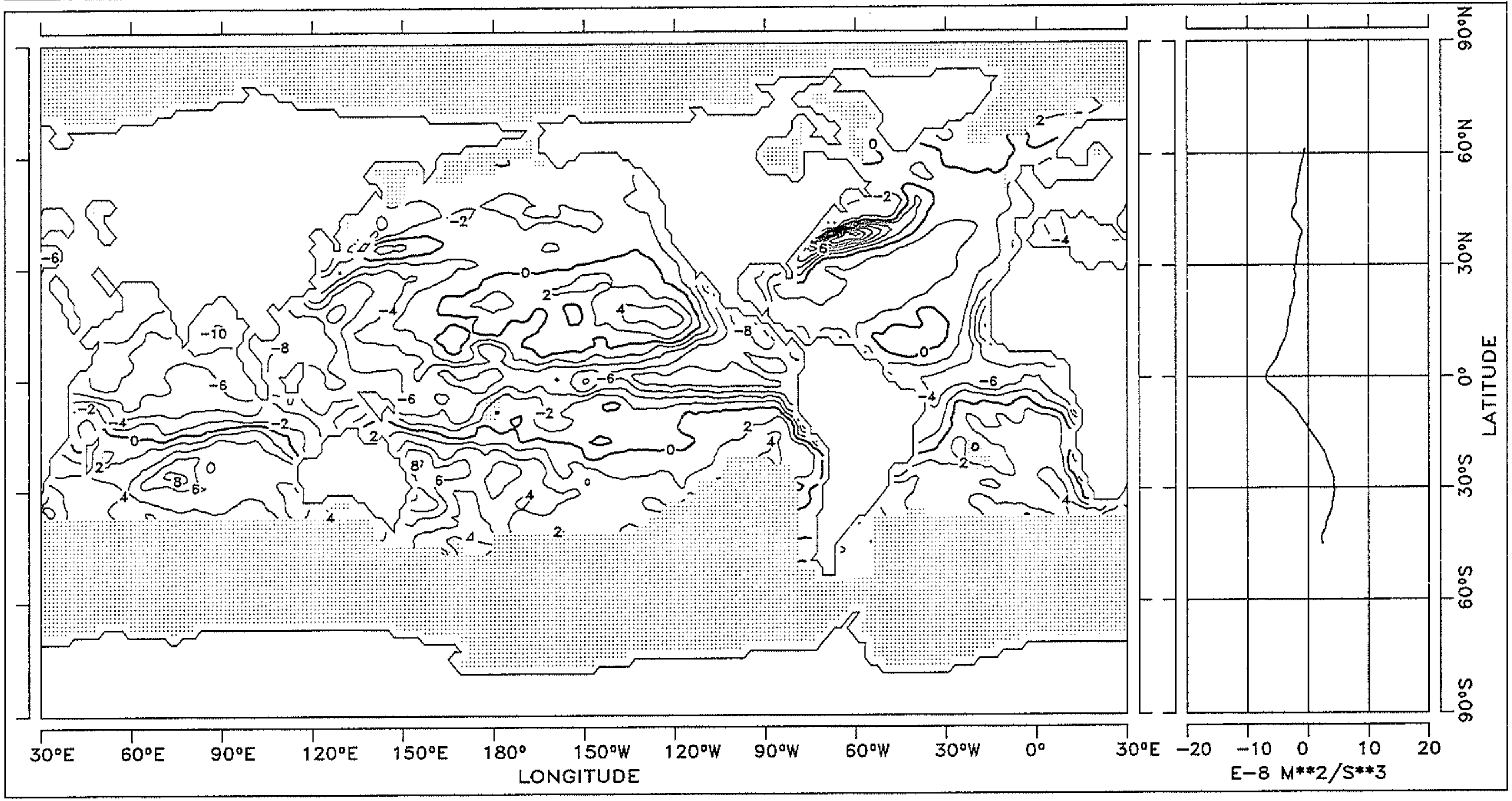

CONTOUR INTERVAL: 2.E-8 M**2/S**3 REFERENCE LINE : 0 M**2/S**3

FIG. 15.5 BUOYANCY FLUX MAY

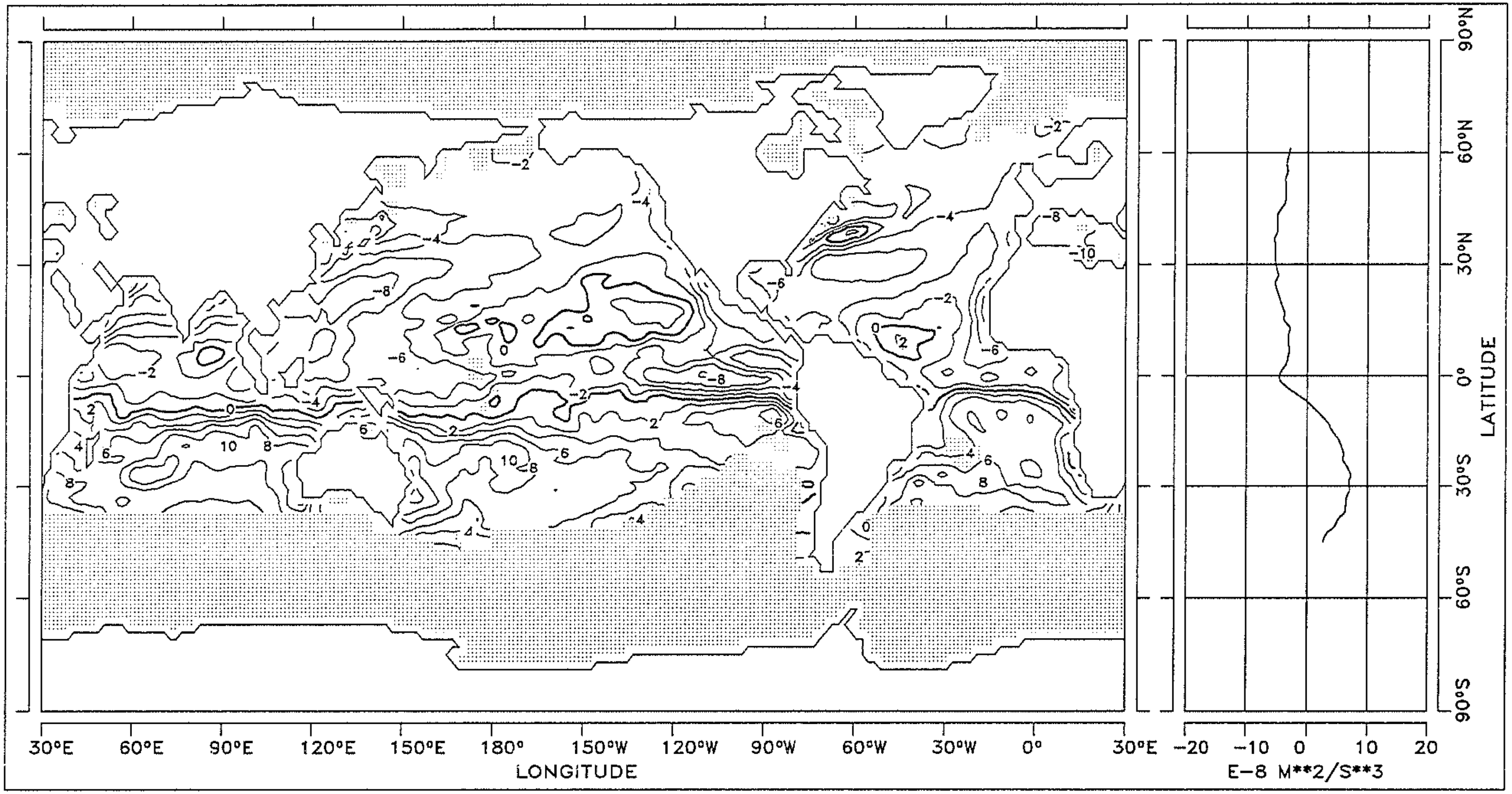

CONTOUR INTERVAL: 2.E-8 M**2/S**3 REFERENCE LINE : 0 M**2/S**3

FIG. 15.6 BUOYANCY FLUX JUNE

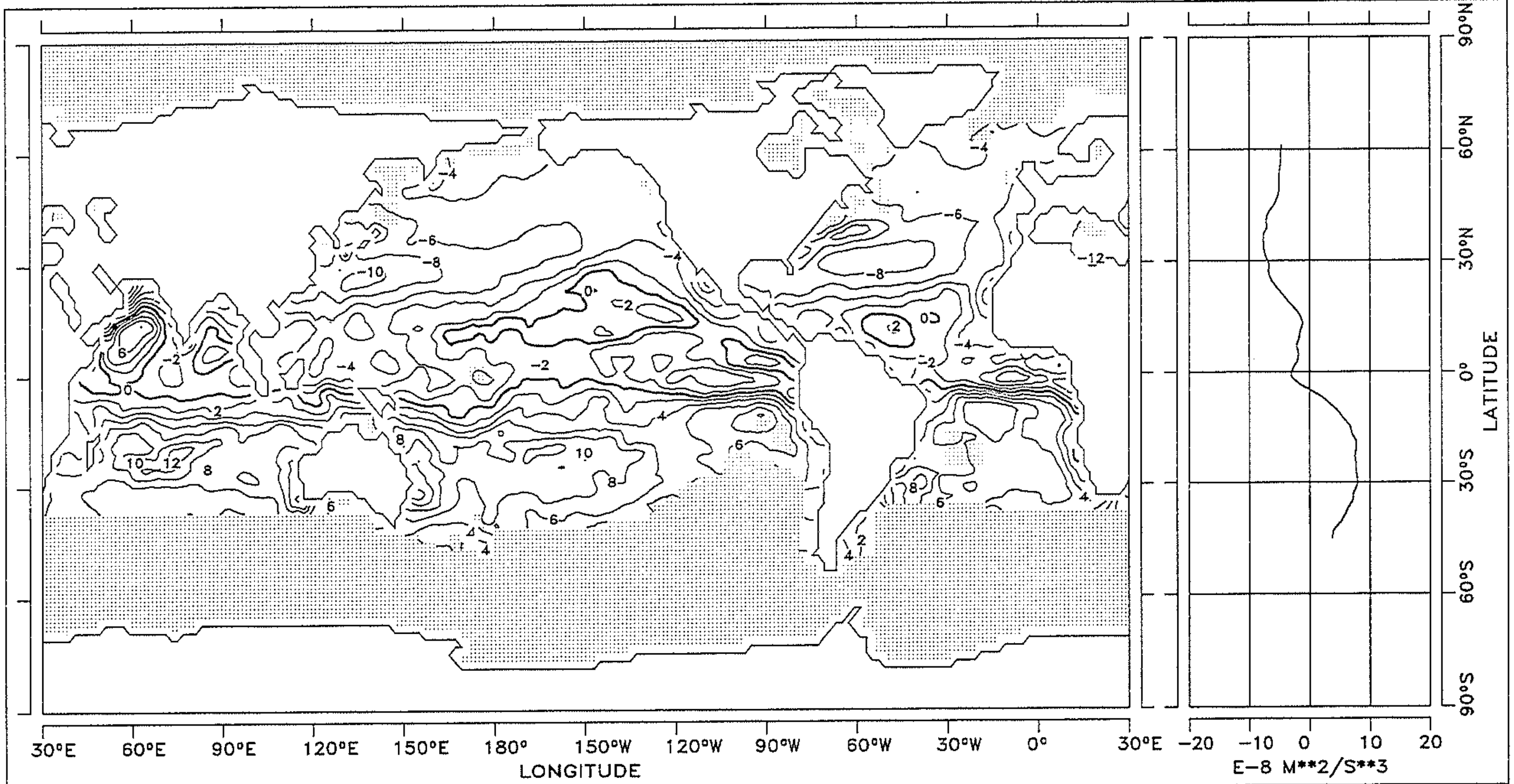

CONTOUR INTERVAL: 2.E-8 M**2/S**3 REFERENCE LINE : 0 M**2/S**3

FIG. 15.7 BUOYANCY FLUX JULY

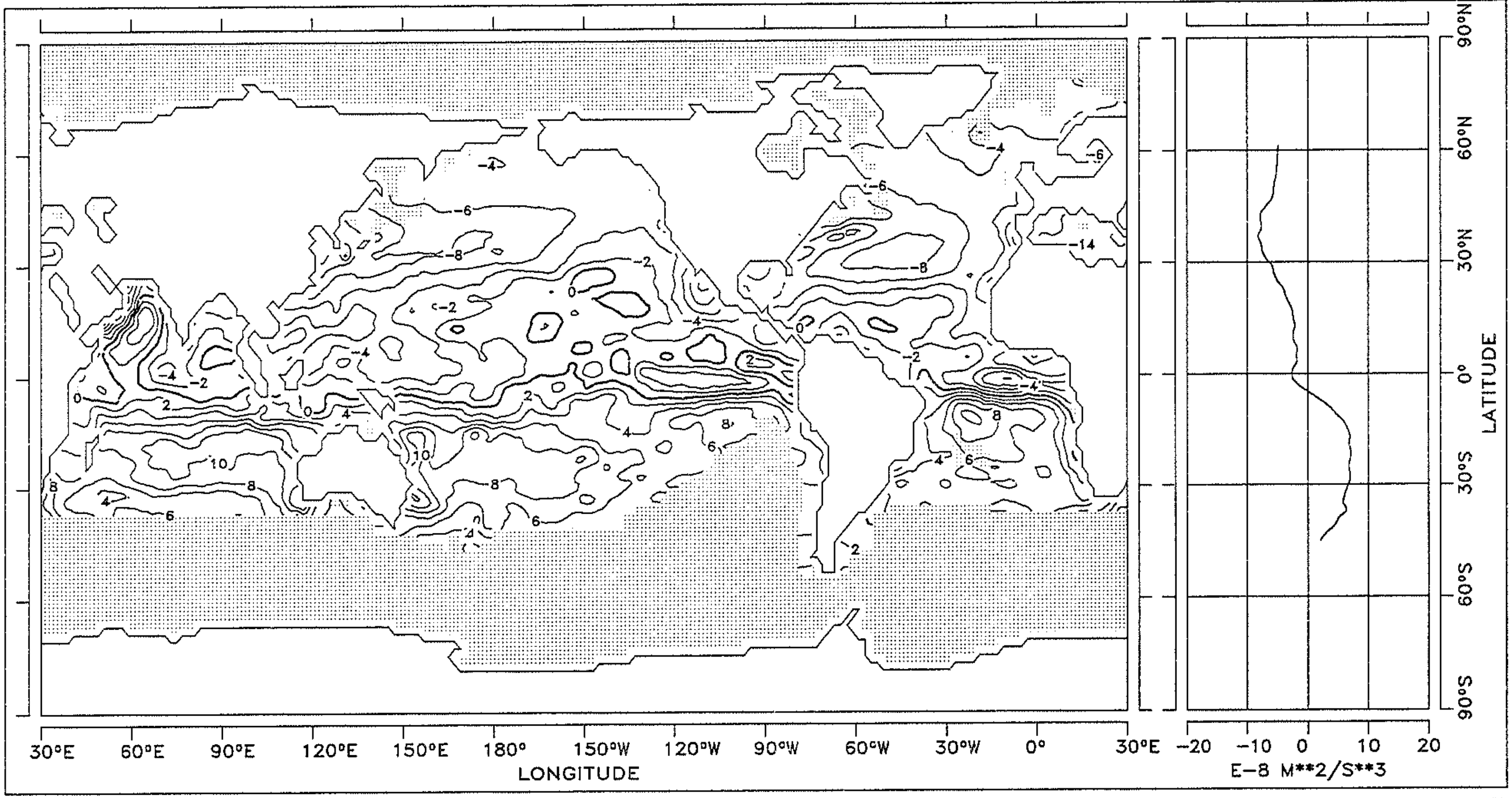

CONTOUR INTERVAL: 2.E–8 M**2/S**3 REFERENCE LINE : 0 M**2/S**3

FIG. 15.8 BUOYANCY FLUX AUGUST

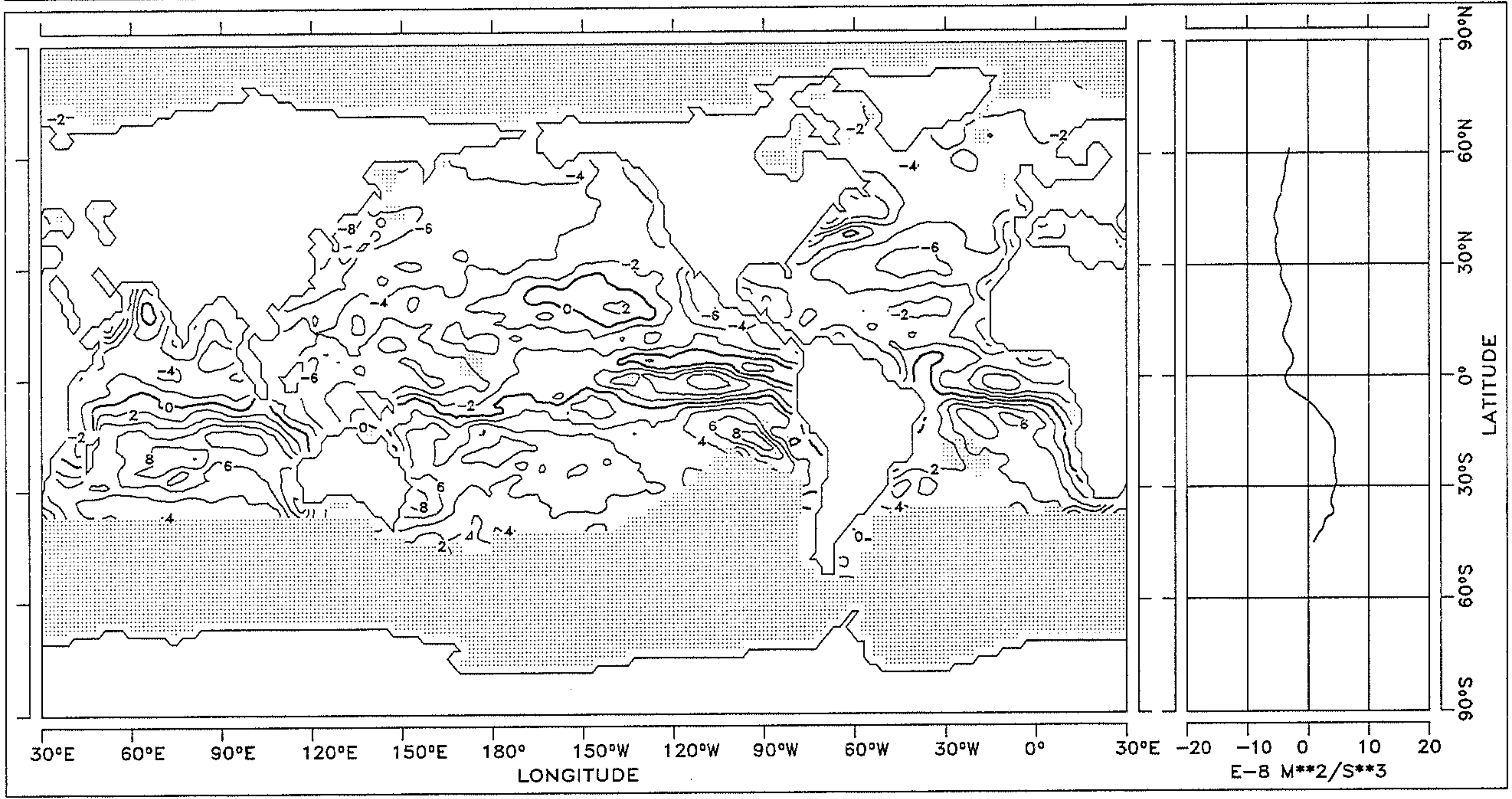

CONTOUR INTERVAL: 2.E-8 M**2/S**3 REFERENCE LINE : 0 M**2/S**3

FIG. 15.9 BUOYANCY FLUX SEPTEMBER

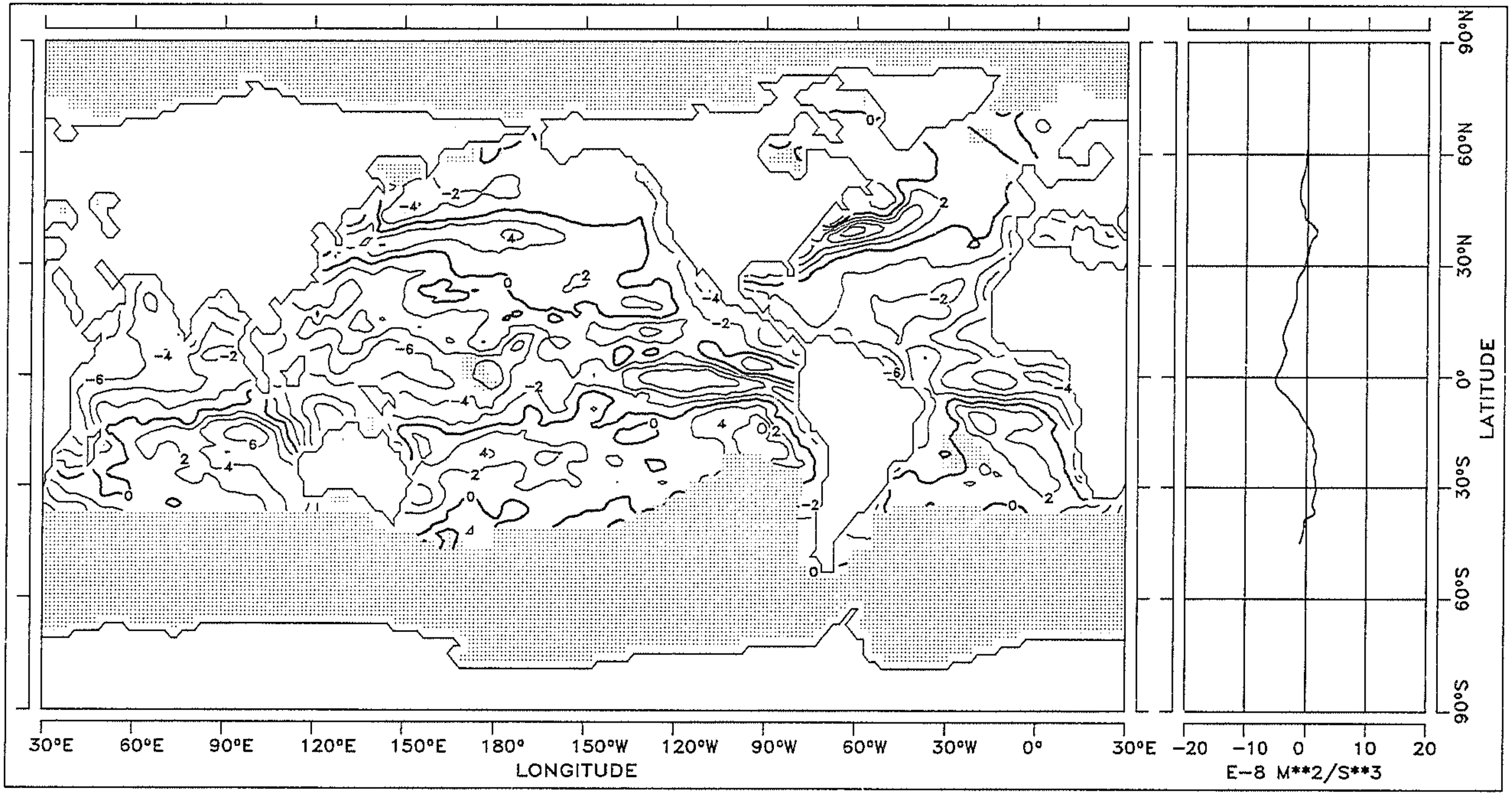

CONTOUR INTERVAL: 2.E-8 M**2/S**3 REFERENCE LINE : 0 M**2/S**3

FIG. 15.10 BUOYANCY FLUX OCTOBER

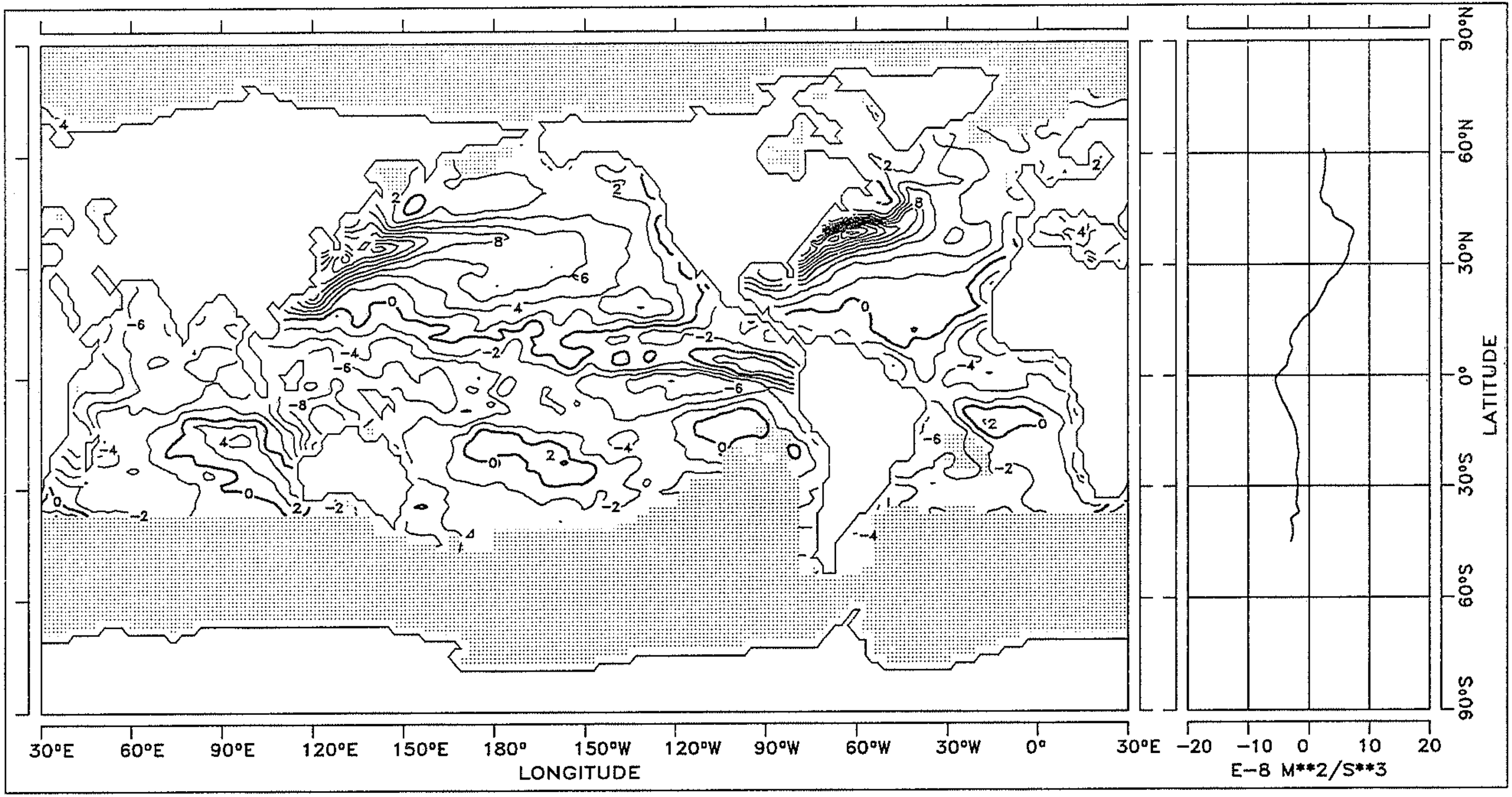

CONTOUR INTERVAL: 2.E-8 M**2/S**3 REFERENCE LINE : 0 M**2/S**3

FIG. 15.11 BUOYANCY FLUX NOVEMBER

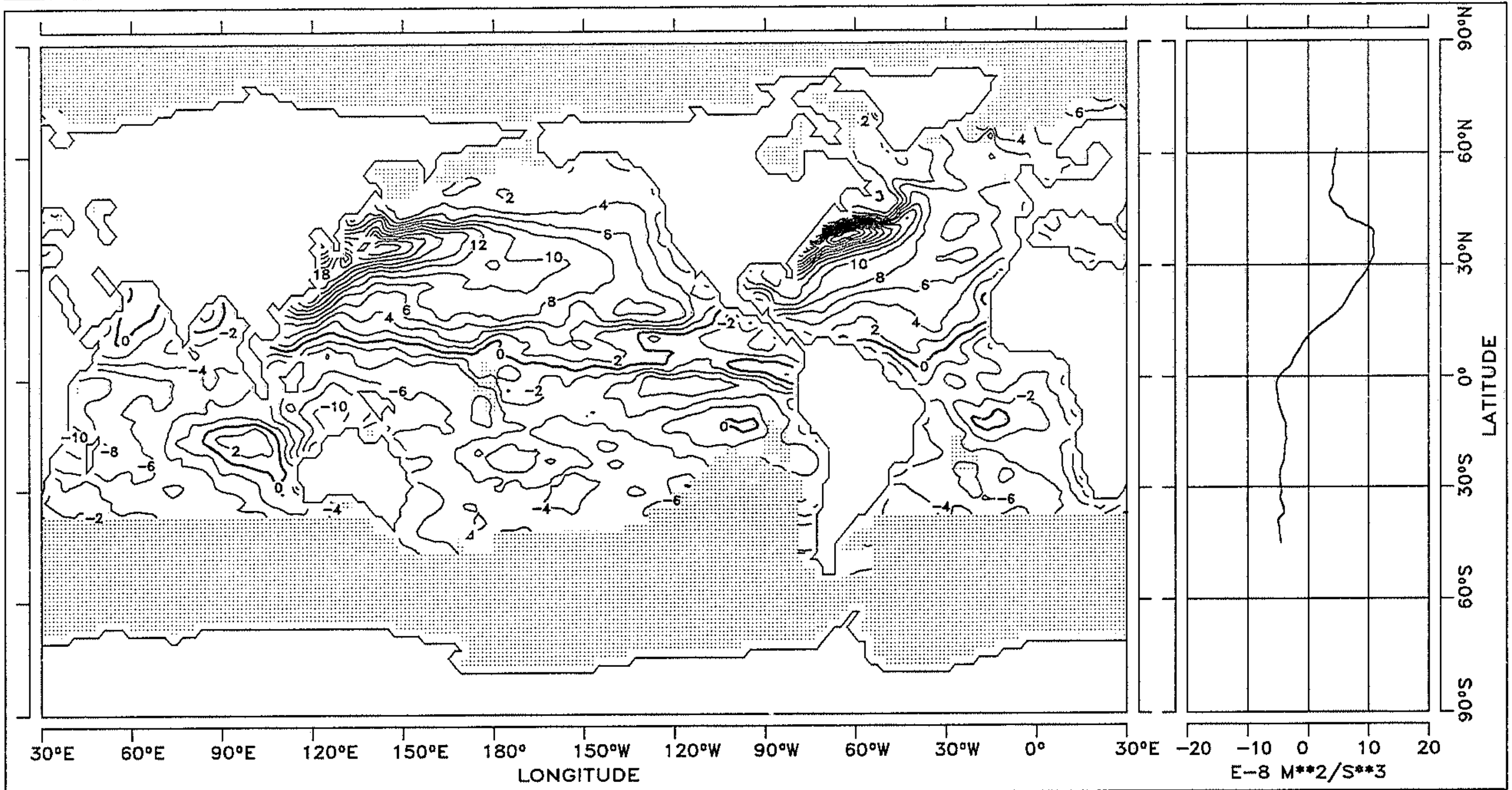

CONTOUR INTERVAL: 2.E−8 M**2/S**3 REFERENCE LINE : 0 M**2/S**3

FIG. 15.12 BUOYANCY FLUX DECEMBER

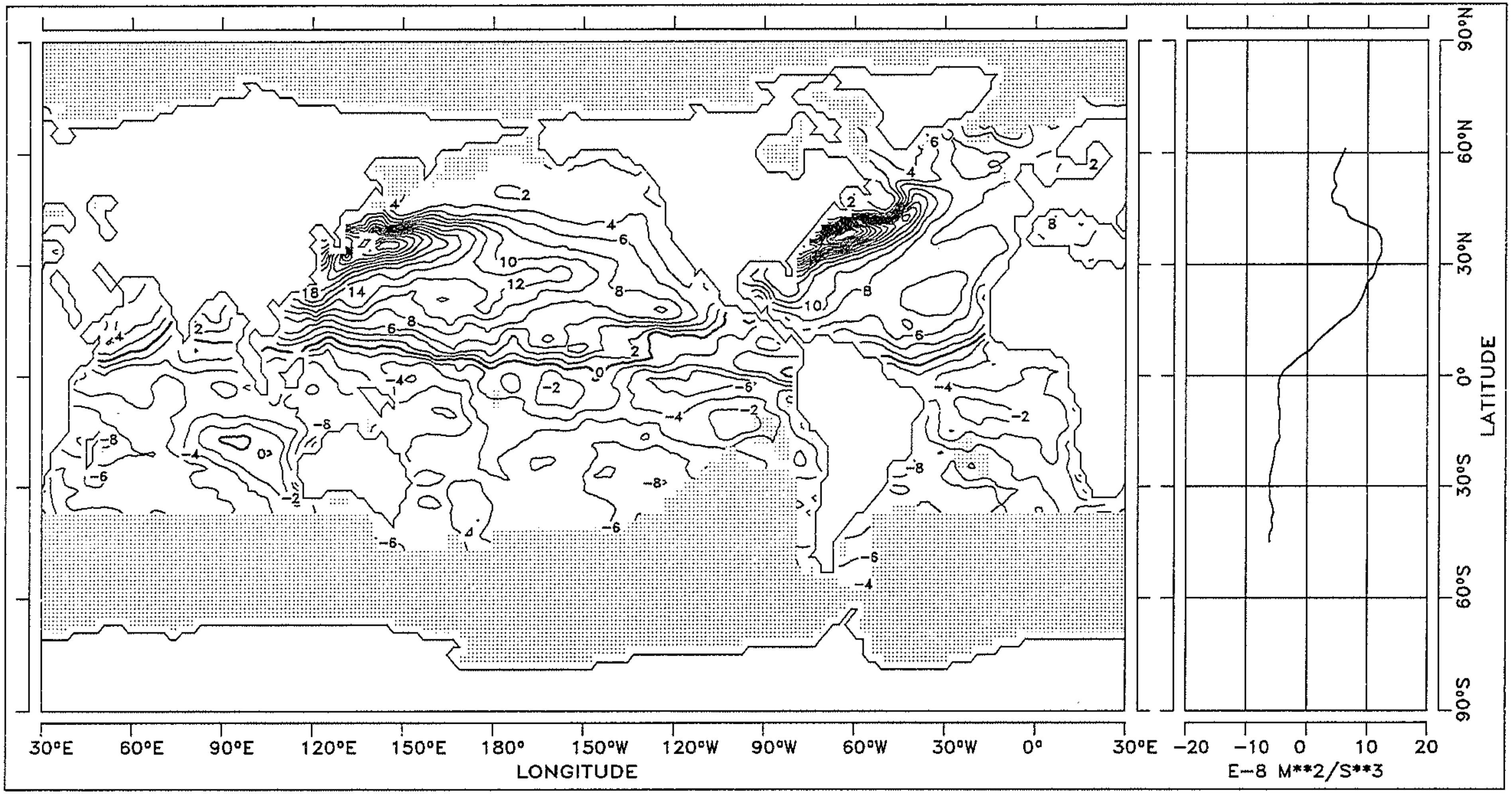

CONTOUR INTERVAL: 2.E−8 M**2/S**3 REFERENCE LINE : 0 M**2/S**3

FIG. 15.13 BUOYANCY FLUX ANNUAL MEAN

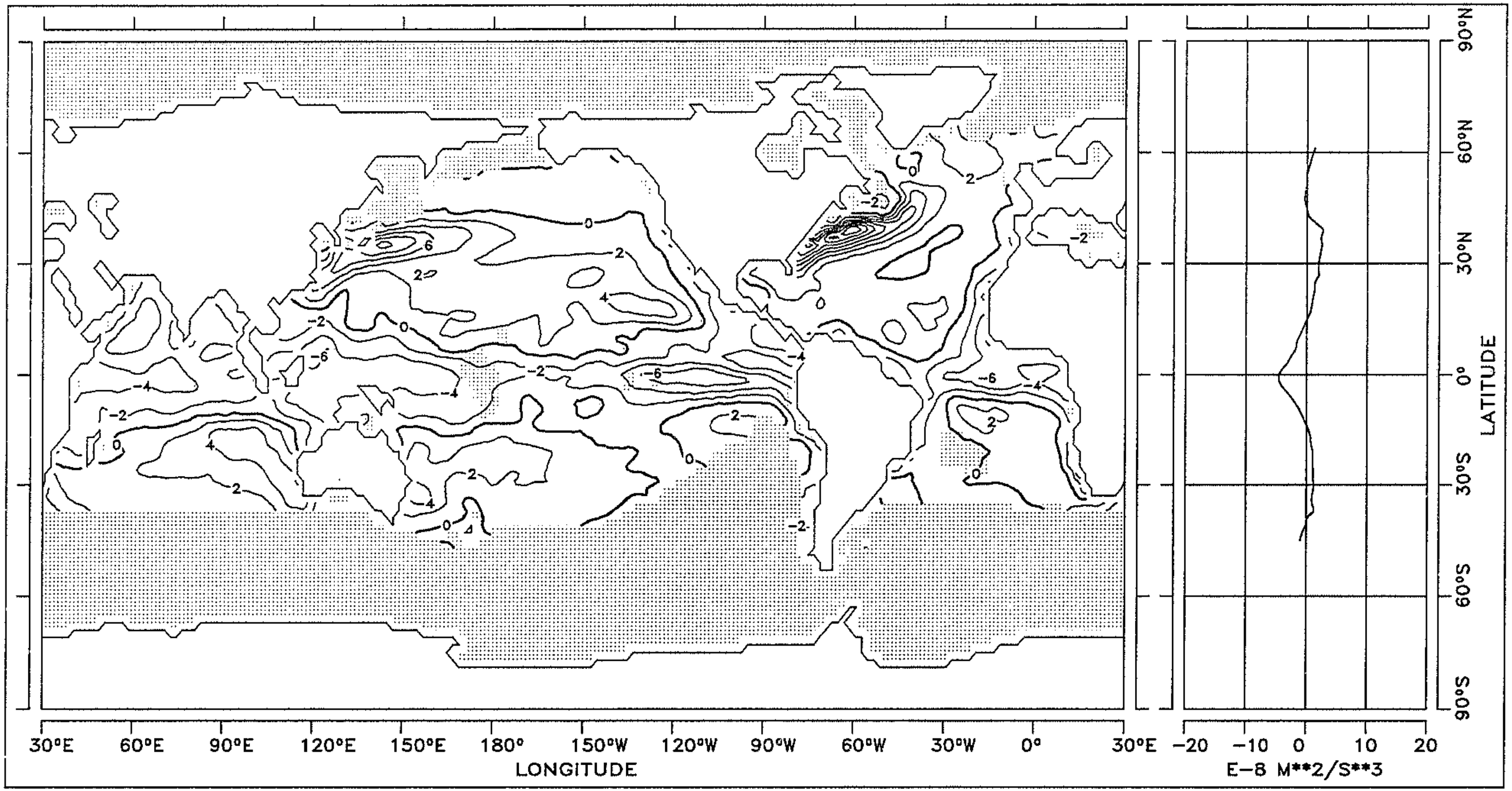

CONTOUR INTERVAL: 2.E-8 M**2/S**3 REFERENCE LINE : 0 M**2/S**3

FRICTION VELOCITY

FIG. 16.1 U_* JANUARY

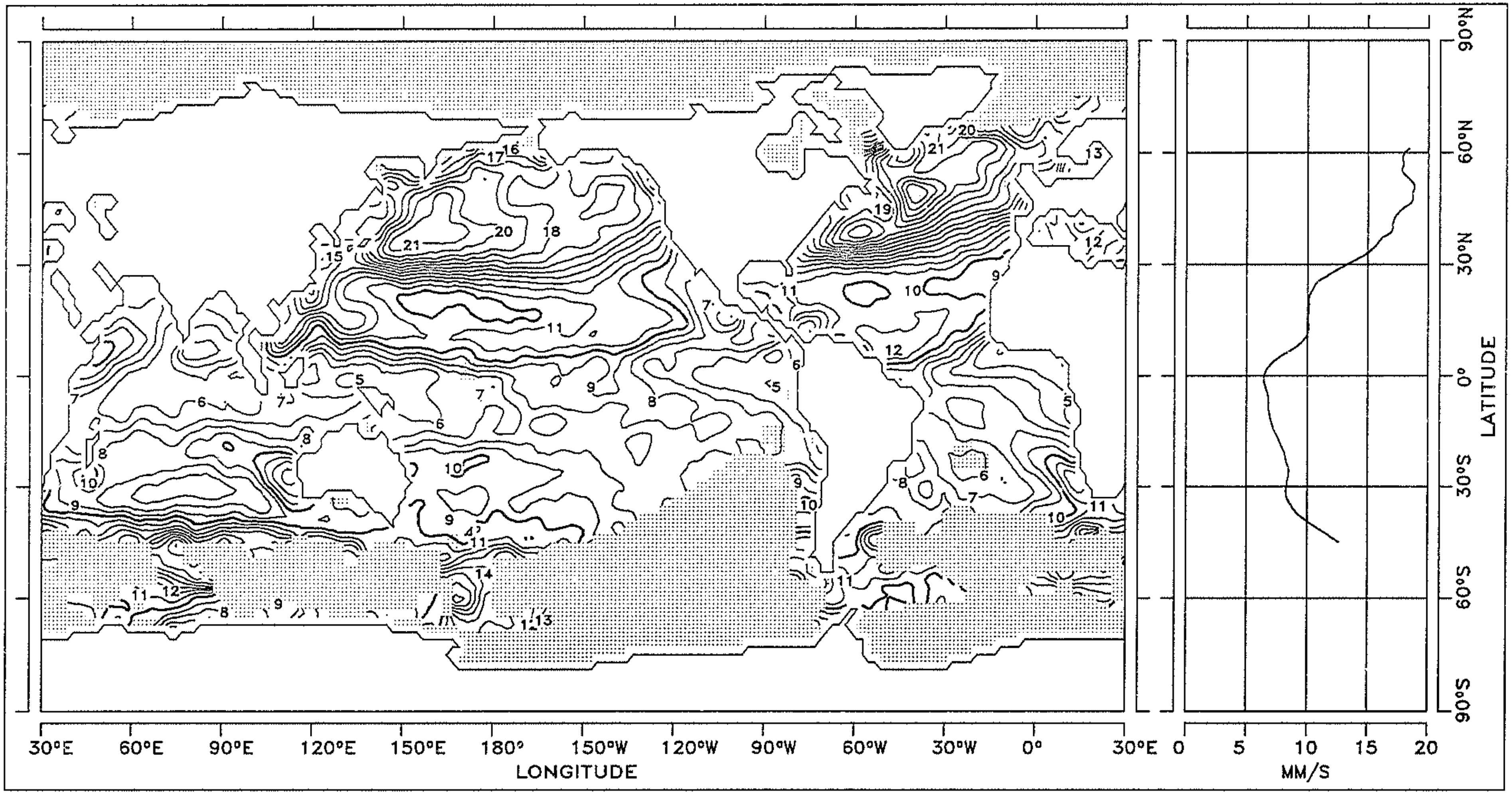

CONTOUR INTERVAL: 1 MM/S REFERENCE LINE : 10 MM/S

FIG. 16.2 U_* FEBRUARY

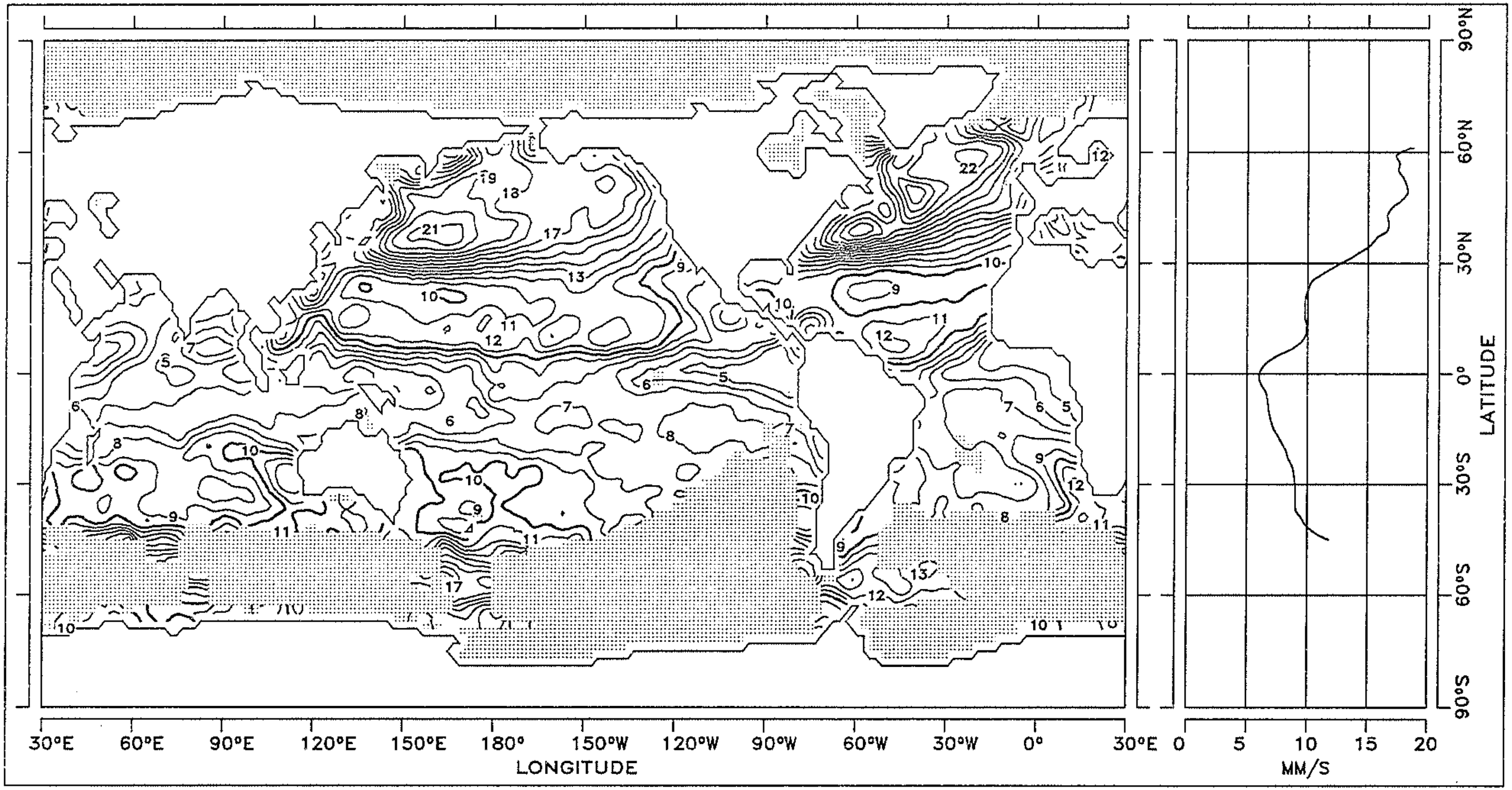

CONTOUR INTERVAL: 1 MM/S REFERENCE LINE : 10 MM/S

FIG. 16.3 U_* MARCH

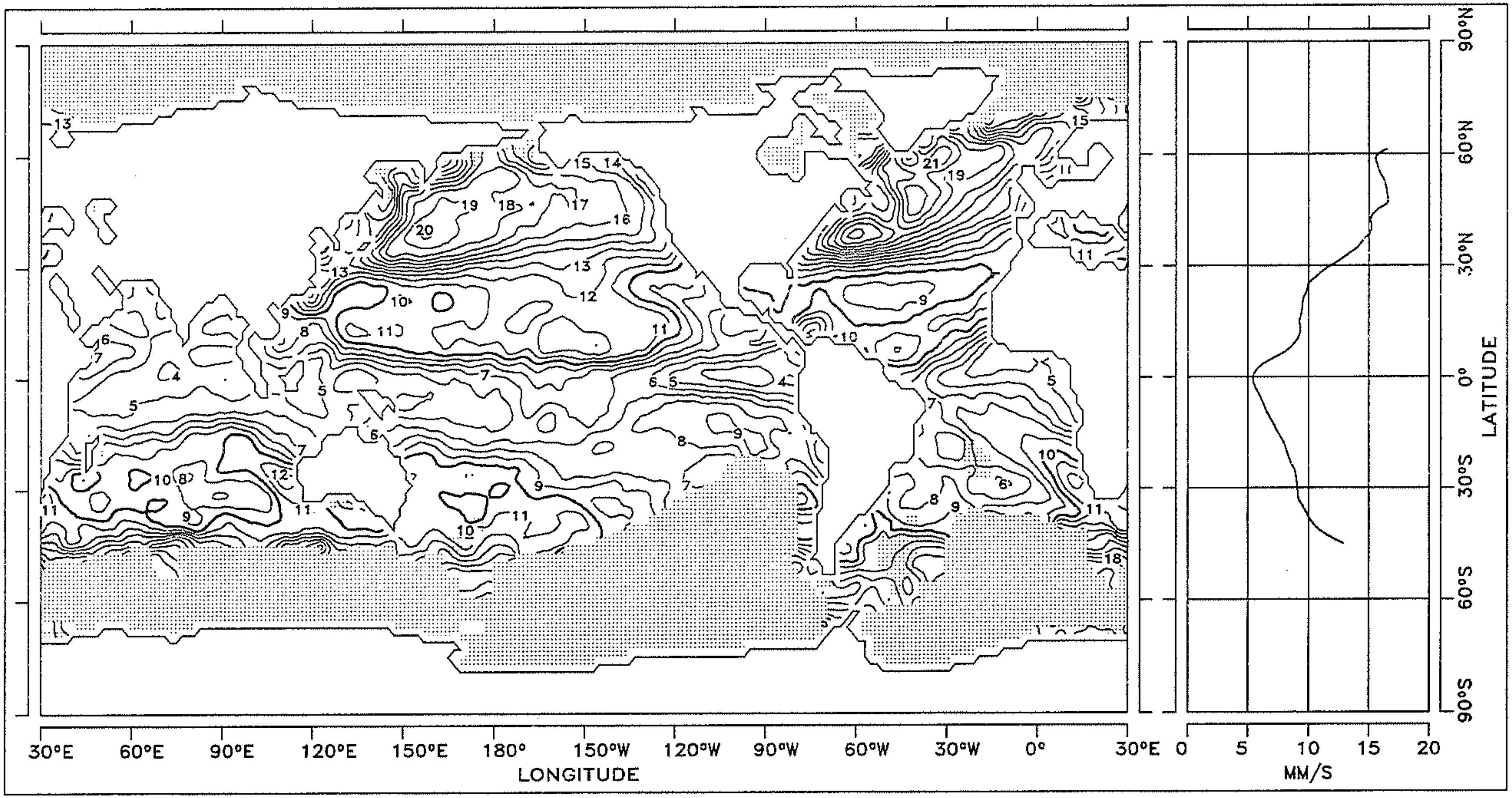

CONTOUR INTERVAL: 1 MM/S REFERENCE LINE : 10 MM/S

FIG. 16.4 U_* APRIL

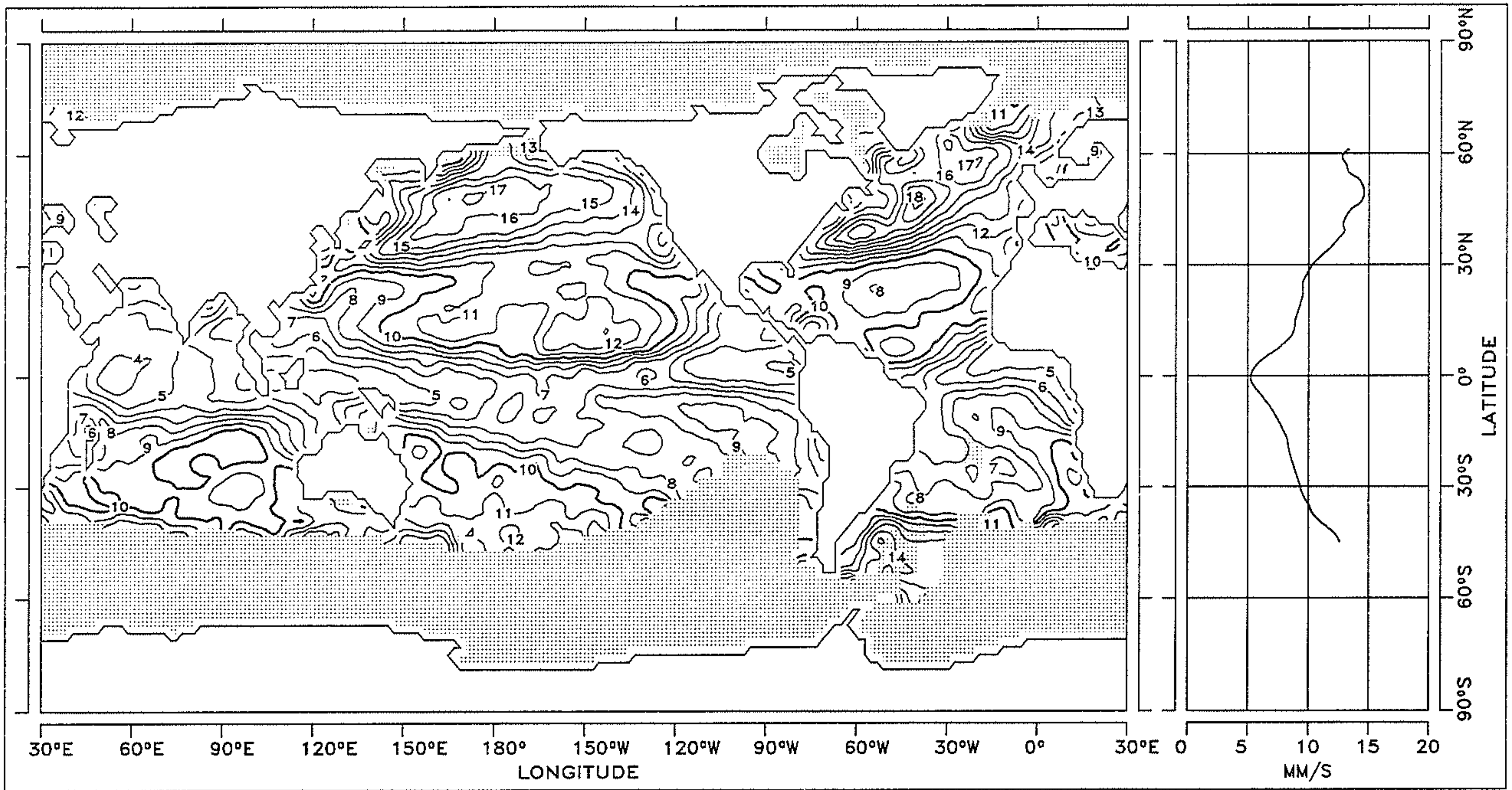

CONTOUR INTERVAL: 1 MM/S REFERENCE LINE : 10 MM/S

FIG. 16.5 U_* MAY

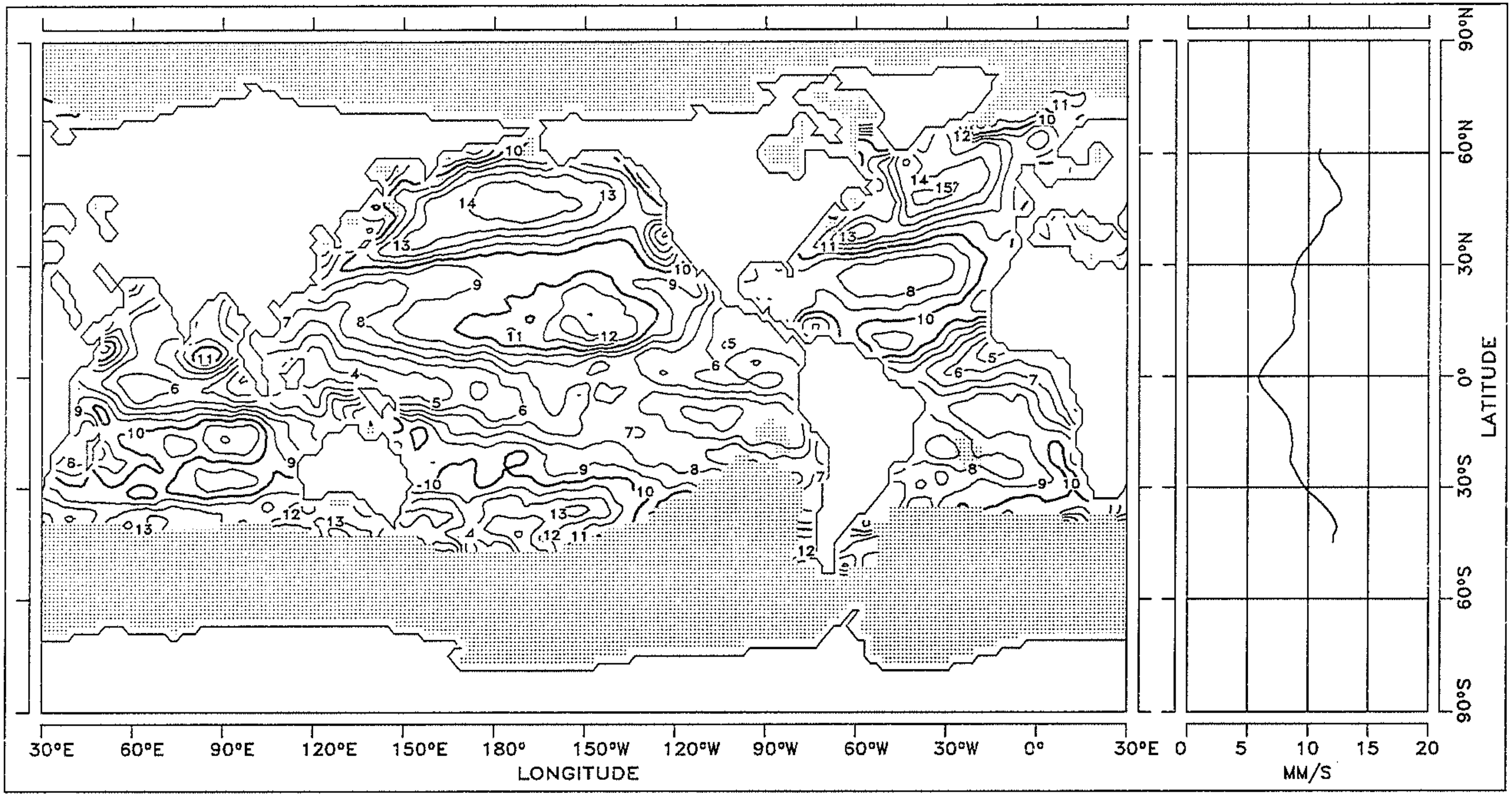

CONTOUR INTERVAL: 1 MM/S REFERENCE LINE : 10 MM/S

FIG. 16.6 U_* JUNE

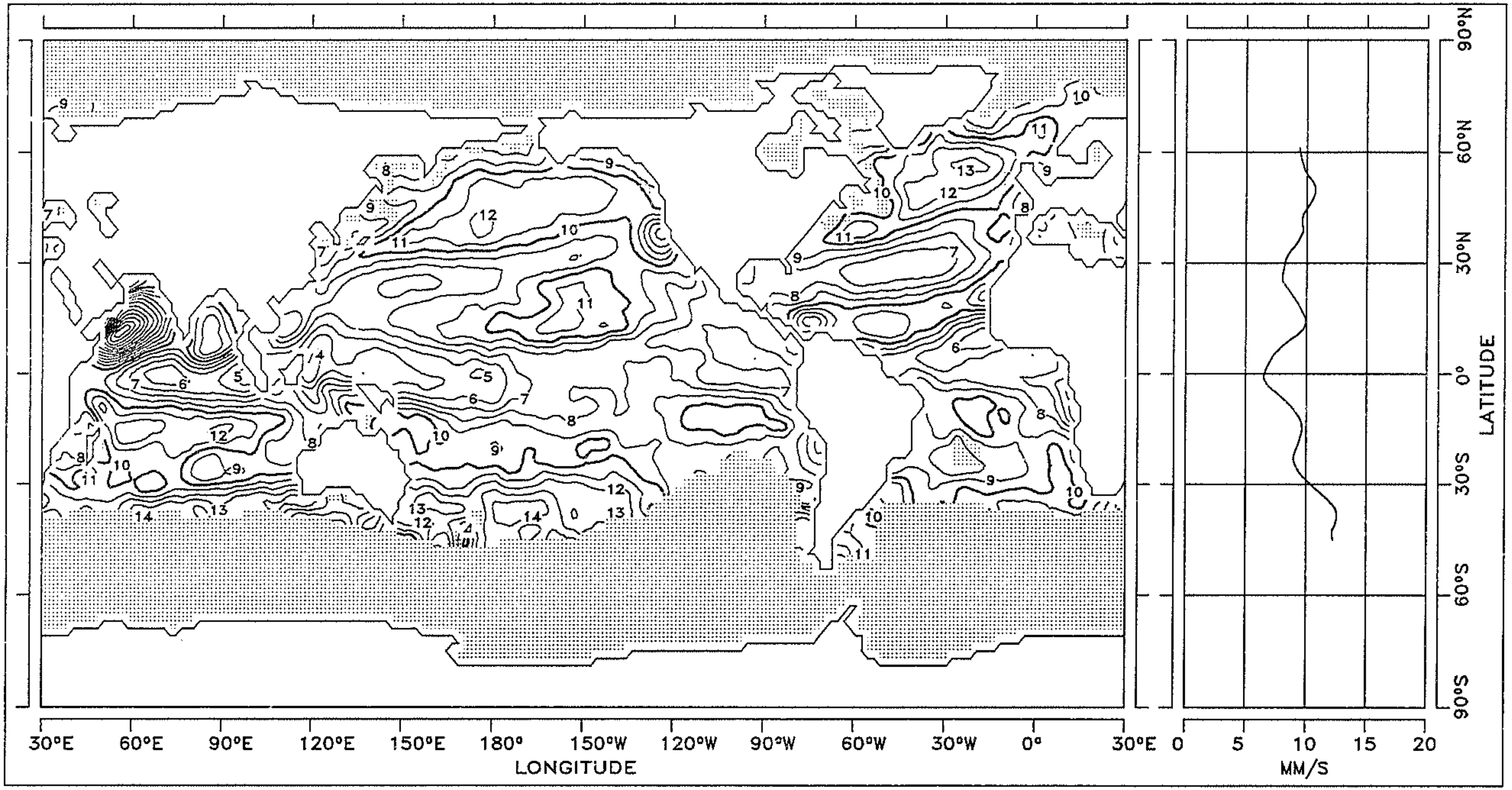

CONTOUR INTERVAL: 1 MM/S REFERENCE LINE : 10 MM/S

FIG. 16.7 U_* JULY

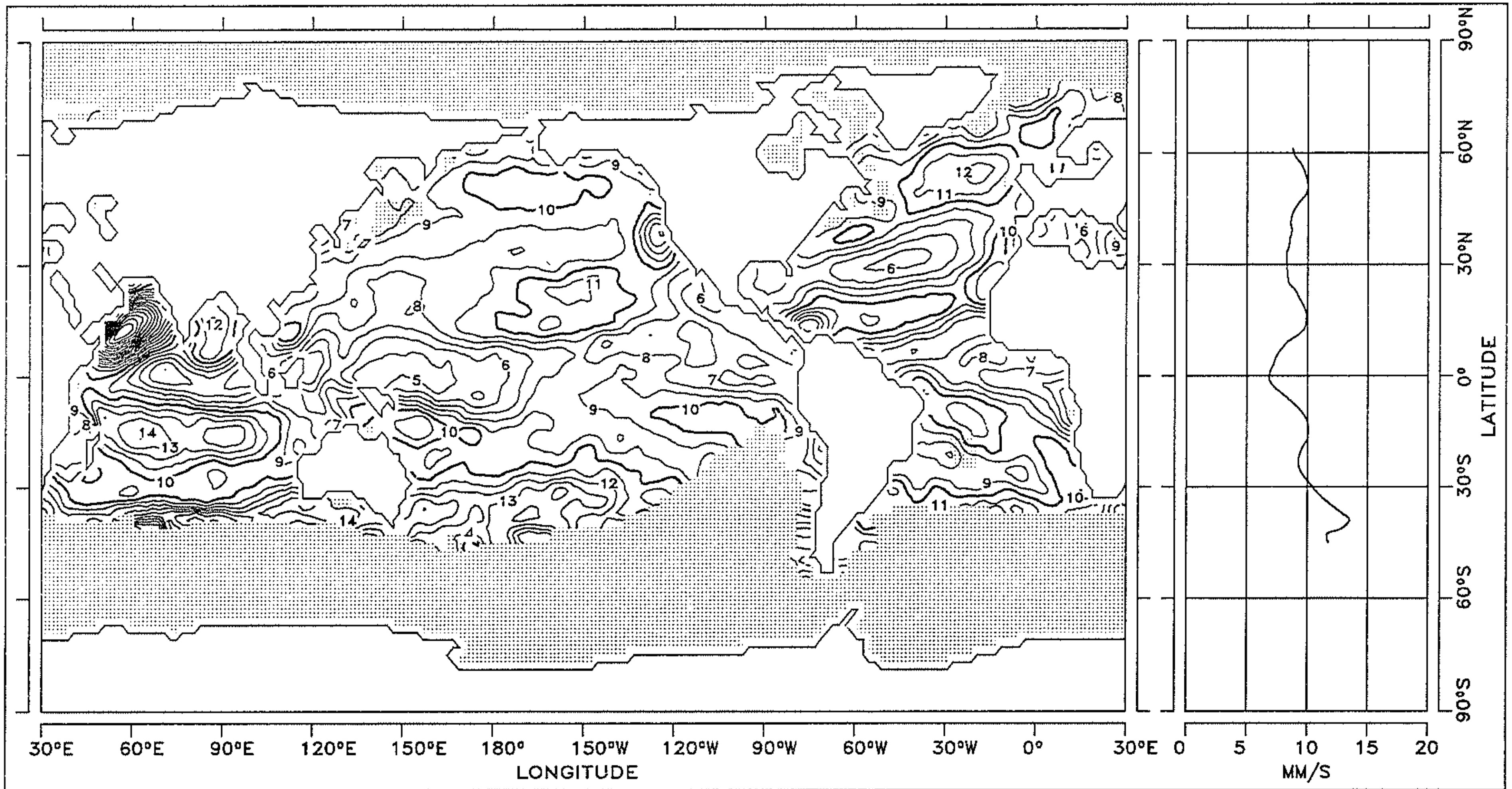

CONTOUR INTERVAL: 1 MM/S REFERENCE LINE : 10 MM/S

FIG. 16.8 U_* AUGUST

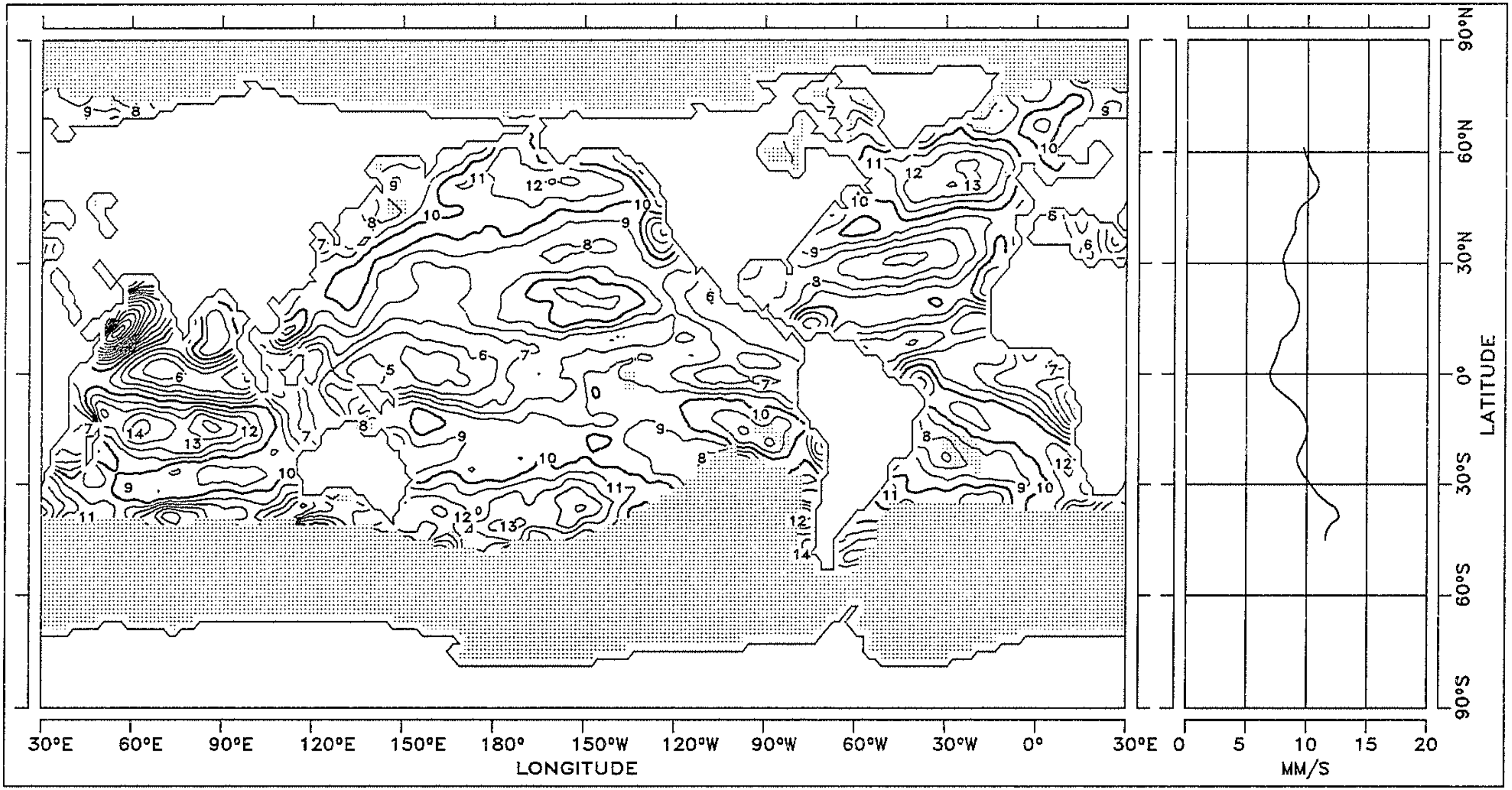

CONTOUR INTERVAL: 1 MM/S REFERENCE LINE : 10 MM/S

FIG. 16.9 U_* SEPTEMBER

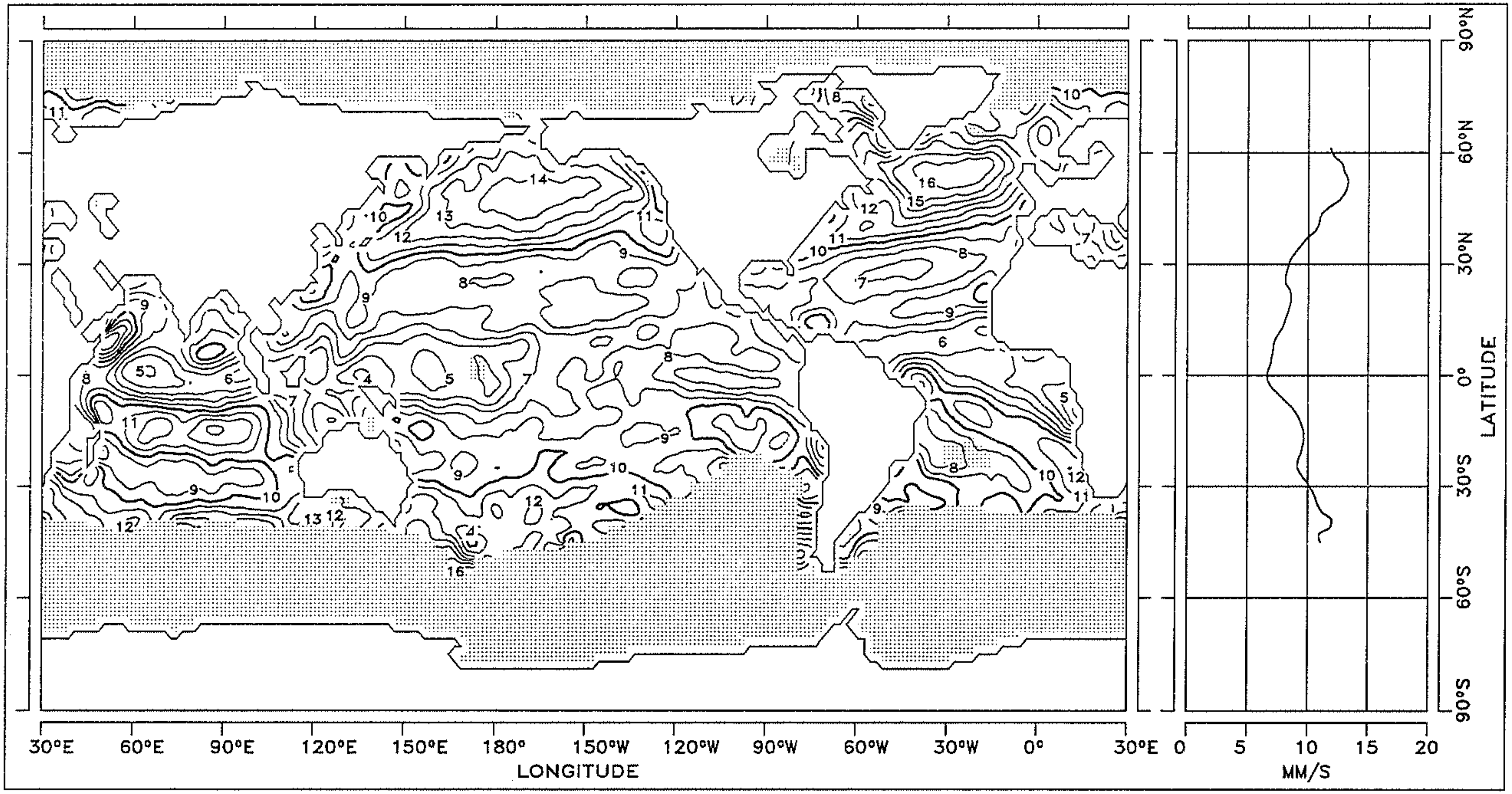

CONTOUR INTERVAL: 1 MM/S REFERENCE LINE : 10 MM/S

FIG. 16.10 U_* OCTOBER

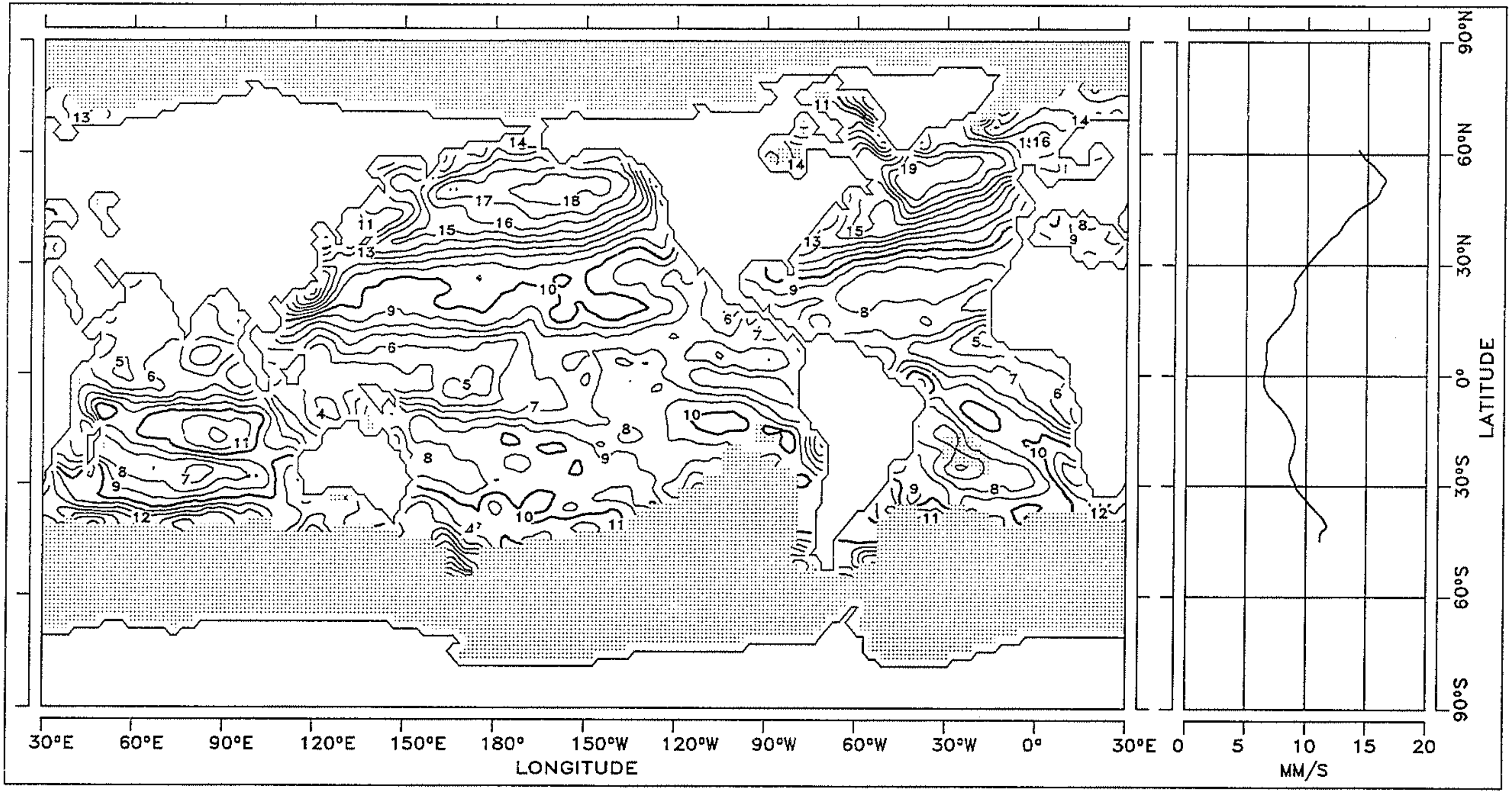

CONTOUR INTERVAL: 1 MM/S REFERENCE LINE : 10 MM/S

FIG. 16.11 U_* NOVEMBER

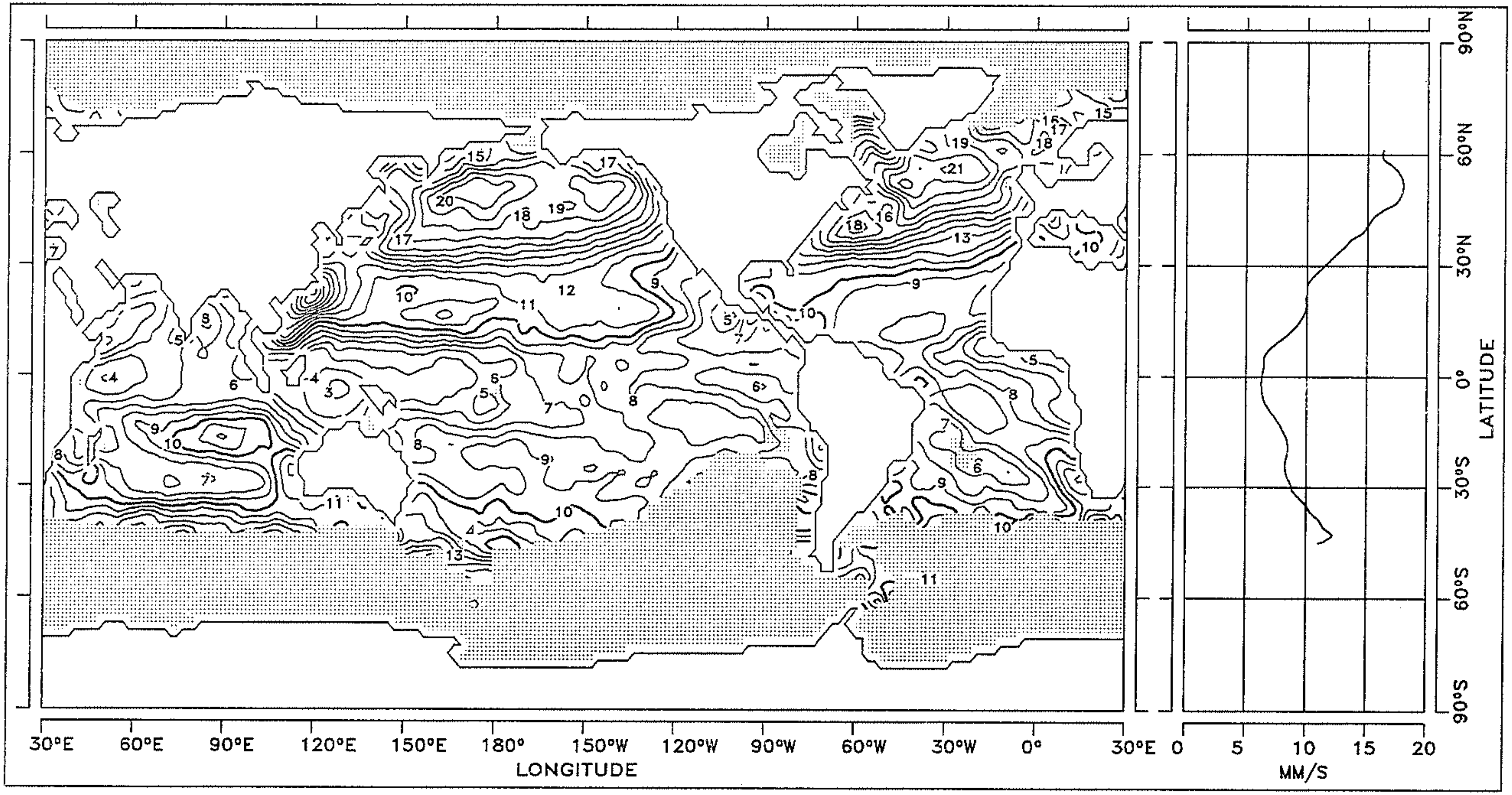

CONTOUR INTERVAL: 1 MM/S REFERENCE LINE : 10 MM/S

FIG. 16.12 U_* DECEMBER

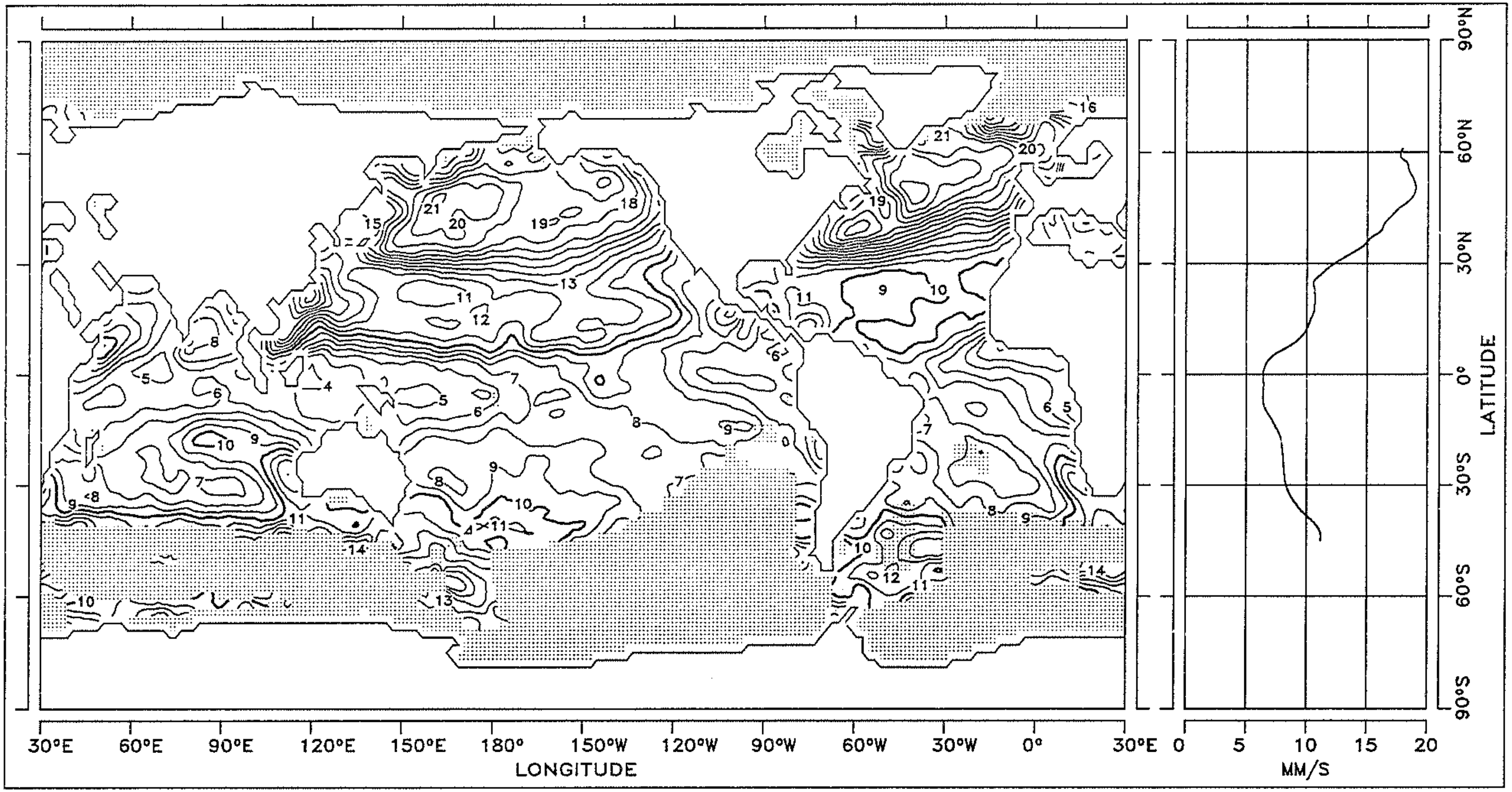

CONTOUR INTERVAL: 1 MM/S REFERENCE LINE : 10 MM/S

FIG. 16.13 U_* ANNUAL MEAN

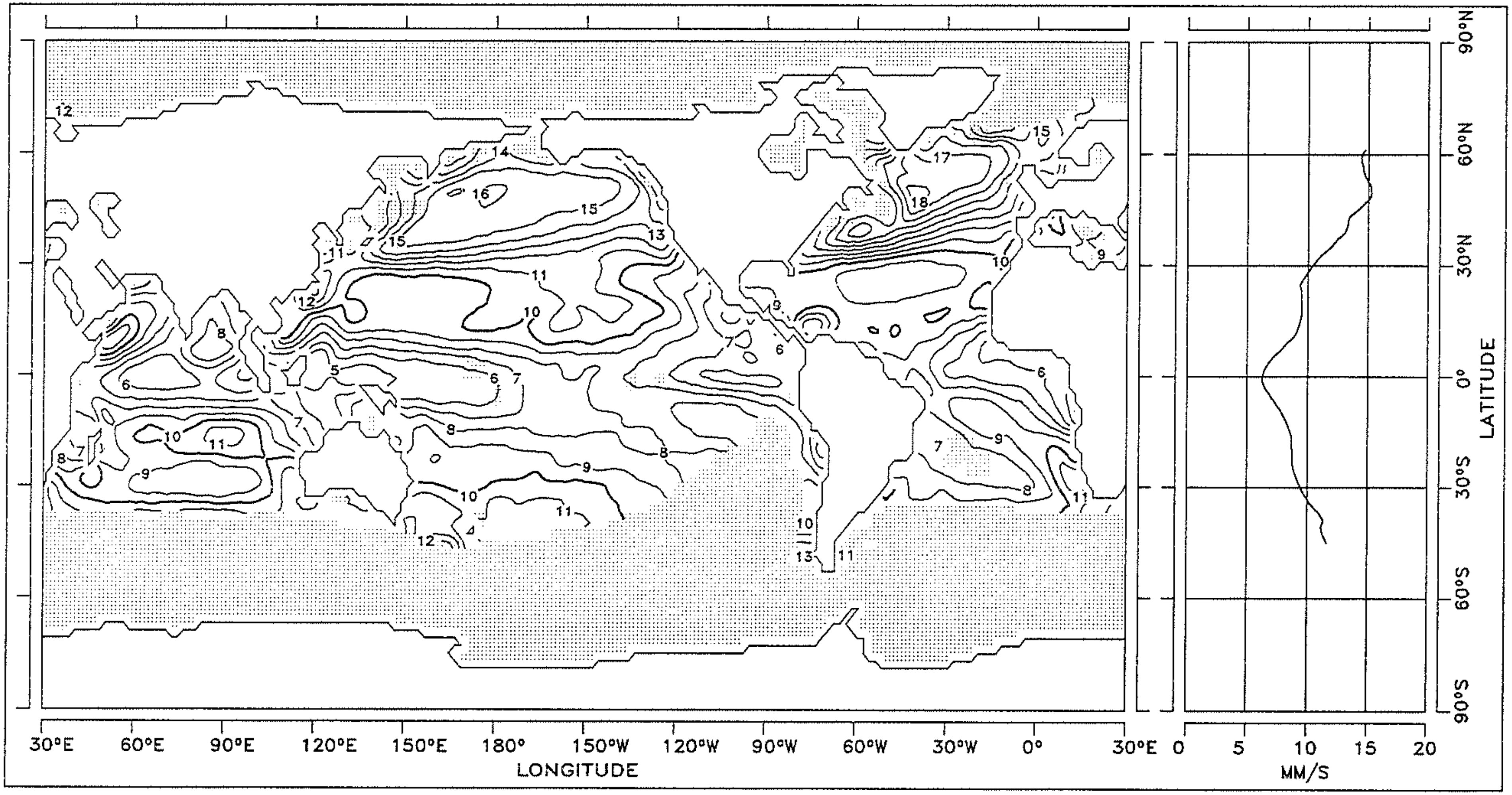

CONTOUR INTERVAL: 1 MM/S REFERENCE LINE : 10 MM/S

ESTIMATED MONIN-OBUKHOV LENGTH

FIG. 17.1 ESTIMATED MONIN–OBUKHOV LENGTH JANUARY

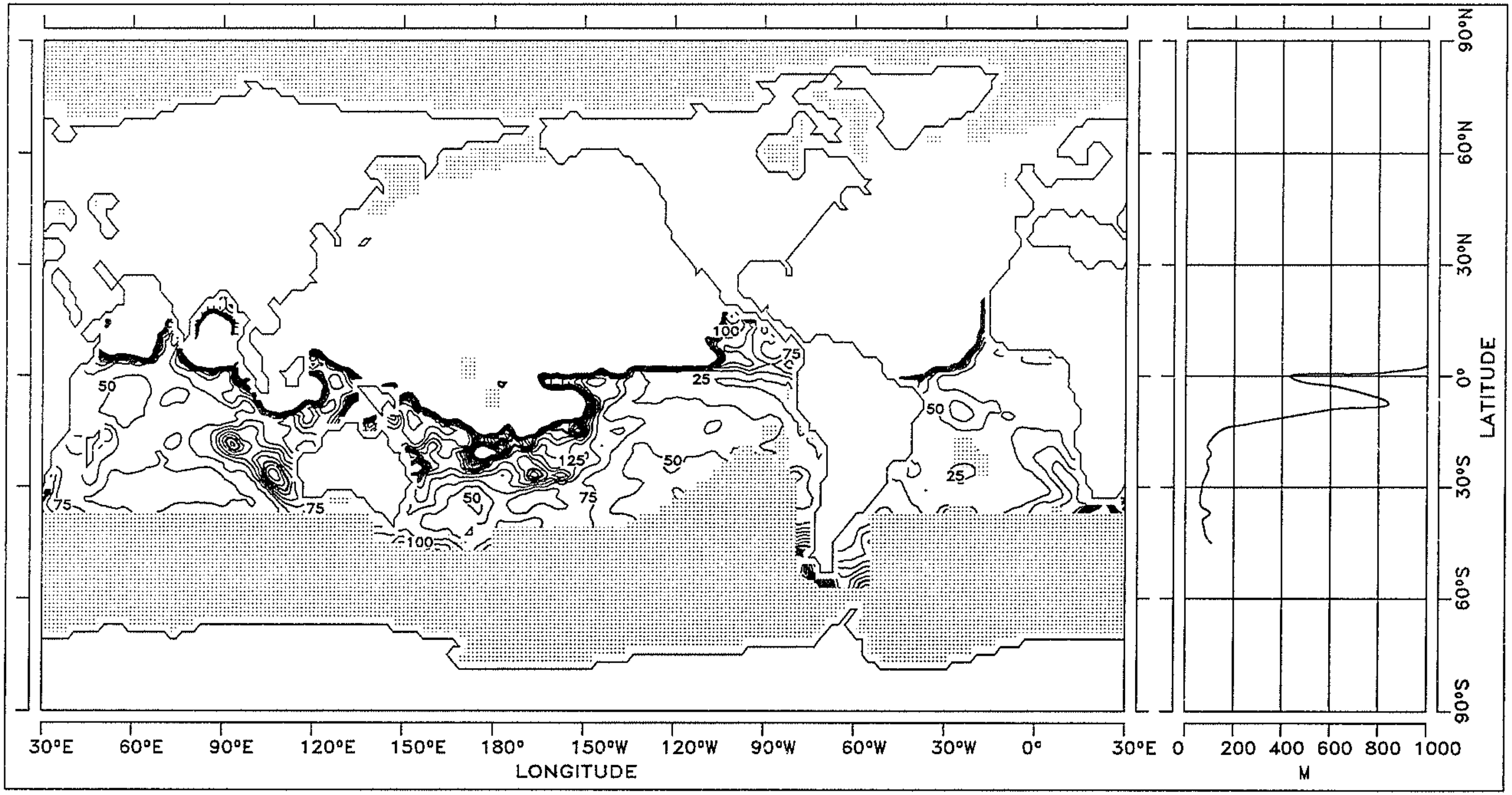

CONTOUR INTERVAL: 25 M REFERENCE LINE : 200 M

FIG. 17.2 ESTIMATED MONIN-OBUKHOV LENGTH FEBRUARY

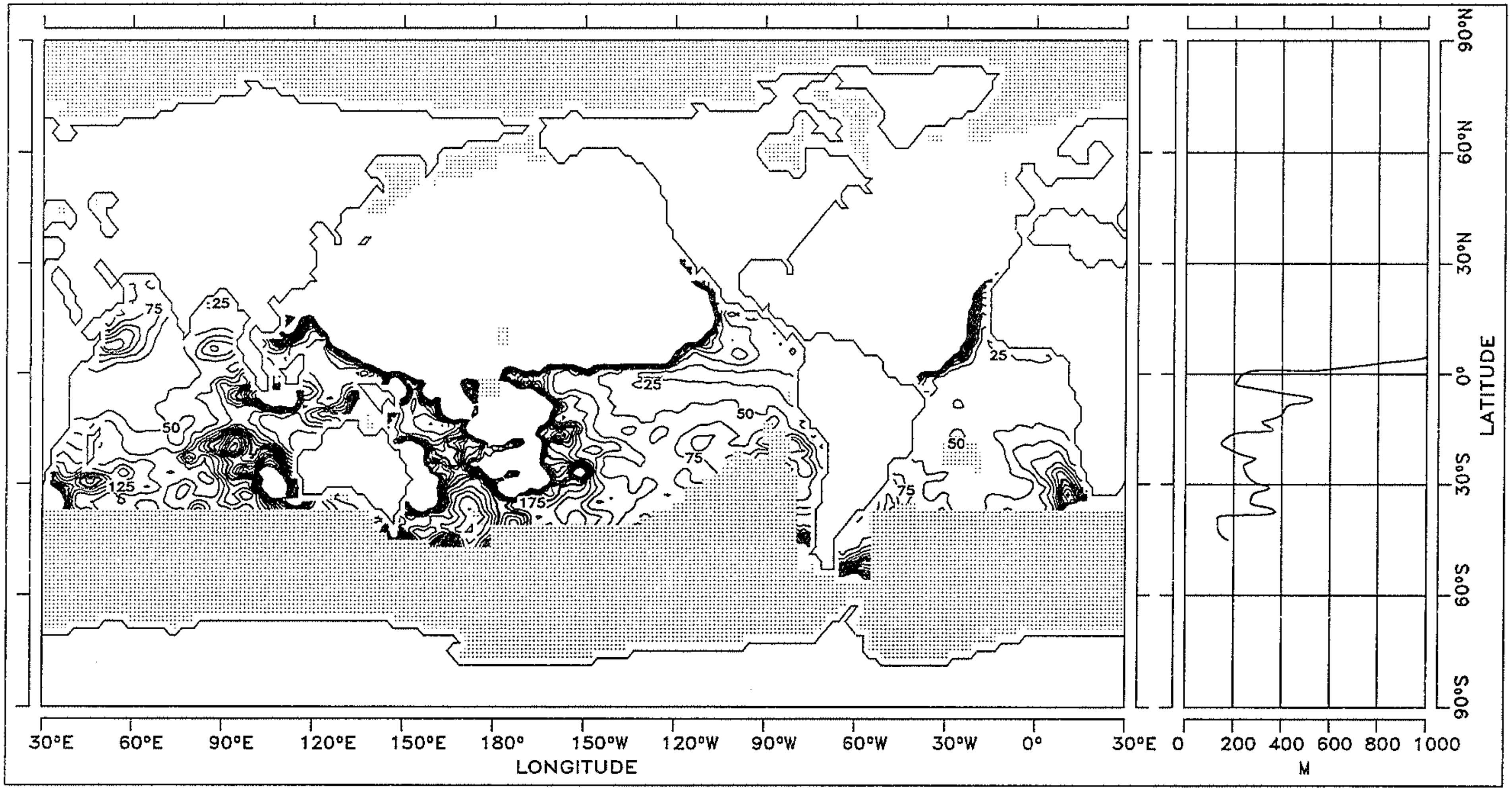

CONTOUR INTERVAL: 25 M REFERENCE LINE : 200 M

FIG. 17.3 ESTIMATED MONIN–OBUKHOV LENGTH MARCH

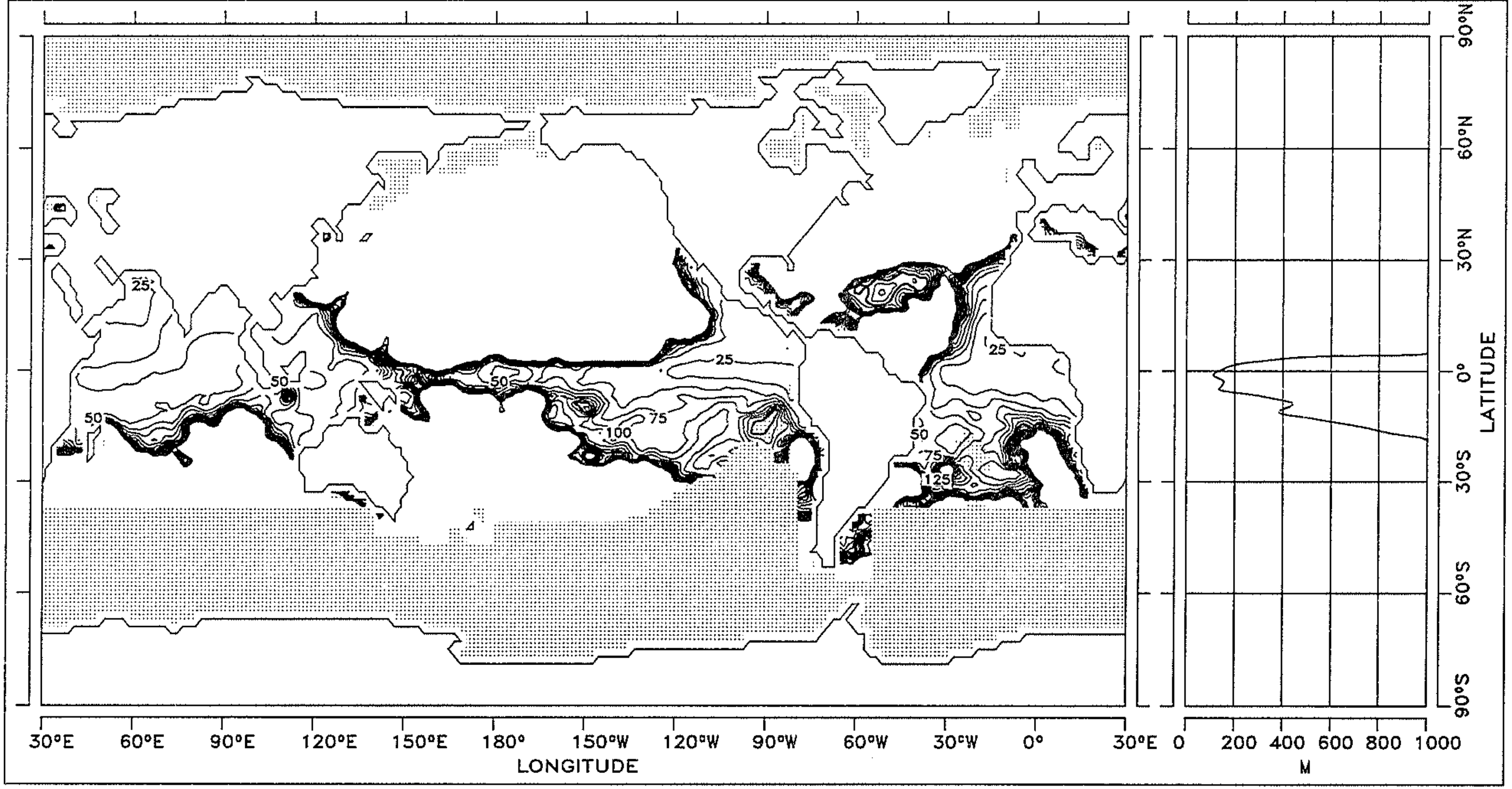

CONTOUR INTERVAL: 25 M REFERENCE LINE : 200 M

FIG. 17.4 ESTIMATED MONIN–OBUKHOV LENGTH APRIL

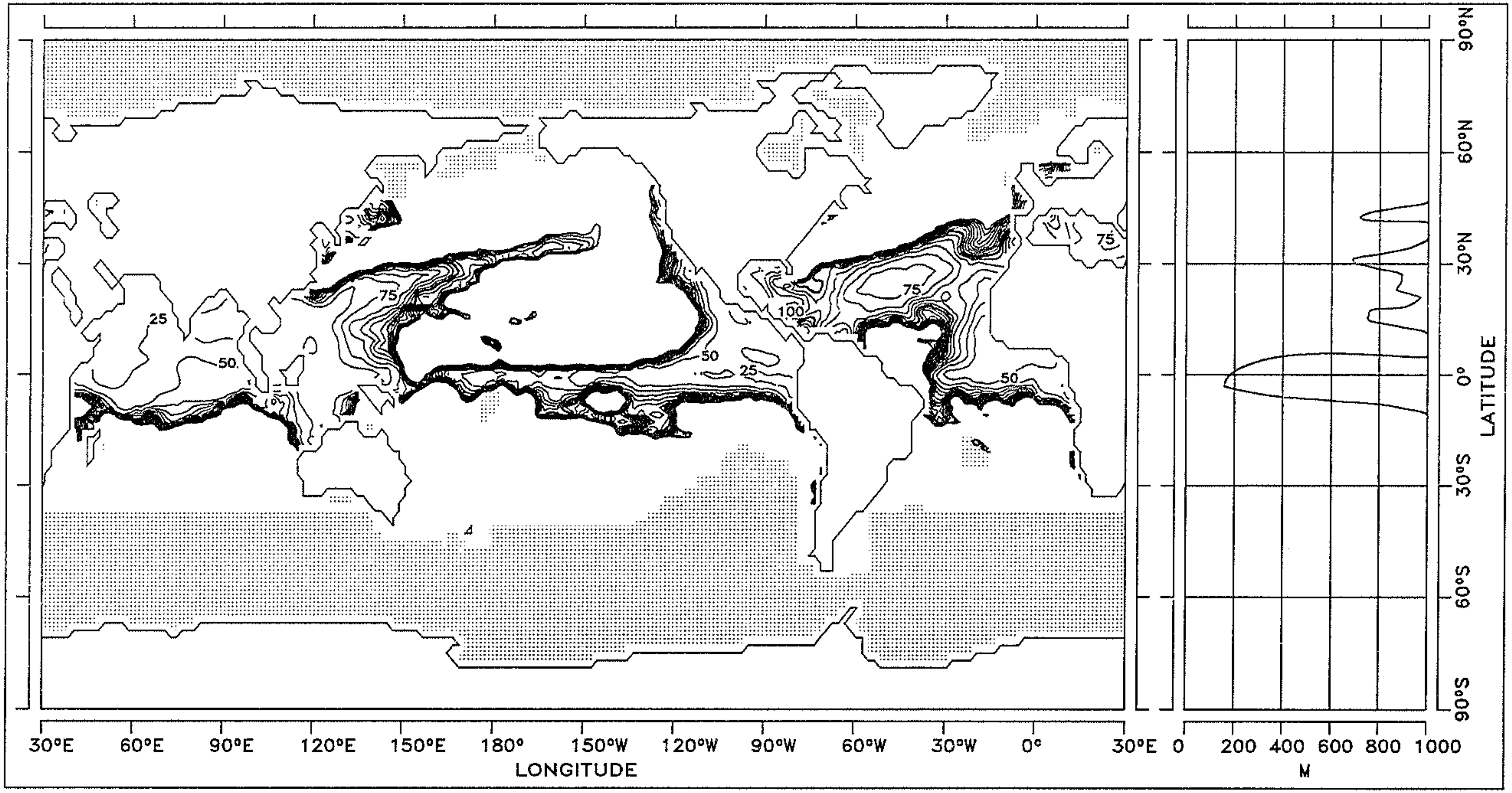

CONTOUR INTERVAL: 25 M REFERENCE LINE : 200 M

FIG. 17.5 ESTIMATED MONIN–OBUKHOV LENGTH MAY

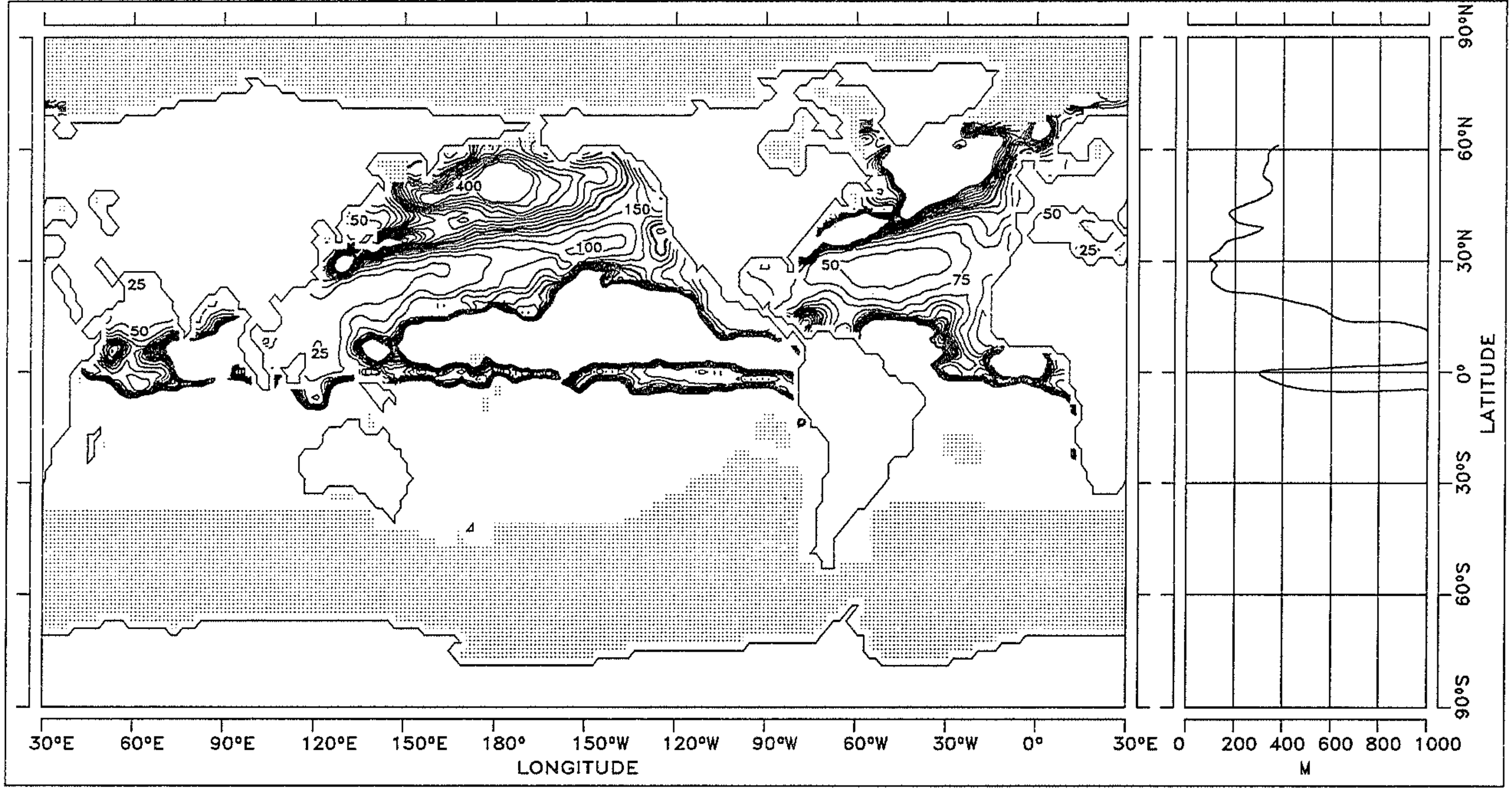

CONTOUR INTERVAL: 25 M REFERENCE LINE : 200 M

FIG. 17.6 ESTIMATED MONIN–OBUKHOV LENGTH JUNE

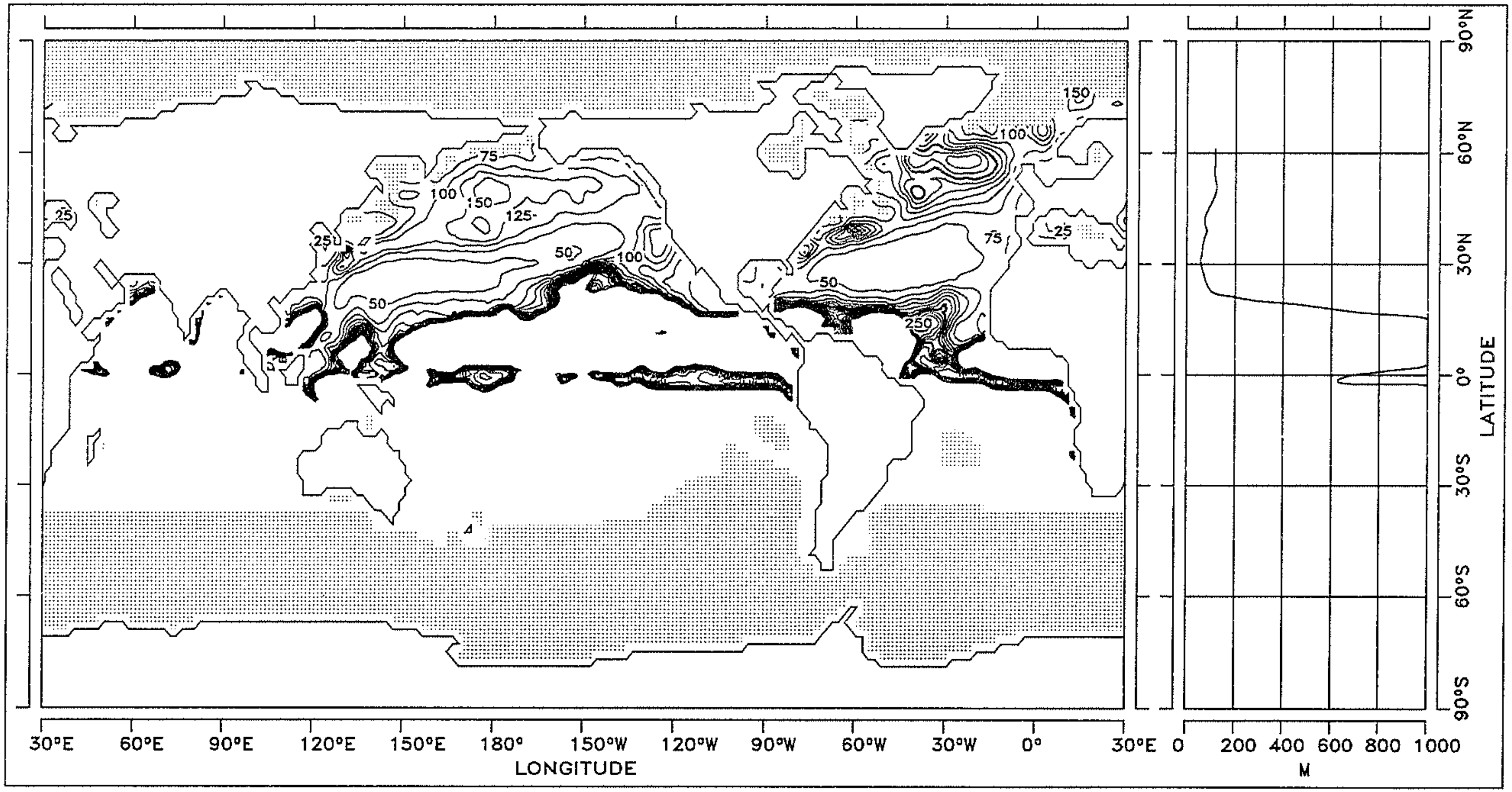

CONTOUR INTERVAL: 25 M REFERENCE LINE : 200 M

FIG. 17.7 ESTIMATED MONIN–OBUKHOV LENGTH JULY

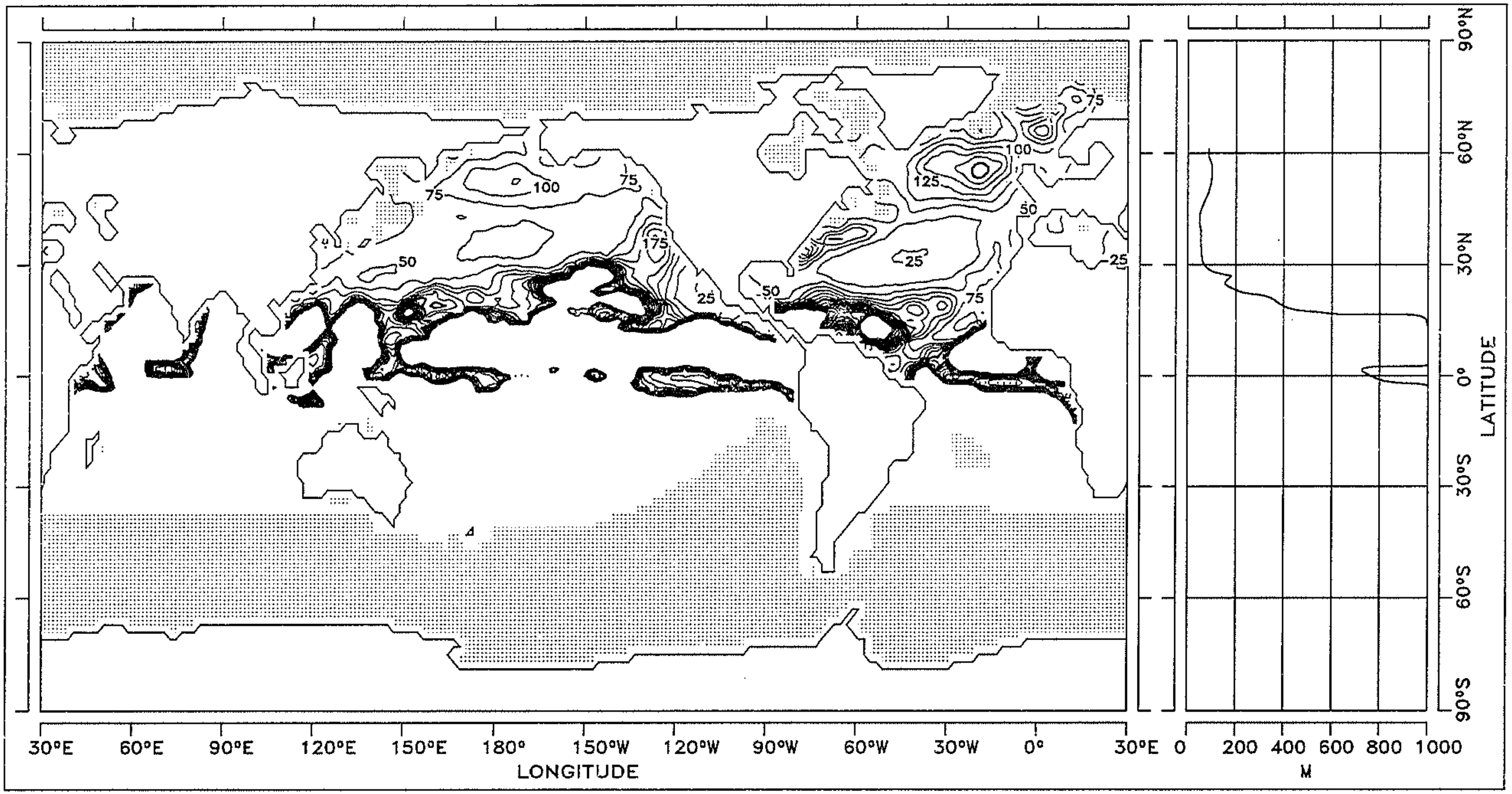

CONTOUR INTERVAL: 25 M REFERENCE LINE : 200 M

FIG. 17.8 ESTIMATED MONIN–OBUKHOV LENGTH AUGUST

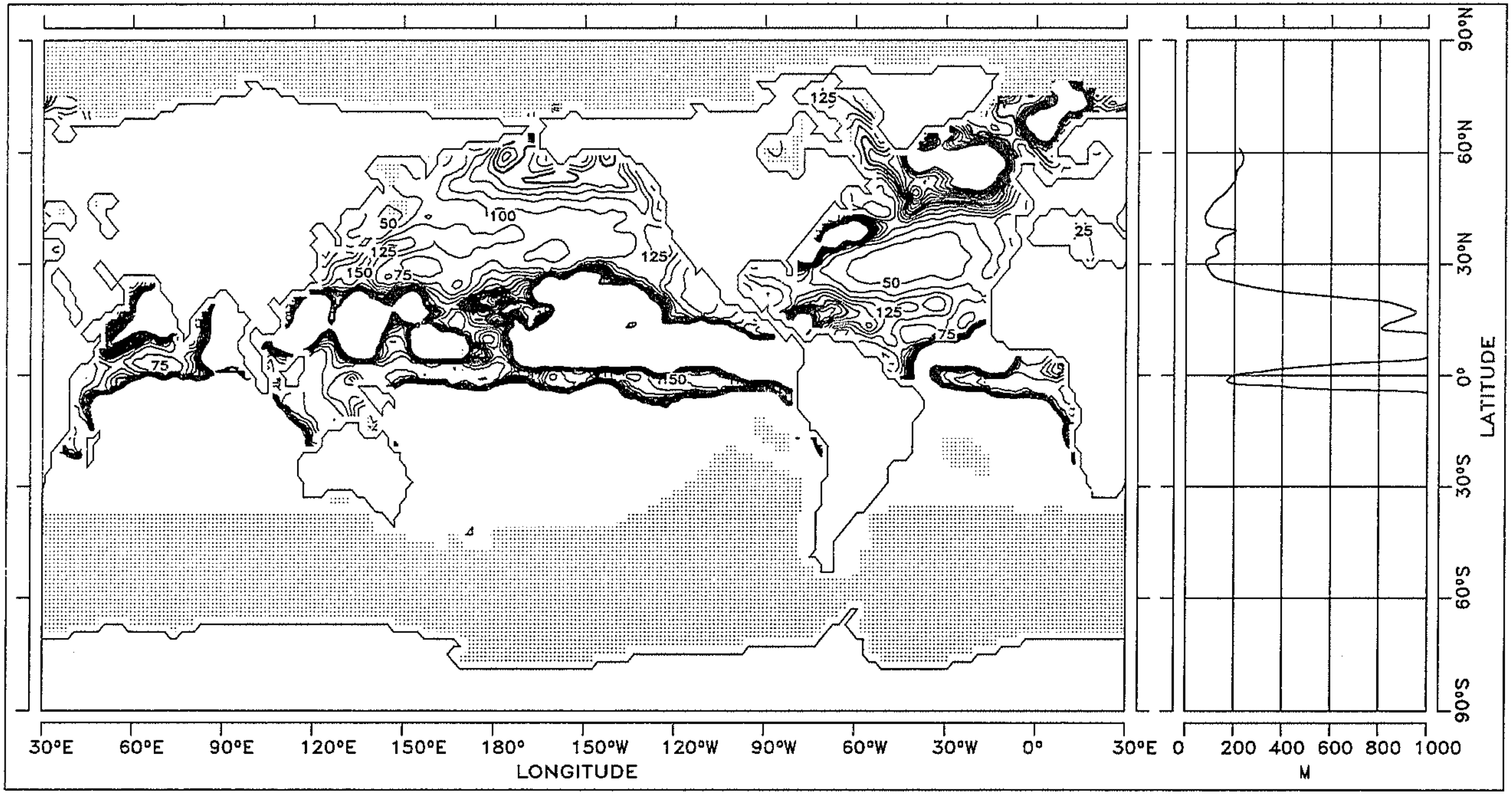

CONTOUR INTERVAL: 25 M REFERENCE LINE : 200 M

FIG. 17.9 ESTIMATED MONIN–OBUKHOV LENGTH SEPTEMBER

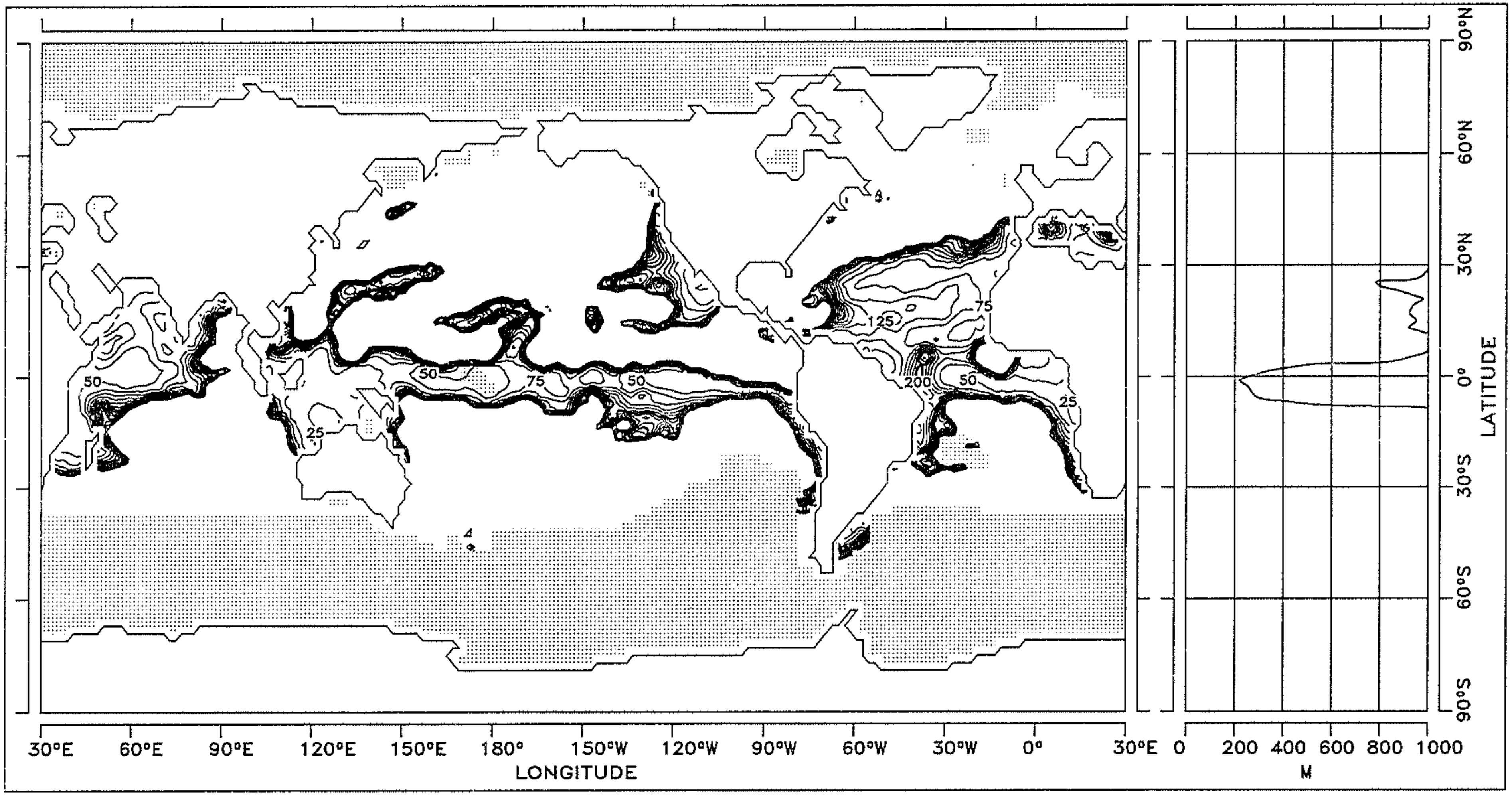

CONTOUR INTERVAL: 25 M REFERENCE LINE : 200 M

FIG. 17.10 ESTIMATED MONIN–OBUKHOV LENGTH OCTOBER

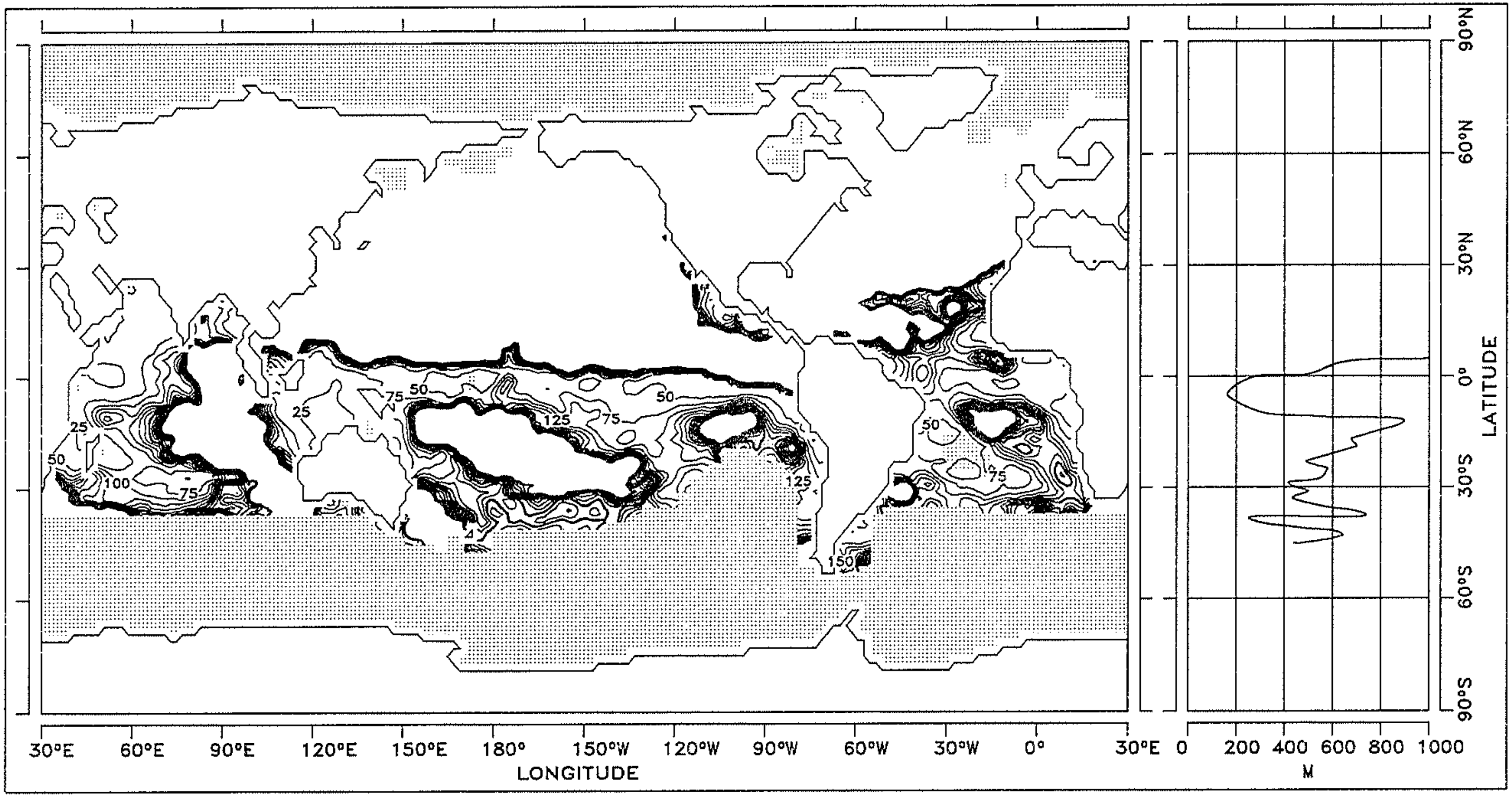

CONTOUR INTERVAL: 25 M REFERENCE LINE : 200 M

FIG. 17.11 ESTIMATED MONIN–OBUKHOV LENGTH NOVEMBER

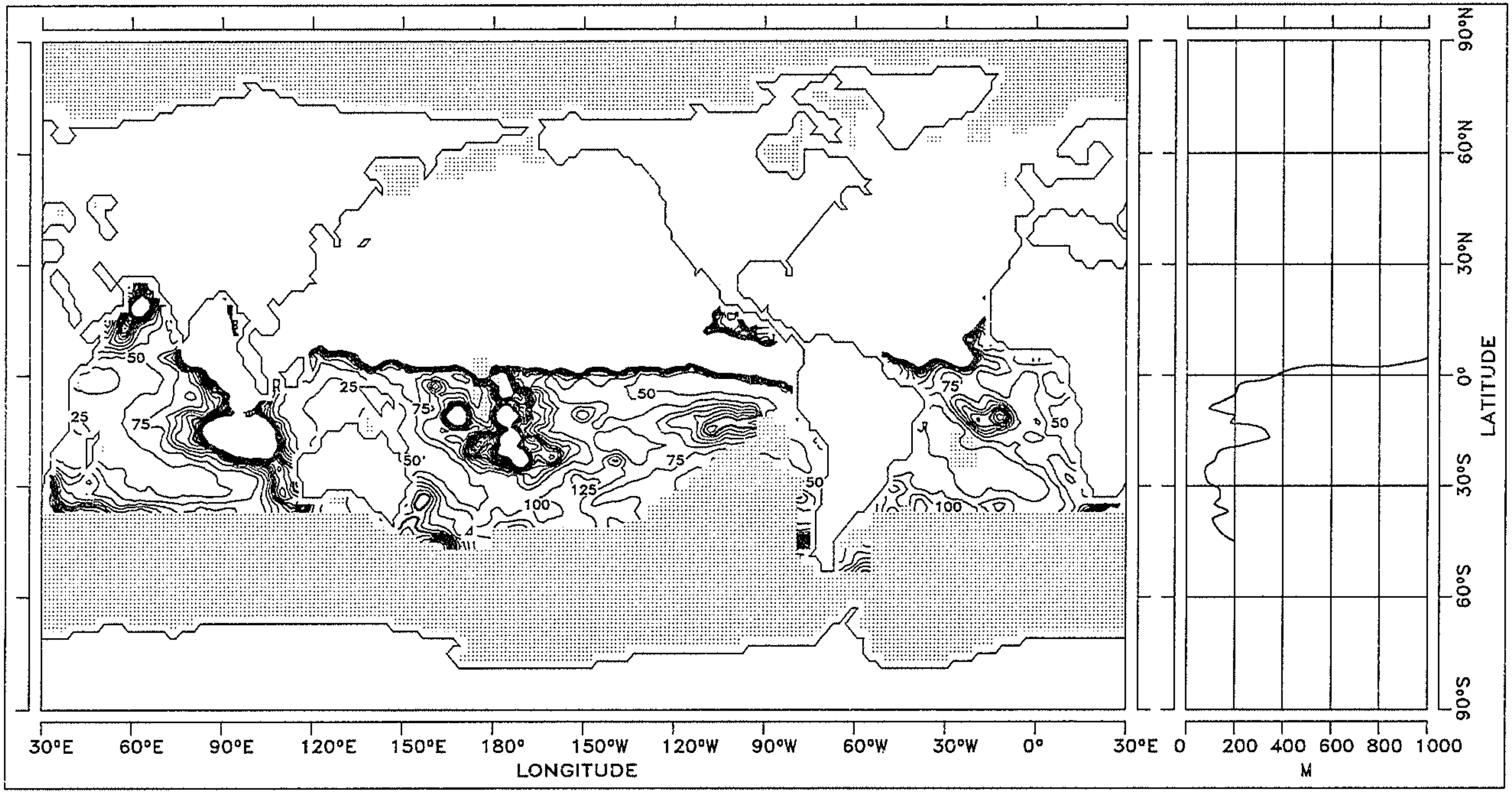

CONTOUR INTERVAL: 25 M REFERENCE LINE : 200 M

FIG. 17.12 ESTIMATED MONIN–OBUKHOV LENGTH DECEMBER

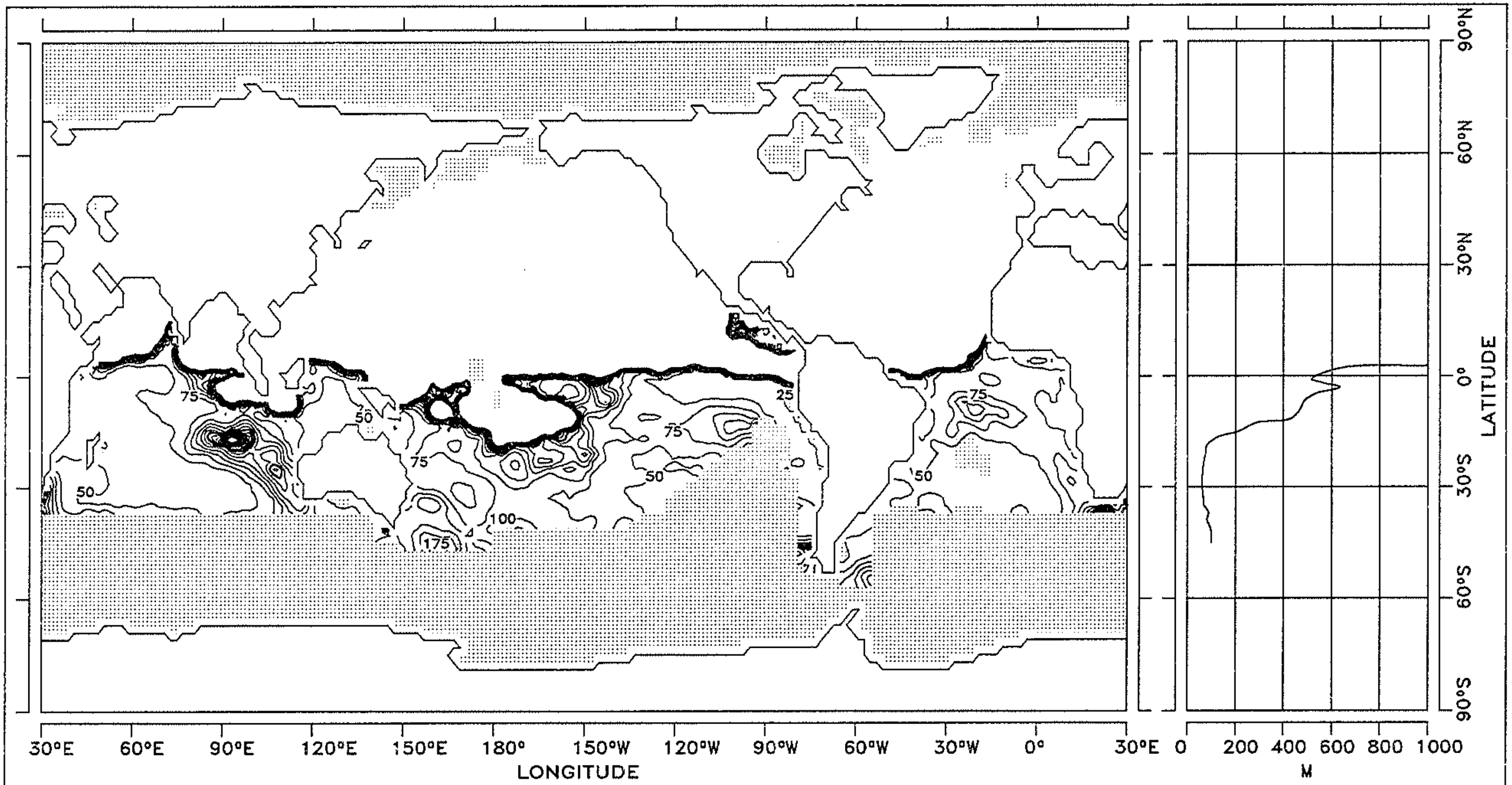

CONTOUR INTERVAL: 25 M REFERENCE LINE : 200 M

ATMOSPHERE-OCEAN COUPLING COEFFICIENT

FIG. 18.1 DQ/DT JANUARY

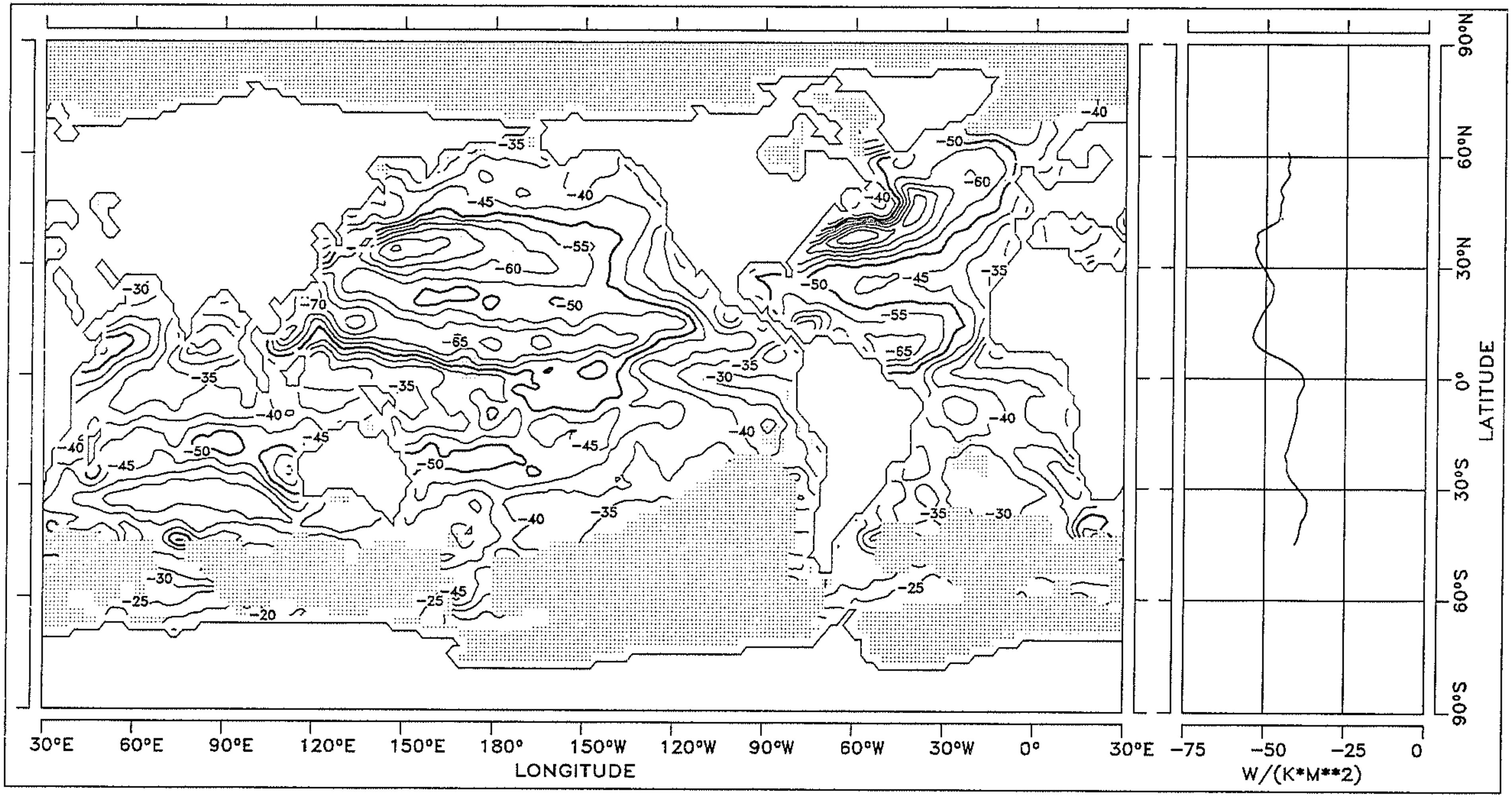

CONTOUR INTERVAL: 5 W/(K*M**2) REFERENCE LINE : -50 W/(K*M**2)

FIG. 18.2 DQ/DT FEBRUARY

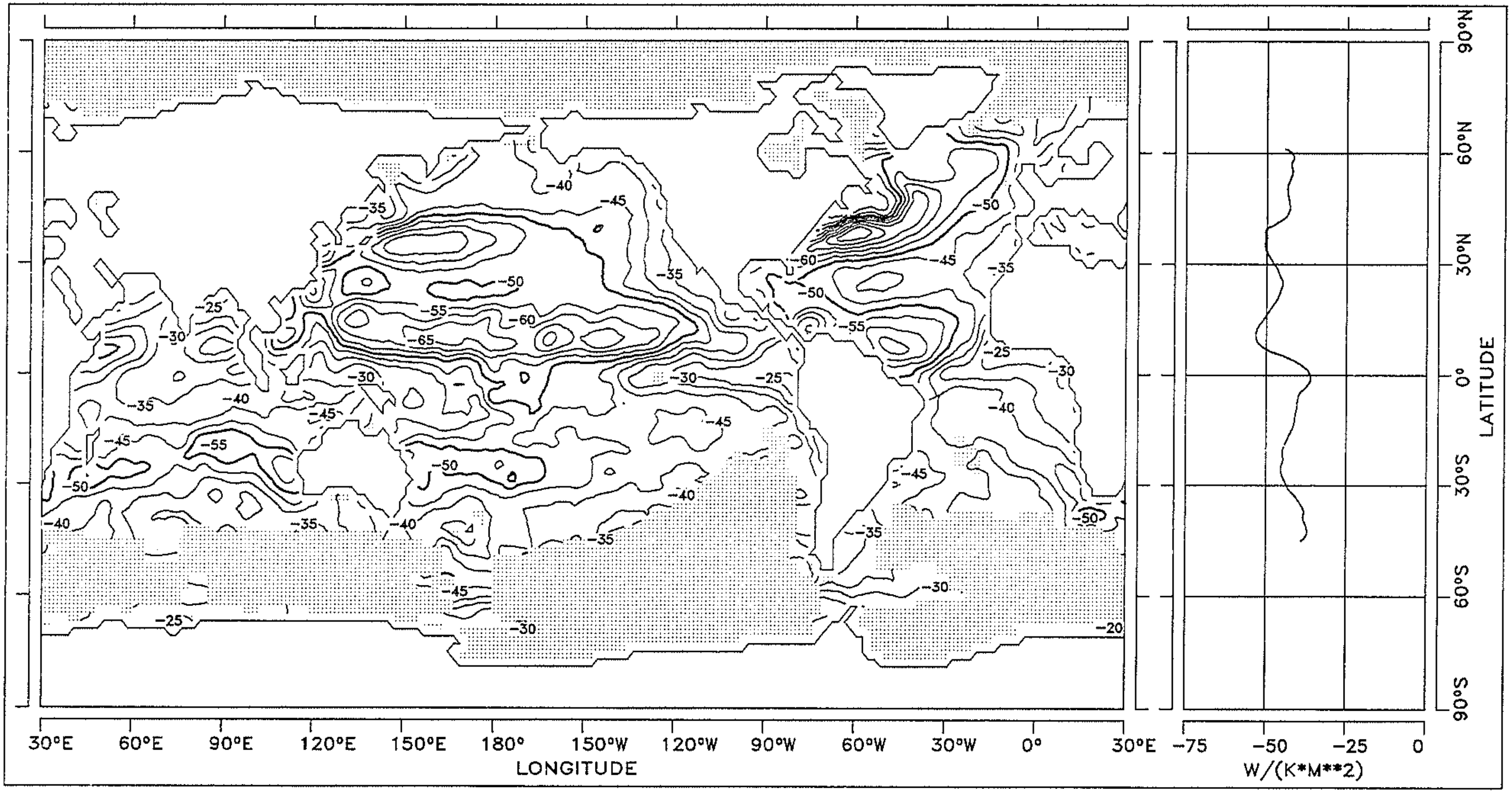

CONTOUR INTERVAL: 5 W/(K*M**2) REFERENCE LINE : -50 W/(K*M**2)

FIG. 18.3 DQ/DT MARCH

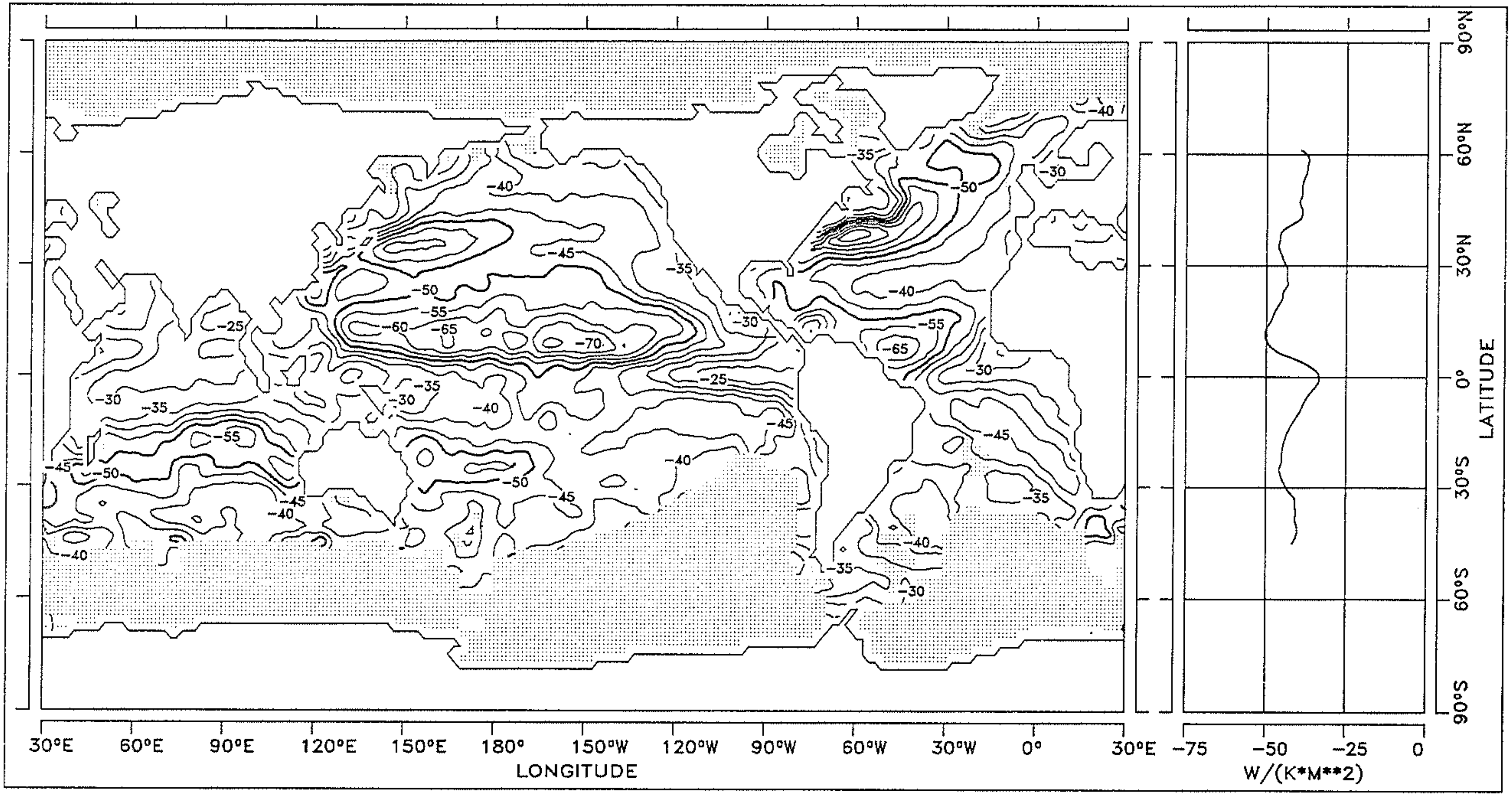

CONTOUR INTERVAL: 5 W/(K*M**2) REFERENCE LINE : −50 W/(K*M**2)

FIG. 18.4 DQ/DT APRIL

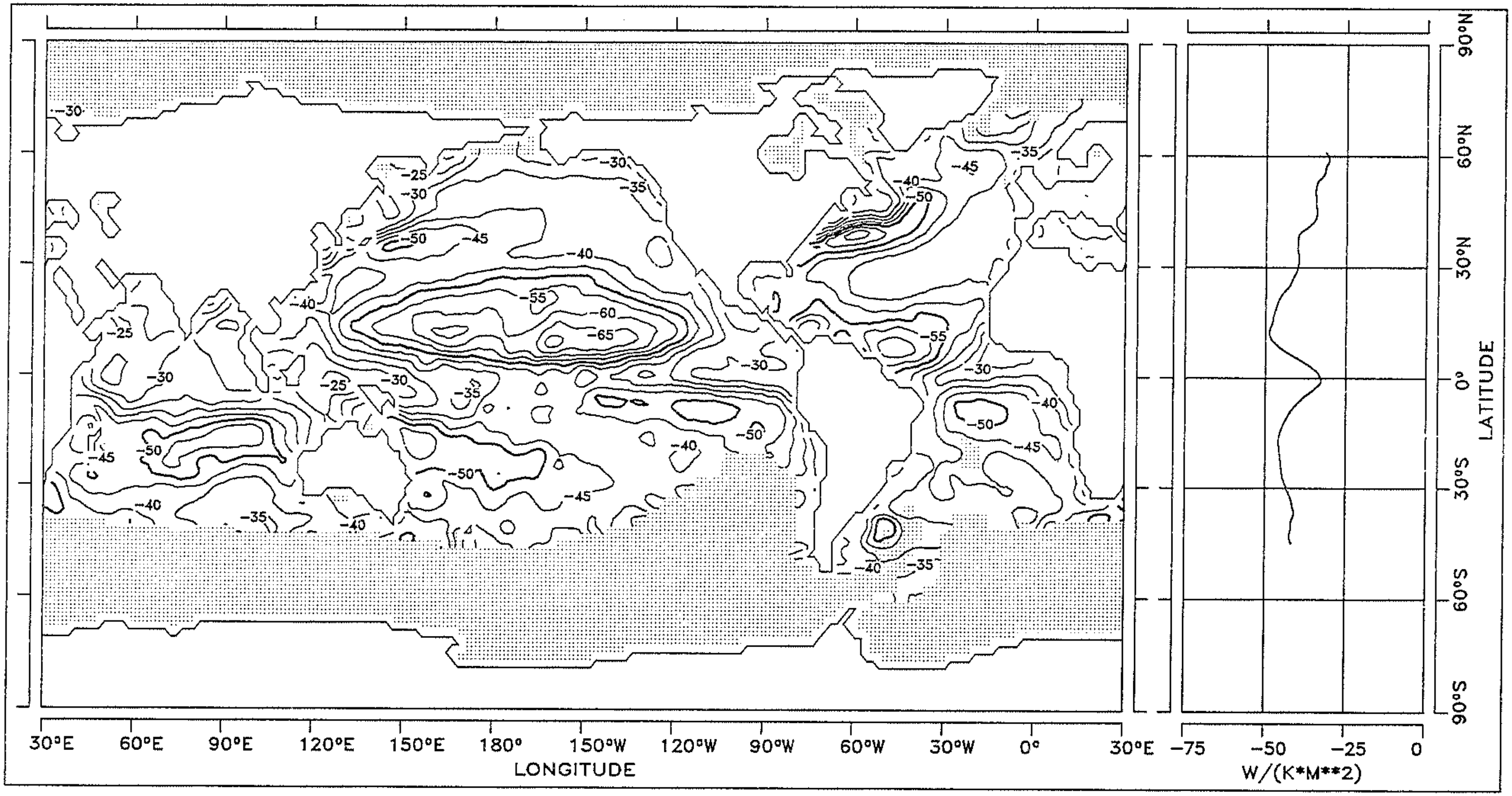

CONTOUR INTERVAL: 5 W/(K*M**2) REFERENCE LINE : −50 W/(K*M**2)

FIG. 18.5 DQ/DT MAY

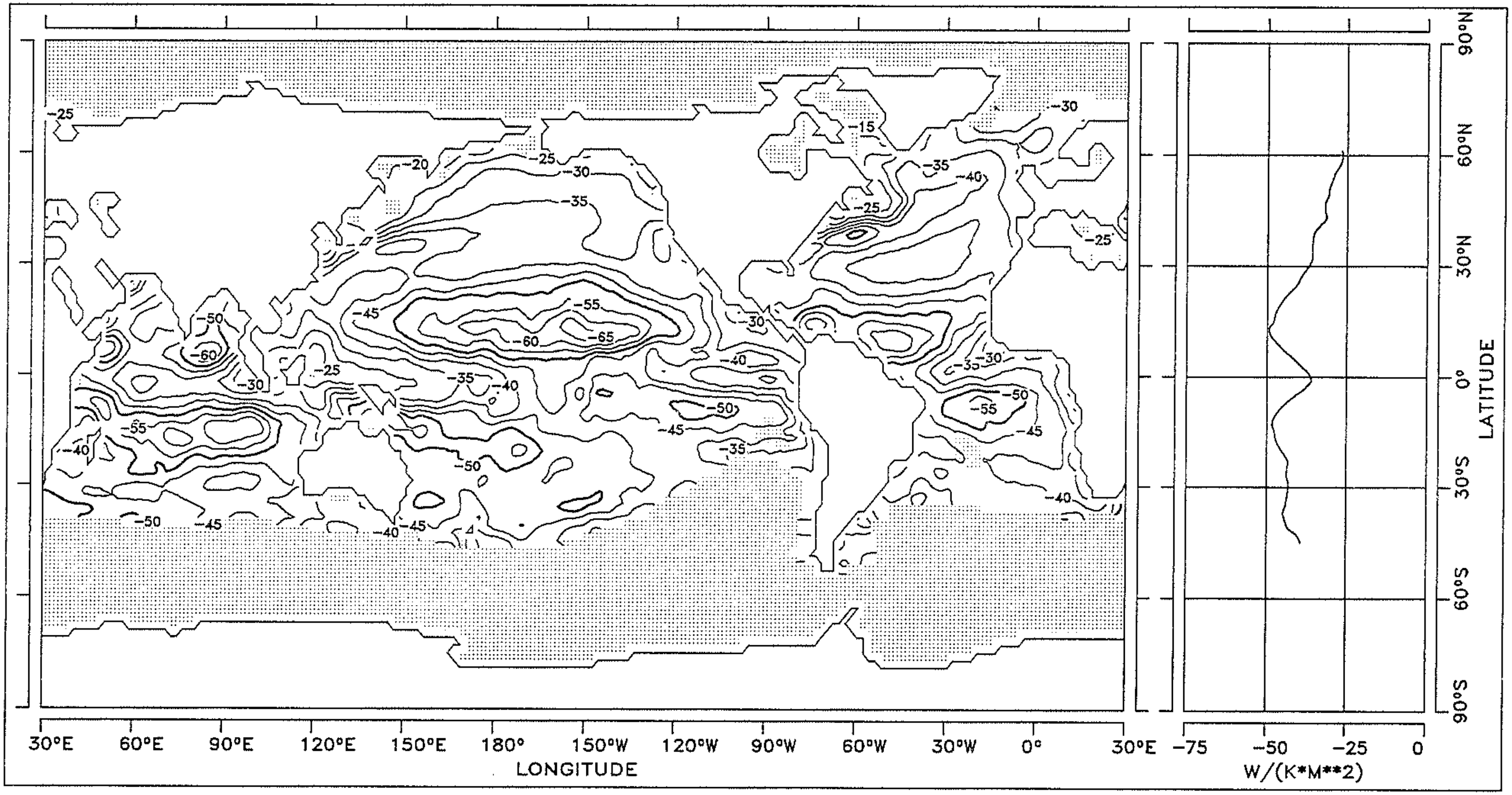

CONTOUR INTERVAL: 5 W/(K*M**2) REFERENCE LINE : −50 W/(K*M**2)

FIG. 18.6 DQ/DT JUNE

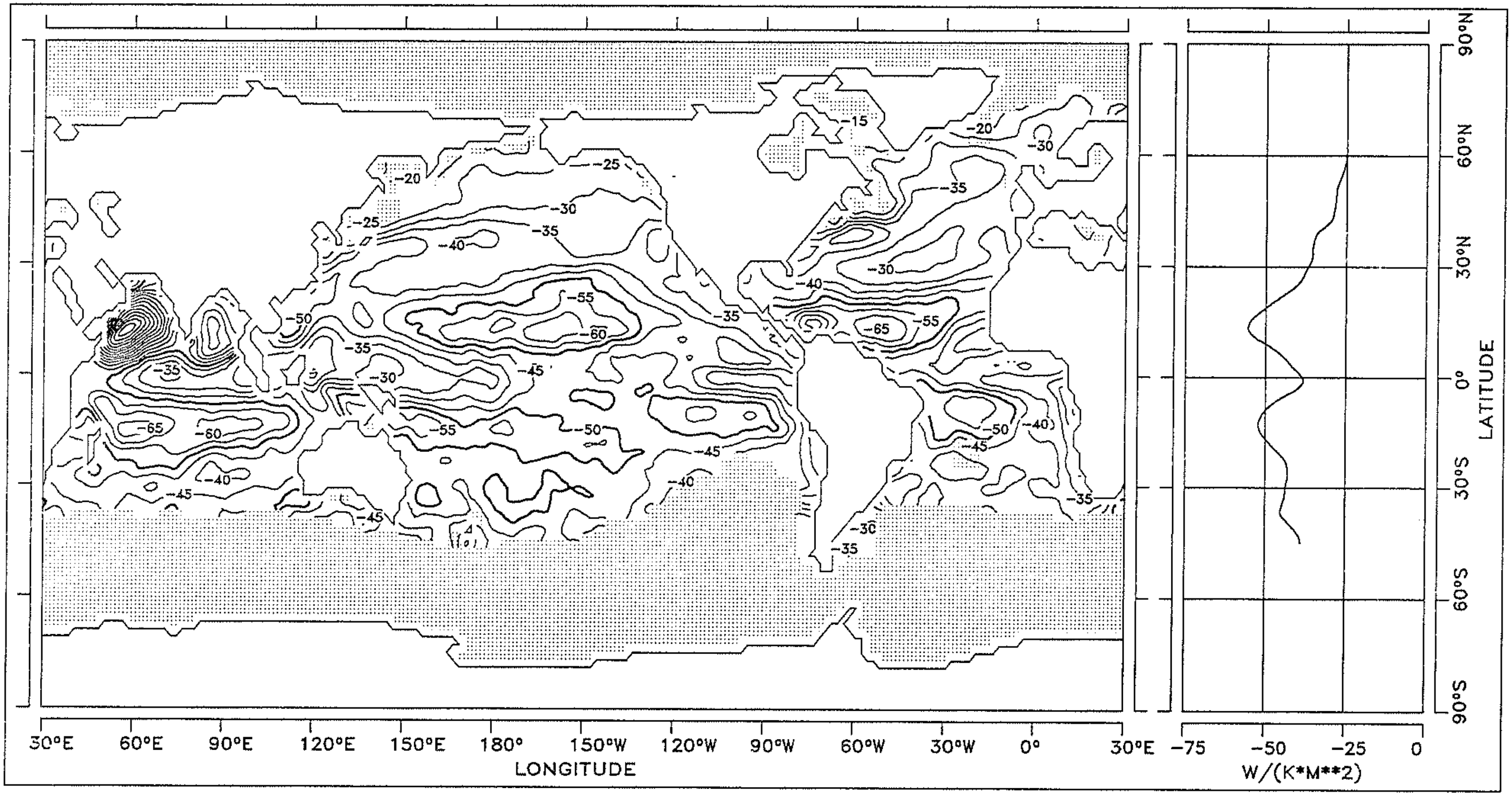

CONTOUR INTERVAL: 5 W/(K*M**2) REFERENCE LINE : -50 W/(K*M**2)

FIG. 18.7 DQ/DT JULY

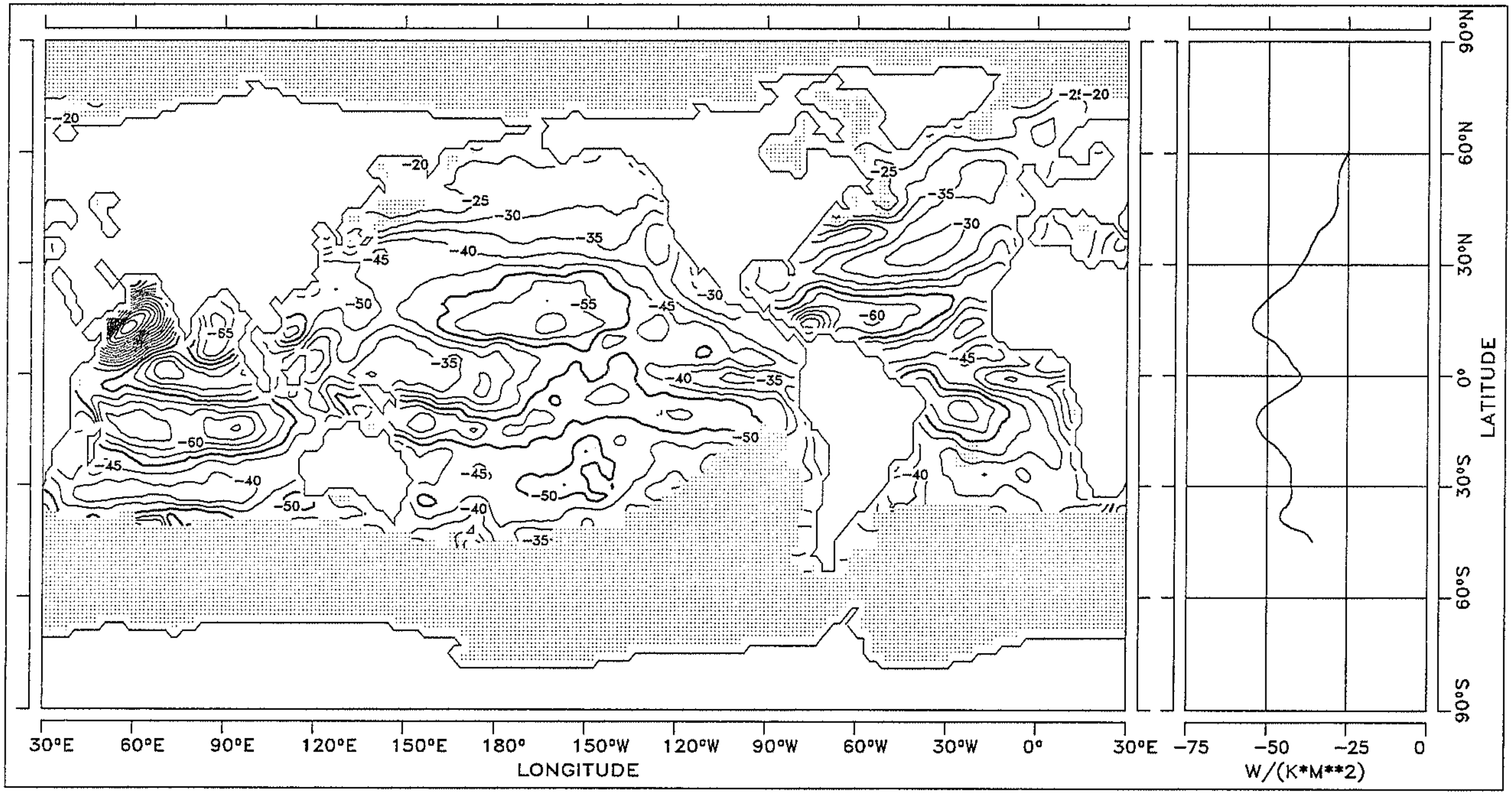

CONTOUR INTERVAL: 5 W/(K*M**2) REFERENCE LINE : -50 W/(K*M**2)

FIG. 18.8 DQ/DT AUGUST

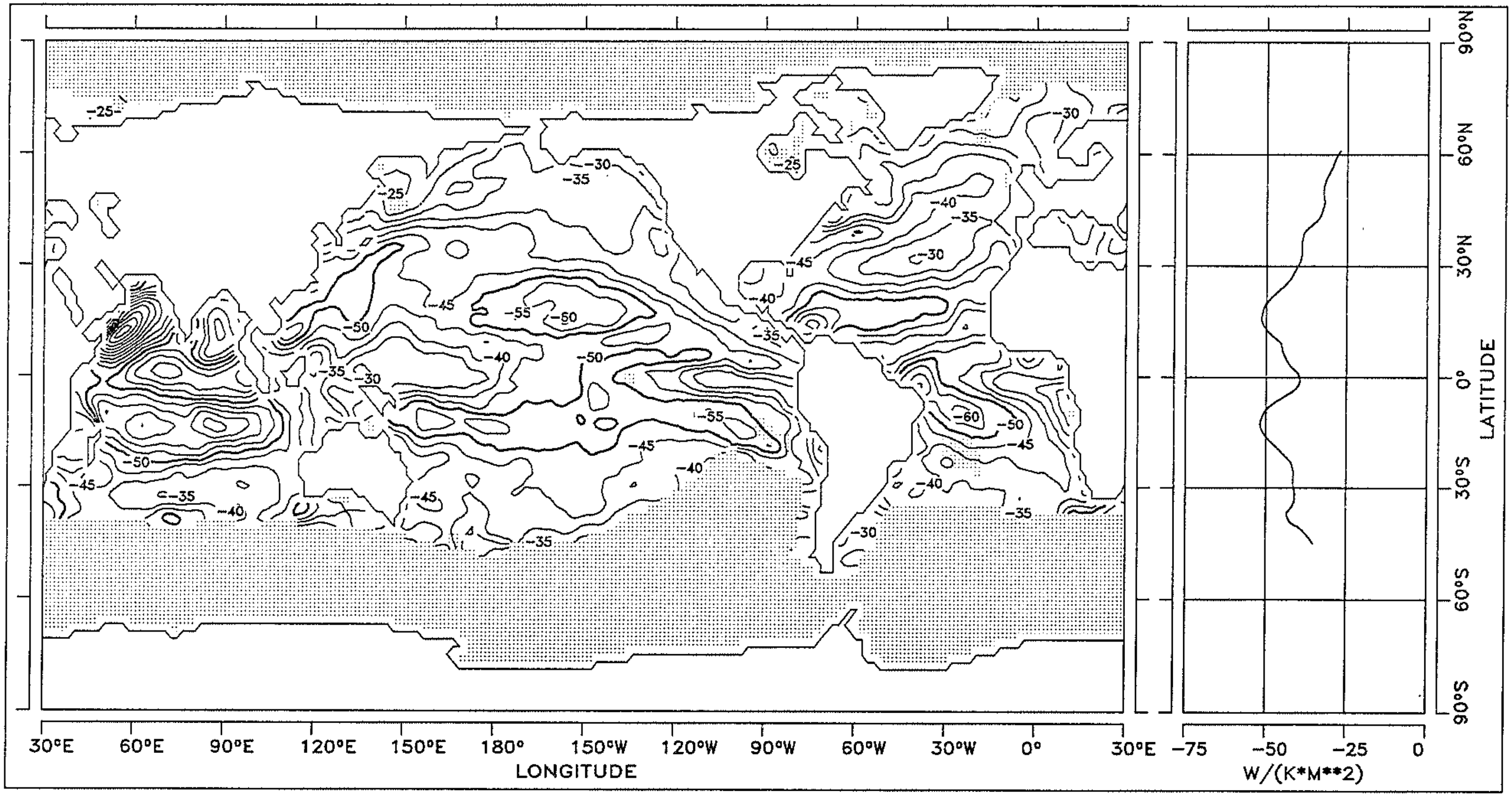

CONTOUR INTERVAL: 5 W/(K*M**2) REFERENCE LINE : -50 W/(K*M**2)

FIG. 18.9 DQ/DT SEPTEMBER

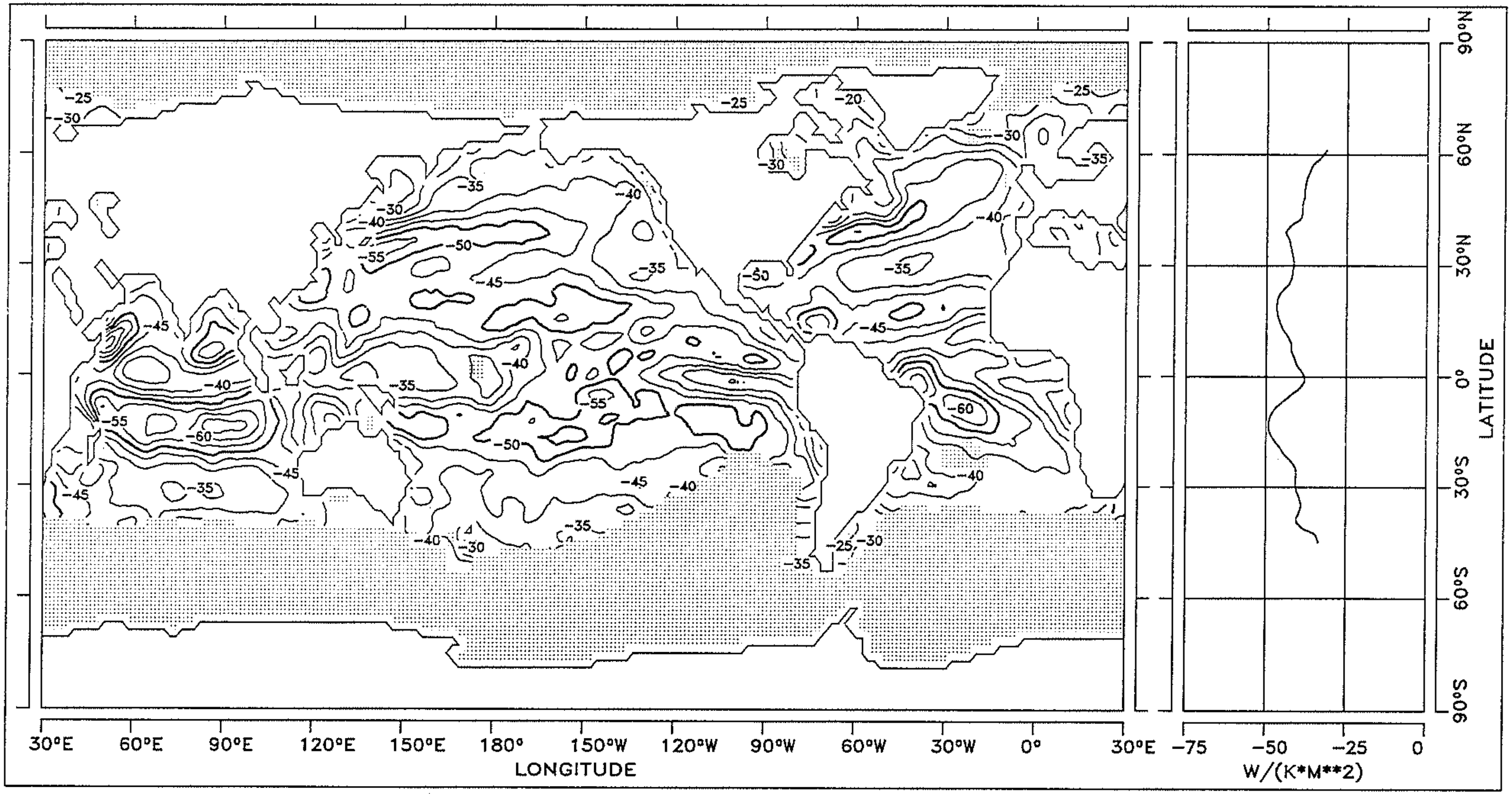

CONTOUR INTERVAL: 5 W/(K*M**2) REFERENCE LINE : -50 W/(K*M**2)

FIG. 18.10 DQ/DT OCTOBER

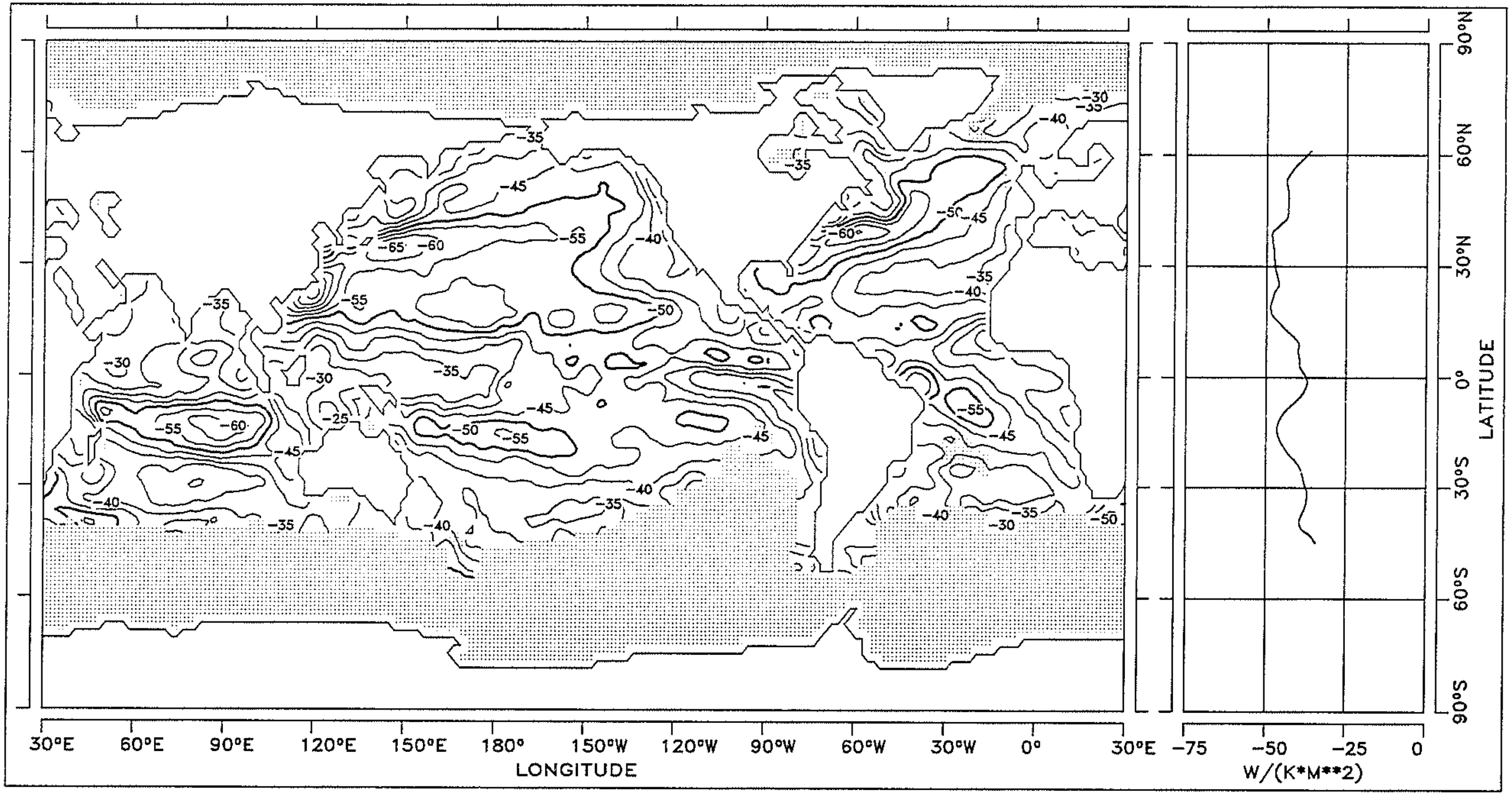

CONTOUR INTERVAL: 5 W/(K*M**2) REFERENCE LINE : -50 W/(K*M**2)

FIG. 18.11 DQ/DT NOVEMBER

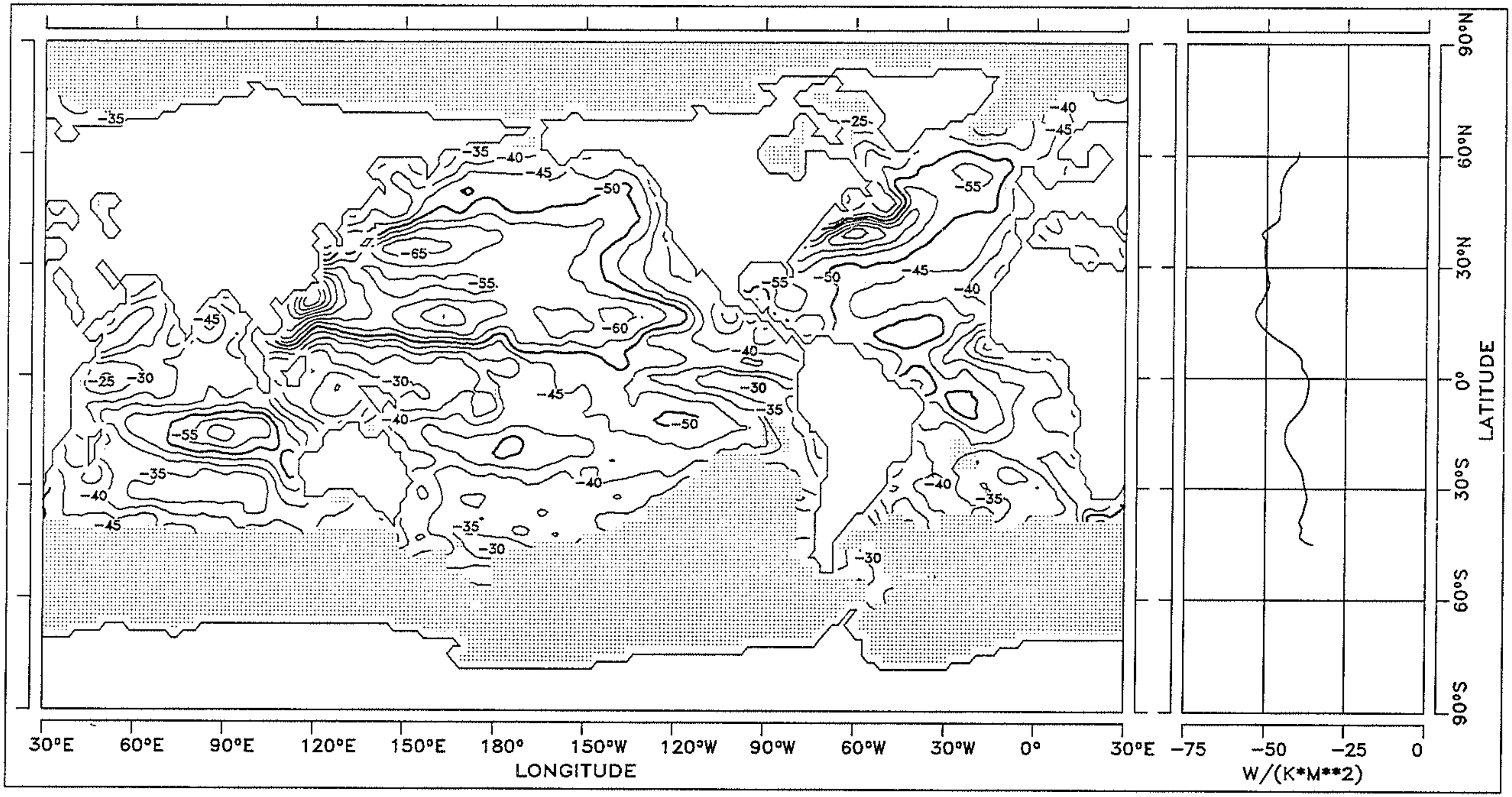

CONTOUR INTERVAL: 5 W/(K*M**2) REFERENCE LINE : -50 W/(K*M**2)

FIG. 18.12 DQ/DT DECEMBER

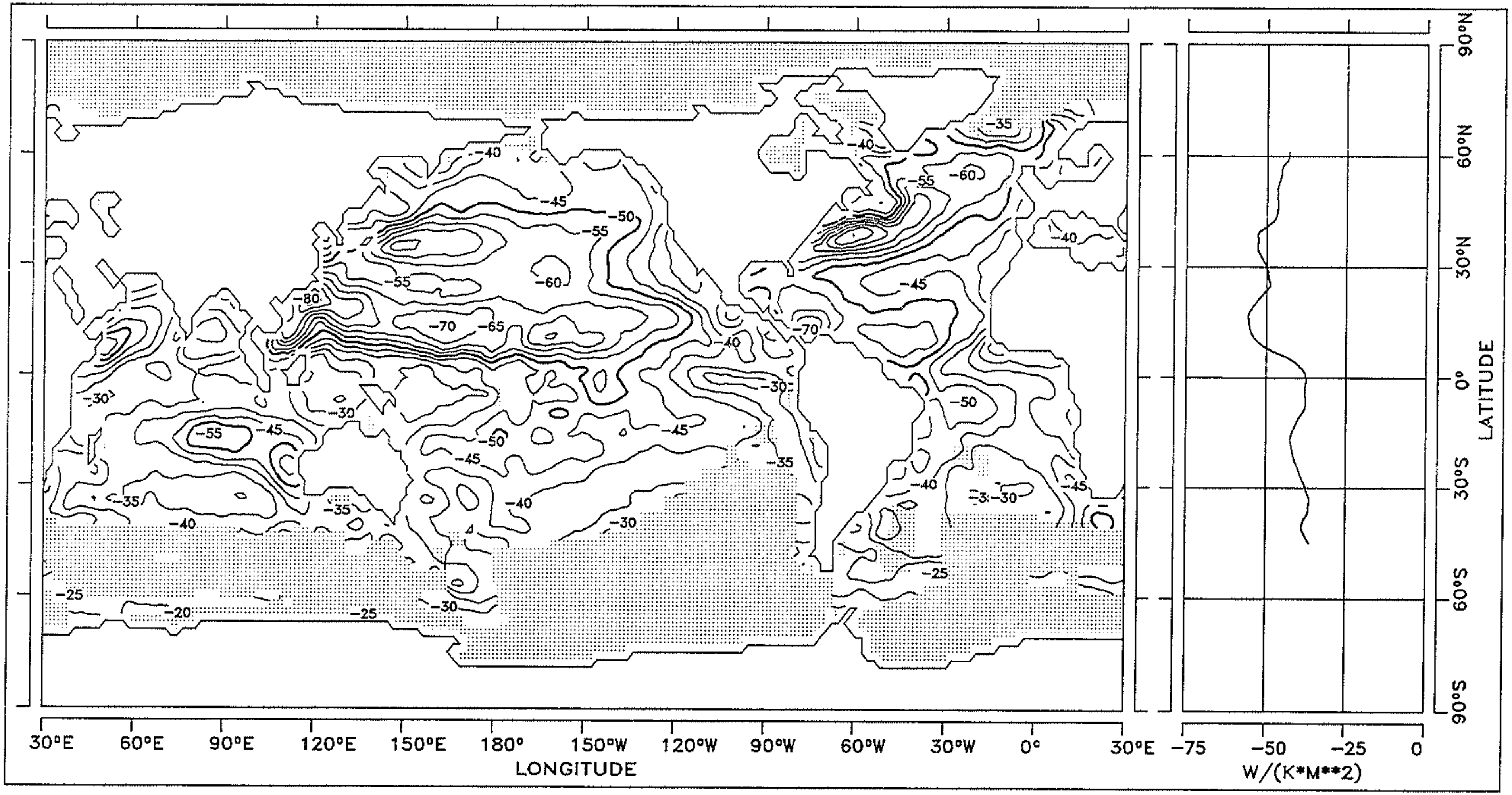

CONTOUR INTERVAL: 5 W/(K*M**2) REFERENCE LINE : -50 W/(K*M**2)

FIG. 18.13 DQ/DT ANNUAL MEAN

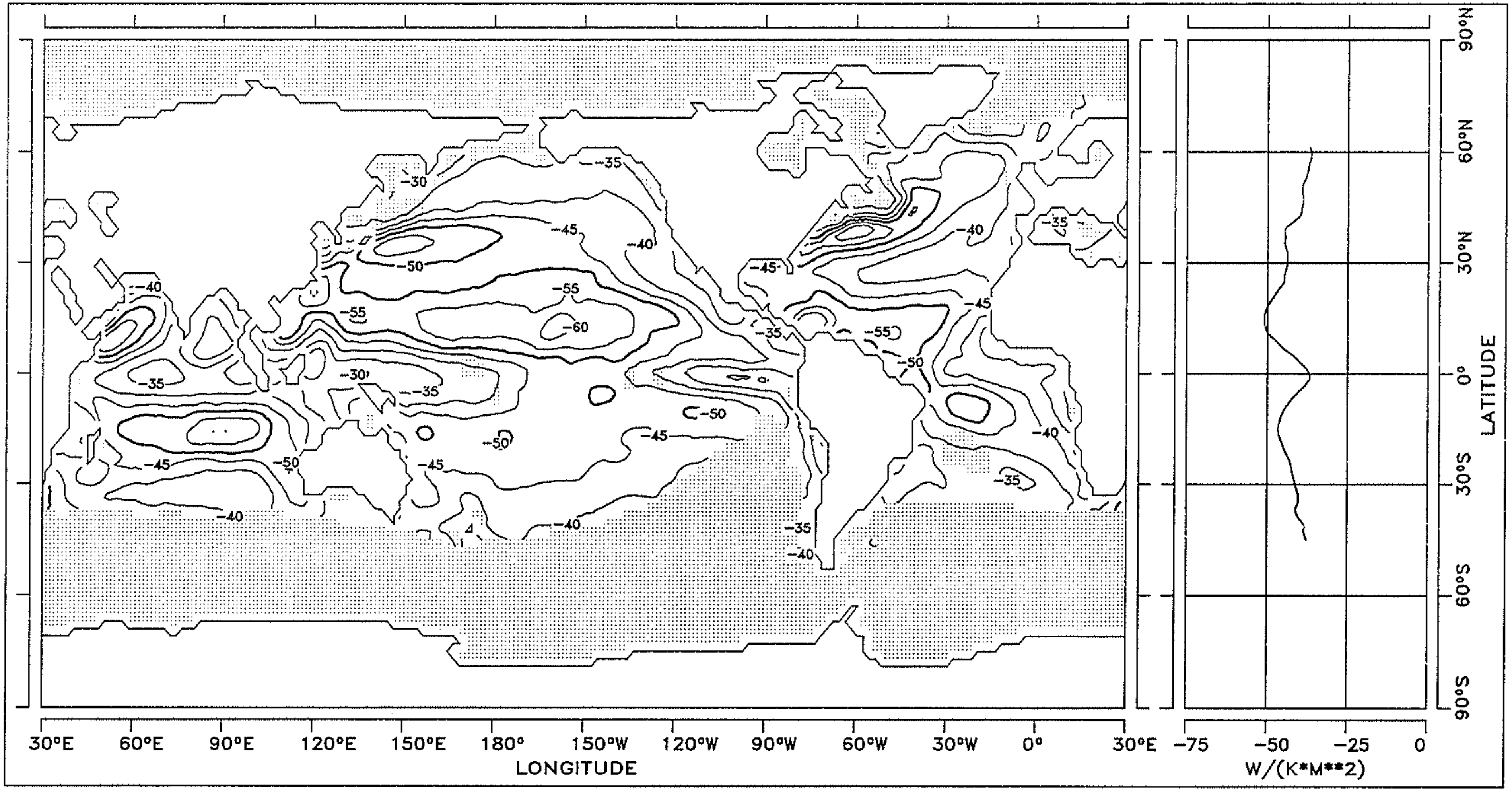

CONTOUR INTERVAL: 5 W/(K*M**2) REFERENCE LINE : -50 W/(K*M**2)

DRAG COEFFICIENT

FIG. 19.1 TRANSFER COEFFICIENT FOR LATENT HEAT JANUARY

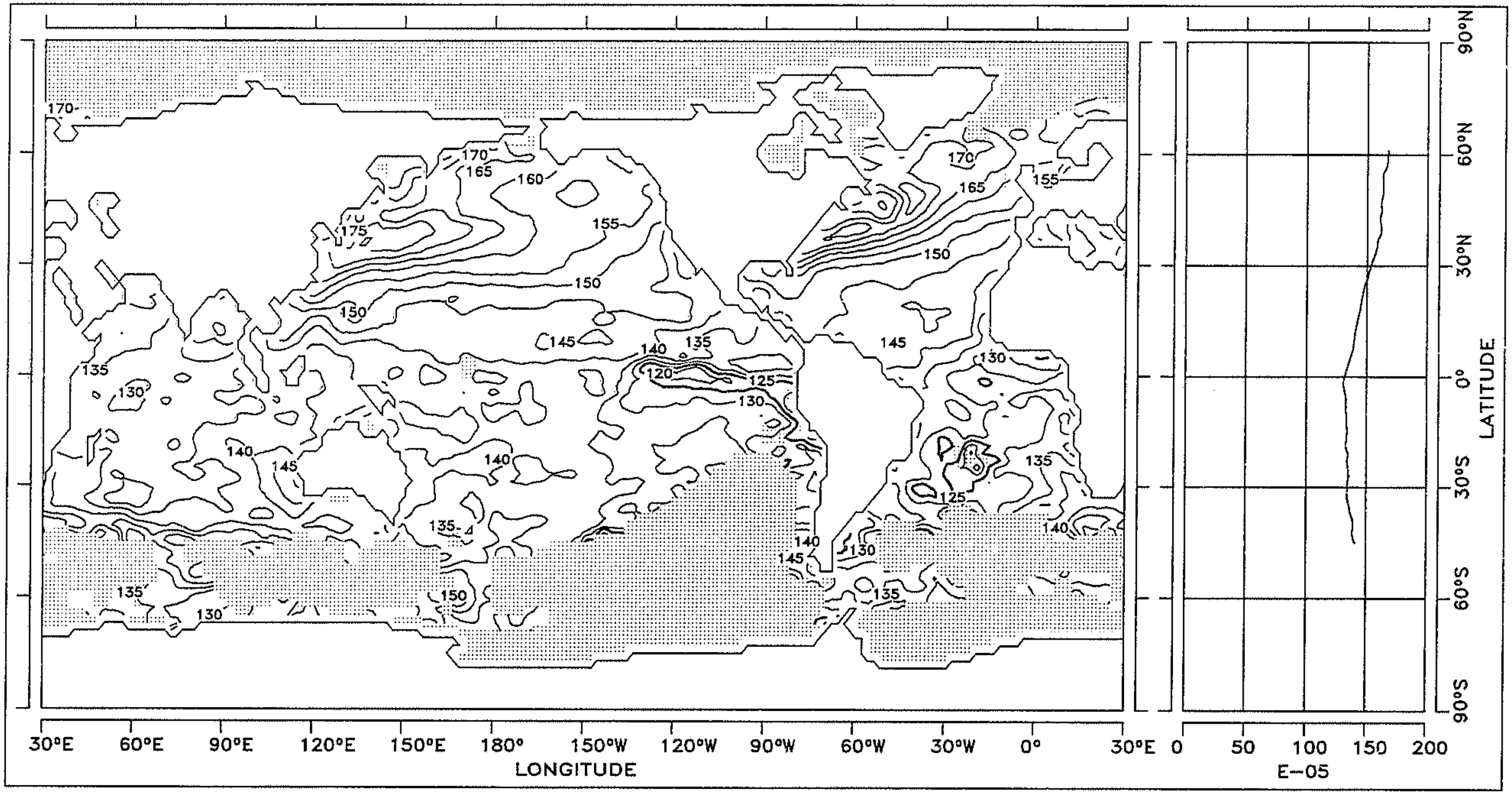

CONTOUR INTERVAL: 5 E−05 REFERENCE LINE : 125 E−05

FIG. 19.2 TRANSFER COEFFICIENT FOR LATENT HEAT FEBRUARY

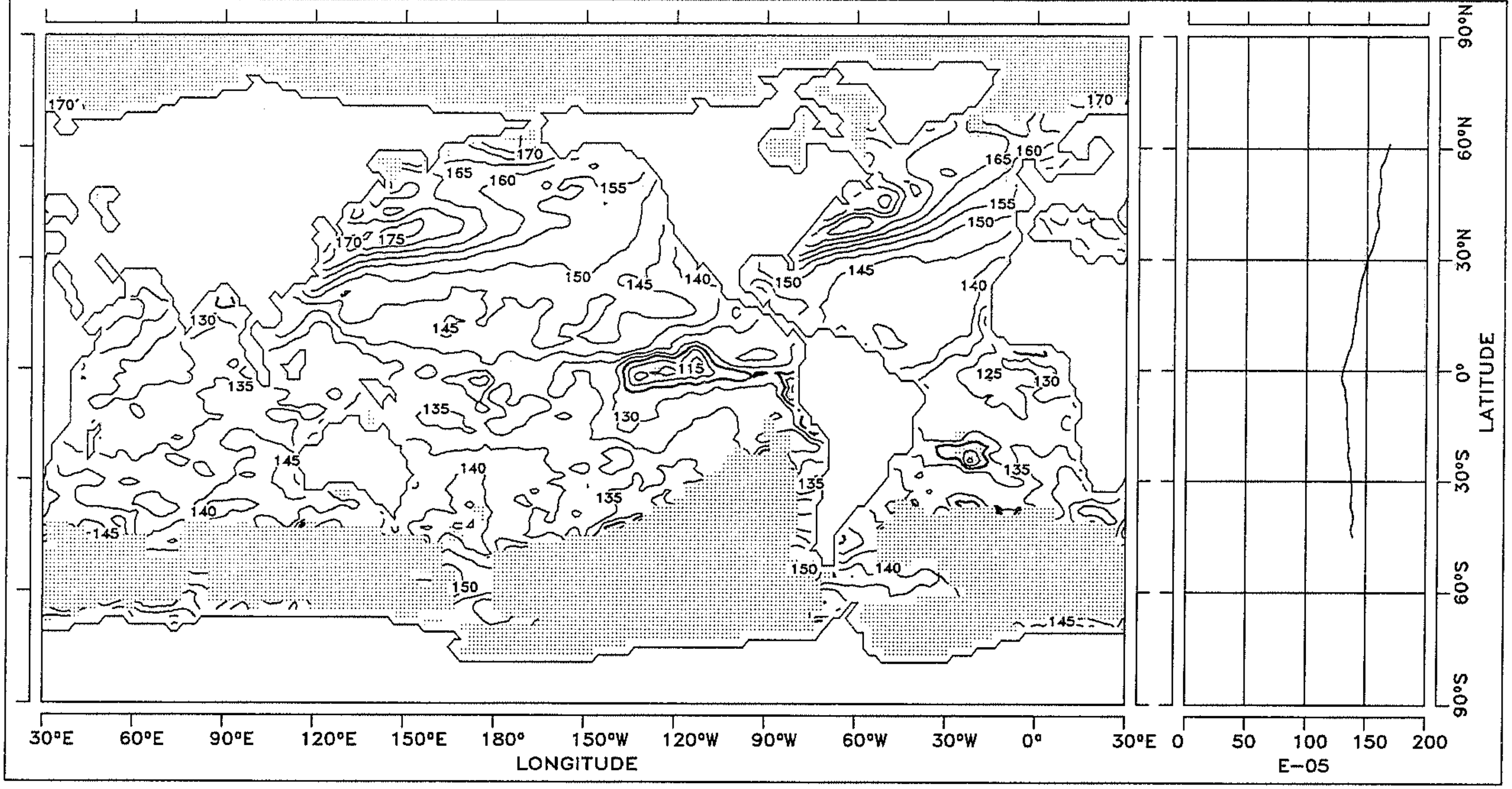

CONTOUR INTERVAL: 5 E–05 REFERENCE LINE : 125 E–05

FIG. 19.3 TRANSFER COEFFICIENT FOR LATENT HEAT MARCH

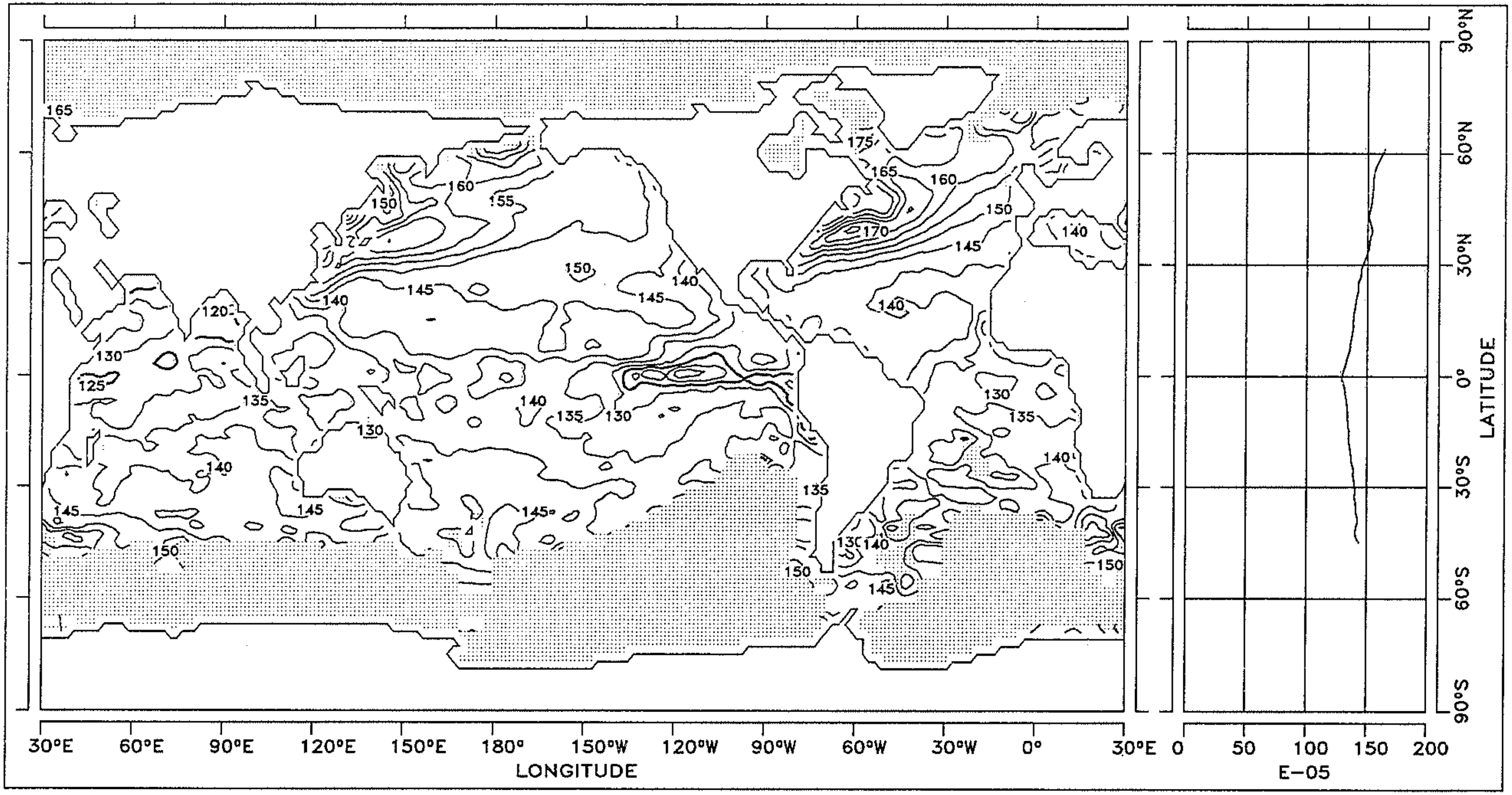

CONTOUR INTERVAL: 5 E-05 REFERENCE LINE : 125 E-05

FIG. 19.4 TRANSFER COEFFICIENT FOR LATENT HEAT APRIL

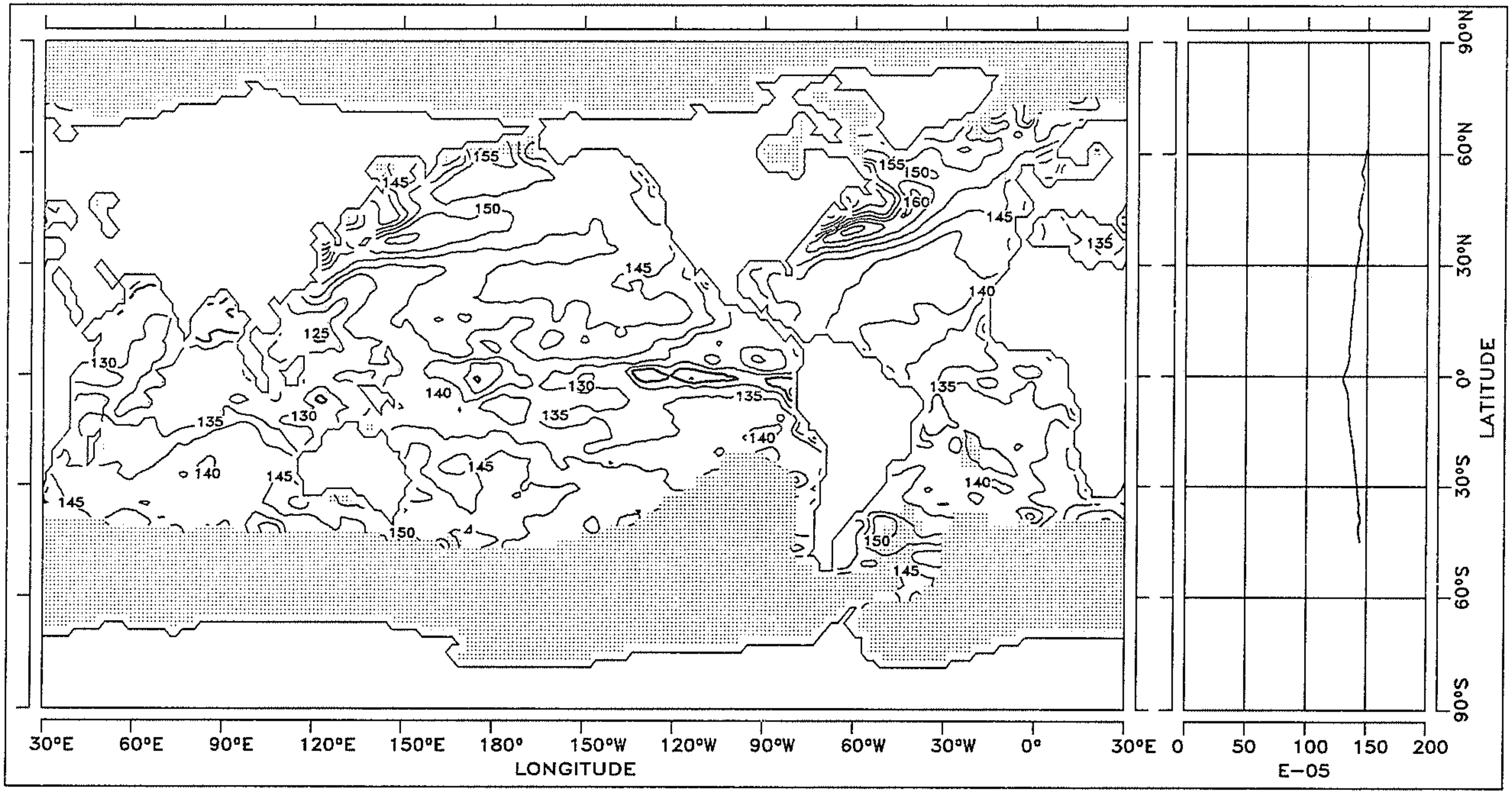

CONTOUR INTERVAL: 5 E−05 REFERENCE LINE : 125 E−05

FIG. 19.5 TRANSFER COEFFICIENT FOR LATENT HEAT MAY

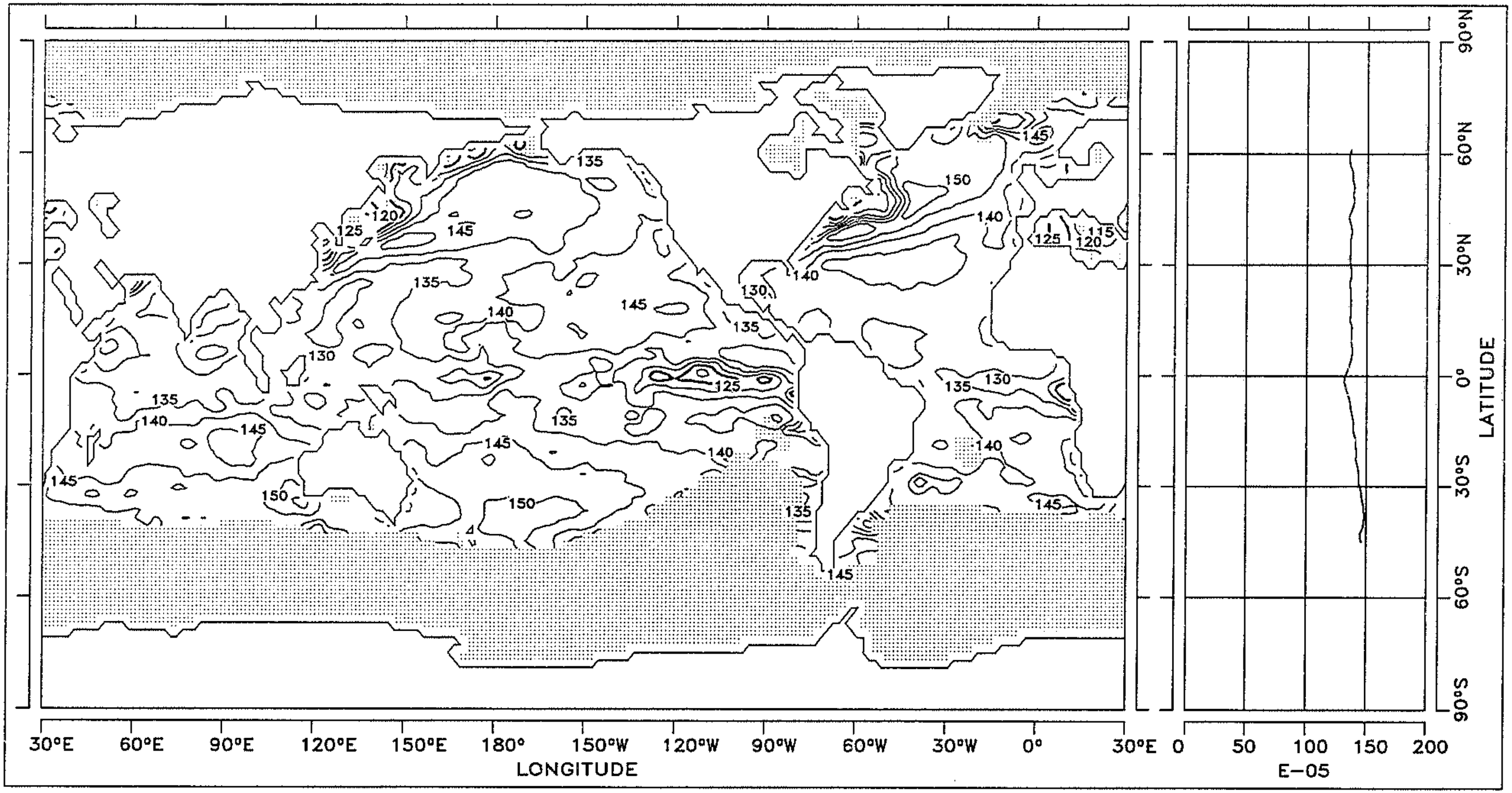

CONTOUR INTERVAL: 5 E-05 REFERENCE LINE : 125 E-05

FIG. 19.6 TRANSFER COEFFICIENT FOR LATENT HEAT JUNE

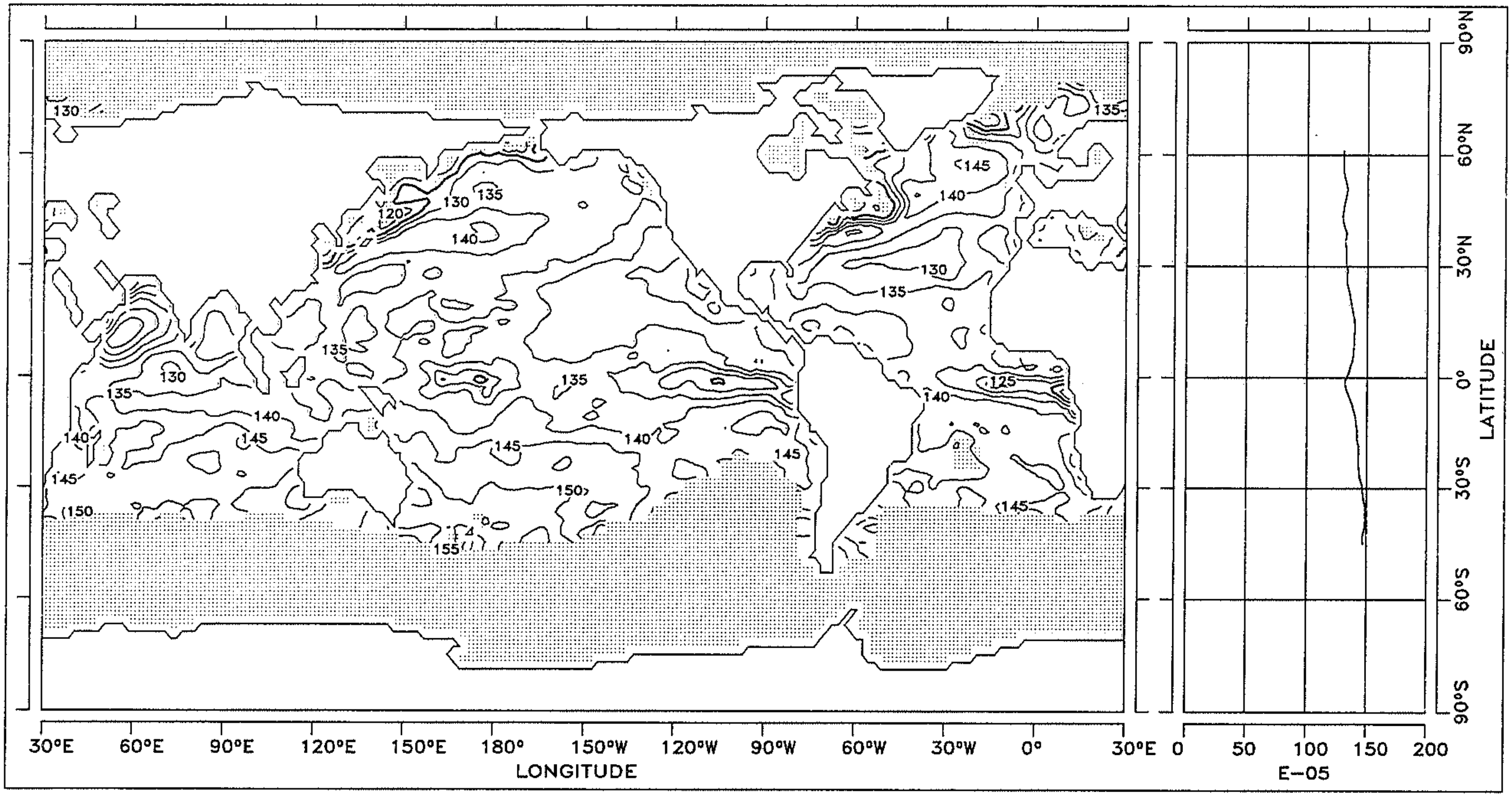

CONTOUR INTERVAL: 5 E−05 REFERENCE LINE : 125 E−05

FIG. 19.7 TRANSFER COEFFICIENT FOR LATENT HEAT JULY

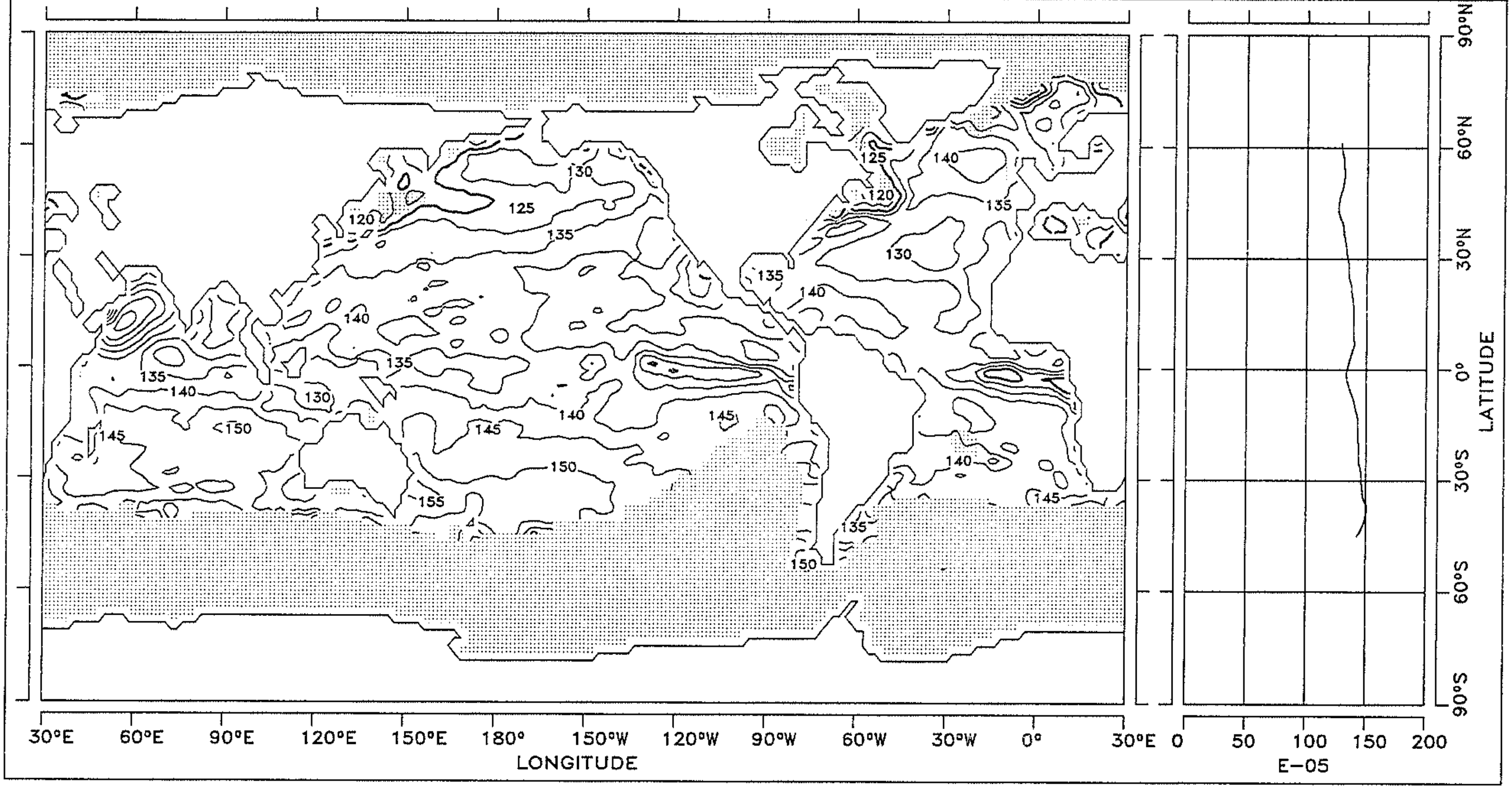

CONTOUR INTERVAL: 5 E-05 REFERENCE LINE : 125 E-05

FIG. 19.8 TRANSFER COEFFICIENT FOR LATENT HEAT AUGUST

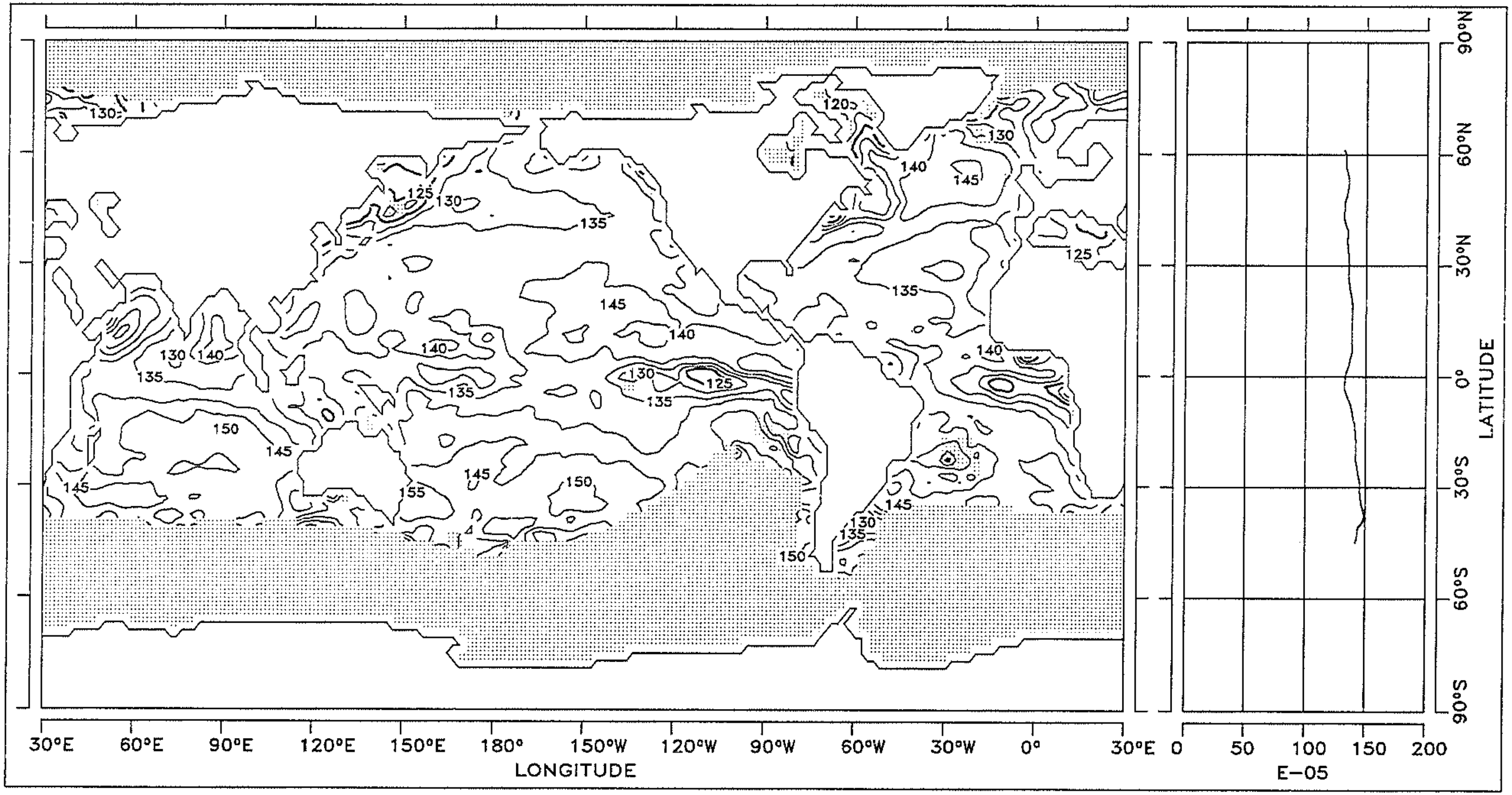

CONTOUR INTERVAL: 5 E−05 REFERENCE LINE : 125 E−05

FIG. 19.9 TRANSFER COEFFICIENT FOR LATENT HEAT SEPTEMBER

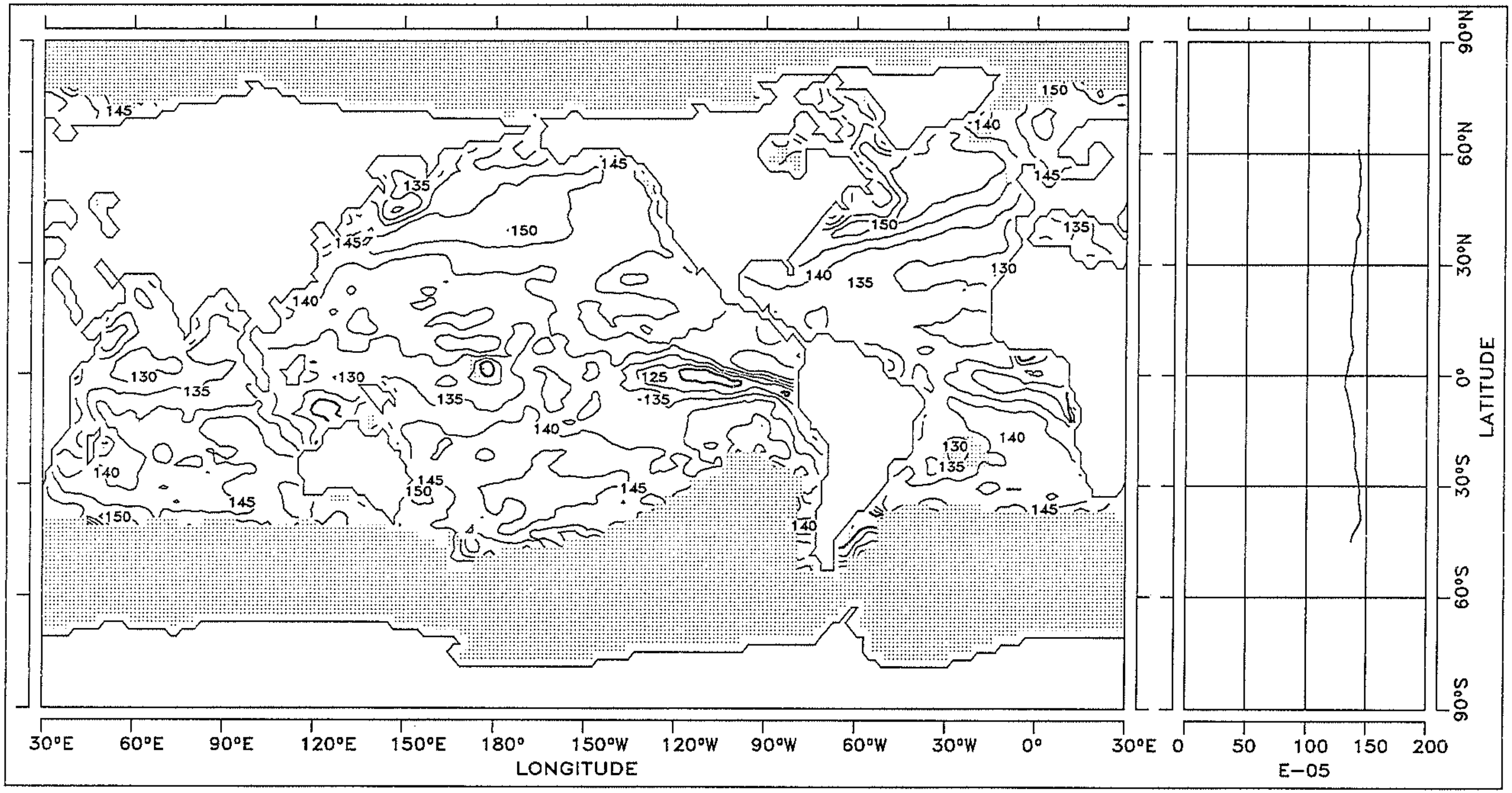

CONTOUR INTERVAL: 5 E-05 REFERENCE LINE : 125 E-05

FIG. 19.10 TRANSFER COEFFICIENT FOR LATENT HEAT OCTOBER

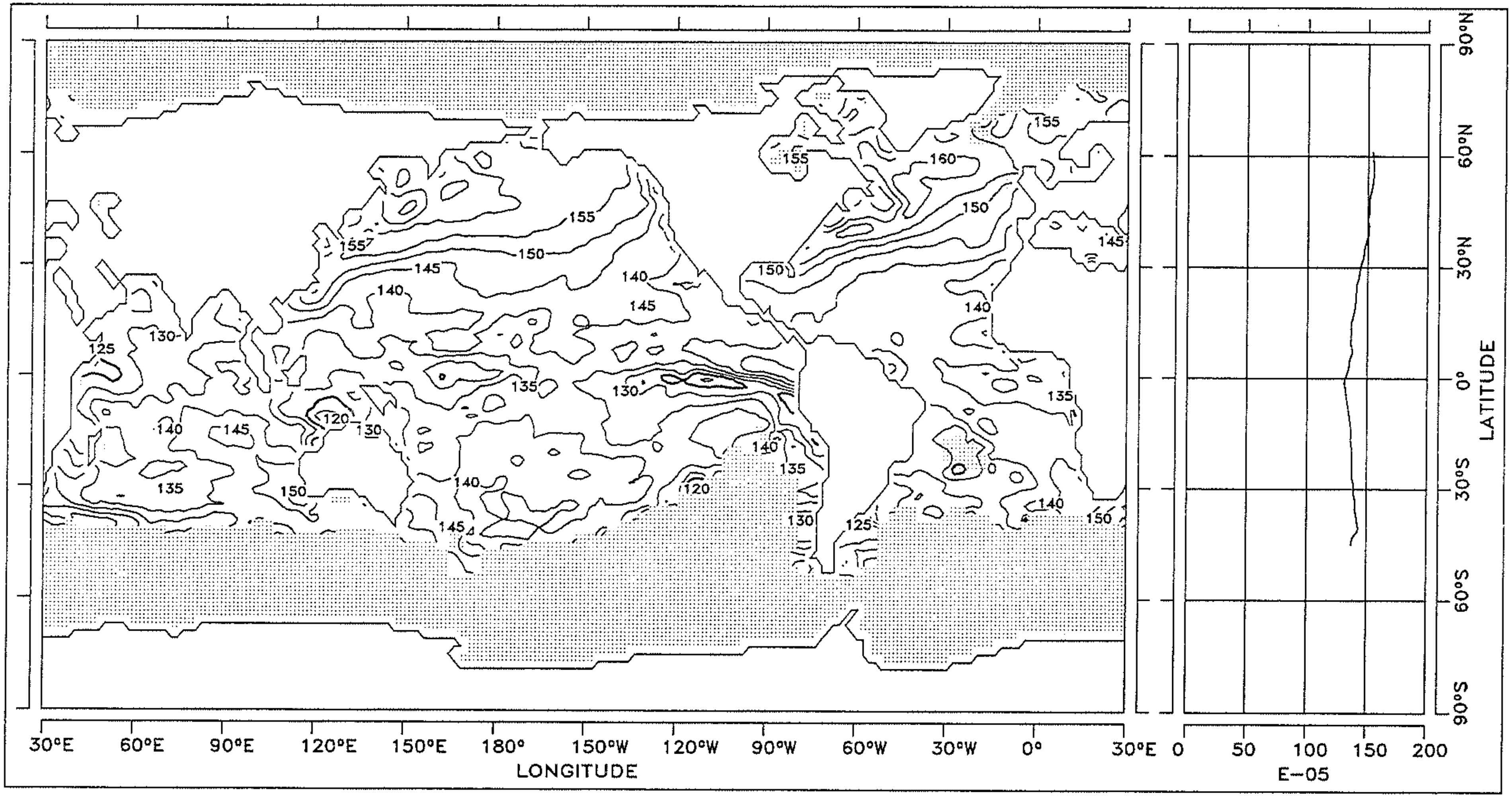

CONTOUR INTERVAL: 5 E–05 REFERENCE LINE : 125 E–05

FIG. 19.11 TRANSFER COEFFICIENT FOR LATENT HEAT NOVEMBER

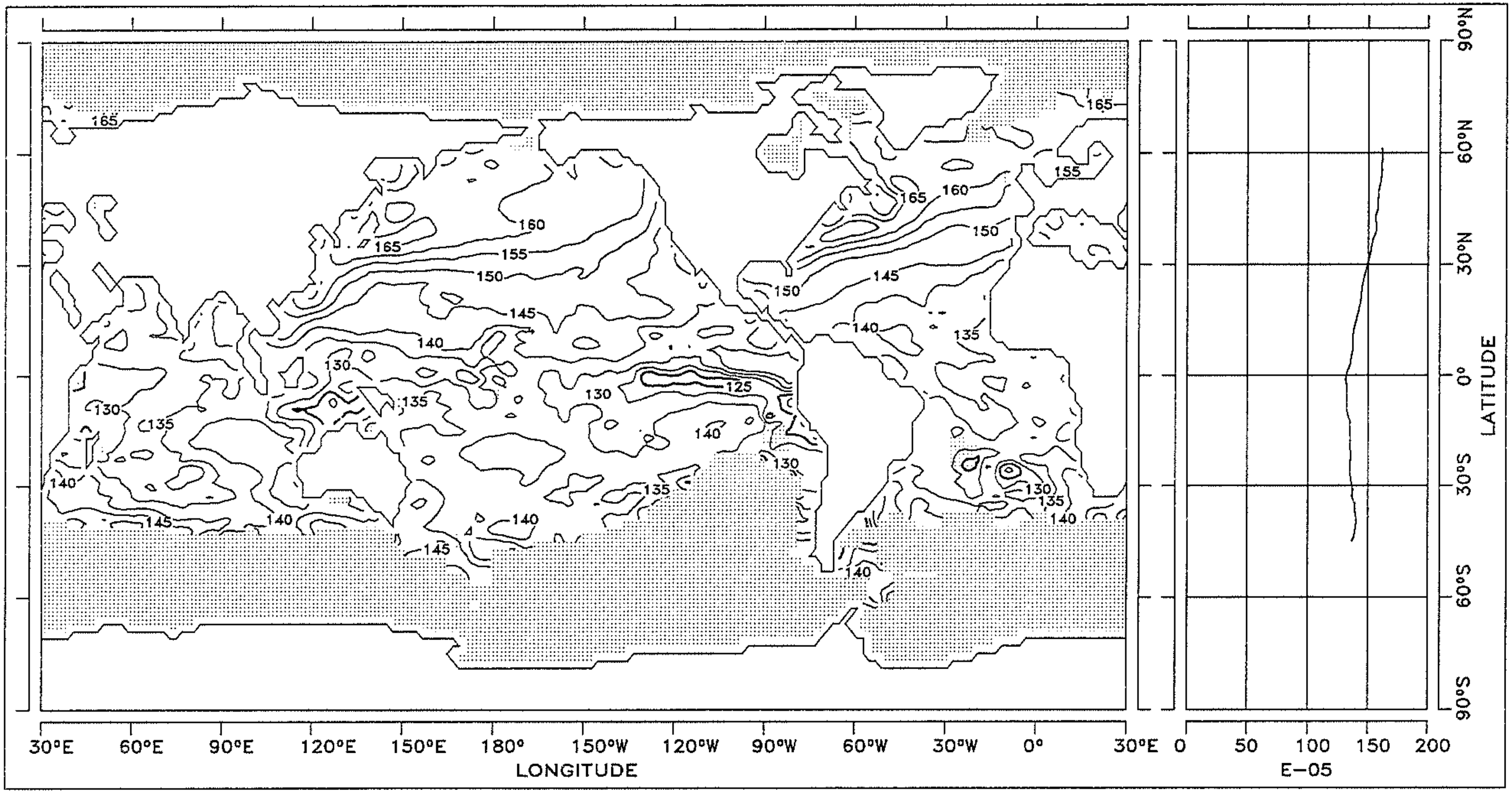

CONTOUR INTERVAL: 5 E-05 REFERENCE LINE : 125 E-05

FIG. 19.12 TRANSFER COEFFICIENT FOR LATENT HEAT DECEMBER

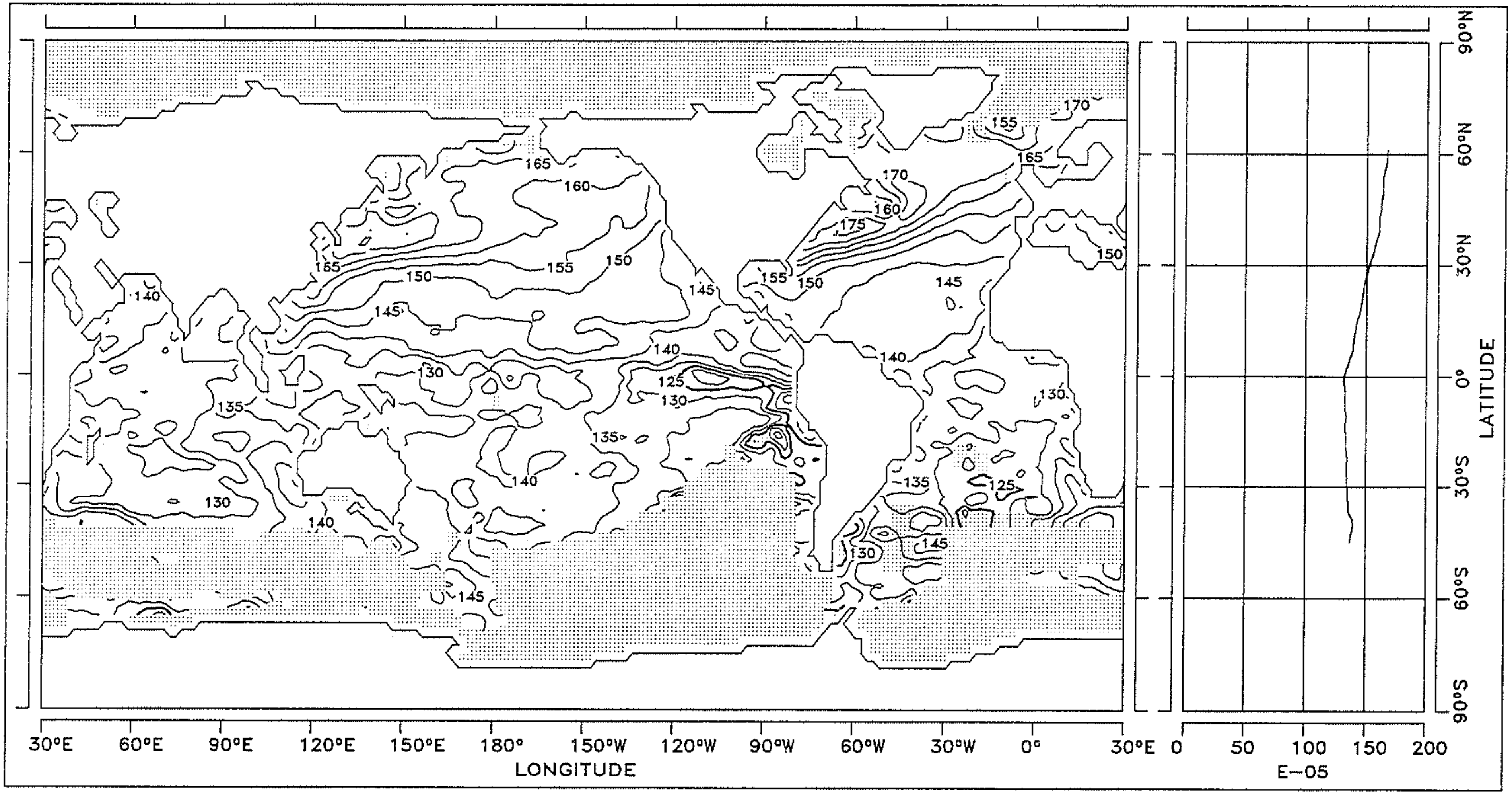

CONTOUR INTERVAL: 5 E–05 REFERENCE LINE : 125 E–05

FIG. 19.13 TRANSFER COEFFICIENT FOR LATENT HEAT ANNUAL MEAN

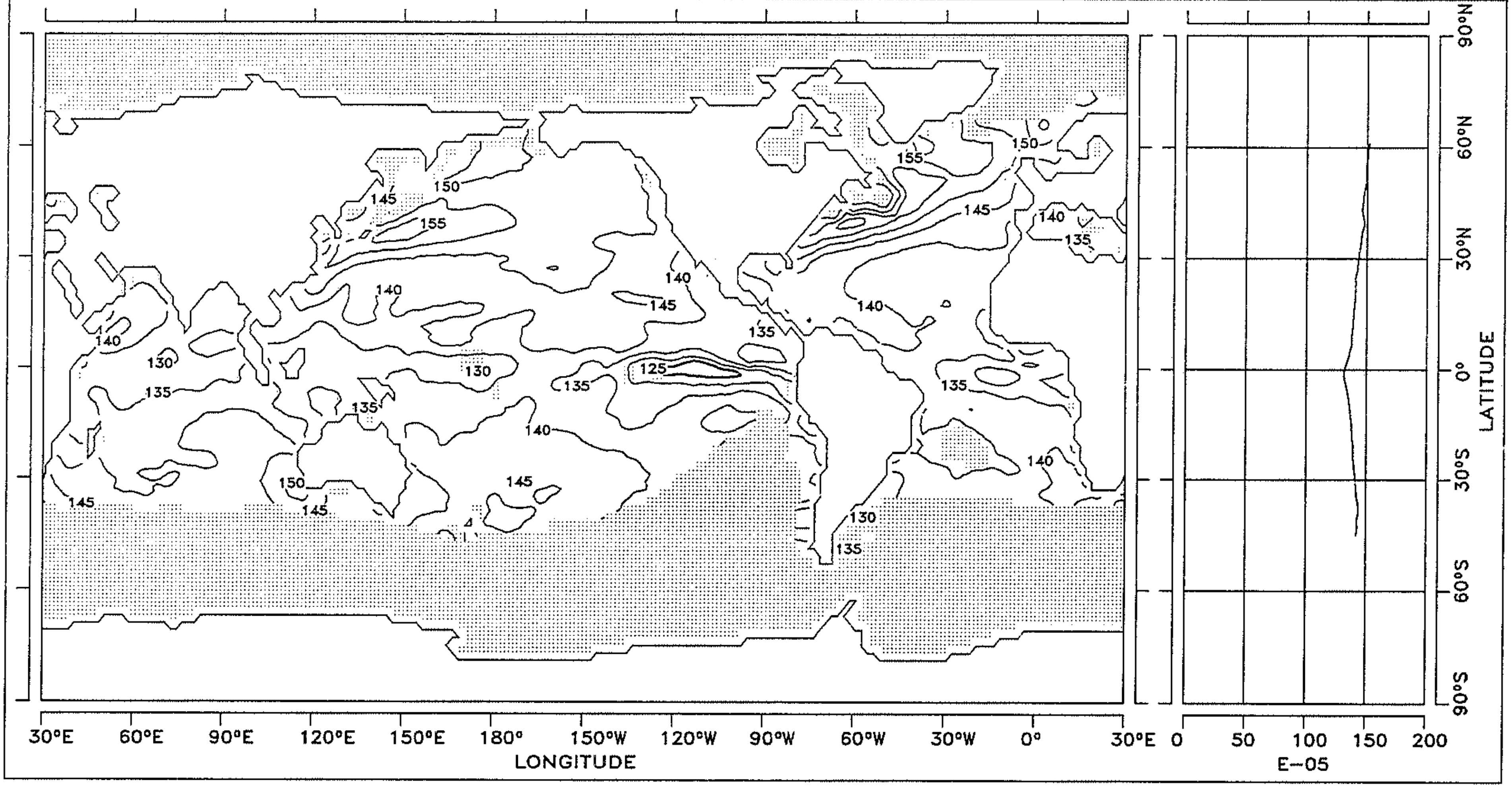

CONTOUR INTERVAL: 5 E−05 REFERENCE LINE : 125 E−05